Lateral Response of Monopiles in Sand under Monotonic and Cyclic Loads

A 3D Finite Element Investigation

FIRMAN HABIB (5041295)

28 September 2023

Delft University of Technology

TU Delft

lpdp

Van Oord
Marine ingenuity

Lateral Response of Monopiles in Sand under Monotonic and Cyclic Loads

A 3D Finite Element Investigation

by

Firman Habib

Student Name	Student Number
Firman Habib	5041295

To obtain the degree of Master of Science
at the Delft University of Technology,
to be defended publicly on Friday 29 Septmeber, 2023 at 15:00 CEST.

Project duration:	December 1, 2022 – September 22, 2023	
Thesis committee:	Federico Pisanò, Ph.D.	TU Delft, Committee Chair
	Luca Flessati, Ph.D.	TU Delft, Committee Vice Chair
	Evangelos Kementzetzidis, Ph.D.	TU Delft
	Haoyuan Liu, Ph.D.	NGI
	Kuen-Wei (Wayne) Wu, Ph.D.	Van Oord Offshore B.V.
	Naoual El Kanfoudi, M.Sc.	Van Oord Offshore B.V.

Faculty of Civil Engineering and Applied Earth Sciences

Cover: Windpark Fryslân (Self-documentation)

TU Delft lpdp Van Oord Marine ingenuity

Preface

In embarking on the journey of completing this master thesis, I am filled with profound gratitude for the multitude of individuals and entities who have played pivotal roles in my academic journey. Their unwavering support, guidance, and encouragement have been instrumental in shaping this work.

First and foremost, I extend my heartfelt thanks to the Almighty God for His blessings and guidance throughout this pursuit of knowledge.

To my cherished family, my mom (Elmi) and dad (Yulfahmi), I extend my deepest thanks. I am grateful for your unwavering support and for all the prayers you have sent my way. This achievement is as much yours as it is mine. To my sisters (Aisha, Fauzia, and Muthia), your constant support, jokes, and shared gossip never failed to lift my spirits. All of you trusted me to complete this academic journey, and I believe that, in the end, I have successfully achieved that goal.

I am deeply appreciative of the LPDP scholarship, which not only provided the financial support necessary for my studies but also instilled in me the responsibility to contribute positively to society through my academic endeavors.

My sincere appreciation goes out to the esteemed members of my thesis committee (Federico, Luca, Haoyuan, Vagelis, Wayne, and Naoual). Their guidance, critical feedback, and wealth of knowledge have been invaluable in shaping the direction and quality of this thesis.

I extend my gratitude to Van Oord for their collaboration, resources, and real-world insights that enriched my research and added practical depth to my academic journey. To my friends in PPI Delft, thank you for the camaraderie, shared stories, and laughter that made this journey memorable. Your support and companionship were a source of motivation and solace.

To my buddies, Widana, Ardhan, and Bagas, I know that your ears must be bleeding from hearing my indecent words and complaints in these last three months. I hope that your ears will fully recover once I graduate. Also to Alya, your encouragement during moments of self-doubt, and your belief in my abilities have been one of the driving forces behind the completion of this thesis. I appreciate your cooking skills though not as good as mine, have undoubtedly been delightful.

To all my friends, peers, mentors, and well-wishers who have contributed in countless ways, I offer my heartfelt thanks.

This thesis is a culmination of the collective efforts of all those mentioned above. It is my hope that it may stand as a small contribution to the field of study. With profound gratitude and humility, I present this work.

Firman Habib
Delft, September 2023

Abstract

Large-diameter monopiles serve as foundations for offshore wind turbines (OWT), and the diameters are now up to 10 meters. These monopiles exhibit lower embedded length-to-diameter (L/D) ratios compared to the conventional monopile that is widely employed in offshore oil and gas platforms. They undergo rotation when subjected to lateral loading like rigid or semi-rigid bodies. This distinct geometry necessitates a different approach to describe the soil reaction that is induced when a lateral load is applied. Previous research introduced a 1D model incorporating four soil spring components to represent four aspects of soil reaction namely lateral soil reaction, distributed moment, base shear force, and base moment. However, questions have arisen regarding the contributions of base components, specifically the base shear force and base moment, to maintaining monopile stability. In response, a series of monotonic loading tests on monopiles in dry sand is conducted to assess the contributions of base shear force and base moment to monopile stability. Following this assessment of base components, parametric analyses are carried out to investigate the effect of pile diameter (D), the L/D ratio, load eccentricity (e), and sand relative density on monopile responses under cyclic and monotonic lateral loading. In this study, the SANISAND-MS material model is employed within 3D Finite Element (FE) software to model ratcheting during cyclic lateral loading. Finally, an investigation is conducted with the aim of constructing a 0D model to represent base shear force and base displacement responses under both monotonic and cyclic lateral loading.

Keywords: *monopile, large-diameter, soil reaction model, monotonic, cyclic, base shear force, base moment, 3D FEM, parametric analysis*

Contents

List of Figures

List of Tables

Nomenclature

Abbreviations

Abbreviation	Definition
CCD	Cyclic Contour Diagram
CSL	Critical State Lines
CSR	Cyclic Stress Ratio
dof	degree-of-freedom
DSS	Direct Simple Shear
FE	Finite Element
LEPP	Linear Elastic Perfectly Plastic
MP	Monopile
OWF	Offshore Wind Farm
OWT	Offshore Wind Turbine
SLS	Serviceability Limit State
ULS	Serviceability Limit State
PTF	Push-To-Fail
R&D	Reserach and Development
RP/ rp	Rotational point
rf	Mesh refining factor
$p-y$	Lateral soil reaction - pile displacement curve
$M_d-\theta$	Distributed moment - pile rotation curve
WIP	Wished in place

Symbols

Symbol	Definition	Unit
c_3	Load transfer factor	[-]
D	Monopile outer diameter	[m]
D_r	Soil relative density	[-]
$D_{r,cr}$	Critical relative density	[-]
$\bar{e}$	Void ratio	[-]
$\bar{e}_{cr}$	Critical void ratio	[-]
e	Load eccentricity	[m]
e/D	ratio of load eccentricity against pile diameter	[-]
E_p	Pile stiffness	$[kN/m]$
E_pI_p	Pile Bending stiffness	$[kNm^2]$
E_{SL}	Soil Elasticity Modulus	$[kN/m]$
F_b	Base shear force	$[kN]$
f_b	Horizontal shear resistance at the pile base	$[kN/m^2]$
$F_{b,max}$	Maximum base shear force	$[kN]$
$f_{b,max}$	Maximum horizontal shear resistance at the pile base	$[kN/m^2]$
$F_{b,ref}$	Maximum hypothetical base shear force	[kN]
f_z	Nodal reaction force in z- direction	[kN/m]
G	Shear modulus	$[kN/m]$
H	Applied lateral load	$[kN]$
H_{ave}	Average amplitude of cyclic load	[kN]

Symbol	Definition	Unit
H_{cy}	Regular cyclic load variation	[kN]
H_{max}	Maximum applied load during cyclic loading	[kN]
H_{min}	Minimum applied load during cyclic loading	[kN]
H_{ult}	Ultimate lateral capacity	$[kN]$
k	Modulus sub-grade reaction	$[kN/m^3]$
$K^{sec}_{cy,b}$	Cyclic secant stiffness at the pile base	[kN/m]
$K^{S}_{m\theta}$	Local shaft $m-\theta$ stiffness	[-]
$K^{B}_{m\theta}$	Base rotational stiffness	[-]
K_r	Relative Stiffness	[-]
k_s	Secant stiffness at the center of cycle	[kN/m]
k_{sl}	Secant loading stiffness	[kN/m]
k_{su}	Secant unloading stiffness	[kN/m]
k_N	Cyclic secant stiffness at N^{th} cycle	[kN/m]
K_b, K_c	Dimensionless parameter depends on the load characteristic and D_r	
L	Monopile embedded length	$[m]$
L/D	ratio of pile embedded length against pile diameter	[-]
M	Applied external moment	$[kNm]$
M_b	Base moment	$[kNm]$
M_d	Distributed Moment	$[kNm/m]$
M_{Fb}	Moment from base shear force	$[kNm]$
M_{ult}	Ultimate moment capacity	$[kNm]$
N	Number of cycles	[-]
p	Lateral Soil Reaction	$[kN/m^2]$
q	Deviatoric stress	$[kN/m^2]$
Q	Weight of tower, substructure, and rotor from OWT	$[kN]$
p'	Mean effective stress	$[kN/m^2]$
p_{atm}	Reference atmospheric pressure	$[101kN/m^2]$
p'_{cr}	Soil mean effective stress at rest	$[kN/m^2]$
T_u, T_b	Parameters that depend on load characteristic and relative density	[-]
U_L	hydrostatic force	$[kN]$
W_t	Total resulting vertical force acting on pile tip	$[kN]$
W_s	Weight of soil within the pile	$[kN]$
y_{acc}	Accumulated displacement	$[m]$
$y_{acc,b}$	Accumulated base displacement	$[m]$
y_b	Displacement at pile base	$[m]$
$y_{b,cr}$	Critical base displacement	$[m]$
y_{sb}	Pile displacement at the mudline	$[m]$
$y_{sb,u}$	Pile ultimate displacement at the mudline	$[m]$
β	Dimensionless shaft friction factor for cohesionless soil	[-]
Δ_z	Discretization size for pile nodal stress extraction	[m]
γ	Unit weight	$[kN/m^3]$
γ_{dry}	Dry unit weight of soil	$[kN/m^3]$
ν	Poisson Ration	[-]
ϕ	angle of friction	$[^o]$
ϕ_{cr}	critical state friction angle	$[^o]$
ϕ_i	interface peak friction angle	$[^o]$
ϕ_{peak}	peak friction angle	$[^o]$
ϕ_{soil}	soil peak friction angle	$[^o]$
Ψ	Soil state parameter	[-]

Symbol	Definition	Unit
ΣM_p	Total moment induce by lateral soil reaction	$[kNm]$
ΣM_d	Total distributed moment	$[kNm]$
σ'_N	Normal effective stress	$[kN/m^2]$
Σp	Integration of lateral soil reaction over embedded length	$[kN]$
σ'_{zz}	Vertical effective stress	$[kN/m^2]$
τ_1	Horizontal shear stress	$[kN/m^2]$
τ_2	Vertical shear stress	$[kN/m^2]$
θ	Rotation along the pile	$[^o]$
θ_{sb}	Rotation at the mudline/seabed	$[^o]$
θ_b	Rotation at the pile base	$[^o]$
θ_L	Lode angle	$[^o]$
θ_N	Pile rotation at Nth cycle at the mudline	$[^o]$
θ_0	Pile rotation at the first cycle	$[^o]$
θ_s	Pile rotation at monotonic load	$[^o]$
ζ_b, ζ_c	cyclic load characteristic parameters	[-]

1 Introduction

In 2019, the European Union (EU) signed the European Green Deal, which aims to reduce net greenhouse emissions by 55% by 2030, compared to the level at 1990's, and make Europe the first climate-neutral continent by 2050 [1]. A massive investment in the required infrastructure to produce cleaner and renewable energy is necessary to meet such an ambitious vision. To date, offshore wind energy is named as one of the innovation accelerators to support a sustainable future [2]. In the future, offshore wind farms will only become larger, generate more power, and have less environmental impact [3].

1.1. Background

Offshore Wind energy is a renewable energy resource that plays a vital role in achieving carbon neutrality. Between 2012 and 2030, the compound annual growth of offshore wind is more than 20% [4]. Offshore wind energy become the main option due to lower carbon dioxide emissions, and the carbon footprint of wind power is comparable to or even lower than other non-fossil energy generation technologies [5]. Despite its competitiveness, a wind energy project is capital intensive, with the fixed assets (wind turbine, gird connection, and civil works) accounting for about 80% of the total cost [6]. To make offshore wind energy projects more competitive and reduce the cost, the R&D to optimize the main component of wind-farm becomes highly important.

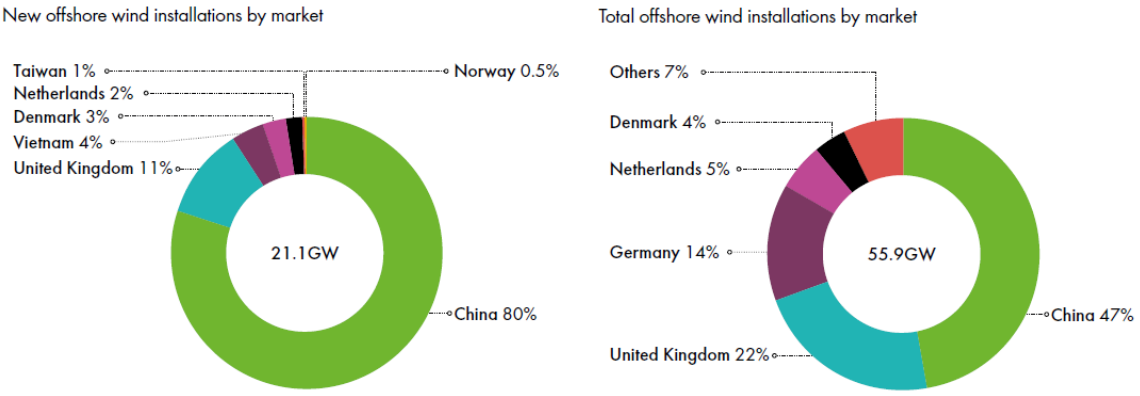

(a) New installation

(b) Total installed capacity

Figure 1.1: Offshore wind energy installation in 2021 (GWEC Market Intelegence; [7]).

By the end of 2021, the cumulative installed capacity reached nearly 56 GW, as illustrated in Figure 1.1a. Among this installed capacity, China and the UK shared the largest portions, constituting 47% and 22% of the total, respectively, as depicted in Figure 1.1b. Beyond these regions, Taiwan (109 MW) and Vietnam (779 MW, inter-tidal only) also registered notable increments in offshore wind energy installations during 2021 [7].

Due to the fluctuations in fossil fuel prices and the influence of global geopolitical dynamics, the long-term outlook for the global offshore wind market is exceedingly promising. An investigation by [7] has indicated an average growth rate of 6.3% leading up to 2026, which is projected to surge to 13.9% until the subsequent decade. By the end of this decade, the installation of 50 GW of offshore wind power is anticipated, as depicted in Figure 1.2. A study [7] suggests that the European and Chinese markets will continue to dominate the offshore wind market, with the European market growth projected to surpass China within this decade.

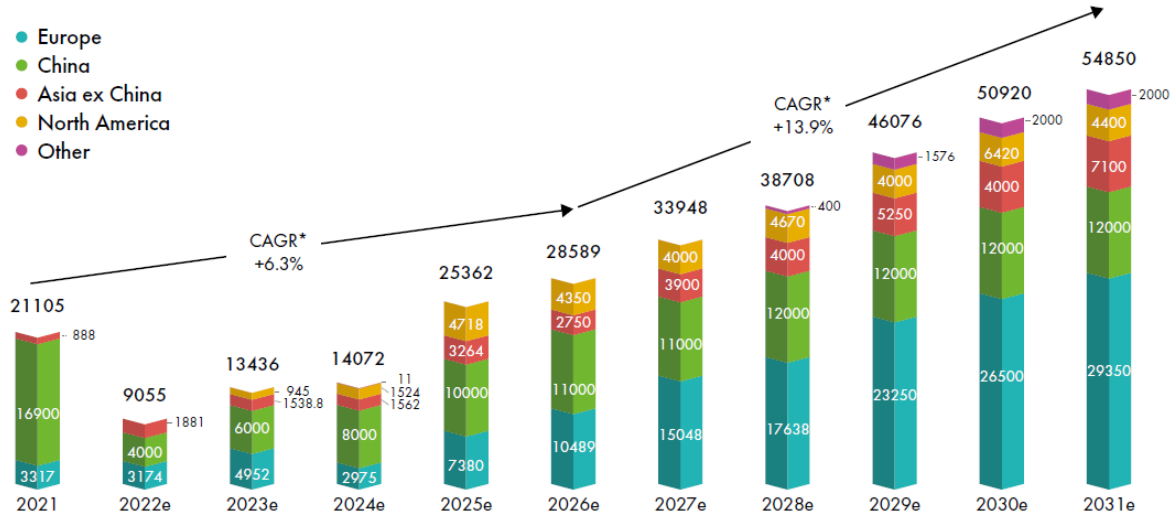

Figure 1.2: Prediction of global new offshore wind installation from 2022 to 2031 [7].

The anticipated expansion of the offshore wind market will involve venturing into deeper waters, which will pose greater wave and wind loads. However, despite upcoming advancements in foundation types, the large-diameter monopile remains the favored choice and is expected to facilitate the rapid growth of offshore wind in the foreseeable future.

Several choices exist for the fixed-bottom foundation, supporting offshore wind turbines (OWTs). These options include gravity base foundation, monopile, mono-caisson, multi-pile, and multi-caisson (Figure 1.3). The site conditions heavily influence the cost-effectiveness of a specific design concept. The utilization of monopile structures becomes advantageous in areas where the surface conditions are unfavorable, and the depth of the water is below 35 meters [8].

Most of the installed OWTs were constructed above the fixed-bottom foundation. At the end of 2021, monopile became the dominant foundation type that supports 64.4% of the total installed capacity in the market [11]. Even there is an indication of a declining proportion of monopile in the newly announced market, representing 56.5% of the overall market. Due to the advanced stage of industrialization and maturity in monopile production, they generally offer a cost advantage and are projected to maintain their dominant position [11].

Currently, the design, manufacturing, and installation of the substructure account for approximately

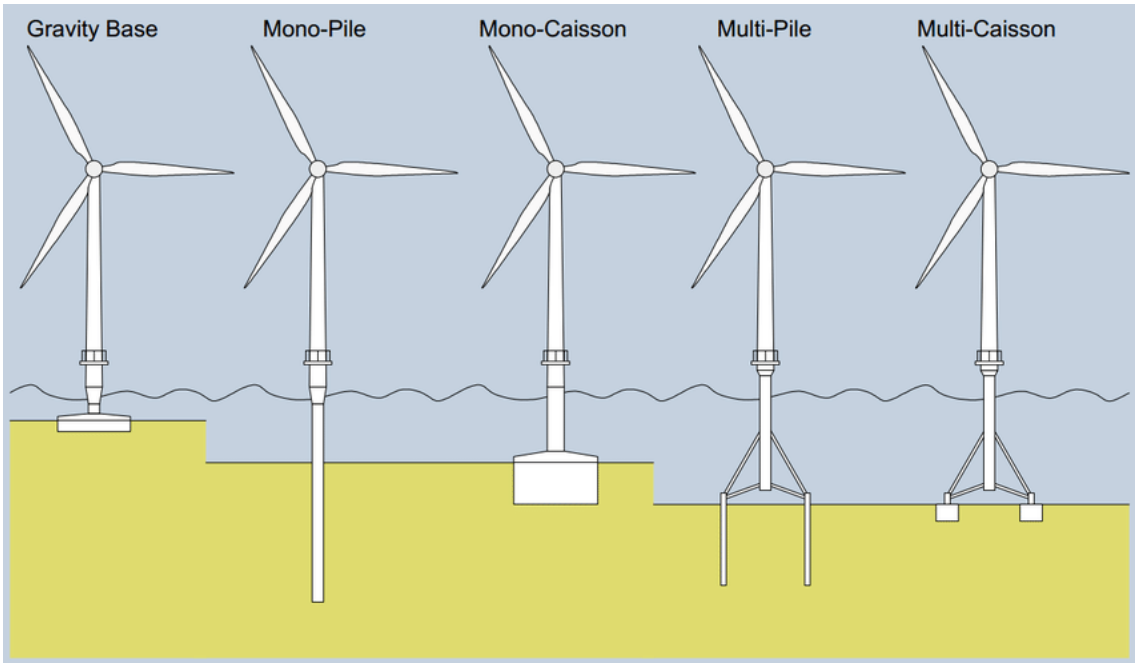

Figure 1.3: Fixed-bottom foundation types for offshore wind turbines ([9]).

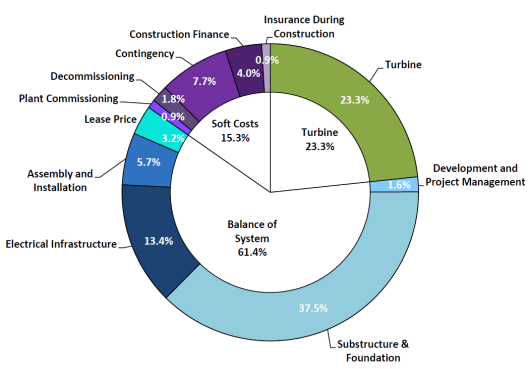

(a) Floating offshore wind

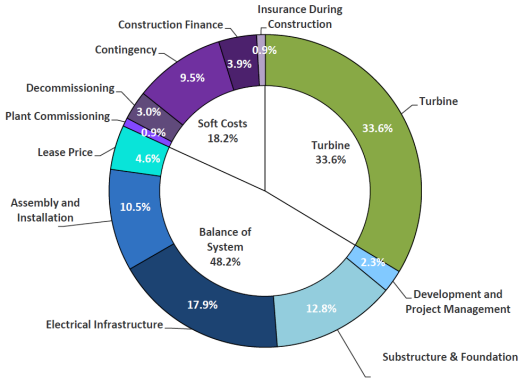

(b) Fixed-bottom offshore wind

Figure 1.4: Offshore wind system capital expenditure component cost breakdown ([10]).

13% to 37% of the total investment necessary for offshore wind turbines, depending on the type of chosen foundation (Figure 1.4). Due to the significant investment in its substructure, such as the monopile, a wind turbine is designed to remain operational for a lifespan of 25 to 30 years to offer economic benefits [12].

Throughout its lifespan, the monopile must endure challenging environmental conditions characterized by multiple loads of moderate intensity ranging from 10^8 to 10^9 cycles [13]. These cyclic loading and unloading processes can result in a permanent rotation of the structure and the accumulation of plastic strain. Throughout the operational lifespan of an OWT, the permanent rotation due to cyclic lateral load should not exceed the serviceability limit state (SLS) failure criteria.

Accurate prediction of cyclic lateral deformation is crucial to meet the strict SLS and ULS criteria. Some literature defines OWT failure criteria as the permanent rotation at the mudline equal to 0.25^o [15] and 0.5^o [16]. However, the cyclic behavior of soils is a complex phenomenon that directly affects the stiffness of the monopile and the accumulation of lateral deformation (Figure 1.5).

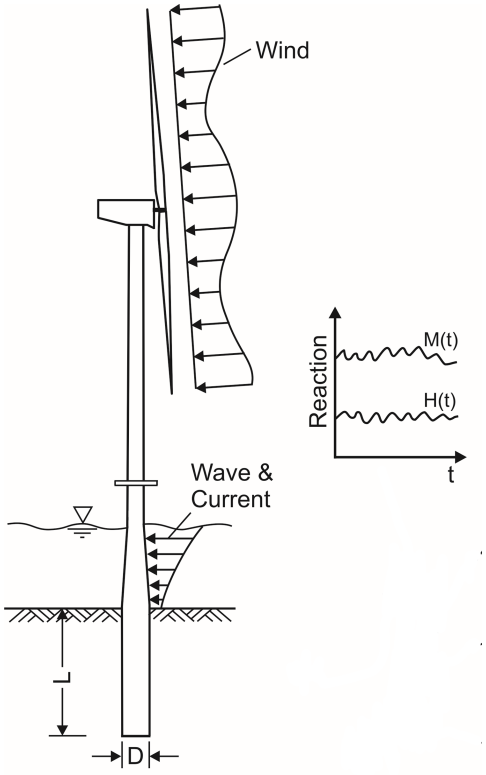

Figure 1.5: Monopile foundation of an offshore wind turbine under lateral load - modified after [14] (M(t) and H(t) indicate moment and lateral load evolution during the OWT lifetime).

To gain insight into this behavior, cyclic testing is typically conducted either in laboratory or field settings, providing valuable information on the interaction between the monopile and soil during cyclic lateral loading. However, due to high costs and experimental complexities, field tests and physical modeling are not always feasible. To encounter this problem, 3D finite element (FE) analysis is employed to simulate this process in the current project. The use of 3D FE analysis is considered advantageous as it allows for a more realistic representation of soil response, requiring fewer simplifications and assumptions in the modeling process.

1.2. Research Motivation

To expedite the growth of offshore wind energy and the impact of cyclic lateral loading, it is crucial to conduct research to optimize the monopile design. The design of monopile that experience lateral and overturning loads commonly employs the *p-y* method, which is based on the Winkler approach [17]. This method is widely recommended by several offshore design codes [15], [18]. It is already known that the conventional *p-y* method fails to accurately depict the behavior of large-diameter monopiles that are widely used in offshore wind turbine construction [8], [19]. However, current design practice continues to rely on 1D soil-spring model by modifying the conventional approach by adding more spring elements or introducing additional parameters. [20].

The utilization of a 1D model such as the *p-y* curve presents the advantage of yielding results with minimal computational time. This has led to significant research endeavors aimed at modifying the conventional *p-y* curve to align it with responses to cyclic loading [14], [20], [21]. Another primary motivation behind advancing the *p-y* curve is to model the soil interaction with large-diameter monopiles,

which initially encounter challenges and uncertainties with the conventional *p-y*. To address uncertainties associated with the behavior of large-diameter monopiles under both monotonic and cyclic lateral loading conditions, numerous research initiatives have been conducted. Notably, projects such as PISA [19], PICASO in the UK [19], [22], and the ongoing MIDAS project in The Netherlands [23] have contributed to this field. This thesis project forms part of the MIDAS (Monopile Improved Design through Advanced cyclic Soil modeling) initiative, with its primary focus being the application of 3D FE analysis to simulate the monopile response to cyclic lateral loading. Moreover, the project seeks to obtain information that can be used to correlate the outcomes obtained through the 3D FE analysis and the 1D model.

The primary objective of this thesis project is to comprehensively investigate the behavior of monopile-soil systems subjected to lateral cyclic loading. This is achieved through the utilization of 3D finite element (FE) analysis, facilitated by the PLAXIS 3D software. To accurately capture the cyclic response of sand, the study incorporates the application of the newly developed SANISAND-MS constitutive model, as introduced by [24]. Within this framework, the research investigates the impact of varying monopile geometry and sand relative density on the cyclic behavior of monopiles. Parameters under investigation encompass pile diameter, embedded length, load eccentricity, and soil relative density. The important aspect of this investigation is the assessment of soil reaction at the base of the pile, an aspect often overlooked in conventional slender monopile analyses. The numerical outcomes generated through the 3D FE analysis are analyzed and discussed, with the intent to provide information for the future development of a 0D model capable of effectively representing the soil base reaction curve.

1.3. Research Questions

Looking at previous studies, it is evident that existing research has not provided a clear directive for evaluating the influence of the force exerted at the pile base on the stability of large-diameter monopiles. As a result, the primary aim of this thesis is to thoroughly investigate the factors originating from the pile base that contribute to the overall stability of both moment and lateral forces. To fulfill this objective, the acquired data from the MIDAS project, involving both centrifuge tests and laboratory experiments, is used to conduct 3D FE analyses. This research aims to address these aspects, and the main as well as sub-research questions, are outlined below.

"How do the base shear force and base moment components affect monopile in sand response against monotonic and cyclic lateral loading?"

1. How do the moment and lateral force components affect the monopile stability?
2. What is the effective soil-spring model to represent the monopile response against lateral loading?
3. What input that can be given to develop a 0D model for Base Shear Force against Base Displacement (F_b - y_b) under monotonic loading?
4. How much base moment (M_b) affect the base rotation (θ_{base}) and the monopile stability ?
5. What considerations must be taken into account when calibrating the 0D F_b - y_b model for cyclic loading?

1.4. Research Outline

This research aims to establish an enhanced framework for evaluating the force and moment components at the base of large-diameter monopiles. To achieve this goal, a series of 3D FE analysis results were

employed to explore the impact of pile geometry on the interaction between the monopile and the surrounding soil. The analysis is centered on piles with diameters (D) of 6, 9, and 12 meters, featuring corresponding embedded length-to-diameter (L/D) ratios of 2, 4, and 6. In most cases, the load eccentricity remains consistent at an eccentricity-to-diameter (e_{cc}/D) ratio of 5, while the relative density of the sand (D_r) is set to 0.9.

To further investigate the effect of the pile geometry on the pile base soil reaction, additional analyses were carried out for pile L/D ratios of 1 and even 0.5. The 3D FE model employs the SANISAND-MS constitutive model within the Plaxis software.Model parameters were adjusted based on laboratory and centrifuge tests conducted on Geba sand, as documented in prior research. Minor calibration of the ratcheting parameter (μ_0) was required during the initial stages of the analysis. The Geba sand sample used in the centrifuge test was compacted to achieve a relative density (D_r) of 0.97, and the collected data from this test were also employed for the purpose of parameter calibration.

The introductory chapter offers insight into the background, the idea, and the driving motivation behind this project. Chapter two provides an extensive literature review that contextualizes the research within the existing body of knowledge. The subsequent chapters, beginning with chapter three, constitute the core of this study, elaborating on its essential content and explanations. Chapter three explains the setup and the parameters necessary for executing the 3D FE analysis. This chapter also outlines the procedure for extracting soil reactions from the 3D FE model and explains the limitations of the model.

Chapter four is dedicated to the presentation of monotonic analyses. Within this chapter, the sensitivity analysis of each investigated parameter on monotonic response is extensively discussed. The following chapter encompasses the outcomes of the cyclic lateral loading analysis. Additionally, stress and strain recording results are presented in chapters four and five, respectively, to illustrate the responses of soil elements during both monotonic and cyclic loading scenarios.

The thesis report concludes with chapter six, summarizing the findings and offering remarks for further research. Additionally, all relevant finite element results can be found in the appendix.

2

Literature Review

This chapter provides a literature review to support the findings and ideas presented in this thesis. It begins with a discussion of research findings concerning failure criteria for monopiles, followed by an explanation of base shear force, base moment, and distributed moment of monopiles under monotonic loading. Subsequently, the focus shifts to the behavior of sand subjected to cyclic loading. This encompasses an exploration of both drained and undrained behaviors of sand under monotonic shearing loads, followed by a review of the cyclic response of sand. This includes a review of ratcheting behavior under drained conditions, as well as the progression of sand stiffness during cyclic loading. Moreover, this chapter also provides an overview of commonly employed methodologies for evaluating soil response under cyclic lateral loads.

2.1. Large Diameter Monopile Under Lateral Load

A monopile foundation comprises a steel pile with a large diameter, currently D up to 9.5 meters [25], essentially serving as an extension of the offshore wind turbine (OWT) tower into the ground. The primary function of the pile is to transmit both lateral and axial loads from the structure to the seabed. Although the large-diameter monopile is an advancement from the pile employed in the offshore oil and gas industry, the same design approach may not be directly applied in this scenario. The conventional *p-y* (lateral soil reaction-pile displacement) curve (e.g. API [26]) design approach leads to an underestimation of pile deformations [27], as well as underprediction of the stiffness of the sand [28].

The *p-y* method was incorporated into the standard *Design of offshore wind turbine* [29]. This approach involves a procedure for constructing non-linear *p-y* curves to characterize the behavior of monopiles in the sand under cyclic loading. A commonly employed method in the industry is the API [30] approach, which characterizes the $p - y$ curve as a function of the static ultimate lateral resistance denoted as p_u. This method is described as follows:

$$p = Ap_u \tanh\left[\frac{kz}{Ap_u}.y\right] \tag{2.1}$$

where A = 0.9 for cyclic loading, z in the depth (m), and k is the initial modulus of sub-grade reaction (kN/m^3) that depends on internal friction angle (ϕ) or sand relative density. Further studies have

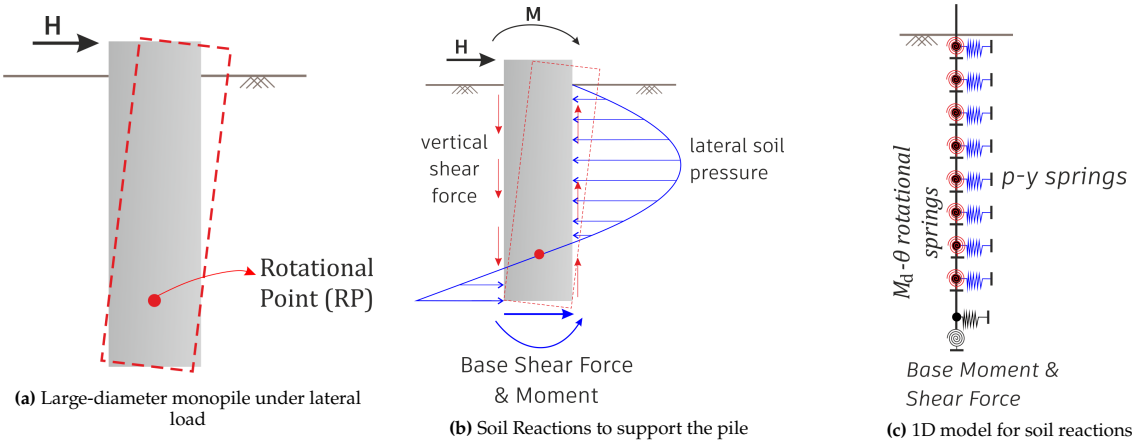

(a) Large-diameter monopile under lateral load

(b) Soil Reactions to support the pile

(c) 1D model for soil reactions

Figure 2.1: Idealisation of soil reaction components acting on large-diameter monopile.

revealed that to accurately represent the behavior of large-diameter monopiles and soil interaction, a minimum of four components is required. These components, identified and discussed in earlier research work [19], [31], encompass the lateral soil reaction force, distributed moment, base shear force, and base moment. Figure 2.1 provides a visual depiction of these components.

Due to the differences in geometric characteristics between the monopiles installed in offshore wind farms (OWFs) and the piles used to develop the original *p-y* curve, additional components are necessary to model the soil reaction accurately. The conventional *p-y* model was primarily based on empirical data from tests conducted on long, slender, and flexible piles. However, as explained by [32], the installed monopiles in OWFs have different geometry compared to the piles used in the development of the initial *p-y* curve (see Figure 2.2). The behavior of pile rotation under lateral load can be addressed by using pile relative stiffness. The pile relative stiffness (K_r) is a dimensionless parameter introduced by [33] and calculated according to the following formula:

$$K_r = \frac{E_p.I_p}{E_{SL}.L^4} \qquad \begin{Bmatrix} K_r > 0.208 & Rigid\ pile \\ K_r < 0.0025 & Slender\ pile \end{Bmatrix} \tag{2.2}$$

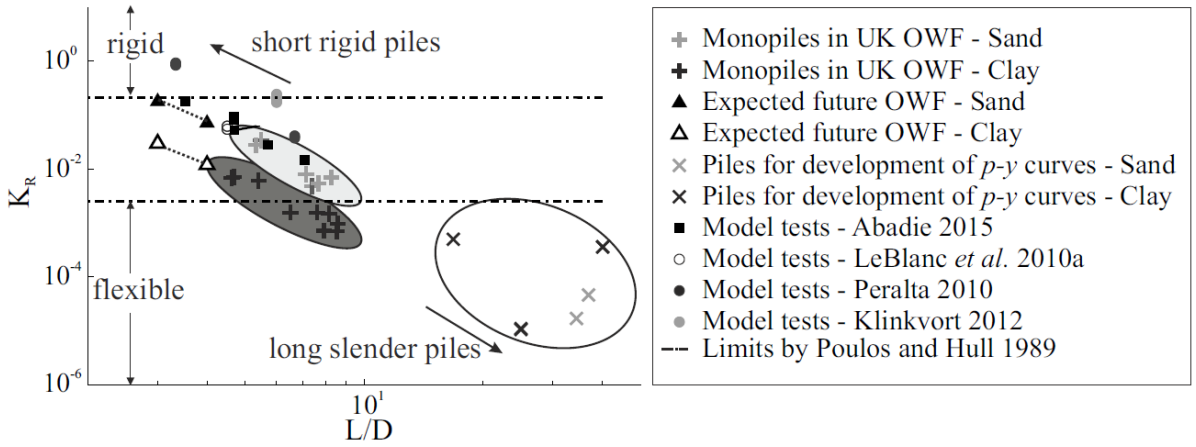

Figure 2.2: Pile flexibility factor against L/D ratio for OWF monopiles in UK and the piles used for the derivation of conventional *p-y* curve [32].

In Equation 2.2, E_pI_p is the pile bending stiffness, L is the pile embedded length, and E_{SL} is the soil modulus at the pile tip, estimated using the small strain shear modulus (G). The area between rigid and flexible will be called semi-rigid in this report.

2.1.1. Failure Criteria of Monopile

The monopile and substructure of OWTs are commonly designed as a soft-stiff structure. These monopiles experience lateral loads caused by aerodynamic impulses and wave forces. The wave spectrum typically exhibits peak frequencies ranging from 0.1 to 0.3 Hz, which can vary based on factors such as wind speed and site conditions [34]. All the load exerted from the tower must be transferred to the ground through the monopile, which is constrained by the allowable deformation value. [35] have explained that the design of monopile in the OWF must meet the following criteria:

1. Ultimate Limit State (ULS)
2. Target Natural Frequency and Serviceability Limit State (SLS)
3. Fatigue Limit State (FLS)
4. Robustness and ease of installation.

Ultimate Limit State (ULS) failure is characterized by the structural collapse that can occur through two mechanisms: (a) soil failure, and (b) the formation of a plastic hinge leading to pile failure. Conversely, Serviceability Limit State (SLS) failure refers to the situation where the deformation exceeds the acceptable limits (Figure 2.3). Both ULS and SLS failures play a significant role in determining the pile dimensions. The pile dimensions, defined by the pile diameter (D), pile wall thickness (t_p), and pile embedded length (L), directly influence the bending stiffness of the monopile and the compliance of the foundation in terms of allowable rotation and displacement at the mudline. Increasing these variables will enhance the bending stiffness of the monopile while also affecting the foundation compliance with the design standard.

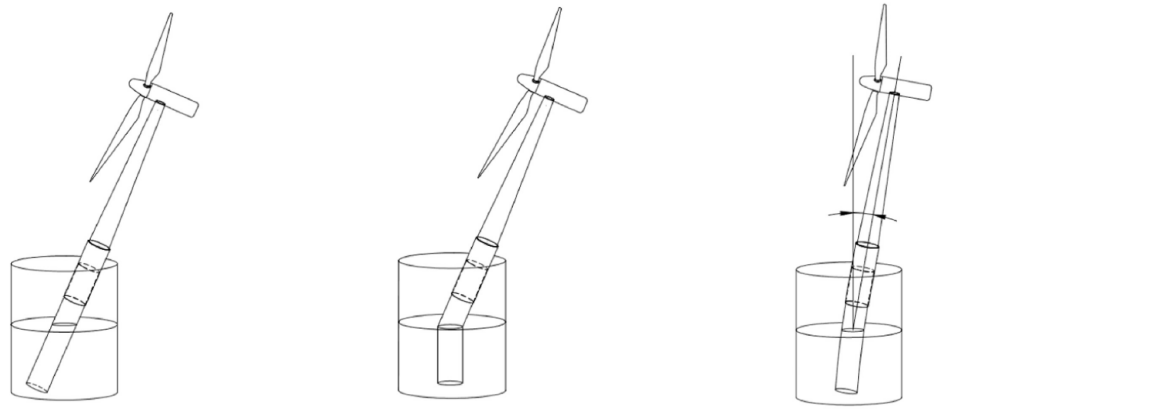

(a) ULS failure due to failure in the soil

(b) ULS failure through plastic hinge of the pile

(c) SLS failure can be due to cyclic loading

Figure 2.3: Explanation of ULS and SLS failure (after [35]).

The serviceability limit state (SLS) of the monopile is determined by either the permanent rotation or permanent displacement at the mudline. The criteria for SLS failure can vary depending on the type of turbine. Some publications and design standards suggest a limit of 0.5^o for permanent rotation [16], while others recommend a limit of 0.25^o [15]. In their 3D FE analysis, [36] suggests that the peak load

occurs when the maximum lateral displacement is limited to $0.1D$. Other studies define the ultimate capacity of the monopile based on a permanent rotation limit of 4^o [37] or 2^o [38]. Although the specific limits for allowable permanent rotation and displacement at the mudline may be somewhat arbitrary, this project defines the ultimate capacity of the monopile as the point where the permanent rotation at the mudline reaches 2^o. This criterion is applied based on the assumption that the monopile behaves as a rigid or semi-rigid body, thereby preventing the formation of plastic hinges under lateral loading conditions.

2.1.2. Base Shear Force

Offshore wind turbines is used to construct using the monopile with a small L/D ratio, which can be classified as short-rigid piles [37]. Due to their geometry and mechanical properties, these monopiles exhibit similar behavior to a rigid or semi-rigid body, with a single rotational point along their embedded length [39]. In contrast to long and flexible piles, which tend to fail through the formation of plastic hinges, short and rigid monopiles may experience relatively large displacements at the pile tip. As a result, a horizontal shear force develops at the pile base [27], [39] or, it is also known as base shear force (F_b).

Limited research has been conducted to explore the magnitude of the base shear force (F_b) [37], [40], [41], [42], and there are still gaps in understanding how to effectively address this aspect. One of the most well-known approaches was proposed by [37], which computes the (F_b) for sand according to Coulomb theory:

$$F_b = \left(c_3.V + \frac{\pi}{4}D^2L\gamma'\right)\sin\phi_{cr} \tag{2.3}$$

In this equation, the base shear force (F_b) is modeled as the combination of the effective overburden stress and the contribution from the gravity force acting on the structure, multiplied by the critical friction angle (ϕ_{cr}). Additionally, a dimensionless constant, denoted as c_3, is introduced, which falls within the range of 0 to 1 (Figure 2.4) This equation was formulated under the assumption that the deformation of the soil below the pile base can be represented by a direct simple shear (DSS) element test. In this scenario, the F_b is assumed to be governed by the residual strength of the soil once it has passed its peak strength.

Subsequently, [40] proposed modifications to this equation by introducing the concept of the maximum base shear force ($F_{b,ref}$), which is calculated using the following formula:

$$\begin{aligned} F_{b,ref} &= W_t \tan(\phi_{peak}) \\ &= ((Q + W_p - U_L)c_3 + W_s)\tan\phi_{peak} \\ &= \left[(Q + W_p - U_L)c_3 + \left(\frac{\pi}{4}D^2L\gamma'\right)\right]\tan\phi_{peak} \end{aligned} \tag{2.4}$$

where W_t = total resulting vertical force acting at the pile tip, which encompasses several components. These components include Q, which denotes the combined weight of the tower, substructure, and rotor assembly; W_p, representing the weight of the pile itself; W_s, indicating the weight of the soil contained within the pile; U_L, denoting the hydrostatic force exerted at the interface between the pile and the soil at the pile base. Additionally, the parameter c_3 is further defined as the load transfer factor, calculated as the ratio between the sum of the vertical forces acting on the pile and the vertical force transferred to the pile base.

[40] estimate the c_3 value using the results from their 3D FE analysis and it align with the following equation:

$$c_3 = \frac{\left(\sigma_{zz,ave} - \gamma' L \frac{D_i^2}{D^2}\right) . \frac{\pi . D^2}{4}}{Q + W_p - U_L} \tag{2.5}$$

where $\sigma_{zz,ave}$ represents the average effective vertical stress exerted on the soil element beneath the pile and the soil within the pile. The results obtained from a 3D finite element analysis conducted on piles with diameters ranging from 5 to 7 meters and embedded lengths between 20 and 30 meters indicate that the factor c_3 is approximately equal to 0.3 [40]. Later, in this project, a hypothetical maximum F_b ($F_{b,ref}$) is introduced by setting the value of $c_3 = 1$.

A potential approach to enhancing the 0D soil spring model for describing the F_b - y_b relationship may involve the incorporation of $F_{b,ref}$. This can be achieved through the utilization of the hyperbolic tangent function, as depicted below:

$$F_b = F_{b,ref} \tanh(c_s \cdot y_b) \tag{2.6}$$

Here, the constant c_s is adjusted to align with the outcomes from finite element simulations. It is evident that Equation 2.6 bears a resemblance to the formula for lateral soil reaction force, which is also expressed using a hyperbolic tangent function concerning its ultimate value (Eq. 2.1).

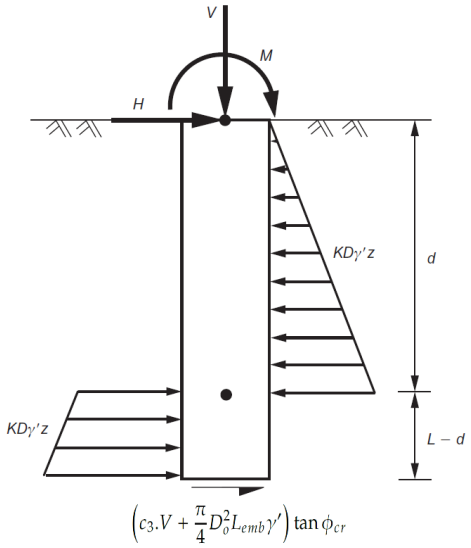

Figure 2.4: Horizontal stress distribution in the ultimate limit state for stiff and rigid pile under lateral load - modified after [37]

.

[42] proposed an alternative method to estimate the base shear force, which was derived from studying rigid monopiles on the crest of a clay slope. Although the stress distribution on the slope crest is different from that in an OWF monopile environment, the fundamental concept can still be applied to analyze OWF monopiles. In their study [42], the F_b was calculated using the following formula:

$$F_b = A_p . f_b \tag{2.7}$$

where A_p is the pile base area, and f_b is the unit of horizontal shear resistance at the pile base. [43]

provided a formula to calculate f_b as follows:

$$f_b = \frac{y_b}{y_{b,cr}}.f_{b,ref} \tag{2.8}$$

where $f_{b,ref}$ is the maximum base shear resistance, and the $y_{b,cr}$ is the base displacement which maximum shear resistance ($f_{b,ref}$) is mobilized. In their study, [44] suggested an estimation method for $f_{b,ref}$ based on the formula for side shear resistance, as outlined in the guidelines provided by [30]. The estimation is given by the following expression:

$$f_{b,ref} = \beta.\sigma'_{zz}(z) \tag{2.9}$$

where the β is the dimensionless shaft friction factor for cohesionless soil according to [30] and σ'_{zz} is the effective overburden stress.

Upon examining the provided equations (Eq. 2.7 - Eq. 2.9), it becomes evident that the analysis carried out by [42] is primarily applicable to situations involving linear elastic perfectly plastic (LEPP) deformations. In this context, the value of f_b is controlled by the ratio between the current displacement and the critical displacement. Consequently, the curve will continue to increase and then remain the same once the displacement reaches $y_{b,cr}$. It is important to be cautious when utilizing these equations, particularly because soil deformation predominantly follows a non-LEPP behavior.

2.1.3. Base Moment and Distributed Moment

The behavior of short and large-diameter monopiles can be characterized as a semi-rigid or rigid body. When subjected to lateral loads, the pile not only undergoes bending but also exhibits distinctive rotation with a noticeable toe kick at the pile base. Studies conducted using laboratory tests [45], [46] have identified three types of plastic flow that occur in the soil around semi-rigid or rigid monopiles when subjected to lateral loads: wedge-type flow, full flow, and rotational flow (Figure 2.5).

This suggests that the lateral load applied to a large-diameter monopile is resisted not only by the lateral soil resistance but also by the base moment, and base shear force. Apart from these three components, the pile is also supported by shear stress around the vertical shaft, referred as the shear force (Figure 2.1b), which generates the distributed moment. [45] has already identified that the contribution of the pile base moment and distributed moment aligns with an increase in pile diameter and a decrease in the L/D ratio.

An investigation conducted by [47] aimed to establish a dimensionless stiffness coefficient for $M_d - \theta$ springs by normalizing the obtained value with respect to the soil shear modulus ($G(z)$). In order to achieve this, they introduced a dimensionless coefficient known as the local shaft $M_d - \theta$ stiffness ($K^S_{m\theta}$), which is calculated locally along the pile length using the following equation:

$$K^S_{m\theta} = \frac{\sum f_z.\Delta y}{\theta G(z) D^2} \tag{2.10}$$

where f_z is the nodal reaction force in the z-direction, Δy denotes the horizontal distance in the y-direction from the node to the central vertical plane of the monopile, and θ represents the local rotation of the pile (see Figure 2.6). On the other hand, the dimensionless coefficient for the base rotational

stiffness ($K^B_{m\theta}$) can be defined as follows:

$$K^B_{m\theta} = \frac{\sum f_z.\Delta y}{\theta G(z) D^3} \tag{2.11}$$

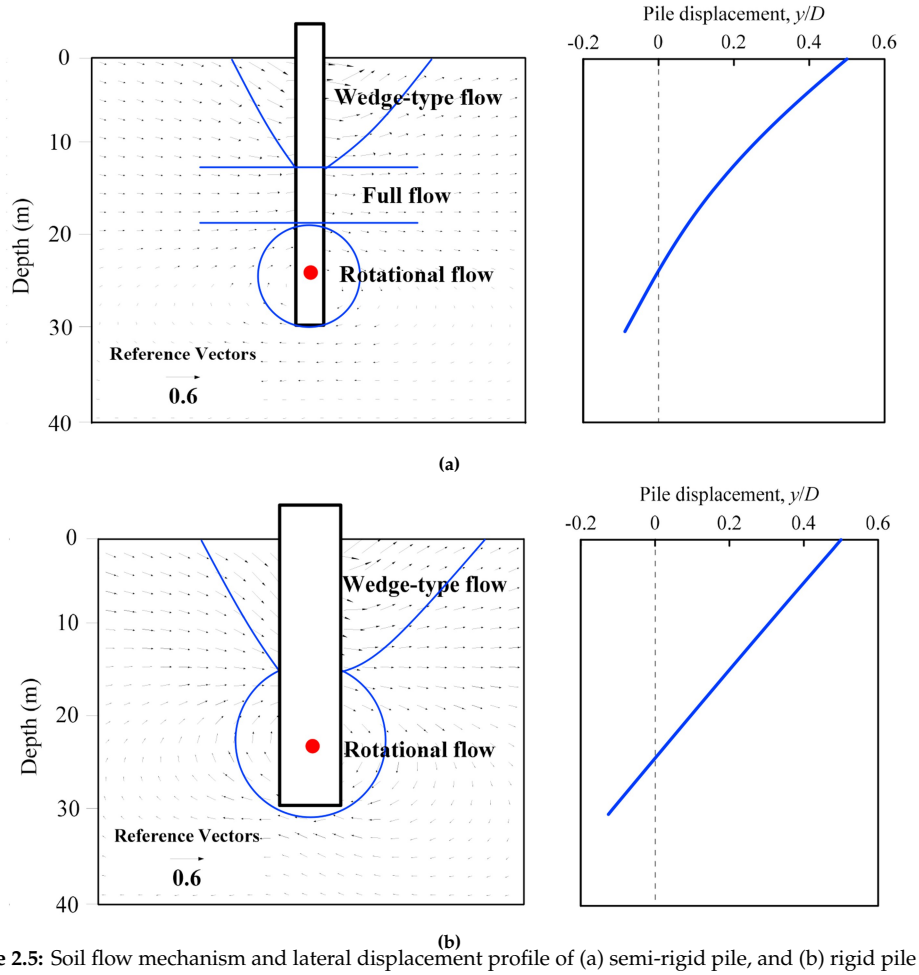

Figure 2.5: Soil flow mechanism and lateral displacement profile of (a) semi-rigid pile, and (b) rigid pile [45].

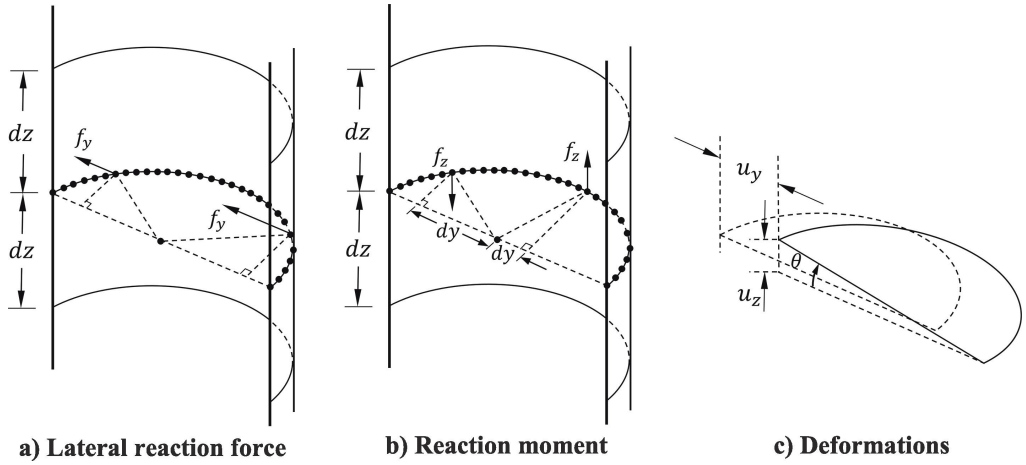

Figure 2.6: Schematic view of the nodal force around the pile shaft [47]

.

To account for the variation of shear modulus against the depth, $G(z)$ was assumed to follow this formula:

$$G(z) = G_D . \left(\frac{z}{D}\right)^a \tag{2.12}$$

where G_D is the shear modulus at the depth equal to the pile diameter (D) and a is the parameter that accounts for soil heterogeneity.

2.2. Cyclic and Monotonic Loading on Sand

Sand response under shearing depends on the state condition of the sand. Loose sand and dense sand will give a different response under monotonic and cyclic loading. One method to learn the behavior of soil under shearing is by doing a triaxial test that can give sand strength parameters by using various stress conditions.

2.2.1. Monotonic Loading

In triaxial test, an undrained test involves two phases: (1) the consolidation phase, where isotropic stress is applied and drainage allowed, and (2) the shearing phase, where the sample is subjected to undrained conditions. Under undrained conditions, water cannot freely migrate from the soil during shearing, leading to the generation of excess pore water pressure [48]. This excess pore water pressure sometimes reduces the effective stress of the soil, as depicted in Figure 2.7.

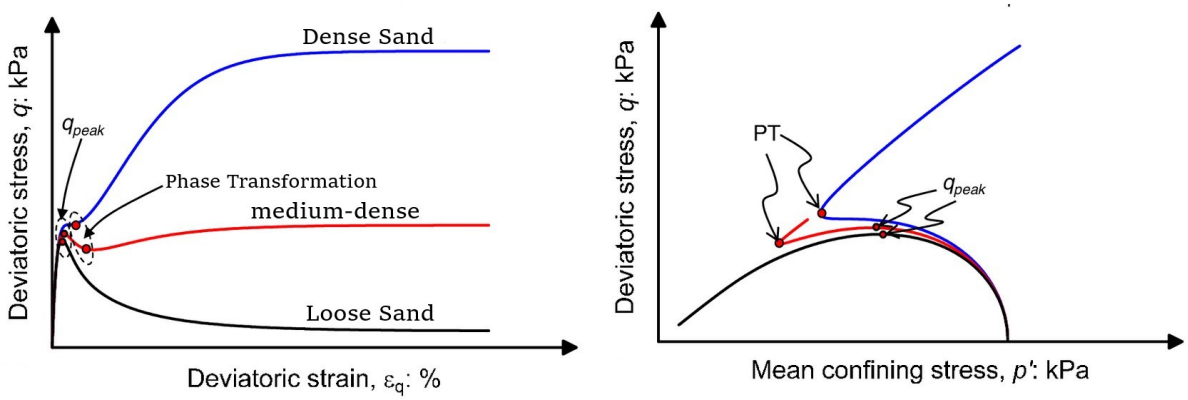

Figure 2.7: The stress-strain response and effective stress path under triaxial undrained test - after [48].

Loose sand exhibits a rapid increase in deviatoric stress (q) until it reaches the peak, followed by a softening process until it reaches equilibrium in a critical state. In loose sand, shearing induces the development of pore water pressure, leading to a decrease in soil strength. Medium dense sand undergoes initial softening but then experiences a hardening process [49], while dense sand continues to harden until it reaches the critical state. On the contrary, negative pore pressure is generated in dense sand, increasing the effective stress and soil strength.

Under drained conditions, water is allowed to move in the soil during both the consolidation and shearing stages. Dense sand initially undergoes compaction or hardening before transitioning to dilation if the applied stress continues to increase (Figure2.8). Loose sand, on the other hand, continues to undergo compaction until it reaches a critical void ratio. The same material under, the same state of stress, will reach the same critical void ratio regardless of the initial density (Figure 2.8.

According to a study by [50], the tendency of soil to dilate is primarily influenced by the density and

arrangement of particle structures. However, tests conducted on granular soils at critical confining stress (p'_{crit}) [51] have demonstrated that increasing confining pressure leads to a reduction in the friction angle (ϕ). The test on granular soils has proof that under high confining pressure soil particles may crush before they even dilate [52].

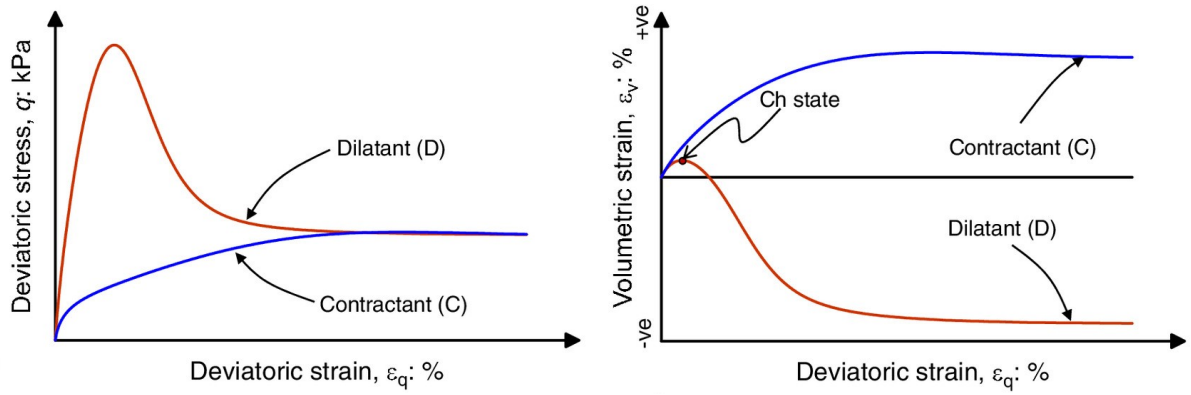

Figure 2.8: The stress-strain response and effective stress path under triaxial drained test - after [48].

2.2.2. Cyclic Loading

Under undrained conditions, a loose soil undergoing cyclic simple shear experiences liquefaction, which occurs in several steps according to [53]:

1. Shear stiffness degradation occurs cycle by cycle, evidenced by increasingly larger shear strain excursions.
2. A significant portion of the large cyclic shear deformation develops rapidly at nearly constant, low shear stress and effective confinement.
3. Once drainage is allowed, the soil gradually regains shear stiffness and strength after these large shear strain excursions, accompanied by an increase in effective confinement (resulting from dilatancy).

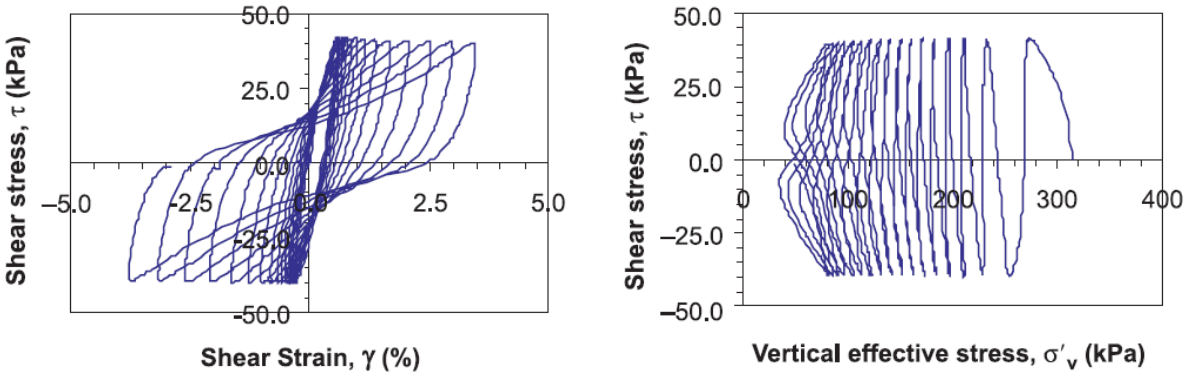

(a) Stress - strain response

(b) stress path response

Figure 2.9: Typical response of copper–gold–zinc tailings in constant-volume cyclic DSS loading - after [54].

Under undrained conditions, the response of sand to cyclic loading is primarily governed by two parameters: soil relative density and the cyclic stress ratio, as indicated by [55]. Loose sand exhibits small dilation prior to failure, followed by significant shear strain. The cyclic stress ratio determines

the number of cycles required for liquefaction to occur and also influences the magnitude of cyclic shear strain. According to a study by [54], under undrained conditions, granular materials exhibit a contractive behavior at the initial stages of cyclic loading. As the number of cycles increases, there is a continuous accumulation of excess pore water pressure (Figure 2.9).

Under drained conditions, cyclic loading can induce progressive and irreversible deformation. Over numerous cycles, these non-recoverable deformations lead to an accumulation of deformation that is also known as ratcheting [56]. Understanding the ratcheting phenomenon is crucial in predicting the long-term stability of the geotechnical structures. As demonstrated in a study by [57], this ratcheting effect can result in significant displacements of the structures that exceed their allowable serviceability limit state (SLS) failure criteria.

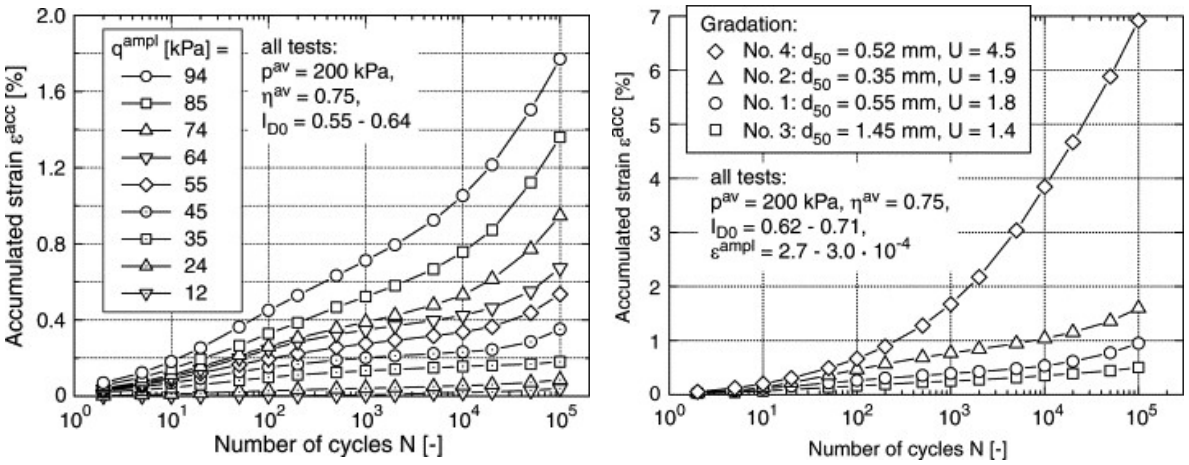

(a) The effect of ε^{amp} on ε^{acc}

(b) The effect of d_{50} on ε^{acc}

Figure 2.10: Typical strain accumulation under drained cyclic test in response to (a) different strain amplitude and (b) different grain size and distribution [57].

A study by [57] examined the influence of soil stress conditions and sand relative density on the magnitude of accumulated strain. The study identified several factors that affect the accumulation of plastic strain, as outlined below:

- The magnitude of accumulated strain (ε^{acc}) is influenced by the strain amplitude (ε^{amp}), with higher strain amplitudes resulting in larger accumulated strains (Figure 2.10a).
- There is a positive correlation between the strain amplitude (ε^{amp}) and the deviatoric stress.
- Initially, the strain amplitude (ε^{amp}) decreases as the number of cycles increases, eventually reaching a terminal value after 10^3 cycles.
- The accumulated strain (ε^{acc}) decreases with increasing mean pressure (p).
- Loose soil exhibits higher accumulated strains.
- The strain amplitude (ε^{amp}) positively correlates with relative densities.
- The accumulated strain (ε^{acc}) increases with an increasing number of cycles (Figure 2.10b).

These findings provide clear insights into the influence of stress conditions and state parameters on ratcheting behavior.

2.3. Monopile Response Under Cyclic Loading

2.3.1. Ratcheting Behaviour

Cyclic lateral loading on the monopile leads to the accumulation of displacement and rotation. Under drained conditions, when a high number of cycles are applied permanent displacement and rotation can accumulate, a phenomenon commonly also referred to as ratcheting. An investigation conducted by [37] found that the accumulated rotation is influenced by various sand relative density and load characteristic parameters (ζ_b and ζ_c). Furthermore, in addition to soil conditions and load characteristics, studies by [58] and [59] have indicated that pile geometry also plays a significant role in influencing the ratcheting response under cyclic loading. In addition to this study [58], [59], further investigation is needed to fully understand the impact of monopile geometry on the ratcheting response.

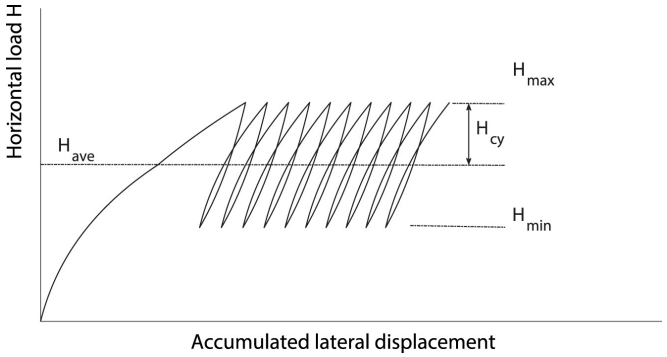

Figure 2.11: Definition of plastic strain accumulation in load-displacement plane [60].

In the analysis of monopiles, cyclic load testing may involve applying a series of different load packages. Each load package is defined by several parameters, including the average amplitude (H_{ave}), regular cyclic variation (H_{cy}), maximum (H_{max}), and minimum (H_{min}) lateral load values (Figure 2.11). To describe the characteristics and magnitude of the cyclic load package, [37] introduced dimensionless parameters denoted as ζ_c and ζ_b, respectively, which can be calculated using the following equations:

$$\zeta_b = \frac{H_{max}}{H_{ult}} \tag{2.13}$$

$$\zeta_c = \frac{H_{min}}{H_{ult}} \tag{2.14}$$

the reference load (H_{ult}) represents the ultimate load to induce 2^o pile rotation at the mudline.

Based on the tests on the sand, [37] suggested that accumulated rotation due to cyclic loading can be calculated as follows:

$$\frac{\Delta\theta(N)}{\theta_s} = \frac{\theta_N - \theta_0}{\theta_s} = T_b(\zeta_b, D_r)T_c(\zeta_c).N^{0.31} \tag{2.15}$$

in which T_b and T_c is dimensionless functions that depend on load characteristic and relative density. The magnitude of rotation increment by cyclic loading denoted by $\Delta\theta(N)$ that calculated by subtracting the rotation at N^{th} cycle θ_N with the rotation at the first cycle θ_0. The θ_s is the rotation that occurs in the static test when the load is equivalent to the maximum cyclic load (defined as $\zeta_b \times M_R$).

2.3.2. Stiffness Evolution During Cyclic Loading

The cyclic response of a monopile in dry sand is characterized by several factors, including the accumulation of permanent displacement (ratcheting), changes in secant stiffness, and the dissipation of energy per cycle [61]. To accurately assess stiffness changes without combining them with ratcheting effects, [61] defined the secant stiffness (k_s) at the center of the cycle (Figure 2.12a, Cycle 1). This stiffness is obtained by taking the inverse of the average of the loading and unloading flexibility is expressed in terms of the secant loading stiffness (k_{sl}) and secant unloading stiffness (k_{su}) (Figure 2.12a) as follows:

$$k_s = 2\left(\frac{k_{sl}k_{su}}{k_{sl} + k_{su}}\right) \tag{2.16}$$

The initial or maximum loading stiffness (Figure 2.12a) is determined by fitting the loading and unloading data during the initial stages of rotation at the mudline (θ_{sb}) when it is less than 0.003 degrees [62]. During unidirectional cyclic testing, the secant stiffness consistently increases with the number of cycles. Eventually, the k_s reaches a plateau and remains constant after a high number of cycles [61].

Another approach to understanding the evolution of monopile stiffness under cyclic lateral loading has been presented by [37]. Drawing upon laboratory testing, [37] has proposed that the change in monopile stiffness over cyclic loading can be anticipated using the following equation:

$$\tilde{k_N} = \tilde{k_0} + A_k \ln(N) \tag{2.17}$$

Here, A_k represents a dimensionless constant, $\tilde{k_N}$ stands for the stiffness at the N-th cycle, and $\tilde{k_0}$ denotes the stiffness value at N = 1. The suggested value for A_k based on laboratory tests is approximately 8.02, while the value of $\tilde{k_0}$ can be calculated using the subsequent equation:

$$\tilde{k_0} = K_b(\zeta_b)K_c(\zeta_c) \tag{2.18}$$

Here, K_b and K_c represent dimensionless functions determined by the load characteristics and D_r. Nonetheless, [37] has argued that the stiffness of sands with low to medium densities seems to be insensitive to their relative density. Furthermore, in situations involving very dense sand ($D_r \rightarrow 1.0$), the stiffness is expected to remain relatively constant.

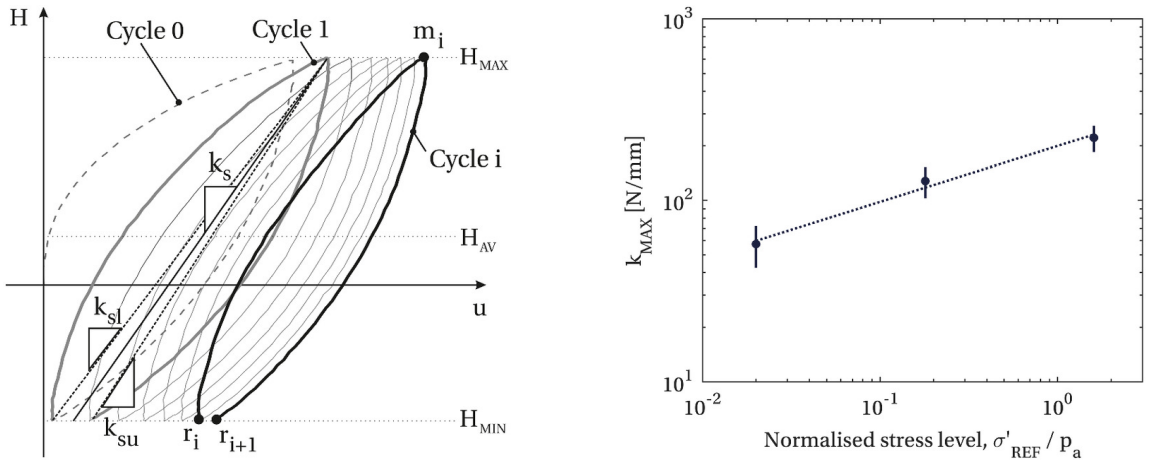

(a) Cycle and stiffness definition

(b) Variation of first loading stiffness (k_{max}) with stress level

Figure 2.12: Definition of maximum stiffness and cyclic secant stiffness - after [61].

2.4. Numerical Model to Predict Monopile and Soil Responses under Cyclic Loading

The numerical modeling of monopile and soil ratcheting response over a specified number of cycles (N) can be approached through at least two methods, commonly referred to in the literature as explicit and implicit approaches [63].

2.4.1. Explicit Method

The explicit method directly associates the accumulated deformation with the parameter N. In this approach, the calculation or accumulation of relevant strain components in the soil is performed solely at the end of each loading cycle. Explicit models typically rely on comprehensive laboratory testing, necessitating significant simplification due to inherent limitations in testing capabilities concerning various aspects of cyclic behavior. An example of a well-established explicit approach for assessing accumulated deformation is the cyclic contour diagram [64].

Cyclic contour diagrams (CCDs) serve as valuable tools for visually tracking soil behavior under cyclic loading conditions. Typically featuring two axes—one indicating the number of loading cycles (N), and the other representing geotechnical parameters like shear strain, shear stress, or pore pressure—these diagrams have played a crucial role in offshore structure foundation design for over three decades [64], [65]. Key elements within CCDs include the cyclic stress ratio (CSR), representing the soil exposure to alternative stress levels, cyclic strain, cycle count, and the failure envelope. Notably, failure criteria can be defined when the permanent strain resulting from a combination of pure cyclic or static loads equals either 15% [66] or 10% [36]. The same underlying concept has also driven the development of advanced FE models such as the undrained cyclic accumulation model (UDCAM) [67] and the partially drained cyclic accumulation model (PDCAM) [68].

While CCDs offer invaluable insights into pore pressure generation and the combined effects of cyclic and static loading leading to defined failure criteria, their construction is notably intricate. These challenges are a common characteristic of explicit models. Constructing a CCD requires certain assumptions, such as strain compatibility and the magnitude of horizontal stress in direct simple shear (DSS) tests, which may not universally hold. Furthermore, interpreting CCDs demands a high level of expertise due to their complexity, where each contour line signifies distinct soil behavior. Moreover, constructing a CCD entails collecting vast amounts of data, given the need to identify stress combinations leading to failure—a process that can be both time-consuming and costly.

2.4.2. Implicit Method

The implicit method relies on the constitutive model to describe the soil response through a sequence of stress-strain increments over each loading cycle. The overall response of cyclic loading history results from the time integration of all stress-strain increments. Since a couple of years ago, some implicit constitutive models have been developed according to different constitutive approaches. The three most well-known approaches are hyperplasticity, hypoplasticity, and elastoplasticity concept.

The hyperplasticity concept is based on a thermomechanical framework [69] and relies on the utilization of internal variables, such as plastic strain for ratcheting analysis, to characterize soil loading history. Achieving an accurate approximation of ratcheting behavior through continuous curves becomes feasible when a sufficient number of internal variables are introduced [70]. One notable

example of a constitutive model founded on hyperplasticity principles is the Hyperplastic Accelerated Ratcheting Model (HARM), specifically designed to capture the accumulation of ratcheting strain [71].

Despite HARM successful testing and calibration against both monotonic and cyclic loads [71], its application still requires extensive parameter calibration. This calibration is a complex process that cannot be fully explained within the soil element test framework. An alternative to the hyperplastic constitutive model involves the utilization of a hypoplastic concept.

Hypoplastic models originate from the framework of Rational Mechanics and are formulated as functions of stress and stretching tensors. They exhibit commendable performance in predicting monotonic responses [72]. Nevertheless, they tend to yield nearly identical stress-strain curves for primary loading and reloading cycles [73]. In order to more effectively capture the impact of the shift in strain path, which typically characterizes cyclic loading, a study by [74] introduced the concept of intergranular strain [75] and a memory surface [76] within the hypoplastic framework. However, this study [74] indicates that the model provides slightly different results when compared to triaxial cyclic undrained tests and suggests that further advancement is required to fully enable it to simulate cyclic soil responses.

Elastoplasticity theory is widely used for the development of constitutive models. In this theory, in addition to the elastic relationship, three components are essential to compute the incremental plastic strain tensor: the yield criterion, plastic flow rule, and hardening rule. An example of such a constitutive model, developed based on elastoplasticity theory, is SANISAND-MS [24]. To account for the ratcheting effect, SANISAND-MS also incorporates a memory surface [76] into the conventional SANISAND model [77], [78]. This enhancement enables SANISAND-MS [24] to capture the ratcheting effect and potentially provides a more practical alternative than constitutive models rooted in hyperelastic and hypoplastic concepts.

3

Finite Element Model

Evaluation of the influence of variations in pile geometry on sand behavior under cyclic loading was conducted through a 3D finite element (FE) analysis. The analysis was performed using Plaxis version 21, and the SANISAND-MS constitutive model was implemented. All simulations were carried out in a dry sand environment with a water content of 0%. This chapter presents the essential steps taken before relying on the results obtained from the 3D FE analysis. It commences with an explanation of the geometry and meshing of the model, followed by a discussion of the materials employed in the model. The subsequent section provides a concise overview of the boundary and initial conditions. Finally, it briefly outlines the methods used for post-processing the results from the 3D FE.

3.1. Finite Element Geometry and Mesh

To conduct the finite element (FE) calculation, the model geometry is subdivided into individual elements, collectively referred to as an FE mesh. In this project, the FE mesh encompasses three distinct materials: soil, the pile, and the pile-soil interface. In the Plaxis 3D software, the horizontal coordinates are denoted by x and y axes, while the vertical coordinate is represented by the z axis.

The model dimensions are expressed relative to the pile diameter (D), with a width of $30D$, a length of $15D$, and a height of $12.5D$ (Figure 3.1). The soil extends approximately $7.5D$ below the pile tip, and the analysis is conducted under dry sand conditions. In order to reduce computational time, only half of the pile and the surrounding soil are modeled in the 3D FE analysis due to the symmetric loading conditions and material properties. The geometry is then discretized into a mesh consisting of 10-node wedges (Figure 3.2).

The monopile is represented as a half-cylinder with varying diameter (D), embedded length (L), and eccentricity (e), which is further subdivided into surfaces and plates. For the piled plate, 6-node elements are employed to simulate the axial and bending stiffness of the monopile wall. The interface elements are employed to simulate the region of intense shearing between the soil and the plate, facilitating the modeling of soil-structure interaction (Figure 3.1b). These interface elements create node pairs at the junction of the structure and soil.

Each interface element consists of six pairs of nodes, with one node from each pair belonging to the

structure, and the other to the soil. The distinction is made between the positive side (the surface facing the positive local z-direction) and the negative side (the surface facing the negative local z-direction) of the interface. The interface stiffness matrix is determined through Gaussian integration using six integration points [79]. The position of these integration points is selected to ensure exact numerical integration for linear stress distribution (Figure 3.3).

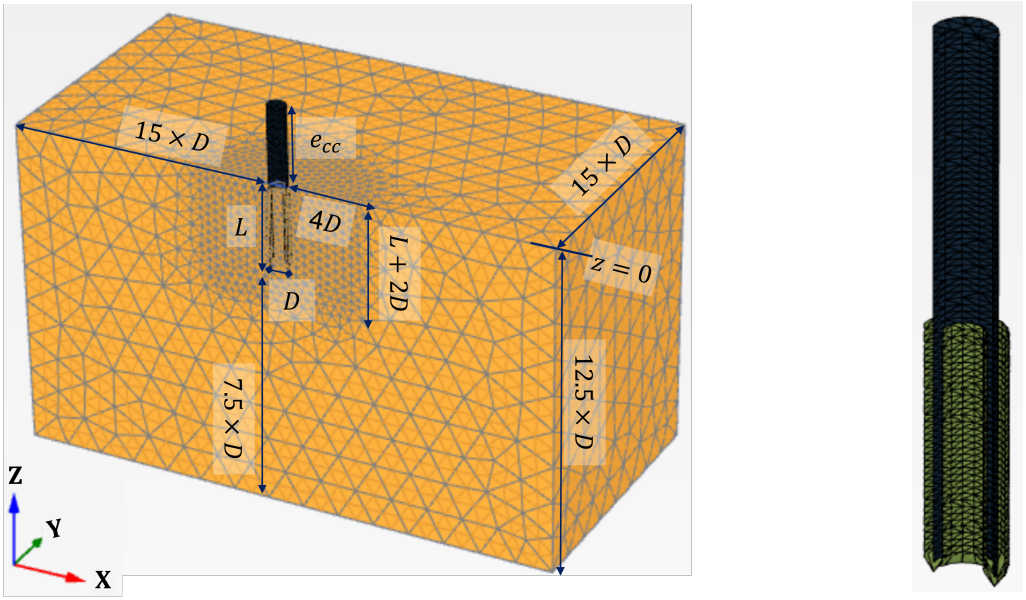

(a) 3D FE geometry in Plaxis

(b) Plate and interface elements

Figure 3.1: The setup for 3D FE analysis consists of (a) the model geometry and (b) pile plate elements (dark blue) and interface elements (green).

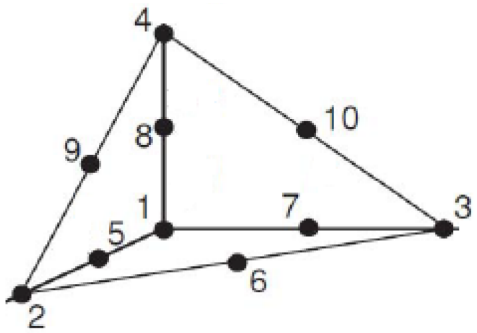

Figure 3.2: Local numbering and positional of nodes in a 10-node wedge element.

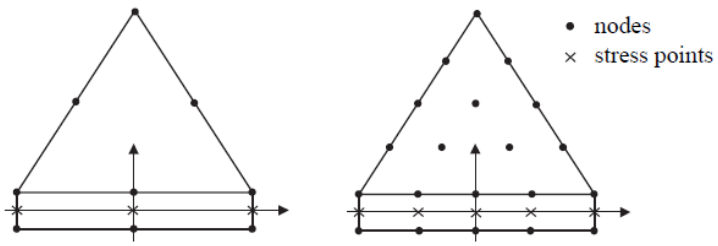

Figure 3.3: Distribution of nodes and integration points in interface element and their connection to the soil element [79].

The meshes were automatically generated using Plaxis. The mesh coarseness was set to medium, with local refinement applied to clusters in proximity to the monopile (as depicted in Figure 3.1a). This

was obtained by creating a circular surface around the pile and applying a refinement factor (rf) of 0.25. In this configuration, the average size of mesh elements is approximately $1.9D$, with the smallest element volume at around $\simeq 0.13D$ and the largest element volume at approximately $\simeq 3.7D$.

3.2. Materials

3.2.1. Soil and SANISAND-MS Material Model

The SANISAND-MS model is an advancement of the SANISAND model [77], [78], [80] and is rooted in the principles of critical soil mechanics. SANISAND-MS [81], [82] introduces an additional memory surface to monitor fabric changes and enhance deformation prediction control. It has undergone testing, demonstrating adherence to Miner rule, which employs load superposition principles [60]. This constitutive model is formulated within the framework of bounding surface plasticity and forms the basis for the development of an enhanced *p-y* curve known as the enhanced memory *p-y* curve [20].

In the SANISAND-MS model, three pivotal surfaces are employed: the yield surface, bounding surface, and memory surface (Figure 3.4). The memory surface plays a crucial role in capturing micro-mechanical phenomena associated with cyclic fabric changes, including variations in stiffness and dilatancy. These variations exhibit attributes of both "intensity" and "directionality" at the micro-scale, which prompted the incorporation of a combined isotropic-kinematic hardening mechanism for the memory surface in SANISAND-MS [24].

The memory surface has a circular shape in the normalized π plane (Figure 3.4). The evolution of the memory surface is described by three key rules:

1. As plastic strains occur, the size of the memory surface changes. An expanding memory surface, characterized by positive plastic volumetric strains, indicates a more stabilized soil fabric response, implying a stiffer condition during shearing. Conversely, the contraction of the memory surface is associated with negative (dilative) plastic volumetric strains, signifying a less compact soil fabric response. This concept of memory surface size change is introduced to account for changes in soil stiffness during both drained and undrained conditions.
2. The yield surface is always enclosed by the memory surface [24], and the minimum size of the memory surface can be considered as the yield surface.
3. The stress state surface at the current moment must always remain within the boundary of the memory surface.

The evolution of the elasto-plastic stiffness of the sand is influenced by both the bounding surface and the memory surface, utilizing the plastic modulus (K_p) as shown in Equation 3.2.

$$K_p = \frac{2}{3} p' h(\boldsymbol{\alpha}^b - \boldsymbol{\alpha}) : \mathbf{n} \tag{3.1}$$

The distance from the bounding-associated back stress to the yield surface, projected along the direction of the unit tensor normal to the yield surface ($\mathbf{n}$), is calculated as $(\boldsymbol{\alpha}^b - \boldsymbol{\alpha}) : \mathbf{n}$, as shown in Equation 3.2. In this equation, p' represents the mean effective stress, h stands for the hardening coefficient, $\boldsymbol{\alpha}^b$ is the projection onto the bounding surface with respect to the relative Lode angle, and $\boldsymbol{\alpha}$ denotes the back-stress ratio tensor.

The hardening coefficient (h) is determined using the following formula (Equation 3.3):

$$h = \frac{b_o}{(\boldsymbol{\alpha} - \boldsymbol{\alpha}_{in}) : \mathbf{n}} . exp \left[\mu_0 . \left(\frac{p'}{p_{atm}} \right)^{0.5} . \left(\frac{b^M}{b_{ref}} \right)^2 \right] \tag{3.2}$$

Here, (b^M) represents the distance between the memory and yield loci, b_{ref} is defined as $\boldsymbol{\alpha}^b - \tilde{\boldsymbol{\alpha}}^b) : \mathbf{n}$, with all terms illustrated in Figure 3.4. $\boldsymbol{\alpha}_{in}$ signifies the initial back-stress ratio tensor at load reversal, b_0 corresponds to the hardening factor, and b_{ref} indicates the reference distance for normalization. The parameter μ_0 controls strain accumulation under drained cyclic loading. To use the SANISAND-MS model, 16 parameters are necessary, which can be determined and calibrated through laboratory and centrifuge testing.

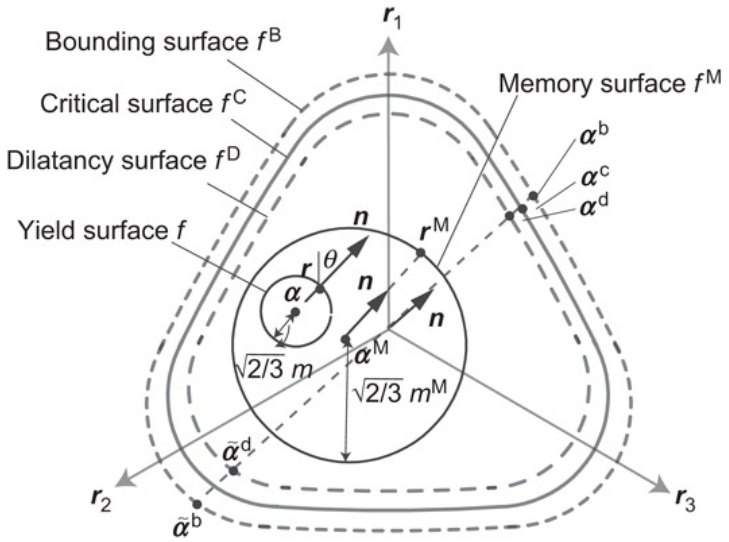

Figure 3.4: SANISAND-MS model loci in the deviatoric stress ratio plane - from [82]

.

Two series of centrifuge tests were performed, and the initial 100 cycles of each test were employed for the calibration of the constitutive relationship. Each test involved a 100 g sample subjected to unidirectional cyclic loading with different load parcels. In the first test (Figure 3.5a), the load amplitudes followed a sequence of $400N \rightarrow 800N \rightarrow 1200N \rightarrow 1600N$, while in the second test (Figure 3.5b), the load amplitudes followed $1600N \rightarrow 400N \rightarrow 800N \rightarrow 1200N$. The physical modeling employed very dense sand with a relative density of 0.97. An aluminum pile was used in the centrifuge tests, and following the scaling law, the pile geometry was transformed to an outer diameter (D) of 6 meters, an embedded length (L) of 36 meters, a load eccentricity (e) of 36 meters, and a pile thickness (t_p) of 0.25 meters.

To utilize the SANISAND-MS model, a total of sixteen parameters are required, and an additional parameter, $M_{b,max}$, is introduced to enhance the stability of SANISAND-MS in Plaxis. $M_{b,max}$ is a constant representing the maximum stress ratio under triaxial compression. The calibration of fifteen parameters for Geba Sand has been conducted in a separate study, using both laboratory and centrifuge tests.

A prior study by Liu et al. [24] suggested that a maximum value of μ_0 equal to 250 was adequate for accurately capturing the ratcheting phenomenon in the soil. However, further calibration was found necessary to determine the correct value of μ_0 that aligns better with the results of the centrifuge

tests. This difference might be attributed to the influence of stress levels, as the previous study by [24] calibrated the μ_0 value based on triaxial element test results by [57].

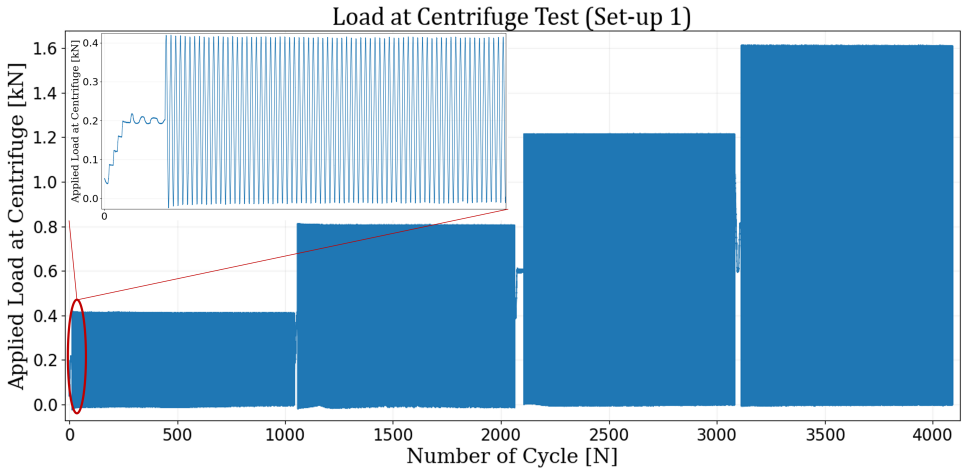

(a) $400N \rightarrow 800N \rightarrow 1200N \rightarrow 1600N$

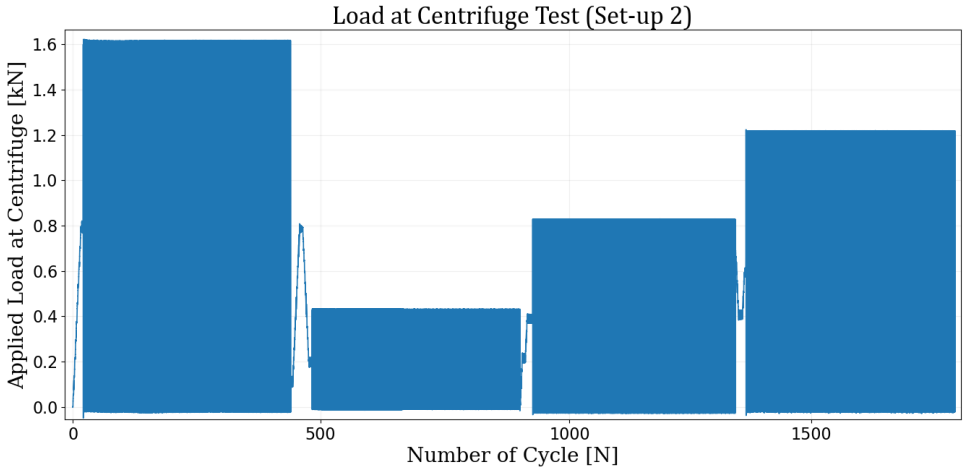

(b) $1600N \rightarrow 400N \rightarrow 800N \rightarrow 1200N$

Figure 3.5: Two sets of centrifuge tests at $100g$ that used for parameter calibration with load sequence (a) $400N \rightarrow 800N \rightarrow 1200N \rightarrow 1600N$ and (b) $1600N \rightarrow 400N \rightarrow 800N \rightarrow 1200N$ (test conducted by H. Wang (2022) and obtained from personal correspondence).

A series of μ_0 values was examined against the centrifuge data. For the lower load of 400 N ($\zeta_b = 0.1$), it was observed that the μ_0 parameter is not very sensitive against the accumulated displacement value (Appendix A). However, further investigation revealed that more accurate displacement calculations could be achieved by selecting μ_0 values within the range of 400 to 500. Subsequently, additional calibration was performed for the higher load of 16 MN ($\zeta_b = 0.4$), and it was determined that a μ_0 value of 500 provided better predictions of the accumulated displacement. The comparison between the load and displacement at the mudline demonstrated a favorable agreement between the 3D FE model and the centrifuge results when μ_0 was set to 500 (Appendix A). Consequently, for the remainder of this project, the value of $\mu_0 = 500$ was adopted consistently across all models.

Sixteen SANISAND-MS parameters used for the 3D FE Method are detailed in Table 3.1. Due to the characteristics of the SANISAND family constitutive model, a Poisson ratio of $\nu = 0.05$ was employed in the model. Additionally, apart from the 16 SANISAND-MS parameters, the maximum void ratio ($\bar{e}_{max}$) was set to 1.07, the minimum void ratio ($\bar{e}_{min}$) is 0.64, and the soil friction angle (ϕ_{soil}) is 30^o. In the model, the influence of D_r on the soil unit weight was taken into account, and at $D_r = 0.9$ the soil dry

unit weight (γ_{dry}) was determined to be $15.85 kN/m^3$.

Table 3.1: The parameters to model Geba sand using SANISAND-MS constitutive model.

Parameters	Description	Value	Dimension
G_0	Dimensionless shear modulus	400	[-]
ν	Poisson ratio	0.05	[-]
M_c	Critical stress ratio in compression	1.25	[-]
c	Compression-to-extension ratio	0.702	[-]
λ_c	CSL shape parameter	0.0015	[-]
ξ	CSL shape parameter	0.7	[-]
$\bar{e}_0$	Reference critical void ratio	0.935	[-]
m	yield locus opening parameter	0.1	[-]
h^0	hardening parameter	8.640	[-]
c_h	hardening parameter	1.09	[-]
n^b	void ratio dependence parameters	0.96	[-]
n^d	void ratio dependence parameters	0.75	[-]
A_0	intrinsic dilatancy parameter	1.104	[-]
μ_0	ratcheting parameter	500	[-]
ζ	memory surface shrinkage parameter	0.0001	[-]
β	dilatancy memory parameter	0	[-]

3.2.2. Pile

The material employed to represent the monopile consists of plate elements, and their behavior is assumed to be linear and isotropic. These plate elements are assigned the properties of steel, as indicated in Table 3.2. Although the analysis is performed in a dry sand environment, impermeability can be introduced into the plate elements by utilizing positive and negative interfaces with the pile elements. The thickness of the plate elements (t_p) is consistently set at $10cm$. In the following chapter, t_p will be presented in terms of pile diameter ratio over t_p (D/t_p).

Table 3.2: Material properties of the plate employed in the monopile

Property	Symbol	Dimension	Value
Unit Weight	γ	kN/m^3	78.5
Young Modulus	E	kN/m^2	$200.E6$
Poisson Ratio	ν	[-]	0.3
Shear Modulus	G	kN/m^2	$76.92.E6$

3.2.3. Pile-Soil Interface

The interface elements are designed to induce negligible deformation, and the Mohr-Coulomb material model is employed to model it. A specific set of interface parameters is chosen to model the area of intense shearing around the soil-monopile contact area (Table 3.3). Although the tensile strength is zero, tension cut-off is considered in this model. The gap closure is not selected for the interface element, as this option is already enabled in the soil model to ensure the restoration of contact between the soil and structure before imposing another compressive force.

The soil elastic modulus (E_{soil}) is determined based on the value of G_0 (Table 3.1), utilizing the

following equation:

$$E_{soil} = G_0.p_{atm}\left[\frac{(2.97-\bar{e}_{ini})^2}{(1+\bar{e}_{ini})}\right]\left(\frac{p'_{cr}}{p_{atm}}\right)^{0.5} \tag{3.3}$$

In this equation, p_{atm} represents the reference atmospheric pressure ($101kPa$), $\bar{e}_{ini}$ denotes the initial void ratio, and p'_{cr} is the mean effective stress ratio of soil at rest. The coefficient of lateral earth pressure at rest (K_0) is automatically calculated, with the same value applied in both the x and y directions.

Table 3.3: Material properties of the Pile-Soil Interface

Property	Symbol	Dimension	Value
Unit Weight	γ	kN/m^3	as soil unit weight
Elastic Modulus	E	kN/m^2	$5.E_{soil}$
Poisson Ratio	ν	[-]	0.3
Initial void ratio	$\bar{e}_{ini}$	[-]	as soil void ratio
Reference level	z_{ref}	m	1
Effective cohesion	c'_{ref}	kN/m^2	0
Interface friction angle	ϕ_i	[^{o}]	$2/3.\phi_{soil}$
Strength reduction ratio	R_{inter}	[-]	0.67

3.3. Boundary and Initial Conditions

To prevent rigid body movement of the FE mesh, constraints are applied at the base, setting all three displacement components in the x, y, and z directions to zero. Additionally, displacements normal to the vertical boundaries are constrained, along with zero forces in the vertical z direction and tangential directions to these boundaries. To ensure that the $x-z$ plane at $y=0$ functions as a plane of symmetry, displacements normal to this plane (i.e., in the y-direction) are constrained, as well as the forces in the x and z directions.

The horizontal surface at the pile head is treated as rigid to prevent deformation under high lateral loads. This rigid body is used to represent the applied load and does not possess any volumetric value. The lateral and moment loads are applied at the coordinates $x=0$, $y=0$, and $z=e$. Within this rigid body, there is a reference point that is defined by a combination of forces, moments, and/or displacements, as described in [79].

Table 3.4: The boundary conditions of the reference point at the rigid body.

	Condition	
Axis	**Translation**	**Rotation**
x	Force	Moment
y	Force	Moment
z	Force	Moment

When an external force is applied, the reference point becomes associated with six independent degrees of freedom (DOF) and contributes six force components to the global equations. This reference point encompasses a separate set of DOFs that is distinct from the rest of the finite element (FE) model. Consequently, boundary conditions for all six DOFs of the reference point must be explicitly specified. These boundary conditions can encompass either force or displacement conditions, and the boundary conditions used in this study are outlined in Table 3.4. It is important to note that the terms "moment"

and "rotation" refer to rotation and moment around their respective axes, with a positive rotation value indicating a clockwise rotation relative to the positive axis direction.

In general, the procedures for the 3D Finite Element (FE) model can be categorized into four distinct phases, each of which is detailed below:

- Initial Phase:
  During this initial phase, soil stress is computed following the K_0 procedure. The impact of sand relative density (D_r) on the sand unit weight is taken into account, with γ_{dry} equal to $15.85 kN/m^3$ for sand with $D_r = 0.9$. The initial void ratio is also determined as a function of D_r, with the maximum void ratio ($\bar{e}_{max}$) at 1.07 and the minimum void ratio ($\bar{e}_{min}$) at 0.64. The applied load originates from the self-weight of the soil, and lateral soil pressure is calculated using the Jaky K_0 method. The deformation is not considered during this phase.
- Equilibrium Phase:
  In the equilibrium phase, the monopile is assumed to be installed in place (WIP), and the effects of its installation are not taken into consideration. This assumption is consistent with a study conducted by [83], which suggests that the response of a monopile to lateral cyclic loading is nearly identical, whether the pile is plugged or unplugged, implying that the installation effect can be deemed negligible. Plastic calculations are employed during this phase, with a time interval set to zero days. The displacements are reset to zero, and small strains are also reset upon the completion of this phase.
- Unloading Phase:
  The unloading phase follows the equilibrium phase and is consistently employed after the loading phase in cyclic analyses. The model is run using plastic calculations.
- Loading Phase:
  The configuration in the loading phase mirrors that of the unloading phase. During this phase, lateral loads are incrementally applied using the rigid body load until the maximum prescribed lateral load is reached.

In these analyses, the contribution of the vertical load resulting from the weight of the pile on the lateral response of the monopile is not taken into account.

3.4. Finite Element Result Post-Processing

3.4.1. Extraction of Lateral Soil Reaction and Distributed Moment

By employing the pile-soil interface, it is possible to extract the stresses that come from the soil-pile interaction. The illustration of the positive orientation of the stresses in the interface elements is provided in Figure 3.6. In the Plaxis 3D FE analysis database, the stress responses are segmented into three components: normal effective stress (σ'_N), horizontal shear stress (τ_1), and vertical shear stress (τ_2).

The soil reaction per unit length along the circumference of the monopile, denoted as p, corresponds to the x-component of the total stress exerted on the pile. This stress component at a specific point within a soil element is represented by the traction vector T_x, as defined by the following expression [84]:

$$T_x = \sigma'_N n_x + \tau_1 n_y \tag{3.4}$$

where, n_x and n_y represent the unit normal components along the x- and y-directions (Figure 3.6, 3.1),

respectively, and can be expressed as:

$$n_x = \cos\theta_x \tag{3.5}$$

$$n_y = \cos\theta_y \tag{3.6}$$

The symbols used in the equations above (Eq. 3.5, 3.6) are depicted in Figure 3.7.

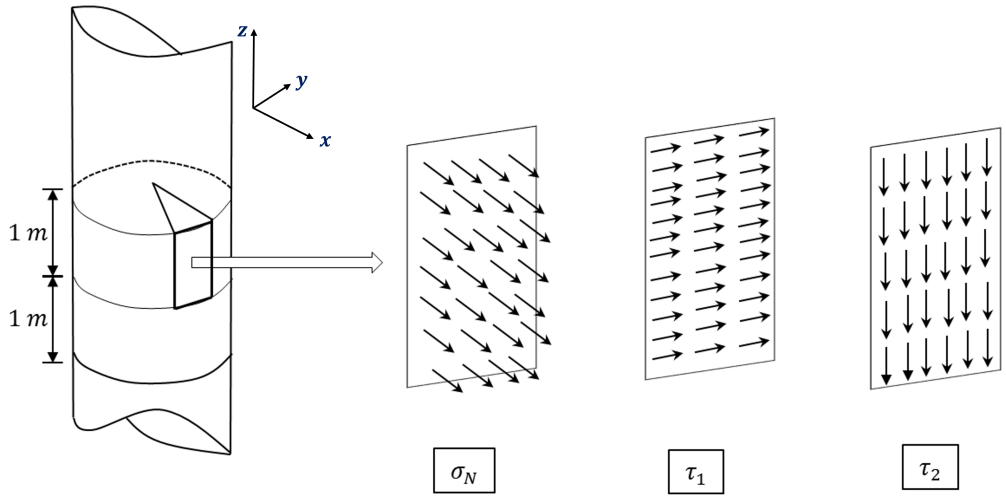

Figure 3.6: From the left to the right: pile slice at a given depth for stress evaluation; positive normal effective stress (σ'_N); horizontal shear stress (τ_1); and vertical shear stress (τ_2) - after [85]

.

Figure 3.7 visually demonstrates the aforementioned expression. To obtain an accurate horizontal soil reaction (p), T_x is recorded at multiple stress points along the circumference of the pile. The horizontal soil reaction (p) is determined by combining the x-components of σ'_N and τ_1 for each interface element. To calculate the total soil reaction per unit length along the pile, p is integrated over the pile circumference (Figure 3.6), resulting in the following expression:

$$p = \int T_x \, dA \tag{3.7}$$

where A represents the circumference of the monopile element.

The stress acting on the z-plane in the x-direction (τ_2) (Figure 3.6) must be accounted for as a distributed moment along the monopile. To calculate the distributed moment, an additional traction vector in the z-direction (T_z) is introduced and determined as follows:

$$T_z = \tau_2 n_z \tag{3.8}$$

Given that τ_2 acts in the same z-direction, the value of n_z equals 1. The process of recording T_z follows the same steps as recording T_x. The total vertical soil reaction is obtained by integrating T_z over the pile circumference, as shown in Figure 3.6. This gives the vertical soil reaction denoted as p_v in kilo-newton per meter and represented by the following expression

$$p_v = \left(\int T_z \, dA \right) \tag{3.9}$$

following this equation (Eq. 3.9), the distributed moment can be calculated as follows:

$$M_d = p_v.r \tag{3.10}$$

where r is the radius of the monopile (Figure 3.7).

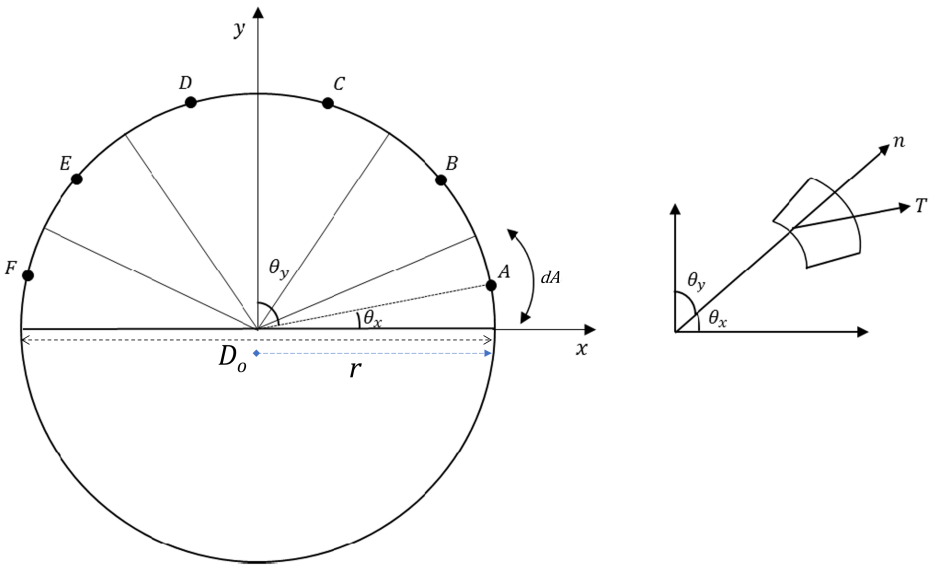

Figure 3.7: Schematic cross-section and example of how the stress points are recorded - after [85]

.

3.4.2. Calculation of Base Shear Force and Base Moment

The study conducted by [83] suggests that the response of a monopile to lateral cyclic loading is nearly identical, whether the pile is plugged or unplugged, implying that the installation effect is negligible. However, the surrounding soil near the pile base influences the lateral capacity of the pile. Based on this assumption, it is necessary to calculate the base shear force for the entire pile base area. To account for the entire pile base area, the base shear force (F_b) and base moment (M_b) are calculated using the equilibrium principle. The calculation of the base shear force (F_b) involves the following equation.

$$\begin{aligned} \int_0^L p(z)\,dz + F_b - H &= 0 \\ F_b &= H - \int_0^L p(z)\,dz \\ F_b &= H - \Sigma p \end{aligned} \tag{3.11}$$

In this model, the integral of the p curve was generated by interpolating the recorded data points (Figure 3.8a). Consequently, achieving an accurate total lateral soil reaction (Σp) through a summation process requires a very fine discretization size (Δ_z), as depicted in Figure 3.8b. However, employing a finer mesh with smaller elements in the FE analysis consumes significant memory resources and extends the simulation duration. To tackle this challenge, a discretization size of 1 meter per element is selected, and the integration of p is carried out using the trapezoidal integration rule (Figure 3.8c). The accuracy of the trapezium integration has been assessed and found to significantly reduce errors

originating from mesh dependency in the extraction processes of lateral soil reaction (Appendix A).

The calculation of the base moment (M_b) is performed based on the equilibrium principle. It involves the following formula:

$$M - \int_0^L p(z)z\,dz - M_{Fb} - \int_0^L M_d(z)\,dz - M_b = 0$$

$$M_b = M - \int_0^L p(z)z\,dz - M_{Fb} - \int_0^L M_d(z)\,dz - M_b$$

$$M_b = M - \Sigma M_p - M_{Fb} - \Sigma M_d - M_b \tag{3.12}$$

$$M_{Fb} = F_b \times L \tag{3.13}$$

$$M = H \times e \tag{3.14}$$

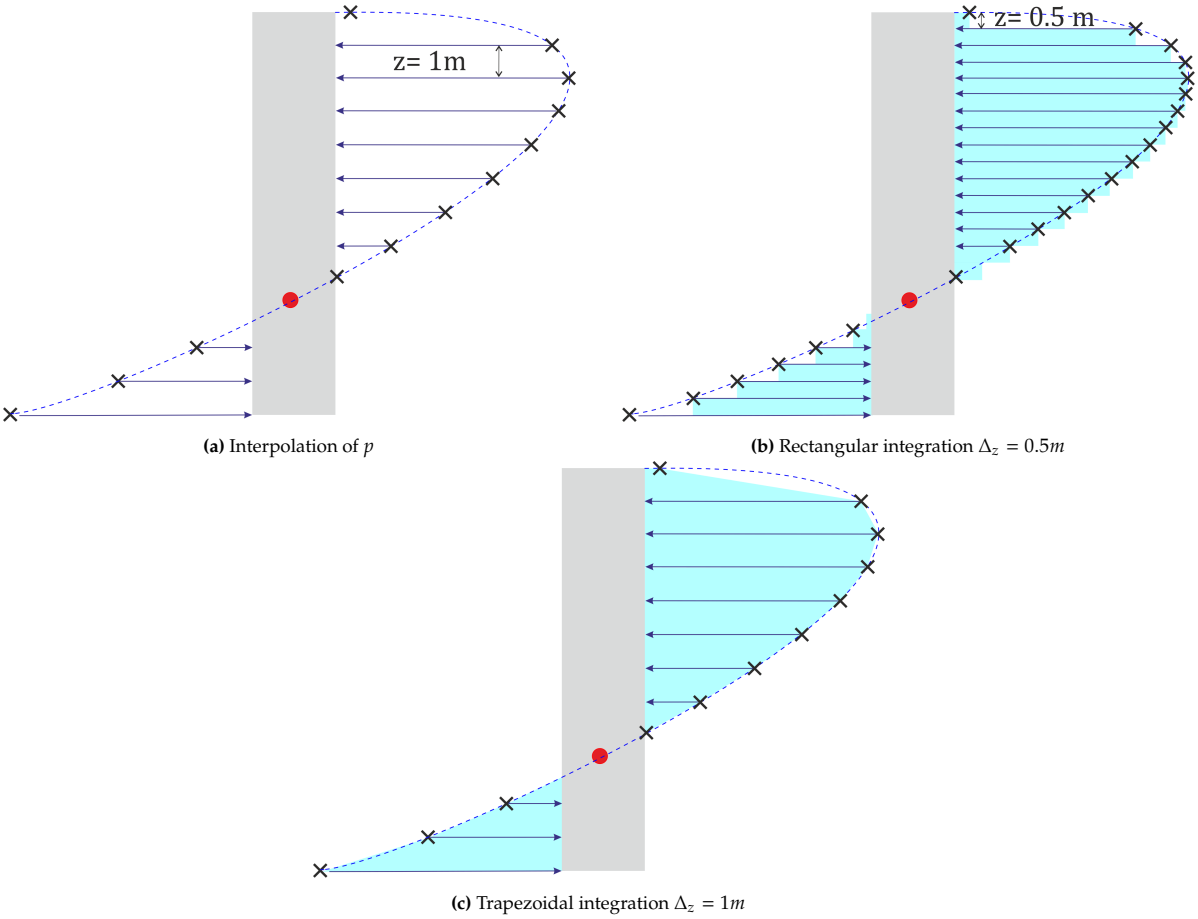

(a) Interpolation of p

(b) Rectangular integration $\Delta_z = 0.5m$

(c) Trapezoidal integration $\Delta_z = 1m$

Figure 3.8: Illustration how to obtain a p curve from recorded points and the method to calculate total p.

Given the utilization of the trapezoidal integration method with a discretization size of $\Delta_z = 1$ meter to determine the total p, the calculation of $(\sum M_p)$ involves dividing the p within each element into two distributed loads, namely rectangular and triangular loads (Appendix A). Near the center of instantaneous rotation, the p is further divided into two triangular distributed loads (Appendix A). The moment is obtained by computing the total load multiplied by the lever arm. However, accurately determining the position of the rotational point (RP) poses significant challenges due to numerical instability. Therefore, careful judgment is required when calculating the bending moment from each p

element (M_p), as the resulting RP may not precisely represent the point where $y = p = 0$ (Appendix A). Furthermore, a comparison between the model responses and the findings of the study by [61] is also presented in Appendix A.

4

Reference Case

The reference case serves as the benchmark for the subsequent analyses. This chapter offers a discussion of the cyclic and monotonic responses pertaining to the reference case. Detailed information regarding the pile geometry and the sand relative density (D_r) employed in the reference case is presented in Table 4.1.

Table 4.1: Pile geometry and soil setup for the reference case

Code	D[m]	L/D [-]	e/D[-]	D/t_p[-]	D_r[-]	K_r[-]	Class
0A	9	4	5	90	0.9	0.0064	Semi-rigid

In the Table 4.1, the ratio of load eccentricity (e) to D is indicated as e/D. One-way cyclic lateral load analyses ($\zeta_c = 0$) are also performed with load parameter (ζ_b) values of 0.4 and 0.1.

4.1. Monotonic Load

4.1.1. Load-Displacement and Moment-Rotation Curves

Load-displacement and moment-rotation curves are constructed with the criterion that the ultimate capacity is achieved when the rotation of the monopile at the mudline or seabed (θ_{sb}) reaches 2^o. These curves for the reference case are illustrated in Figure 4.1. In the load-displacement curve, the ultimate lateral capacity (H_{ult}) and ultimate displacement are reached when the monopile (MP) rotation at the mudline (θ_{sb}) is approximately 2^o.

The load-displacement ($H - y$) and moment-rotation ($M - \theta$) curves are also present in their normalized form (Figure 4.2). The normalization process is performed following the method proposed by Leblanc et al. [37], as following expressions:

$$\frac{H}{L^2 D \gamma_{dry}} \tag{4.1}$$

$$\frac{M}{L^3 D \gamma_{dry}} \tag{4.2}$$

Here, γ_{dry} denotes the dry unit weight of the soil. Additionally, the pile displacement at the mudline (y_{sb}) is normalized with respect to D. The purpose of this normalized plot is to facilitate the comparison of the results with responses obtained from scaled tests, such as centrifuge tests or pile tests with smaller values of D. While such tests are not included in this study, future works possibly require a comparable plot presented in a normalized form.

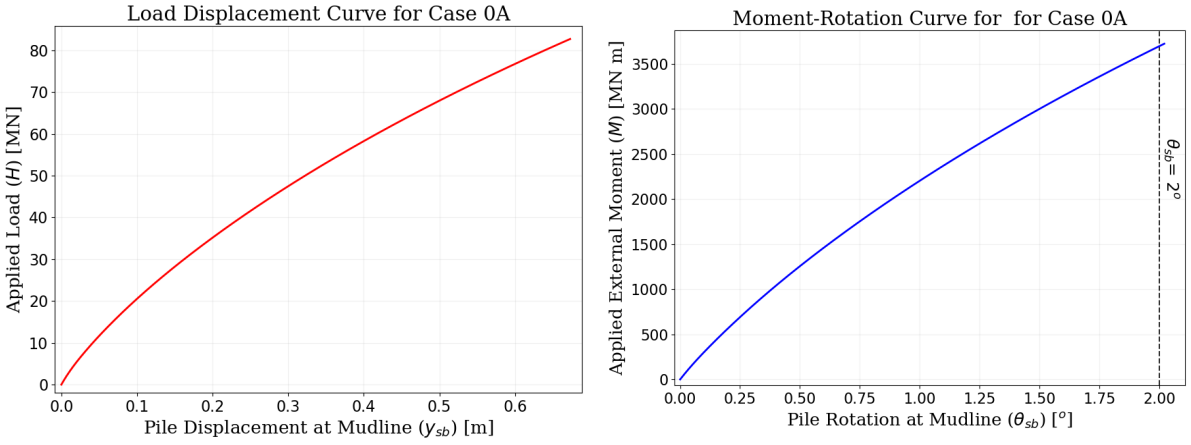

(a) Load-displacement curve

(b) Moment-rotation curve

Figure 4.1: The ultimate capacity of monopile represent in term of (a)Load-displacement and (b)Moment-rotation curve for the reference case (The maximum displacement obtained when $\theta_s b = 2^o$).

Based on the analysis of the $H-y$ and $M-\theta$ curves (Figure 4.1), it is determined that for the reference case, $H_{ult} = 82.7MN$, $y_{ult} = 0.673m$, and $M_{ult} = 3721.5MNm$. Upon inspecting the normalized $H-y$ curve (Figure 4.2a), it is observed that the ultimate normalized displacement is $y_{ult}/D = 0.075$.

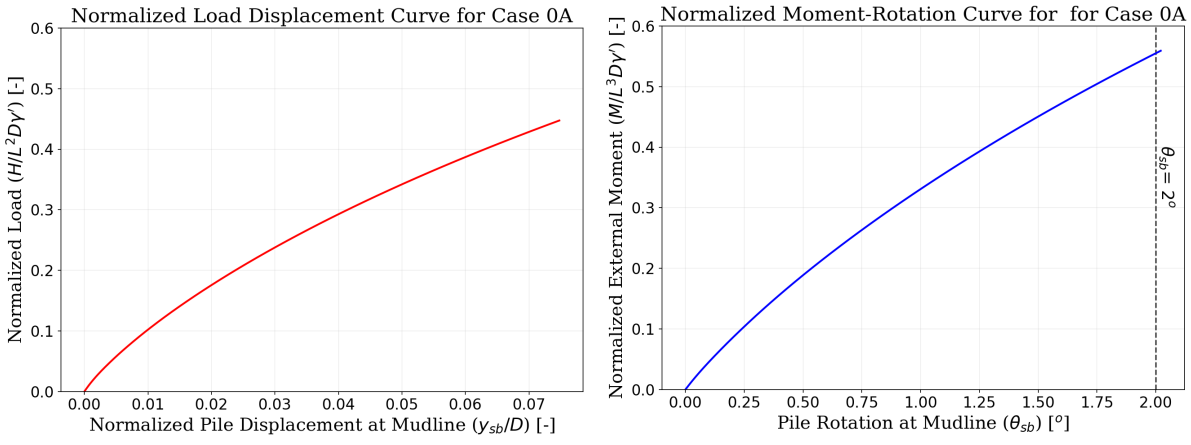

(a) Load-displacement curve

(b) Moment-rotation curve

Figure 4.2: The Normalized (a)Load-displacement and (b)Moment-rotation curve for the reference case (The maximum displacement obtained when $\theta_{sb} = 2^o$).

4.1.2. p-y curve

The distribution of p along the monopile can be represented as a simplified distribution model (Figure 4.3). This model aligns with the simplified model proposed by [86].

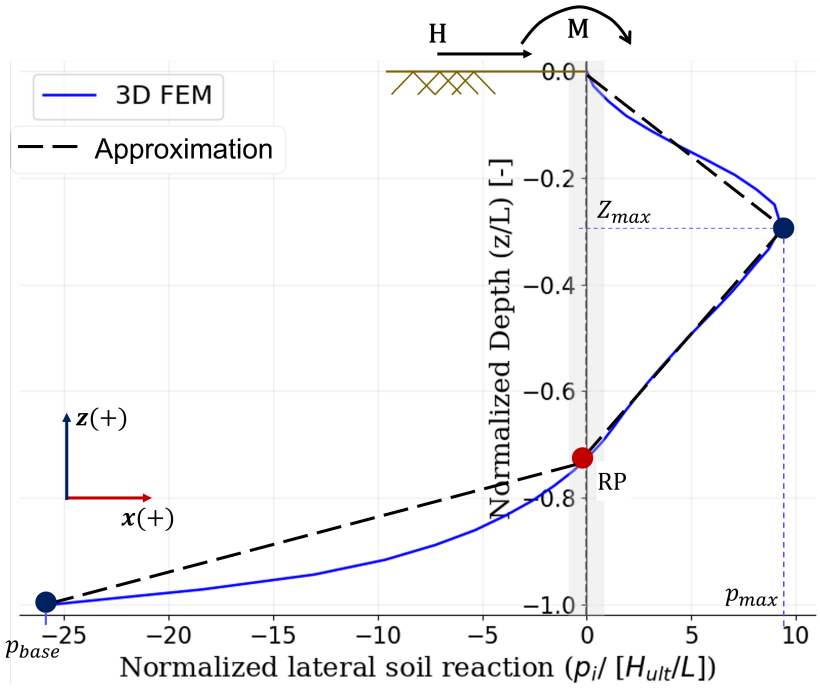

Figure 4.3: The lateral soil reaction (p) curve at ultimate load (H_{ult}) over the monopile length from the 3D FE model and the model to approximate the curve (Case 0A). This model is suggested to be used only for rigid and semi-rigid monopiles.

In the model (Figure 4.3), the distribution of p is assumed to be adequately represented by two triangles. Four parameters are required to derive the distribution: $p_{\max}$, p_{base}, $z_{\max}$, and rotational point (RP) (Figure 4.3). This approach enables estimation of Σp and allows for the determination of the F_b value based on the equilibrium principle (Eq. 3.11). Additionally, this approach can be used to calculate the bending moments along the monopile.

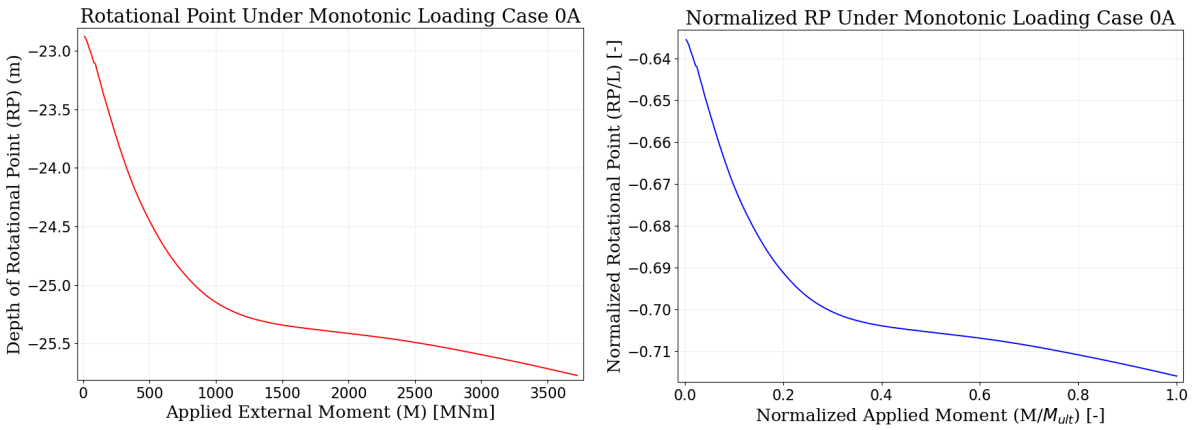

(a) Depth of Rotational Point

(b) Normalized Rotational Point

Figure 4.4: The depth of rotational point for reference case present in (a)absolute value and (b) normalized value

The rotational point (RP) is precisely defined as the location along the monopile where the pile displacement (y) approaches zero ($y \simeq 0$). In the vicinity of this region ($y \simeq 0$), the lateral soil pressure (p) is assumed to have converged to zero as well. However, due to mesh dependency effects and the fact that the Δ_z for recording p is $1m$ while for y it is $0.5m$, there is a small disparity between the RP obtained through the interpolation of p and that obtained through the interpolation of y. Nonetheless, this disparity is considered negligible, amounting to only up to $42cm$. To ensure precision and consistency,

the RP is consistently calculated as $y \simeq 0$ in all cases.

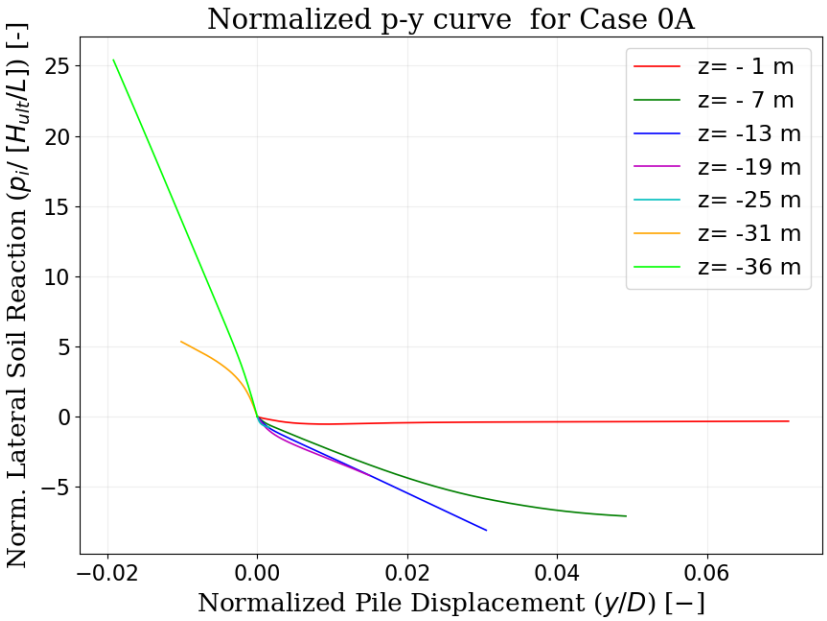

(a) $p - y$ at different depth

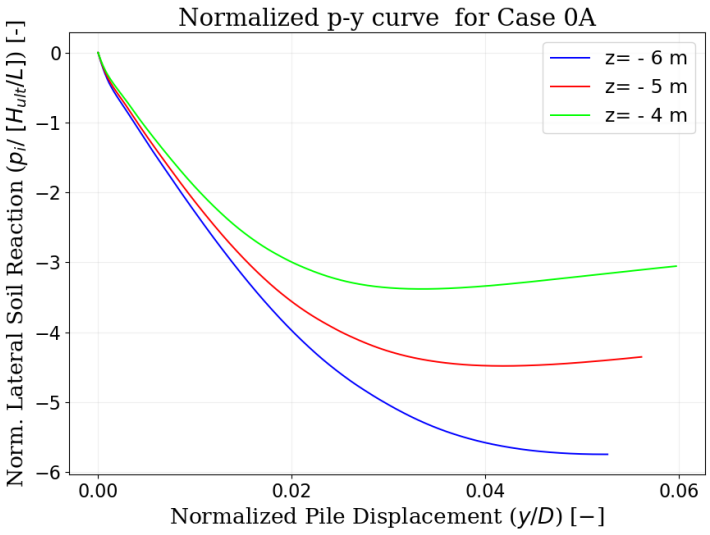

(b) $p - y$ curve where softening occurs

Figure 4.5: The normalized $p - y$ curves for reference case when the ultimate load (H_{ult}) is applied for (a)multiple depth and (b) the depth where softening is observed .

The analysis of the RP for the reference case is depicted in Figure 4.4. Examining the evolution of the RP (Figure 4.4a), it is evident that in the early stages of loading, the RP is situated at a shallow depth. As the applied load increases, the RP gradually shifts to a deeper level. The normalized plot (Figure 4.4b) indicates that the final value of RP is located at a depth of approximately $z \simeq 0.72L$. This observation closely aligns with the findings of [86], which reported that the rotational point is typically situated at a depth of $0.75L$.

Examining the normalized $p - y$ curves along the depth of the monopile reveals that the behaviors of p and y are influenced by the position of the soil element relative to the rotational point (RP) (Figure 4.5a). At a depth less than RP (Figure 4.3), the p acts in the opposite direction of H, and y acts in the positive direction. While the p and y act in the opposite manner for the depth higher than RP (Figure

4.3 4.5). In the vicinity of the RP, both p and y tend to converge to zero, as evident in the $p - y$ curve for $z = -25m$ (Figure 4.5a).

Further examination of the $p - y$ curve at shallow depths (Figure 4.5b) reveals a softening behavior in the $p - y$ response. The conventional approach to the $p - y$ curve (e.g., [30]) (Eq. 2.1) estimates the $p - y$ relationship based on soil hardening response alone. However, there is an indication that the $p - y$ response should also account for softening behavior, especially in shallow soil layers. This suggests the need for additional investigation into the response of soil elements in these conditions.

4.1.3. Local Soil Response under Monotonic Load

Stress and strain measurements were conducted to investigate the behavior and response of soil elements under monotonic loading conditions. The analysis primarily focused on the soil surrounding the monopile in axial (Figure 4.6a), lateral (Figure 4.6b), and radial directions (Figure 4.6c). Additionally, the analysis extended to include the soil elements at the pile base (Figure 4.6d). The configuration of the analysis is depicted in Figure 4.5 and detailed in Tables 4.2, 4.3, 4.4, and 4.5.

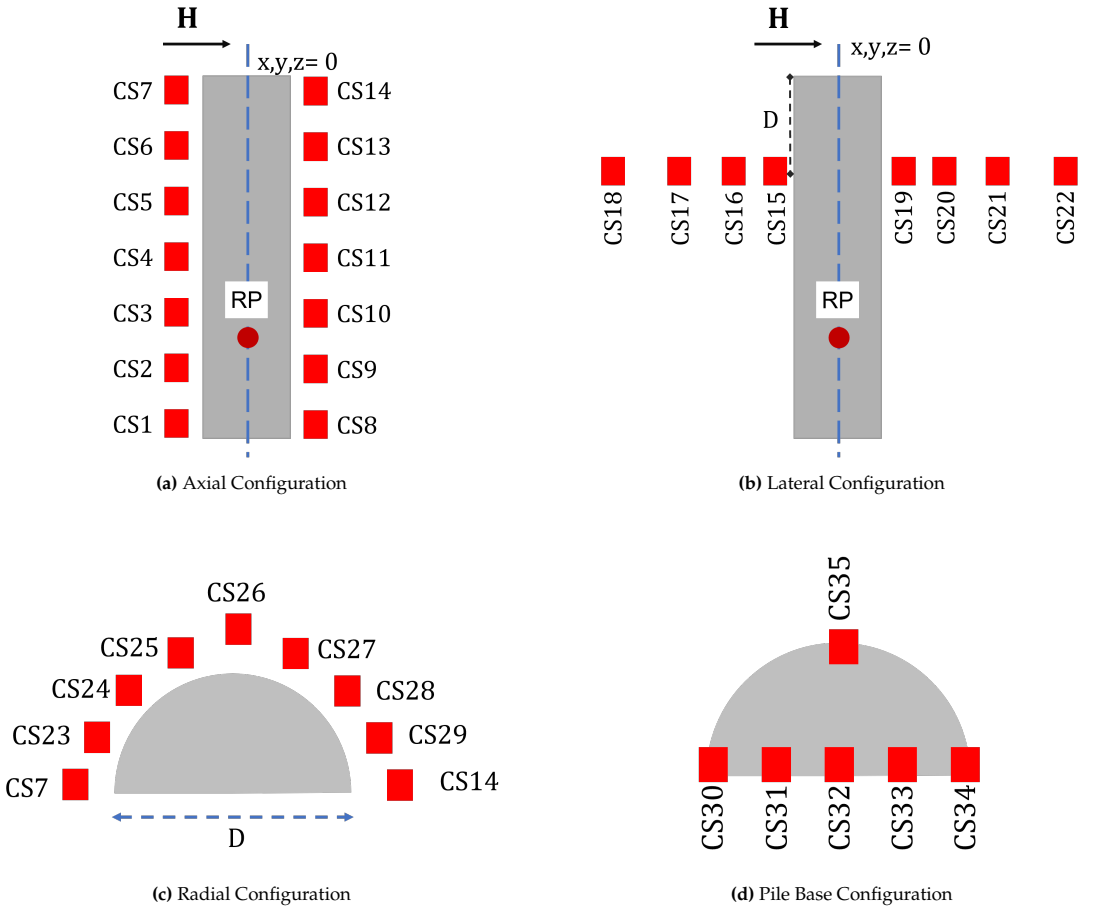

(a) Axial Configuration

(b) Lateral Configuration

(c) Radial Configuration

(d) Pile Base Configuration

Figure 4.6: The configuration of stress and strain recording in the soil around the monopile for configuration in (a) axial direction, (b) lateral direction, (c) radial direction on the pile top, and (d) pile base.

The recorded data were utilized to create void ratio-mean effective stress ($\bar{e} - p'$) diagrams for each element. To further explore the distance between the state of each soil element to their respective critical state line (CSL) during lateral loading, an additional analysis of the state parameter (Ψ) is provided. The void ratio (e) is extracted from Plaxis, and p' is calculated using the following equation:

$$p' = \frac{\sigma'_x + \sigma'_y + \sigma'_z}{3} \tag{4.3}$$

Here, $\sigma'_x, \sigma'_y, \sigma'_z$ represent the effective stress components in Cartesian coordinates.

The assessment of state parameters (Ψ) has been conducted by calculating Ψ using the following expressions:

$$\Psi(\bar{e}, p) = \bar{e} - \bar{e}_{cr} \tag{4.4}$$

$$\bar{e}_{cr} = \bar{e}_0 - \lambda_c(\frac{p'}{p_{atm}})^{\xi} \tag{4.5}$$

Here, $\bar{e}_{cr}$ is the critical void ratio, $\bar{e}_0$ is the reference critical void ratio, λ_c and ξ are CSL shape parameters (Table 3.3), p' is soil mean effective stress, and p_{atm} is the reference atmospheric pressure ($101kPa$). A positive Ψ signifies that the soil is in a loose state and tends to compact under shearing forces, while a negative Ψ indicates that the soil is in a dense state and tends to dilate under shearing.

Table 4.2: Coordinate of stress and strain recording configuration along the monopile in axial direction

Code	X [m]	Y [m]	Z [m]	Code	X [m]	Y [m]	Z [m]
CS 1	-0.7D	±0	-L	CS 8	0.7D	±0	-L
CS 2	-0.7D	±0	-5L/6	CS 9	0.7D	±0	-5L/6
CS 3	-0.7D	±0	-2L/3	CS 10	0.7D	±0	-2L/3
CS 4	-0.7D	±0	-L/2	CS 11	0.7D	±0	-L/2
CS 5	-0.7D	±0	-L/3	CS 12	0.7D	±0	-L/3
CS 6	-0.7D	±0	-L/6	CS 13	0.7D	±0	-L/6
CS 7	-0.7D	±0	±0	CS 14	0.7D	±0	±0

Table 4.3: Coordinate of stress and strain recording configuration along the monopile in lateral direction

Code	X [m]	Y [m]	Z [m]	Code	X [m]	Y [m]	Z [m]
CS 15	-0.6D	±0	-D	CS 19	0.6D	±0	-D
CS 16	-D	±0	-D	CS 20	D	±0	-D
CS 17	-1.5D	±0	-D	CS 21	1.5D	±0	-D
CS 18	-3D	±0	-D	CS 22	3D	±0	-D

Table 4.4: Coordinate of stress and strain recording configuration at the top of monopile (z= ±0) in the radial direction

Code	X [m]	Y [m]	Code	X [m]	Y [m]
CS 23	$(-0.7D)\cos 22.5^o$	$(0.7D)\sin 22.5^o$	CS 27	$(0.7D)\cos 22.5^o$	$(0.7D)\sin 22.5^o$
CS 24	$(-0.7D)\cos 45^o$	$(0.7D)\sin 45^o$	CS 28	$(0.7D)\cos 45^o$	$(0.7D)\sin 45^o$
CS 25	$(-0.7D)\cos 67.5^o$	$(0.7D)\sin 67.5^o$	CS 29	$(-0.7D)\cos 67.5^o$	$(0.7D)\sin 67.5^o$
CS 26	±0	0.7D			

An investigation into the mesh dependency effect was carried out to assess the influence of mesh size on the recorded stress data. Three different refining factors (rf) of 0.1, 0.15, and 0.25 were applied to the soil surrounding the monopile (Figure 3.1) for this evaluation. Higher rf values indicate a coarser mesh, whereas lower rf values represent a finer mesh.

Even though the mesh dependency effect is observed, the results indicate that changing the mesh sizes does not change the trend in the soil element (Appendix B). Since these analyses are focused on the trend that can be obtained from the stress path and void ratio analyses, looking at the result it is concluded that the mesh dependency effect is negligible.

Table 4.5: Coordinate of stress and strain recording configuration at the base of monopile

Code	X [m]	Y [m]	Z [m]	Code	X [m]	Y [m]	Z [m]
CS 30	-0.6D	±0	-L	CS 33	0.25D	±0	-L
CS 31	-0.25D	±0	-L	CS 34	0.6D	±0	-L
CS 32	±0	±0	-L	CS 35	±0	0.6D	-L

Analyzing the $\bar{e} - p'$ space and the evolution of Ψ during the loading phase in the axial direction (Figure 4.7, 4.8) reveals that the rotational point (RP) significantly influences soil deformation in both the positive and negative x-axes. Below the RP, specifically in the negative x-axis (CS 1 and CS2) (Figure 4.7a, 4.8a), compaction occurs due to the rotation from the pile. Conversely, for elements in the positive x-axis (CS 8 and CS 9) (Figure 4.7b, 4.8b), the void ratio increases due to volumetric expansion.

Observing the elements situated above the RP, the elements in the negative x-axis (CS 4 and CS 6) (Figure 4.7a, 4.8a) reveal a rise in void ratio due to volumetric expansion. Meanwhile, elements in the positive x-axis (CS 11 and CS 13) (Figure 4.7b, 4.8b) experience dilation caused by the shear force transferred from the monopile. A comparison between CS 13 and CS 11 (Figure 4.8) indicates that the rate of soil dilation is influenced by the overburden stress (σ'_{zz}), with a more pronounced dilation effect observed at CS 13 ($z = -L/6$) than at CS 11 ($z = -L/2$).

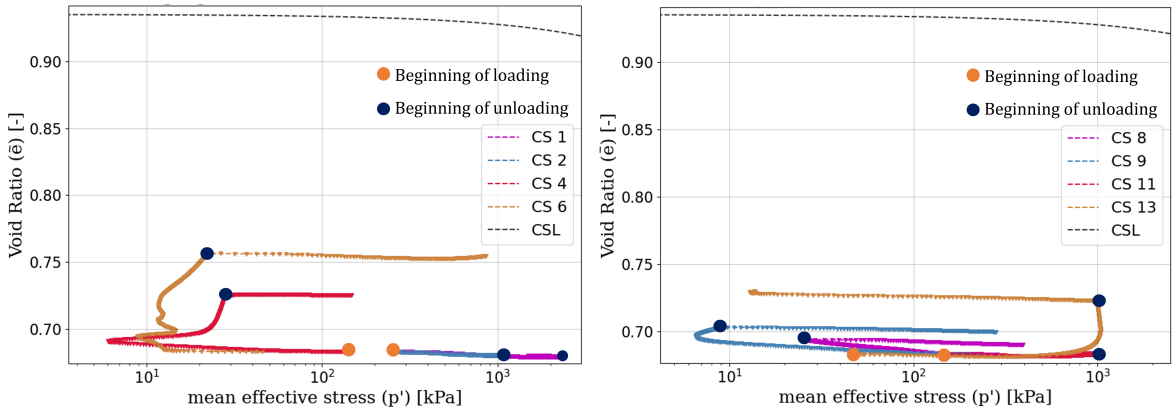

(a) negative x-axis **(b)** positive x-axis

Figure 4.7: The $\bar{e} - p'$ space for soil elements around the monopile in the axial direction at (a) negative $x-$axis and (b) positive $x-$axis for reference case (0A).

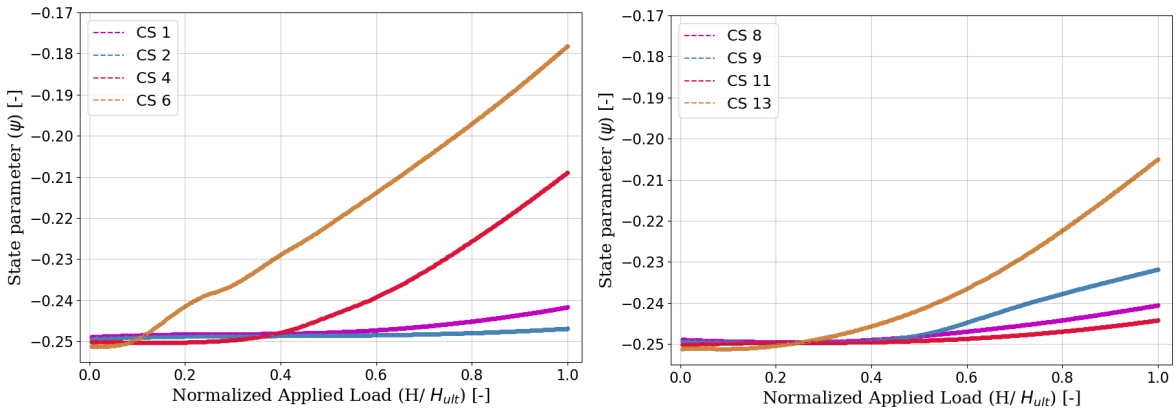

(a) negative x-axis **(b)** positive x-axis

Figure 4.8: The plot of state parameters (Ψ) during loading phase for soil elements around the monopile in the axial direction at (a) negative $x-$axis and (b) positive $x-$axis for reference case (0A).

Upon closer examination of the elements positioned at $z = -L/6$ (CS 6 and CS 13) (Figure 4.8), it becomes evident that both elements ultimately exhibit a substantial increment of void ratio during the loading phase. This observation aligns with the softening trend observed in the $p - y$ curve at a depth approximately around $-6m$, as depicted in Figure 4.5. When analyzing the $p' - q$ space (Figure 4.9), a reduction in p' is observed for element CS 6 (Figure 4.9a), with the p' value almost reaching 0 during loading. On the other hand, for CS 13 (Figure 4.9b), the stress path has already moved beneath the CSL during the loading phase. These observed phenomena in the $p - q'$ space possibly also align with the softening response in the p (Figure 4.5).

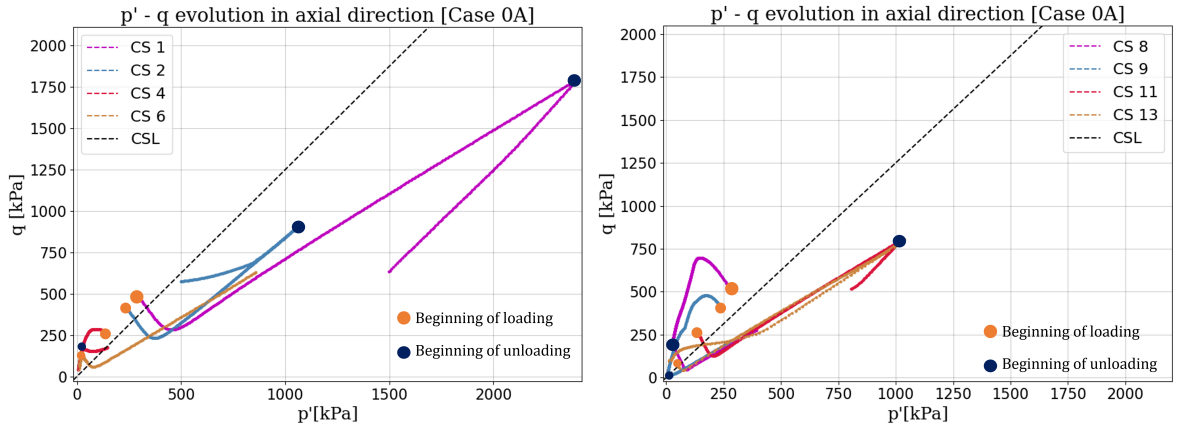

(a) negative x-axis **(b)** positive x-axis

Figure 4.9: The p′- q space for soil elements around the monopile in the axial direction at (a) negative $x-$axis and (b) positive $x-$axis for reference case (0A).

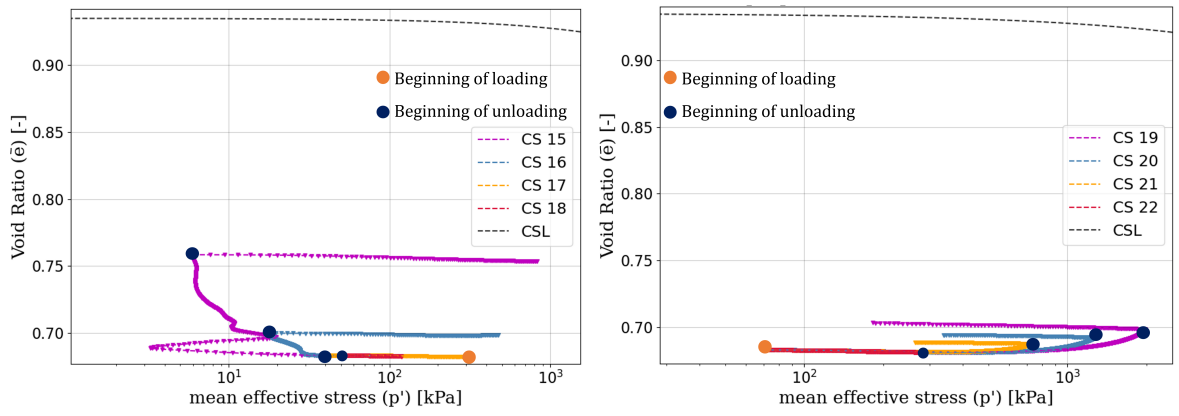

(a) negative x-axis **(b)** positive x-axis

Figure 4.10: The $\bar{e} - p'$ space for soil elements around the monopile at $z = -D$ in the lateral direction at (a) negative $x-$axis and (b) positive $x-$axis for reference case (0A).

The analysis in the lateral direction was conducted at a depth corresponding to $z = -D$, indicating a consistent trend among soil elements located on the same side of the monopile (Figure 4.10, 4.11). For the neighboring elements situated along the negative $x-$axis (CS 15 to CS 17), the void ratio exhibits an initial increase owing to volumetric expansion during the loading phase, followed by relatively minor compaction during the unloading phase (Figure 4.10a). In contrast, the surrounding elements located on the positive $x-$axis (CS 19 to CS 21) undergo compaction in the early loading phase, followed by pronounced dilation induced by the lateral load in the later stages (Figure 4.10b). Subsequent to unloading, these elements (CS 19 to CS 21) experience a slight increase in void ratio due to volumetric

expansion.

Moreover, an observation in the $\bar{e} - p'$ space (Figure 4.10, 4.11) suggests that soil elements located at a distance of $2.5D$ from the monopile (CS 18 and CS 22) do not appear to experience significant void ratio changes during when lateral load is imposed. The indication that dilation is not prominent under high overburden stress conditions is visually depicted in Figure 4.11b. Upon examining the evolution of Ψ, it becomes evident that, under high overburden stress, the void ratio increase due to volumetric expansion (Figure 4.11a) is substantially more pronounced compared to the influence of dilation (Figure 4.11b).

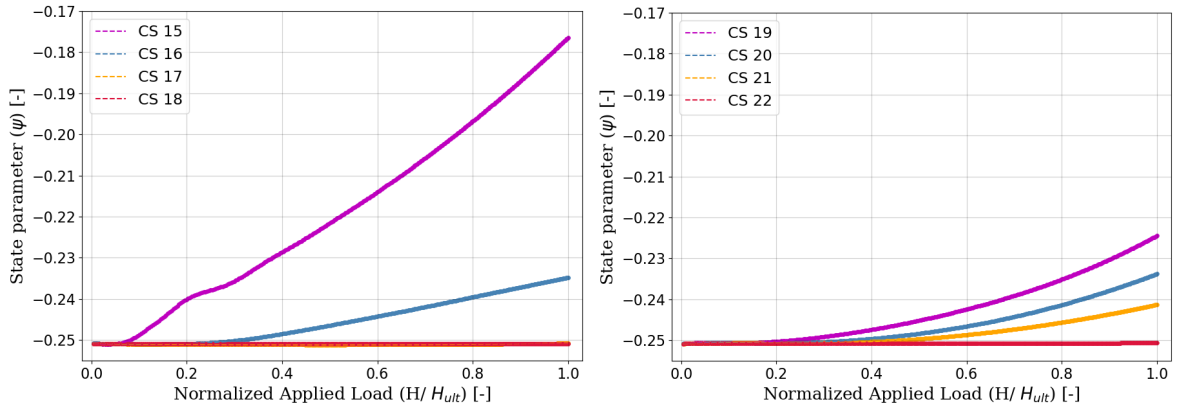

(a) negative x-axis **(b)** positive x-axis

Figure 4.11: The plot of state parameters (Ψ) during loading phase for soil elements around the monopile at $z = -D$ in the lateral direction at (a) negative $x-$axis and (b) positive $x-$axis for reference case (0A).

The assessment of the $\bar{e} - p'$ relationship for the soil elements situated at the mudline in the radial direction reveals a consistent increase in void ratio throughout both the loading and unloading phases (Figure 4.12a). This phenomenon is likely attributed to the relatively low confining stress imposed on these soil elements.

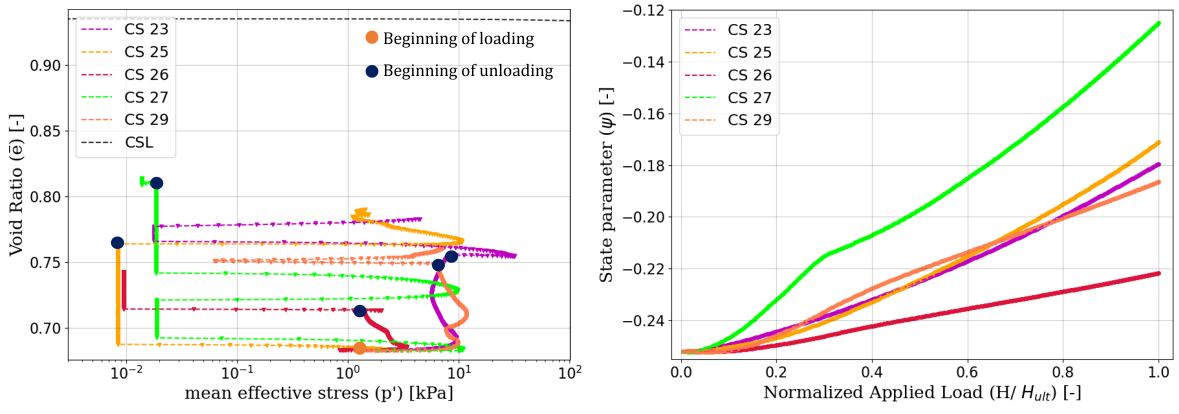

(a) $\bar{e} - p'$ space **(b)** Ψ plot during loading phase

Figure 4.12: The analysis results for soil elements around the mudline in radial direction presented in (a) $\bar{e} - p'$ space and (b) Ψ evolution during the loading phase for the reference case (0A).

When examining the evolution of Ψ (Figure 4.12b), it becomes evident that the most significant change in void ratio does not occur within the elements closest to $y = 0$ (CS 23 and CS 29). Instead, the highest void ratio change is observed in CS 27. This deviation may be ascribed to the location of CS 27, which results in the load from the monopile affecting the soil in a manner resembling a torsional

moment. A study by [87] indicates that applying torsional moment on lower confining stress can induce a higher dilation rate.

The recording of stress at the pile base entails the placement of elements beneath the rotational point (RP) and conducting measurements at approximately the same depth. A thorough examination of the $\bar{e} - p'$ space reveals that the majority of soil elements undergo shearing and dilation during the loading phase, with the exception of CS 34 and CS 35 (Figure 4.13a). Interestingly, the stress release within element CS 35 appears to be counteracted by the overburden stress, causing this element to continually experience compaction.

The analysis of Ψ evolution for CS 34 (Figure 4.13b) illustrates that the soil experiences volumetric expansion due to a substantial stress release. This stress release can likely be attributed to the rotation of the monopile, resulting in reduced overburden stress within this soil element.

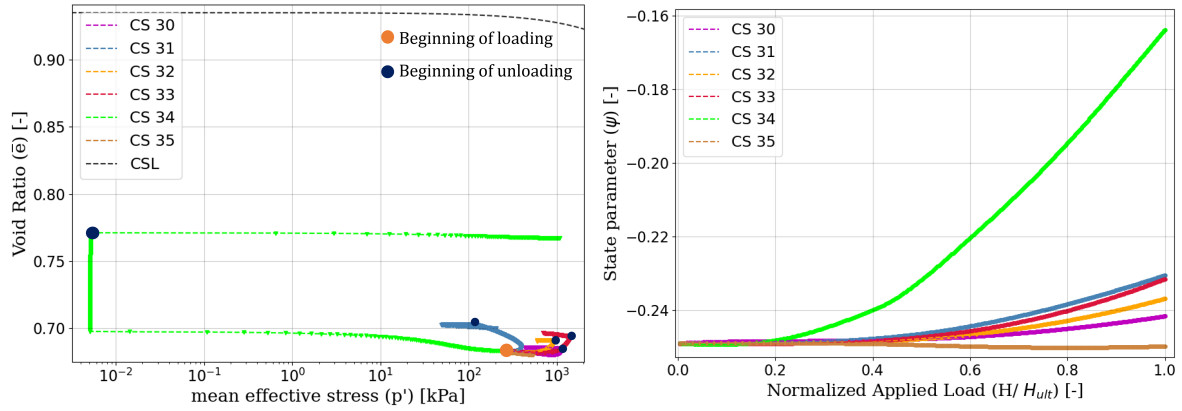

(a) $\bar{e} - p'$ space

(b) Ψ plot during loading phase

Figure 4.13: The analysis results for soil elements at the pile base presented in (a) $\bar{e} - p'$ space and (b) Ψ evolution during the loading phase for the reference case (0A).

4.1.4. Pile Base Components Response

The response observed at the pile base comprises two fundamental components: the base shear force (F_b) and the base moment (M_b). The response stemming from the base shear force (F_b) is inherently coupled with the displacement at the pile base (y_b), and this relationship is illustrated for the reference case in Figure 4.14a. It is noteworthy that ultimate base shear force ($F_{b,u}$), attained when the θ_{sb} reaches 2^o, is $29.2MN$ or equivalently, approximately 35.3% of the H_{ult}. The base displacement at ultimate capacity ($y_{b,u}$) is determined to be $0.673m$, corresponding to approximately 25.7% of $y_{sb,u}$, with y_b acting in the direction of the negative x-axis.

In addition to the base shear force, the base moment (M_b) response is coupled with the base rotation (θ_b). The response characteristics of $M_b - \theta_b$ for the reference case are presented in Figure 4.14b. Notably, the ultimate base moment ($M_{b,u}$) observed when θ_{sb} equals 2^o is $30.6MNm$, which represents approximately 1.64% of the ultimate moment capacity (M_{ult}). Meanwhile, the ultimate rotation at the base ($\theta_{b,u}$) amounts to 1.03^o or approximately 51% of $\theta_{sb,u}$. A close examination of the F_b and M_b responses clearly reveals that the magnitude of $F_{b,u}$, relative to H_{ult}, significantly larger than the ratio of $M_{b,u}$ against the M_{ult}.

Upon normalizing the F_b and Σp components relative to H (Figure 4.15a), it is found that F_b always acts in the same direction as the applied lateral load. Furthermore, the values of F_b and Σ_p progressively

increasing following the increment of H.

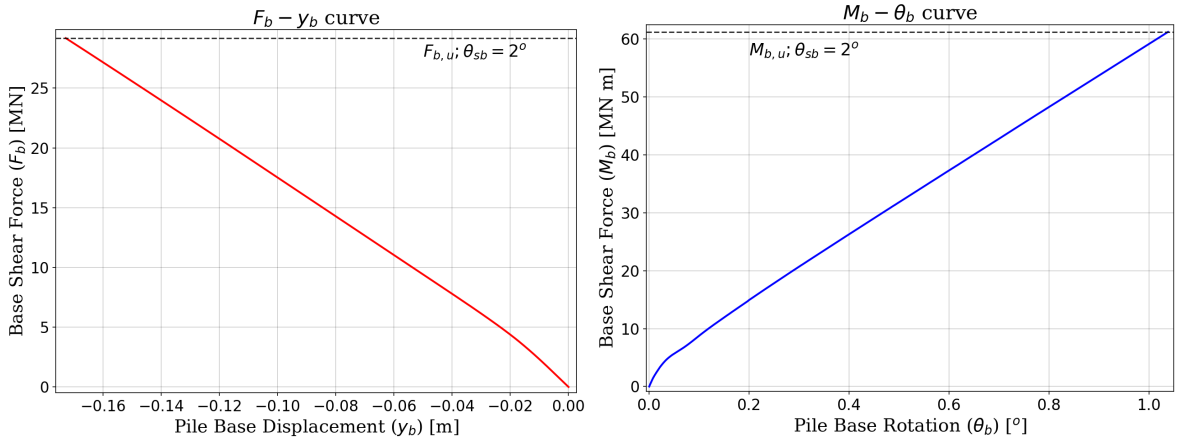

(a) $F_b - y_b$ **(b)** $M_b - \theta_b$

Figure 4.14: The curve for base component responses in terms of (a) $F_b - y_b$ and (b) $M_b - \theta_b$ for the reference case.

The same analysis was also done for the moment component by calculating the ratios of ΣM_p, M_{Fb}, ΣM_d, and M_b relative to M (Figure 4.15b). The result indicates that these four-moment components always act in the opposite direction of M. It is also observed that, while the contribution of ΣM_p diminishes, the contributions of other moment components (M_{Fb}, ΣM_d, and M_b) increase with the rise in M (Figure 4.15b). Upon comparing these analyses (4.15), it is deduced that the contribution of F_b to the lateral balance is substantial, whereas the contribution of M_b to the moment balance is not significant.

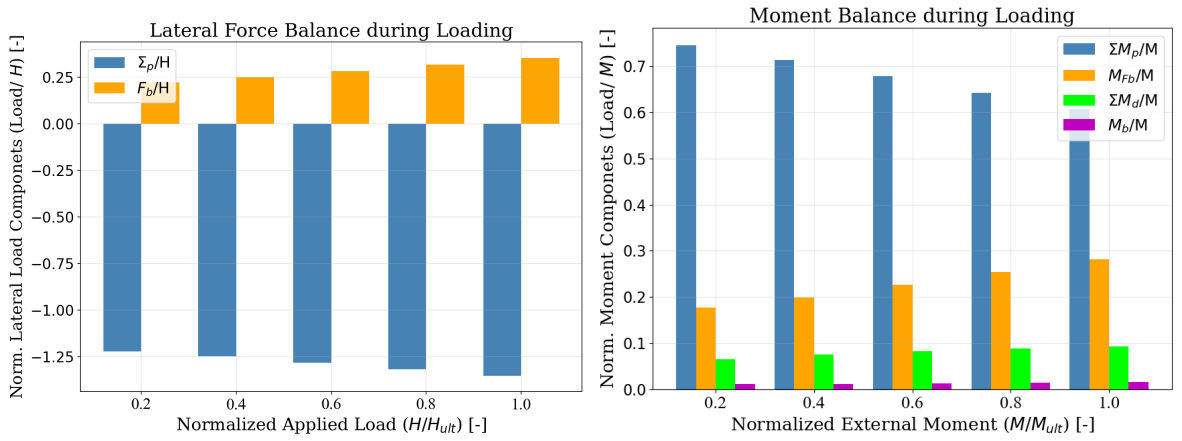

(a) Lateral force components **(b)** Moment components

Figure 4.15: The balance equilibrium assessment for the model in terms of (a) Lateral balance equilibrium and (b) Moment equilibrium for the reference case.

4.2. Cyclic Load

4.2.1. Cyclic Load Response at The Mudline

The cyclic load response of the monopile for the reference case is depicted in Figure 4.16, presenting load-displacement (Figure 4.16a) and moment-rotation (Figure 4.16b) curves. It is evident that, after 100 cycles, the analysis with $\zeta_b = 0.4$ does not reach the ultimate displacement ($y_{sb,u}$) (Figure 4.16a) or rotation ($\theta_{sb,u}$) (Figure 4.16b). Following load release at the end of the 100 cycles, the cyclic test with $\zeta_b = 0.4$ yielded a displacement accumulation (y_{acc}) of approximately $0.172m$, equivalent to 25.6% of

($y_{sb,u}$). Similarly, this analysis indicates an accumulated rotation (θ_{acc}) of 0.37^o, which corresponds to 18.3% of $\theta_{sb,u}$. This θ_{acc} is known to exceed the SLS criteria by [15], which limited the θ_{acc} at the mudline to 0.25^o.

The same analysis for the cyclic test with $\zeta_b = 0.1$ resulted in $y_{acc} = 0.0125m$ or 1.86% of $y_{sb,u}$. This cyclic test left $\theta_{acc} = 0.028^o$ or 1.39% of $\theta_{sb,u}$ upon unloading at cycle-100. Upon examining the y_{acc} and θ_{acc} results, it is evident that the cyclic test with $\zeta_b = 0.1$ induces minimal accumulated deformation, which is not significant. Consequently, the analyses in this chapter will focus on the cyclic test with $\zeta_b = 0.4$. Results for the cyclic test with $\zeta_b = 0.1$ are presented only if deemed important, otherwise, they can be found in Appendix C.

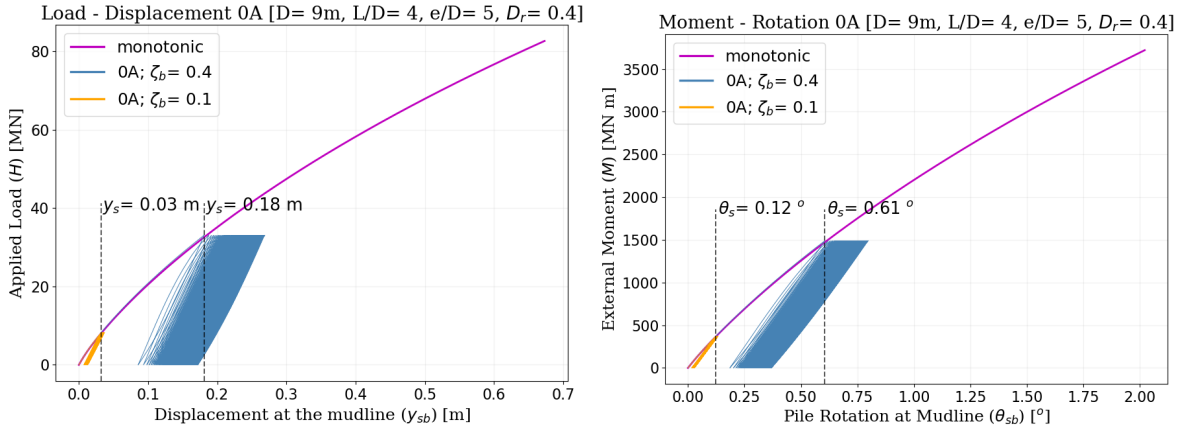

(a) Load-Displacement **(b)** Moment-Rotation

Figure 4.16: The monopile global response with respect to the mudline presented in terms of (a) Load- Displacement curve and (b) Moment-Rotation curve for the refernce case ($D = 9, L/D = 4$,e/D= 5, $D_r = 0.9$.

To evaluate the accumulated rotation, a dimensionless ratio is employed, following the formula introduced by [37] (Eq. 2.15). As observed in Figure 4.16, it becomes evident that under constant sand D_r and pile geometry, the deformation curves during the first cycle are the same as the monotonic load response. Therefore, the term θ_0 is equivalent to θ_s (Eq. 2.15), and Equation 2.15 can be adjusted as follows:

$$\frac{\theta_N - \theta_0}{\theta_s} = \frac{\theta_N - \theta_0}{\theta_0} = \frac{\theta_N}{\theta_0} - 1 = \frac{\Delta\theta(N)}{\theta_s} = T_b(D_r, \zeta_b).T_c(\zeta_c).N^{\alpha} \tag{4.6}$$

The formulation, originally introduced by [37], underlined that the development of the accumulated rotation ratio ($\Delta\theta(N)/\theta_s$) concerning the number of cycles can be effectively described using a power law. The study by Leblanc et al. ([37]) also suggested that the slope of the power law function can be depicted by $\alpha = 0.31$ (Eq. 2.15). Furthermore, for a test with $\zeta_c = 0$ the $T_c(\zeta_c)$ value is 1.

In this subsection, the accumulated rotation analyses are conducted both when the monopile is subjected to the maximum cyclic load and when the load is completely removed from the monopile. The analysis is also extended to investigate the accumulated displacement at the mudline, for which Equation 2.15 is modified by substituting the θ value with the y value. The dimensionless ratio of accumulated displacement is also assumed to follow a power law function (Eq. 2.15).

The results of θ_{acc} analyses are presented in Figure 4.17 for the loading phase (Figure 4.17a) and unloading phase (Figure 4.17b). Furthermore, the analyses of y_{acc} are illustrated in Figure 4.18 for the loading phase (Figure 4.18a) and unloading phase (Figure 4.18b). Both the ratios of $\Delta\theta(N)$ and $\Delta y(N)$

as functions of N can be effectively represented using a power law with $\alpha = 0.51$. The $\alpha = 0.51$ value is different compared to Equation 2.15.

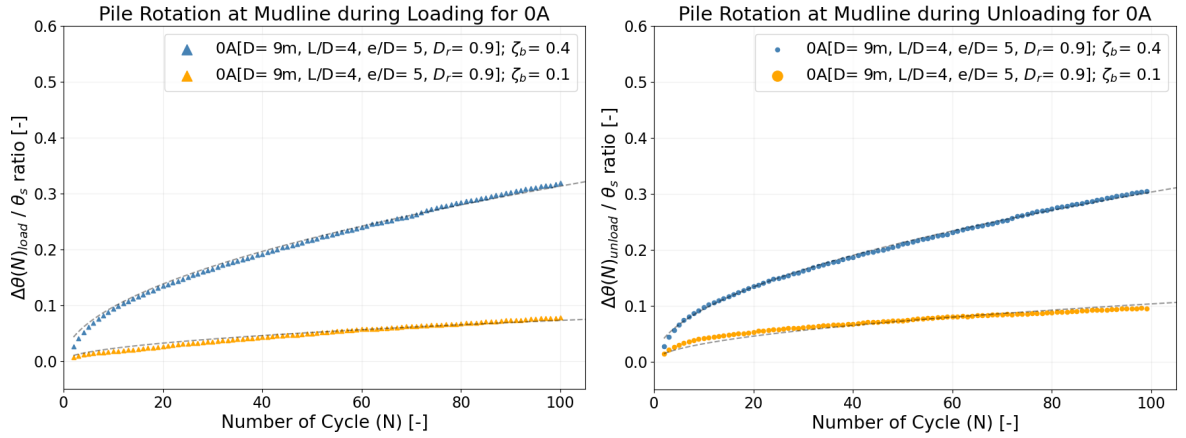

(a) Loading phase **(b)** Unloading

Figure 4.17: The accumulated rotation (θ_{acc}) at the mudline for the reference case 0A presenting during (a) loading phase and (b) unloading phase.

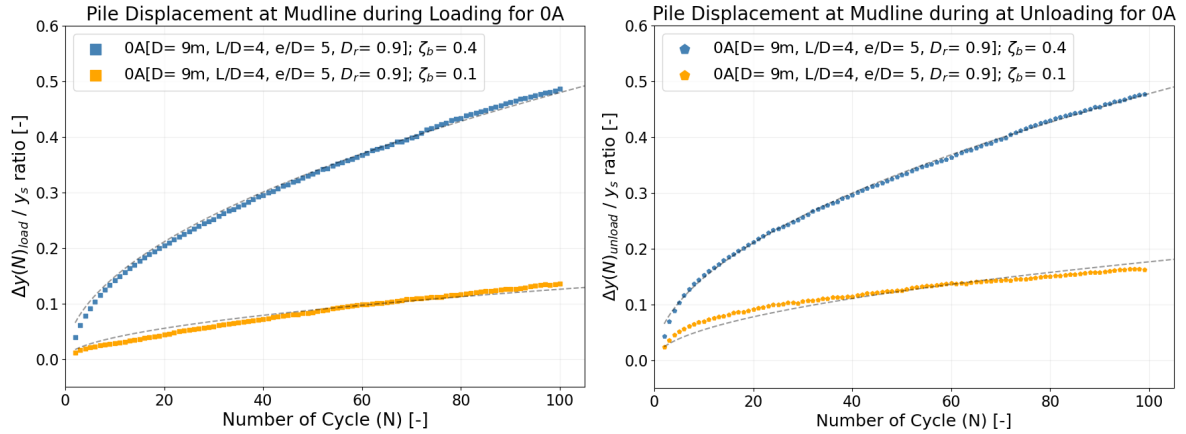

(a) Loading phase **(b)** Unloading

Figure 4.18: The accumulated displacement (y_{acc}) at the mudline for the reference case 0A presenting during (a) loading phase and (b) unloading phase.

Observing the analysis of θ_{acc} and y_{acc} (Figure 4.18 and 4.19), it becomes evident that both the rotation and displacement at the mudline continuously accumulate. This phenomenon is observed in both model setups, whether with $\zeta_b = 0.4$ or $\zeta_b = 0.1$, during both the loading and unloading phases. However, the deformation accumulation is more pronounced in the test with $\zeta_b = 0.4$. Furthermore, it is also observed that even after 100 cycles, the values of $\Delta\theta(N)/\theta_s$ and $\Delta y(N)/y_s$ have not reached their respective asymptotic values, with this trend being more apparent in the test with $\zeta_b = 0.4$.

4.2.2. p-y Curve Response Under Cyclic Load

The $p-y$ response under cyclic load relationship at various depths is illustrated in Figure 4.19. Examining the normalized $p - y$ curves for two cyclic tests (Figure 4.19), it is evident that the soil reaction (p) and pile element displacement (y) from the cyclic test with $\zeta_b = 0.4$ (Figure 4.19a) are significantly larger than those from the test with $\zeta_b = 0.1$ (Figure 4.19b). Under a higher load parameter (Figure 4.19a), a softening response in the $p - y$ curve is observed at a depth of $z = -13m$ and $z = -7m$.

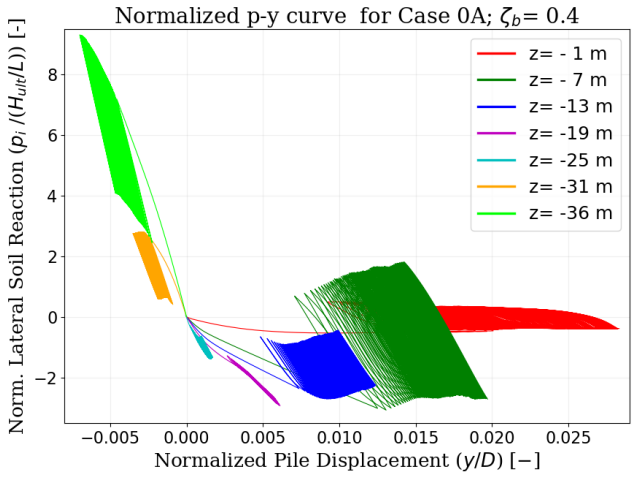

(a) $\zeta_b = 0.4$

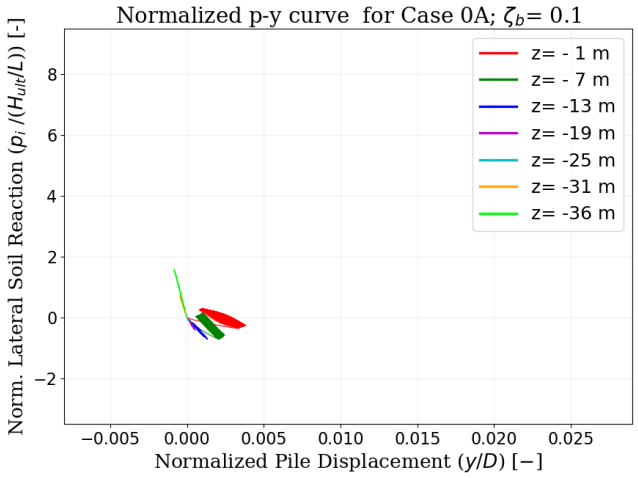

(b) $\zeta_b = 0.1$

Figure 4.19: Normalized $p - y$ curve at cyclic loading at differnt depths for the reference case with load characteristic (a) $\zeta_b = 0.4$ and $\zeta_b = 0.1$.

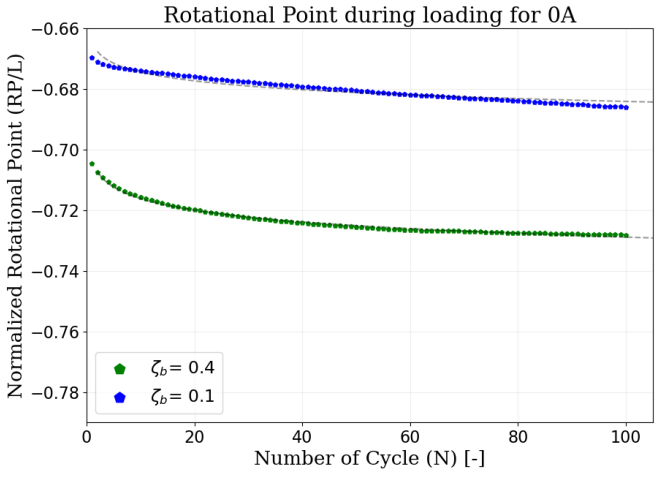

Figure 4.20: Normalized Rotational Point (RP) during loading phase for the reference case with $\zeta_b = 0.4; 0.1$

Upon closer examination of the $p - y$ curve at $z = -13m$ (Figure 4.19a), the softening response becomes more apparent during the later cyclic loading phases, following some initial hardening effects in the initial cycle phases. When referring back to the monotonic response (Figure 4.5a), it is evident

that the $p - y$ response at $z = -13m$ exhibited a linear behavior. On the other hand, the $p - y$ response at $z = -6m$ (Figure 4.19a) indicates a softening behavior in the earlier stages of the cycles, followed by a transition to hardening in the later cyclic phases. This $p - y$ response at $z = -6m$ differs from the $p - y$ response under monotonic loading, which only displays a softening response (Figure 4.5a).

Analysis of the rotational point (RP) (Figure 4.20) also indicates that the position of the RP moves deeper into the soil during cyclic loading. This phenomenon is also observed in the monotonic load analyses (Figure 4.4). The RP movement during cyclic loading is more pronounced for the cyclic test with $\zeta_b = 0.4$ compared to $\zeta_b = 0.1$. However, for the cyclic load with $\zeta_b = 0.4$, after 60 cycles, the depth of the RP is nearly constant. At the first cycle, the depth of the RP for $\zeta_b = 0.4$ is at $z = -25.37m$, while for $\zeta_b = 0.1$, it is at $z = -24.1m$.

The evaluation of y_{acc} at different depths is conducted using the same method applied to calculate y_{acc} at the mudline (Figure 4.18). Analyses are performed for both the loading (Figure 4.21a) and unloading phases (Figure 4.21b). The results from the cyclic test with $\zeta_b = 0.4$ indicate that the $\Delta y(N)$ ratio for all depths can be effectively modeled using a power law with $\alpha = 0.51$.

Observation of the y_{acc} at different depths (Figure 4.21) also indicates that after 100 cycles, the y_{acc} values are still increasing. This is evident from the fact that the values of $\Delta y(N)/y_s$ have not reached their respective asymptotic values upon completing cycle-100. Additionally, it is noteworthy that the $\Delta y(N)$ ratio for $z = -25m$ is significantly larger compared to other depths. This is primarily due to the proximity of the element to the RP during the first cycle, resulting in an almost 0 value of y_0 since near the RP, both the developed p and y values must be very small.

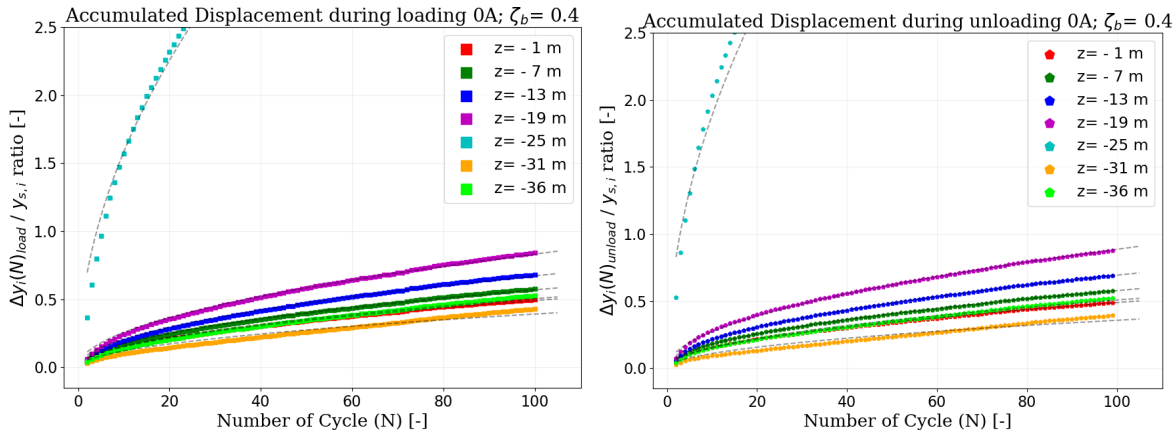

(a) Loading phase **(b)** Unloading Phase

Figure 4.21: Normalized accumulated displacement (y_{acc}) at different depths for the reference case during (a) loading and (b) unloading, with load characteristic $\zeta_b = 0.4$.

4.2.3. Local Soil Response under Cyclic Load

The investigation into the response of soil elements under monotonic loading has revealed compaction, dilation, and volumetric expansion phenomena occurring during both the loading and unloading phases, attributed to stress increments and releases (Figure 4.7 to 4.13). The evolution of void ratios during cyclic loading is presented in terms of the $\bar{e} - p'$ space (Figure 4.22) and Ψ evolution (Figure 4.23). Examining the soil elements surrounding the monopile in the axial direction (Figure 4.22a and 4.23a), it is observed that the elements in the negative x-axis and below the RP (CS 1 and CS 2) experience slight compaction under cyclic loading. Conversely, the elements located above the RP (CS 4 and CS 6)

undergo volumetric dilation.

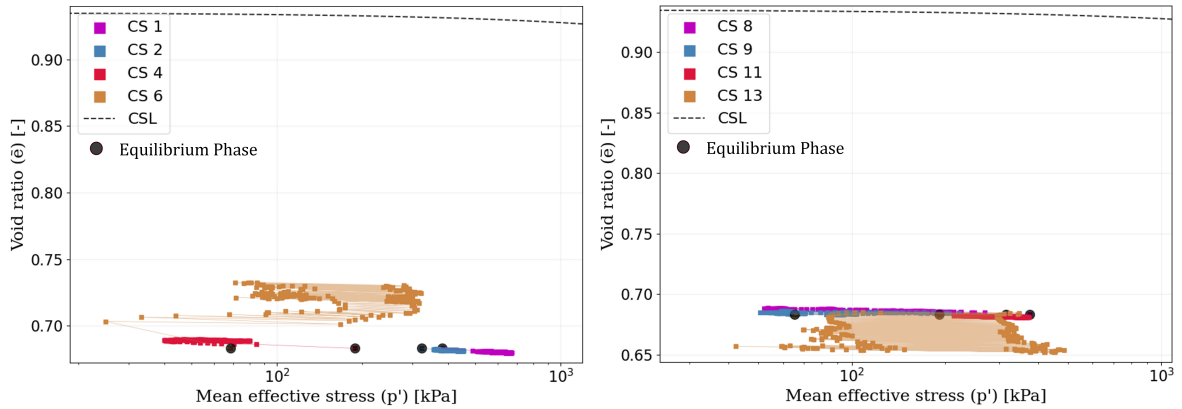

(a) negative $x-$ axis **(b)** positive $x-$ axis

Figure 4.22: The $\bar{e} - p'$ space for the soil elements around the monopile recorded in axial direction for the elements in (a) negative $x-$ axis and (b) positive $x-$axis ($\zeta_b = 0.4$).

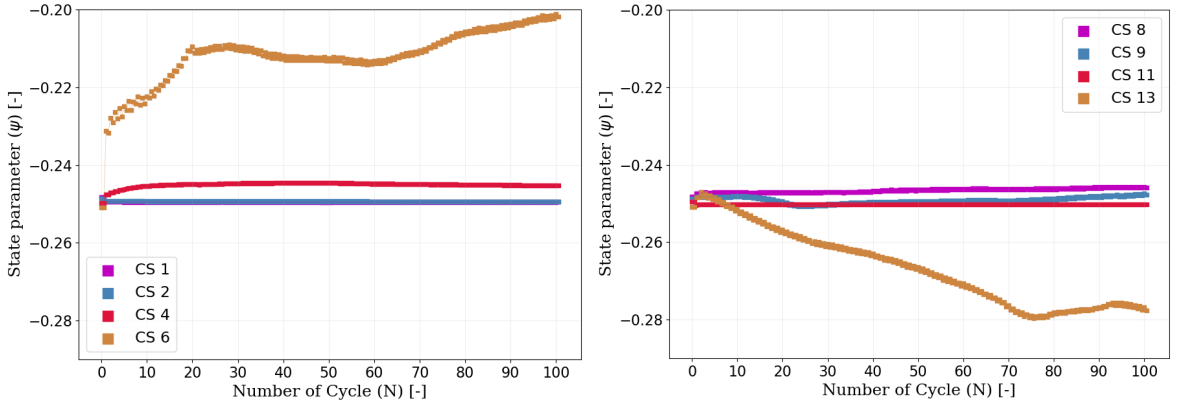

(a) negative $x-$ axis **(b)** positive $x-$ axis

Figure 4.23: The Ψ evolution for the soil elements around the monopile recorded in the axial direction for the elements in (a) negative $x-$ axis and (b) positive $x-$axis ($\zeta_b = 0.4$).

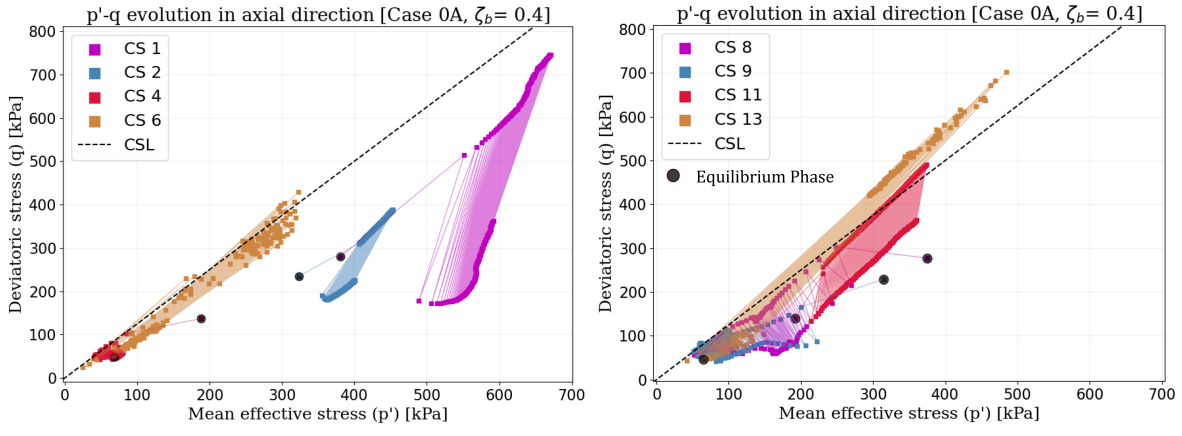

(a) negative $x-$ axis **(b)** positive $x-$ axis

Figure 4.24: The stress path of the soil elements around the monopile recorded in the axial direction for the elements in (a) negative $x-$ axis and (b) positive $x-$axis ($\zeta_b = 0.4$).

The trend in the void ratio evolution for the elements in the positive x-axis (Figure 4.22b and 4.23b) is opposite to that observed for the elements in the negative x-axis. In the positive x-axis, the soil

elements above the RP (CS 11 and CS 13) are getting compacted significantly due to the transferred load from the monopile. For the elements below the RP, an increase in void ratio is observed, although it is not particularly significant. Based on this analysis, it can be deduced that the rates of compaction and dilation are influenced by the confining stress. When the confining stress is higher, the effect of relatively small loading on the void ratio changes becomes less significant.

The stress path (Figure 4.24) illustrates that all soil elements around the pile are situated below the CSL once the pile is installed. In the positive $x-$axis (Figure 4.24a), elements below the Rotational Point (RP) (CS 1 and CS 2) exhibit a clear pattern of stress increments during cyclic loading, followed by releases, consistently remaining beneath the CSL. However, for the elements above the CSL (CS 4 and CS 6), their stress paths oscillate around the CSL. The trend for soil elements in the positive $x-$axis (Figure 4.24b) is more pronounced, indicating that the stress path for these elements evolves very close to the CSL.

Upon examining the response of soil elements in the lateral direction at a depth of $-9m$, it becomes evident that the area impacted by the load is also influenced by the load characteristic parameters (ζ_b). While the significant $\bar{e}$ changes in the monotonic analysis extend up to D in the lateral direction from the monopile, the impacted area for cyclic loading with $\zeta_b = 0.4$ only reaches up to $0.5D$ (Figure 4.25 and 4.26). When looking at the elements in the negative x-axis (Figure 4.25a and 4.26a), it can be observed that the closest element to the pile (CS 15) experiences volumetric dilation during the cyclic loading. As for CS 16, after undergoing volumetric dilation during the initial cyclic phases, the compaction that occurs during later cyclic phases and stabilizes the void ratio after $N = 60$.

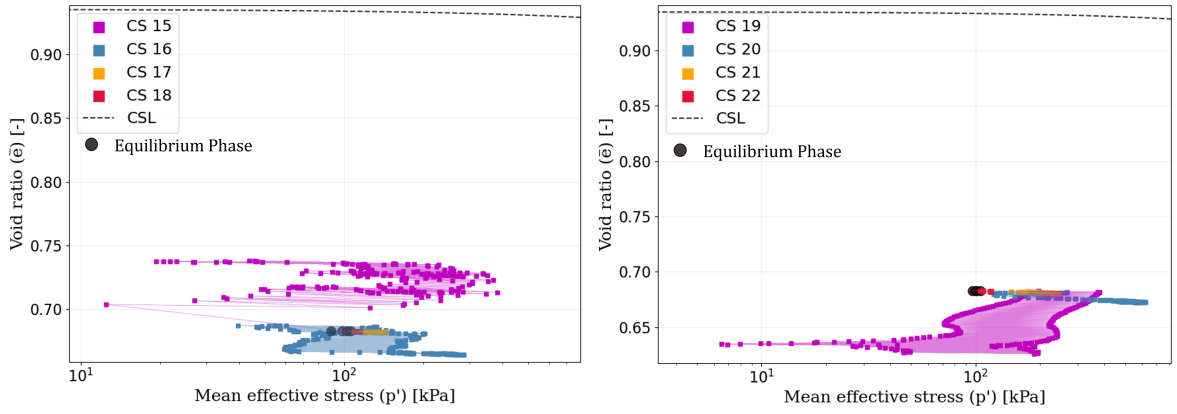

(a) negative $x-$ axis **(b)** positive $x-$ axis

Figure 4.25: The $\bar{e} - p'$ space for the soil elements around the monopile recorded in the lateral direction for the elements at $z = -D$ in (a) negative $x-$ axis and (b) positive $x-$axis ($\zeta_b = 0.4$).

Similarly, elements in proximity to the monopile in the positive x-axis direction (CS 19 and CS 20) experience compaction under cyclic loading (Figure 4.25b and 4.26b). While the compaction for CS 19 continues even after 100 cycles, the void ratio of element CS 20 remains constant after 30 cycles. The compaction processes for CS 20 stabilize its void ratio after 40 cycles. The continuous compaction of CS 19 even results in this element having a void ratio below the minimum void ratio ($\bar{e}_{min}$). A similar response has been observed in a previous study [88], which indicates gradual densification due to repeated shear loading on the soil adjacent to the monopile. Furthermore, upon completing 100 cycles, all of the elements in positive and negative $x-$axis are still positioned below and distant from the Critical State Line (CSL) (Figure 4.25).

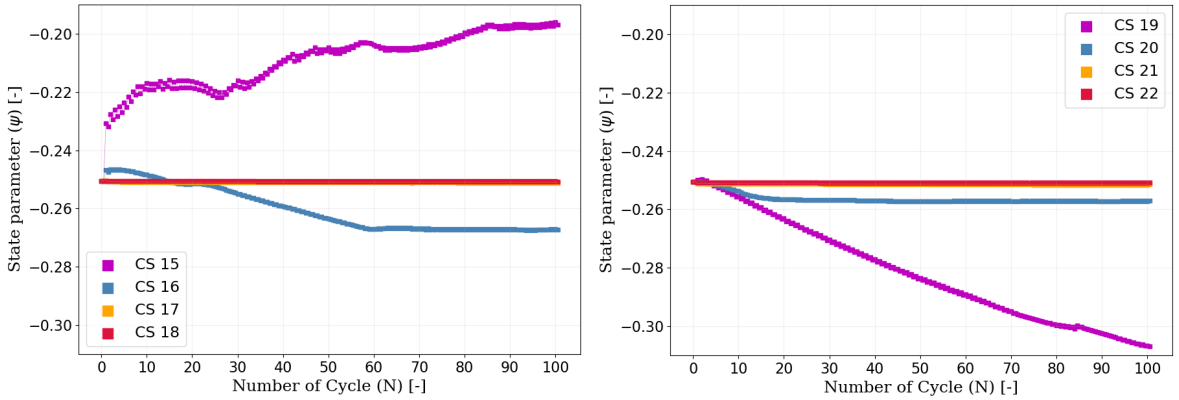

(a) negative $x-$ axis **(b)** positive $x-$ axis

Figure 4.26: The Ψ evolution for the soil elements around the monopile recorded in the lateral direction for the elements at $z = -D$ in (a) negative $x-$ axis and (b) positive $x-$axis ($\zeta_b = 0.4$).

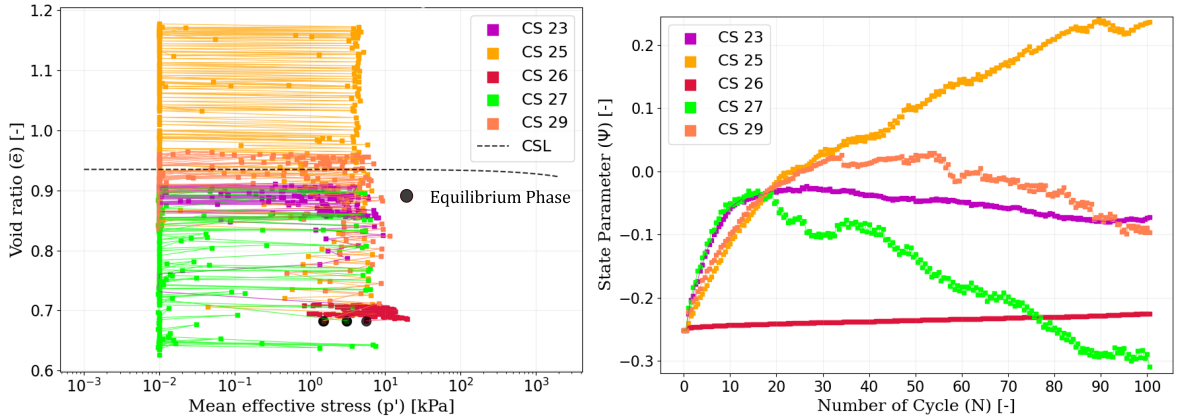

(a) $\bar{e} - p'$ space **(b)** Ψ evolution

Figure 4.27: The void ratio evolution for the soil elements near the mudline recorded in the radial direction and presented in (a) $\bar{e} - p'$ space and (b) Ψ evolution.

Observing the evolution of the void ratio of the soil elements around the mudline (Figure 4.27), it is apparent that two points positioned at the same angle in the positive and negative x-axis tend to exhibit similar trends. Both CS 23 and CS 29 undergo compaction in the later stages of cyclic loading after experiencing dilation in the early stages (Figure 4.27b). In contrast, CS 25 and CS 27 display opposing trends. CS 25 consistently undergoes volumetric expansion and dilation during the loading and unloading phases, respectively. Meanwhile, CS 27 experiences compaction after initially undergoing dilation in the early stages of cyclic loading.

The sole element situated along the positive y-axis, CS 26, also exhibits volumetric dilation under cyclic loading. However, the changes in the void ratio for CS 26 are relatively insignificant when compared to other soil elements adjacent to the monopile head. Unlike the response under monotonic loading (Figure 4.12), the highest increment in the void ratio occurred in element CS 25. Since the same angle from the $x-$axis is applied for CS 25 and CS 27, this phenomenon may be due to the same underlying reason. It is also observed that, with the exception of CS 26, most of these elements experience conditions where the effective stress approaches zero ($10^{-2} kPa \approx 0$) at certain stages (Figure 4.27a).

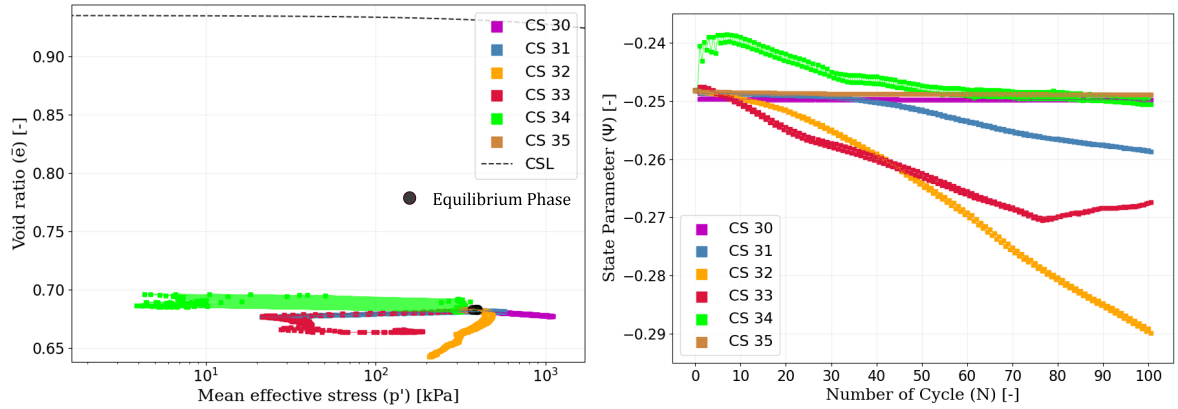

(a) $\bar{e} - p'$ space **(b)** Ψ evolution

Figure 4.28: The void ratio evolution for the soil elements near the pile base presented in (a) $\bar{e} - p'$ space and (b) Ψ evolution.

The analyses of the soil elements at the pile base (Figure 4.28) indicate that the elements situated in the negative x-axis direction (CS 30 and CS 31) were observed to undergo compaction during loading phases, followed by a slight rebound in void ratio during unloading phases. Remarkably, the element at the center of the pile base (CS 32) experienced compaction during the cyclic loading process, which make the void ratio approaching the $\bar{e}_{min}$.

In contrast, soil elements positioned along the positive x-axis (CS 33 and CS 34) exhibited dilation in the initial cyclic stages, followed by compaction after a certain number of cycles (Figure 4.28). The compaction at the later phases is possibly due to the high overburden stress imposed on these elements, Notably, the dilatancy effect is more pronounced for CS 34 compared to CS 33. Similarly, the element situated on the positive y-axis (CS 35) displayed a phenomenon similar to that of CS 34, although the compaction and volumetric extension effects were less distinct. In addition, analyses on the cyclic load with $\zeta_b = 0.1$ are provided in Appendix C.

4.2.4. Pile Base Components Response Under Cyclic Load

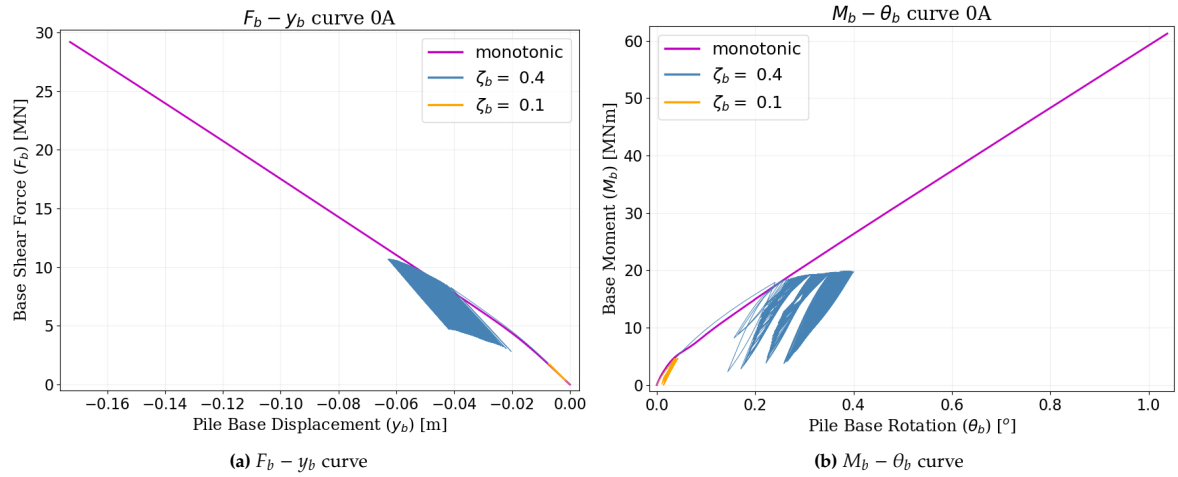

(a) $F_b - y_b$ curve **(b)** $M_b - \theta_b$ curve

Figure 4.29: The base response under monotonic and cyclic loading for the reference case presented in term of (a) $F_b - y_b$ curve and (b) $M_b - \theta_b$ curve.

The base components response under cyclic lateral load is presented in terms of $F_b - y_b$ and $M_b - \theta_b$ curves (Figure 4.29). Looking at the $F_b - y_b$ curve (Figure 4.29a), it is observed that the ratcheting

phenomenon also occurs in the F_b component. This is indicated by the residual F_b and y_b that exist upon releasing the load, and these residual values also grow as the number of cycles increases. Moreover, cyclic load with $\zeta_b = 0.1$ induces very small F_b and y_b values.

It is observed that the ratcheting effect on the base components is highly affected by ζ_b parameters. Looking at the very small F_b and y_b accumulation (Figure 4.31a), it is possible to assume that the ratcheting effect is not involved in the model with $\zeta_b = 0.1$ (Figure 4.31a). In addition to $F_b - y_b$ response, a $M_b - \theta_b$ response is also provided in Figure 4.31b.

The analysis of the F_b values when the maximum lateral load (H_{max}) is applied ($F_{b,max}$) and when the load is completely released (H_{min}) ($F_{b,min}$) is presented in Figure 4.30. These analyses indicate that the magnitudes of $F_{b,max}$ and $F_{b,min}$ increase with an increment in ζ_b (Figure 4.30a, 4.30b). It is also observed that the magnitudes of $F_{b,max}$ and $F_{b,min}$ increase as the number of cycles increases. Looking at the $F_{b,min}$ values (Figure 4.30), it is evident that the F_b value never becomes 0 even when the load is completely released ($H = 0$).

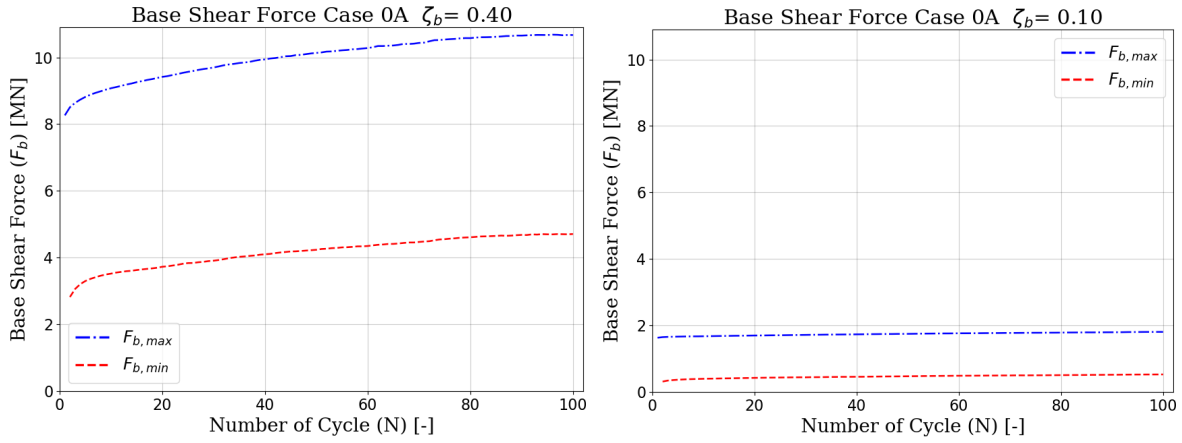

(a) $F_{b,max}$ and $F_{b,min}$ for $\zeta_b = 0.4$

(b) $F_{b,max}$ and $F_{b,min}$ for $\zeta_b = 0.1$

Figure 4.30: The evolution of F_b when the maximum load H_{max} is imposed ($F_{b,max}$) and F_b when during unloading ($F_{b,min}$) for the cyclic test with (a) $\zeta_b = 0.4$ and (b) $\zeta_b = 0.1$.

Upon normalizing the $F_{b,max}$ against the H_{max}, it is evident that the contribution of F_b to the monopile lateral balance at cyclic test is significant (Figure 4.31a). Furthermore, the contribution of F_b becomes larger following the value of ζ_b (Figure 4.31a, Appendix C). Therefore the F_b component must be also included in the cyclic 1D soil-spring model.

Normalizing four-moment components against M_{max} indicates that the contribution of M_b is not significant on the monopile balance during cyclic lateral loading (Figure 4.31b), even for the cyclic test with $\zeta_b = 0.4$. The M_b contribution is even smaller when the load characteristic is reduced to $\zeta_b = 0.1$ (Appendix C). The analysis also suggests that the contribution of the moment from p (ΣM_p) to the moment balance decreases with an increasing number of cycles (Figure 4.31b). Conversely, the contribution of other moment components ($\Sigma M_d, M_{Fb}, M_b$) increases with an increasing number of cycles. Given that the contribution of M_b is not significant and may even be removed from the 1D soil-spring model, and the following chapter does not provide any further explanation for M_b for the monopile.

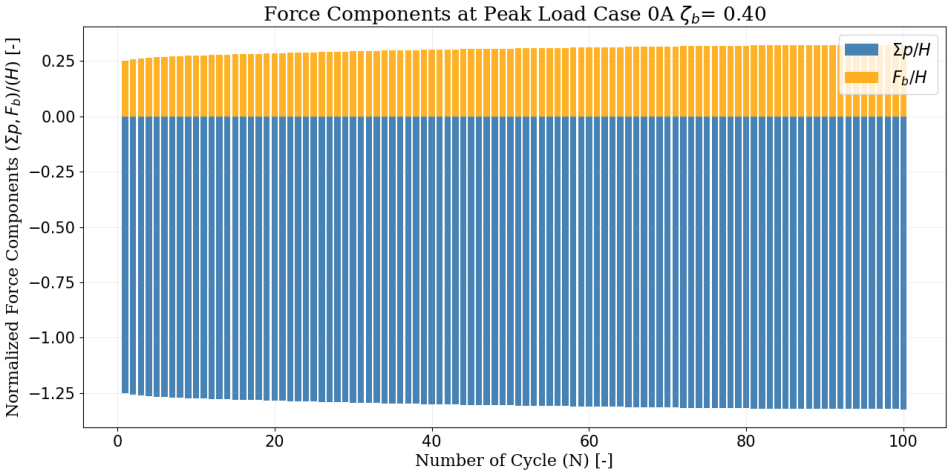

(a) Lateral force balance

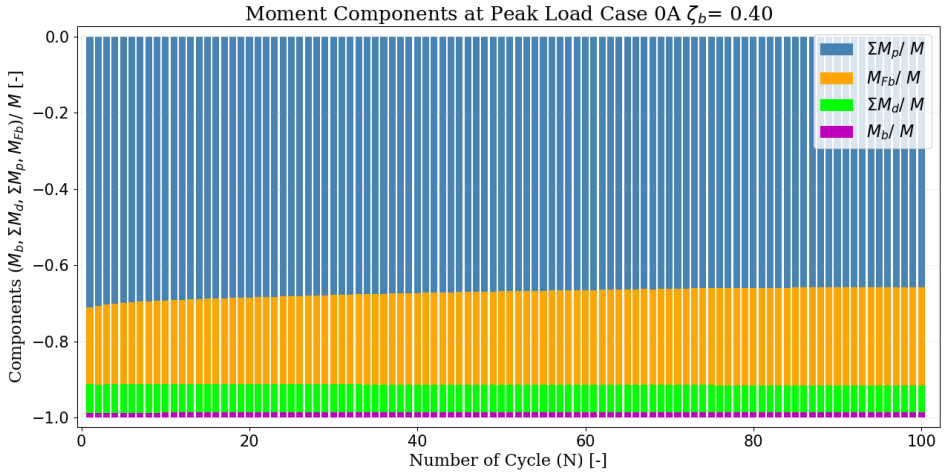

(b) Moment balance

Figure 4.31: The equilibrium analysis for the model under cyclic loading performed for (a) lateral balance and (b) moment balance (ζ_b = 0.4).

5

Parametric Study

After obtaining the material model parameters and conducting a thorough review of the model setup, a parametric analysis was performed. The parameters under investigation encompassed the pile diameter (D), the L/D ratio, the e/D ratio, and D_r. The specific tests and their corresponding parameters are detailed in Table 5.1. Throughout all tests, the pile thickness (t_p) was consistently maintained at a fixed value of 10 cm.

Table 5.1: List of tests conducted in the parametric study.

Code	D[m]	L/D	e/D	D/t_p	D_r [-]	K_r [-]	Class	Cyclic Test[a]
1A	9	2	5	90	0.9	0.1458	Semi-rigid	$\zeta_b = 0.4; 0.1$
2A	9	6	5	90	0.9	0.001	Slender	$\zeta_b = 0.4; 0.1$
3A	6	4	5	60	0.9	0.012	Semi-rigid	$\zeta_b = 0.4; 0.1$
4A	6	2	5	60	0.9	0.263	Rigid	$\zeta_b = 0.4; 0.1$
5A	6	6	5	60	0.9	0.0019	Slender	$\zeta_b = 0.4; 0.1$
6A	12	4	5	120	0.9	0.0042	Semi-rigid	$\zeta_b = 0.4; 0.1$
7A	12	2	5	120	0.9	0.0955	Semi-rigid	$\zeta_b = 0.4; 0.1$
8A	12	6	5	100	0.9	0.0008	Slender	$\zeta_b = 0.4; 0.1$
9A	9	4	0	90	0.9	0.0064	Semi-rigid	$\zeta_b = 0.4; 0.1$
10A	9	4	15	90	0.9	0.0064	Semi-rigid	$\zeta_b = 0.4; 0.1$
11A	9	4	5	90	0.5	0.0083	Semi-rigid	$\zeta_b = 0.4; 0.1$
12A	12	1	5	100	0.9	2.58	Rigid	$\zeta_b = 0.4$
13A	9	1	5	90	0.9	3.30	Rigid	$\zeta_b = 0.4; 0.1$
14A	6	1	5	100	0.9	3.65	Rigid	$\zeta_b = 0.4$
15A	12	0.5	5	100	0.9	58.37	Rigid	-
16A	9	0.5	5	90	0.9	46.46	Rigid	-
17A	3	2	5	90	0.9	0.253	Rigid	-

Continued on next page

Table 5.1 – continued from previous page

Code	D[m]	L/D	e/D	D/t_p	D_r [-]	K_r [-]	Class	Cyclic Test[a]
18A	3	4	5	90	0.9	0.011	Semi-rigid	-
19A	3	6	5	90	0.9	0.0018	Slender	-
20A	9	4	5	90	0.15	0.0104	Semi-rigid	$\zeta_b = 0.4$
21A	9	4	10	90	0.9	0.0064	Semi-rigid	$\zeta_b = 0.4$
22A	9	4	3	90	0.9	0.0064	Semi-rigid	$\zeta_b = 0.4; 0.1$
23A	9	4	5	90	0.7	0.0074	Semi-rigid	-
24A	9	4	5	90	0.3	0.0095	Semi-rigid	$\zeta_b = 0.4$;
25A	9	2	5	90	0.5	0.167	Semi-rigid	-
26A	9	2	5	90	0.5	0.1895	Semi-rigid	-
27A	9	2	5	90	0.3	0.2155	Rigid	-
28A	9	2	10	90	0.9	0.1471	Semi-rigid	-
29A	9	2	3	90	0.9	0.1471	Semi-rigid	-
30A	9	2	1	90	0.9	0.1471	Semi-rigid	-
31A	9	4	5	90	0.1	0.0108	Semi-rigid	-
32A	12	4	0	120	0.9	0.00426	Semi-rigid	-
33A	12	4	3	120	0.9	0.00426	Semi-rigid	-
34A	12	4	10	120	0.9	0.00426	Semi-rigid	-
35A	12	4	20	120	0.9	0.00426	Semi-rigid	-
36A	6	4	0	60	0.9	0.011742	Semi-rigid	-
37A	6	4	3	60	0.9	0.011742	Semi-rigid	-
38A	6	4	10	60	0.9	0.011742	Semi-rigid	-
39A	6	4	20	60	0.9	0.011742	Semi-rigid	-

[a] [-]= only monotonic test performed.

5.1. Monotonic Load

5.1.1. Effect of Pile Geometry

The influence of monopile geometry (D and L) on its load-bearing capacity is elucidated through load-displacement and moment-rotation curves (Figure 5.1 to 5.4). Inspection of the load-displacement curves for varying L/D (Figure 5.1a, 5.2a, 5.3a, 5.4a) reveals that an increase in D corresponds to higher values of H_{ult} and $y_{sb,u}$. Given the limitation of θ_{sb} to 2^o, the y_{sb} is found to be always less than $01.D$. Analysis of moment-displacement curves (Figure 5.1b, 5.2b, 5.3b, 5.4b) indicates that a larger D also leads to higher M_{ult}.

The examination of the impact of the pile L/D ratio (Figure 5.5) demonstrates that increasing L/D results in higher H_{ult} and $y_{sb,u}$, and this trend holds true for both rigid and semi-rigid monopiles (Figure 5.5a). For slender piles with $L/D = 6$, H_{ult} is notably the highest on the plot (Figure 5.5a), but $y_{sb,u}$ is lower compared to piles with $L/D = 4$. This discrepancy is possibly due to the fact that, for flexible piles, pile rotation does not act homogeneously along the monopile. A summary of the impact of pile geometry (L/D ratio and D) on lateral load and moment capacity, is provided in Figure 5.6.

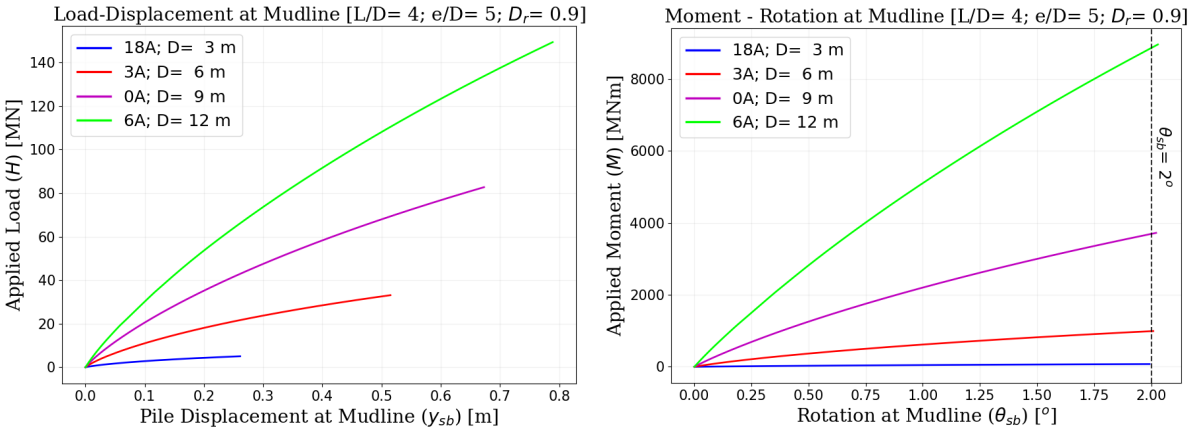

(a) Load-displacement curve

(b) Moment-rotation curve

Figure 5.1: The parametric analyses on the effect of pile geometry (D and L) into the monopile ultimate capacity presented in (a)Load-displacement and (b) Moment-rotation curves for the pile with L/D = 4

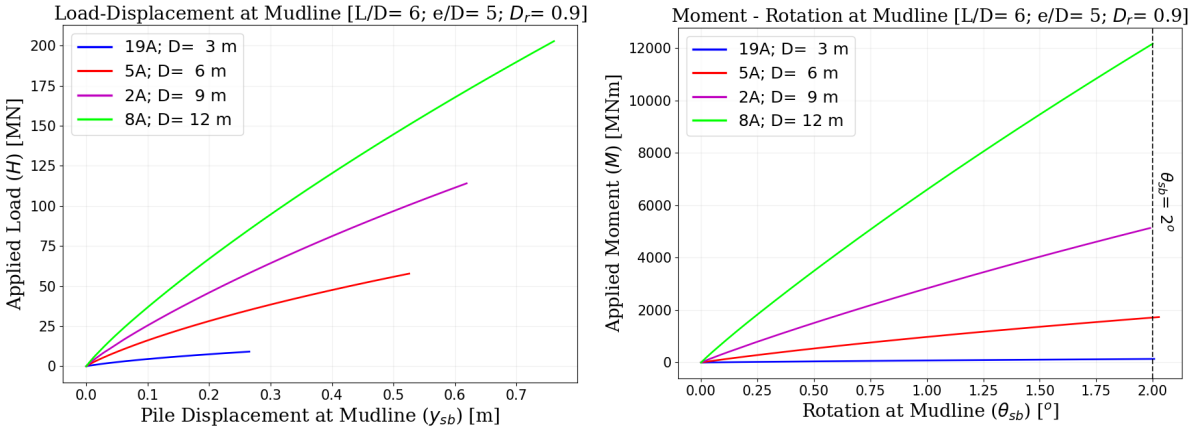

(a) Load-displacement curve

(b) Moment-rotation curve

Figure 5.2: The parametric analyses on the effect of pile geometry (D and L) into the monopile ultimate capacity presented in (a)Load-displacement and (b) Moment-rotation curves for the pile with L/D = 6

In the preceding chapter, a simplified model was introduced to approximate the distribution of p and bending moment along the pile (Figure 4.3). Four components, namely p_{max}, z_{max}, RP, and p_{base}, need to be examined to understand these distributions. Information regarding the effect of pile geometry on the distribution of these four components, when H_{ult} is applied, is presented in Figure 5.7 and 5.8.

The maximum p (p_{max}) always acts in the opposite direction to H. Increasing the pile L/D is known to increase the ratio between p_{max}/H_{ult} (Figure 5.7a). However, as L/D is increased from 4 to 6, the increase in the p_{max} ratio is relatively small compared to when L/D changes from 2 to 4. Regarding the depth of p_{max} (z_{max}), increasing L/D causes it to occur at shallower depths (Figure 5.7b). When D is increased, the ratio of p_{max} to H_{ult} is become lower, and z_{max} moves to shallower levels upon reducing D (Figure 5.7b).

The pile base lateral soil reaction (p_{base}) consistently exerts force in the same direction as the H. It is observed that increasing the pile L/D ratio reduces the ratio of p_{base} to H_{ult} (Figure 5.8a). Conversely, decreasing the pile diameter (D) is observed to increase these values. Analysis of the normalized rotational point (RP) (Figure 5.8b) reveals that reducing L/D causes the RP to shift to a deeper layer. Conversely, increasing D results in the RP migrating to a shallower depth.

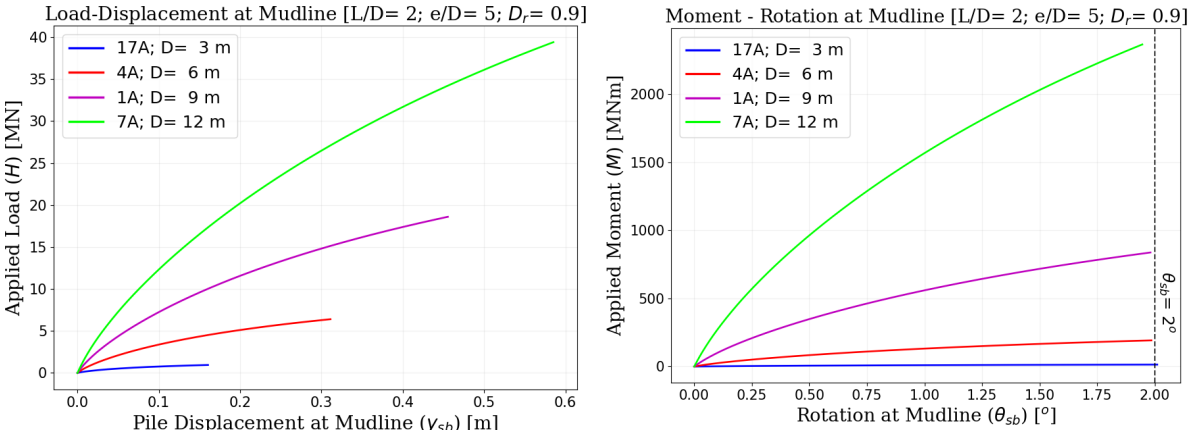

(a) Load-displacement curve

(b) Moment-rotation curve

Figure 5.3: The parametric analyses on the effect of pile geometry (D and L) into the monopile ultimate capacity presented in (a)Load-displacement and (b) Moment-rotation curves for the pile with $L/D = 2$

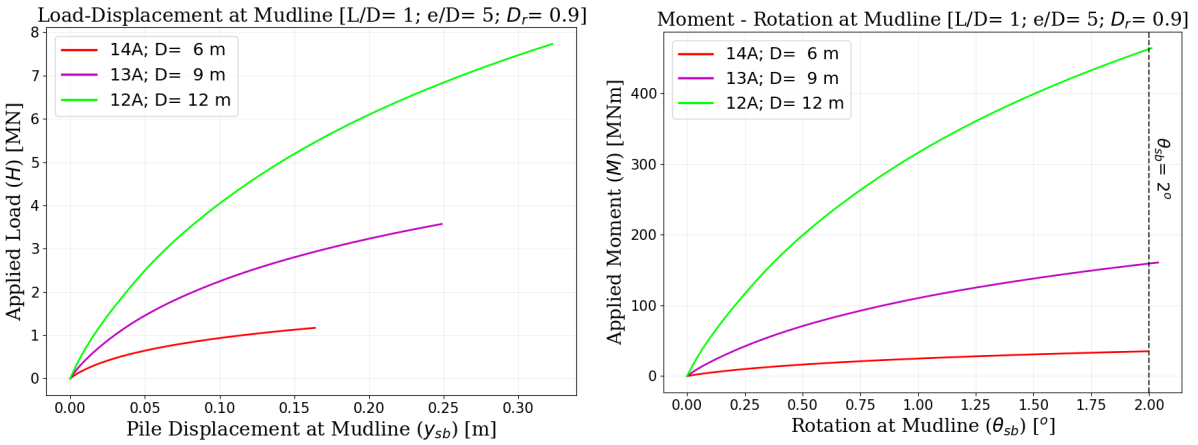

(a) Load-displacement curve

(b) Moment-rotation curve

Figure 5.4: The parametric analyses on the effect of pile geometry (D and L)into the monopile ultimate capacity presented in (a)Load-displacement and (b) Moment-rotation curves for the pile with $L/D = 1$

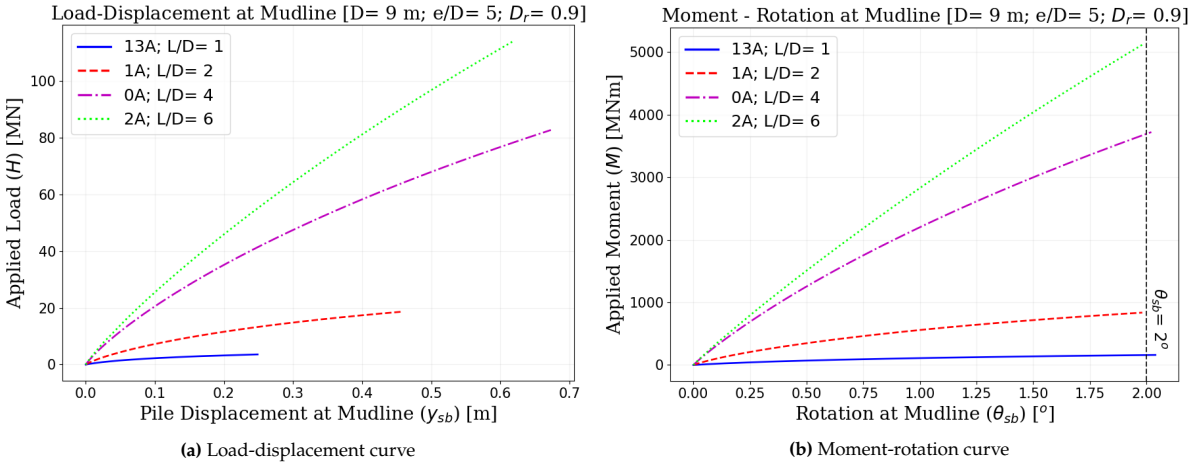

(a) Load-displacement curve

(b) Moment-rotation curve

Figure 5.5: The parametric analyses on the effect of pile L/D ratio into the monopile ultimate capacity presented in (a)Load-displacement and (b) Moment-rotation curves for the pile with $D = 9m$.

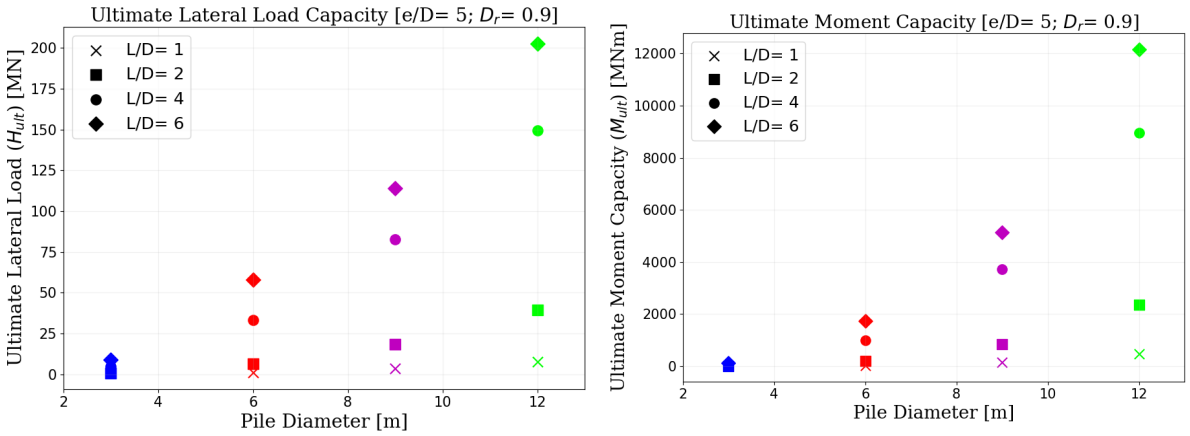

(a) Lateral load capacity

(b) Moment capacity

Figure 5.6: The effect of pile geometry (D and L/D) on (a) lateral load ultimate capacity and (b) ultimate moment capacity of the monopile.

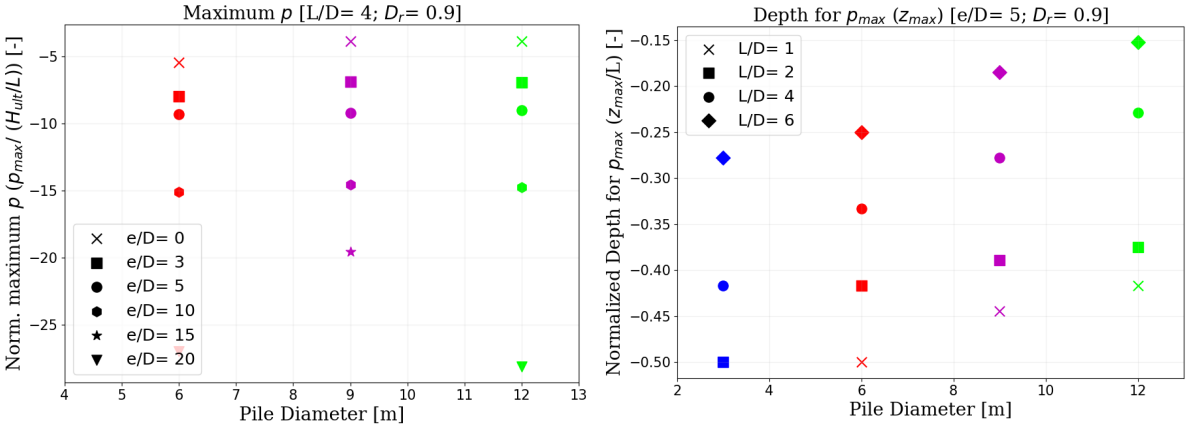

(a) Normalized p_{max}

(b) Normalized z_{max}

Figure 5.7: The effect of pile geometry (D and L/D) into the $p-y$ response in term of (a) Normalized maximum p response and (b) depth of maximum p response.

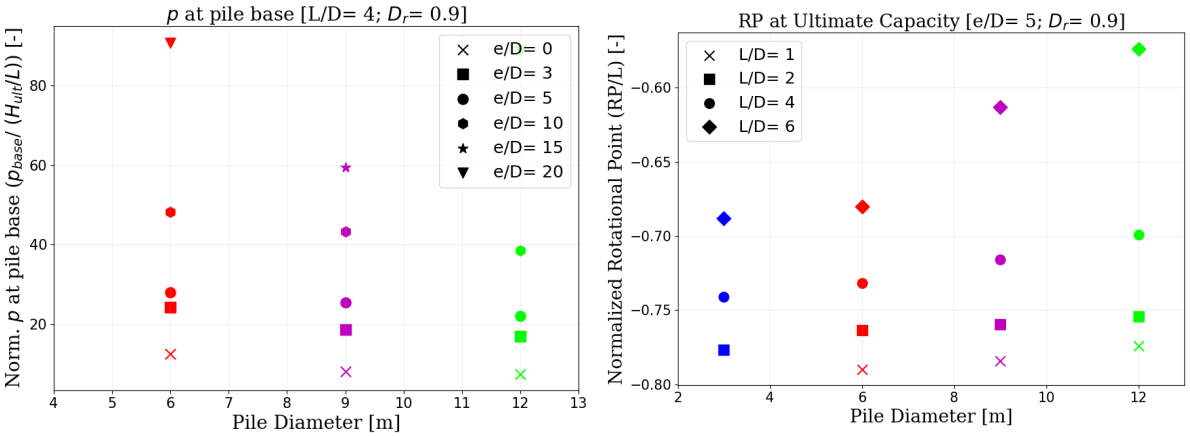

(a) Normalized p_{base}

(b) Normalized RP

Figure 5.8: The effect of pile geometry (D and L/D) into the $p-y$ response in term of (a) Normalized p response at pile base and (b) depth of rotational point.

Additionally, an analysis of the effect of pile geometry (D and L/D) on the pile base reaction components was performed under conditions where H_{ult} is applied (Figure 5.9). Examination of base

shear force when the ultimate load is applied ($F_{b,u}$) (Figure 5.9a) reveals that increasing D and the L/D ratio results in a lower $F_{b,u}/H_{ult}$ ratio. A similar trend is observed in the plot for the base moment when the ultimate moment is applied ($M_{b,u}$) (Figure 5.9b). In conclusion, base shear force and base moment components become increasingly significant for monopile stability as D and L/D decrease. However, considering the reasonable pile geometry ($D = 9 - 12m, L/D = 2 - 4$), the contribution of M_b is always negligible (Figure 5.9b).

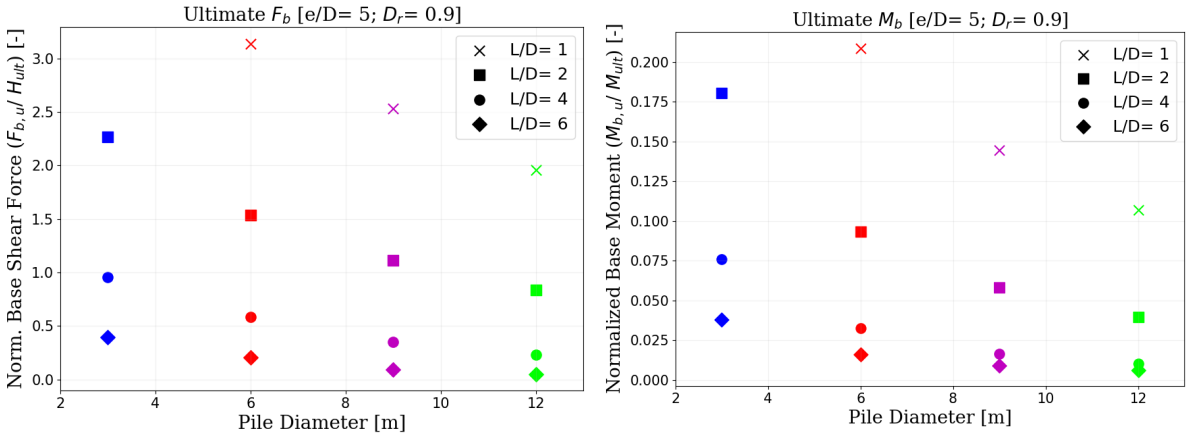

(a) Normalized $F_{b,u}$ **(b)** Normalized $M_{b,u}$

Figure 5.9: The effect of pile geometry (D and L/D) into the base response when the ultimate load is applied presented in terms of normalized (a) Base Shear Force and (b) Base Moment.

5.1.2. Load Eccentricity Effect

This subsection explores the influence of load eccentricity (e) in terms of the e/D ratio while keeping other parameters, including D, D_r, and the L/D ratio, constant. The analysis of the e/D effect on pile bearing capacity is once again presented in terms of load-displacement and moment-rotation curves (Figure 5.10, 5.11, and 5.12). Examination of the load-displacement curve reveals that decreasing the e/D ratio leads to higher values of H_{ult} and $y_{sb,u}$ (Figure 5.10a, 5.11a, and 5.12a). However, the ultimate moment capacity (M_{ult}) is found to increase as the e/D ratio rises (Figure 5.10b, 5.11b, and 5.12b). Comparing the load-displacement (Figure 5.10a) and moment-rotation (Figure 5.10b) curve, it becomes evident that $\theta_{sb} = 2^o$ consistently corresponds to $y_{sb} < 0.1D$.

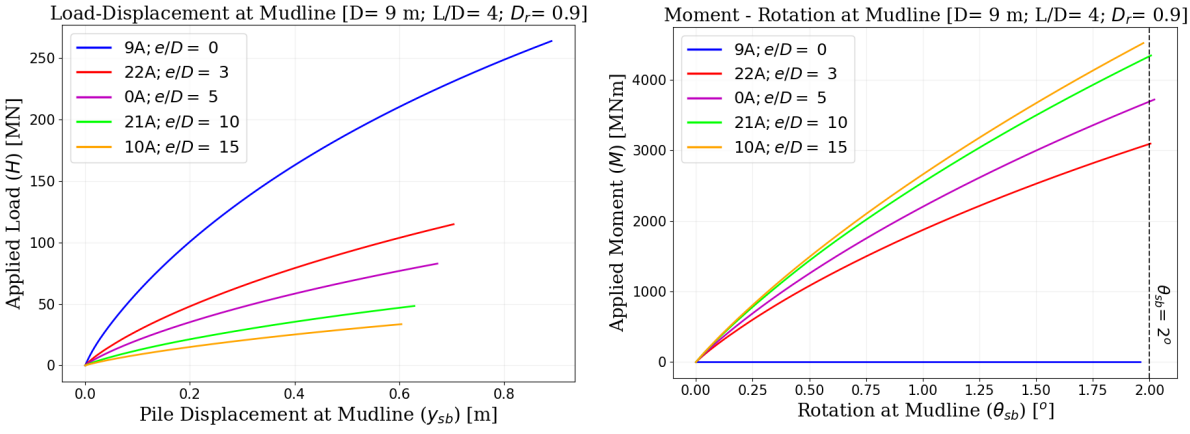

(a) Load-displacement curve **(b)** Moment-rotation curve

Figure 5.10: The parametric analyses on the effect of pile e/D ratio into the monopile ultimate capacity presented in (a)Load-displacement and (b) Moment-rotation curves for the pile with $D = 9m, D_r = 0.9$.

The analyses of the moment-rotation curve (Figure 5.10, 5.11, and 5.12) indicate that the increment of M_{ult} starts to reach a terminal value when the e/D is continuously increased. The same trend in the reduction of H_{ult} is also observed in the load-displacement curve analysis (Figure 5.10b, 5.11b, and 5.12b). For a deeper understanding of the effect of e/D on monopile capacity, an interaction diagram between moment and lateral load is provided (Figure 5.13 and 5.14).

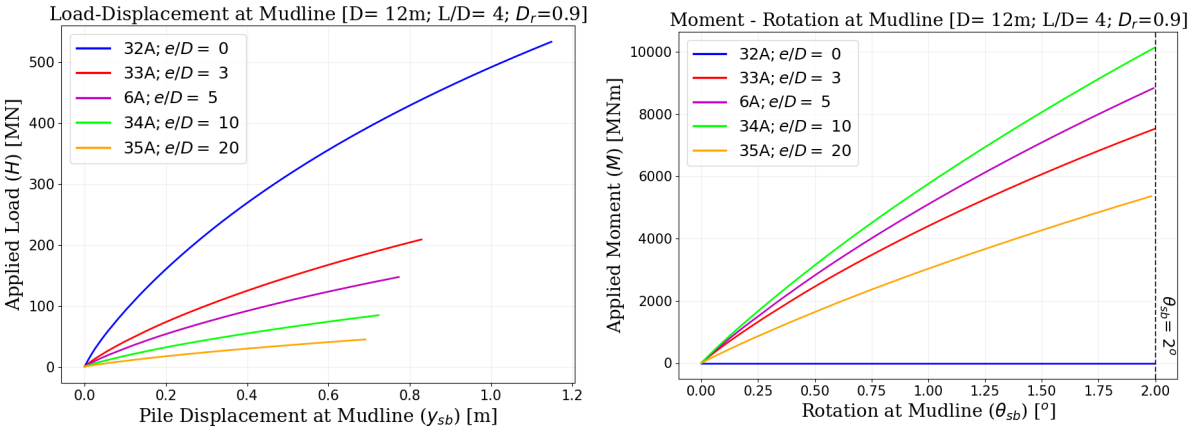

(a) Load-displacement curve

(b) Moment-rotation curve

Figure 5.11: The parametric analyses on the effect of pile e/D ratio into the monopile ultimate capacity presented in (a)Load-displacement and (b) Moment-rotation curves for the pile with $D = 12m, D_r = 0.9$.

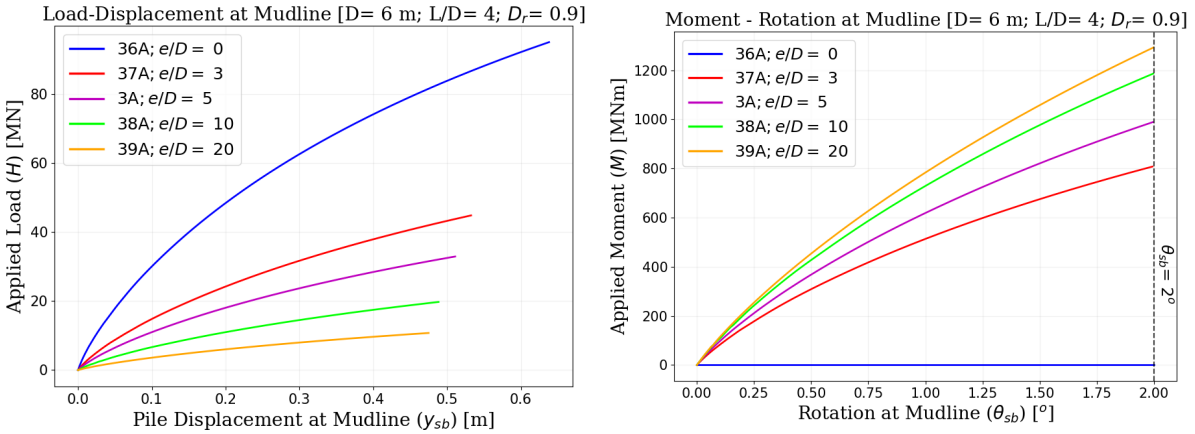

(a) Load-displacement curve

(b) Moment-rotation curve

Figure 5.12: The parametric analyses on the effect of pile e/D ratio into the monopile ultimate capacity presented in (a)Load-displacement and (b) Moment-rotation curves for the pile with $D = 6m, D_r = 0.9$.

An interaction diagram is a method used to analyze rigid caisson movement and shallow foundations, illustrating the yield surface of the caisson under the influence of three loads: vertical load (V), lateral load (H), and moment (M). This domain is commonly referred to as VMH space [89]. A 3D-FEM study by [90] suggests that a complete moment-lateral load (M-H) diagram can be constructed through a curve-fitting process using an ellipse function. However, a study in clay soil by [91] suggests that the shape of the interaction diagram is not a perfect ellipse but rather resembles a rugby ball.

Examining the results (Figure 5.13a and 5.14a), it is apparent that the size of the envelope increases with higher values of D, L/D, and sand D_r. Due to the small possibility of combinations other than a positive moment and positive lateral load, the curve fitting process was performed using a linear function. The results of the fitting process are already plotted in Figure 5.13a and 5.14a. Based on the

curve fitting analysis, the required lateral load to cause monopile failure under solely lateral load (H_{max}), as well as the required moment to cause pile failure under a pure moment (M_{max}), can be determined.

Normalizing each data point representing H_{ult} and M_{ult} with their respective H_{max} and M_{max} results in all data points, as well as the trendline, converging into a single trendline (Figure 5.13b, 5.14b). This outcome aligns with findings from studies by [91] and [90]. Additional analysis through curve-fitting the data points using the ellipse function was also conducted (Appendix B) following [90].

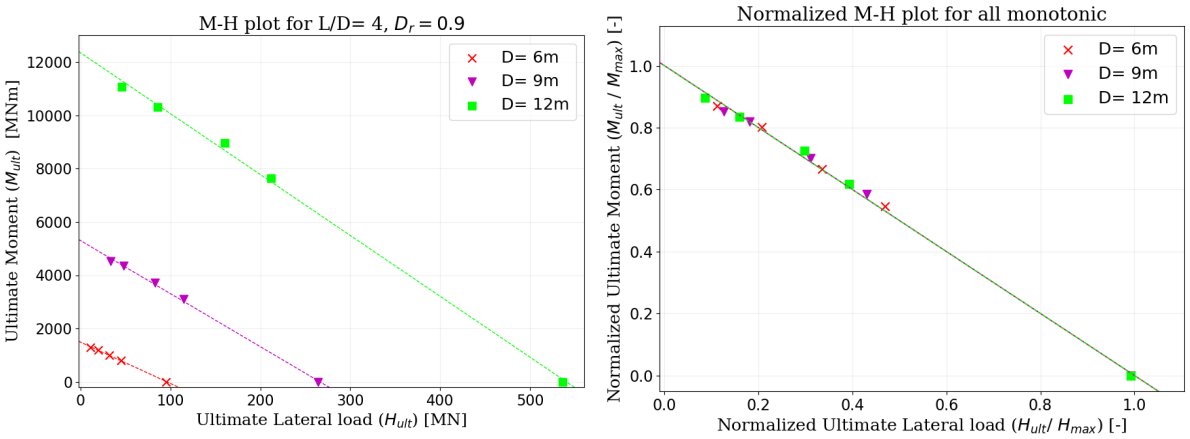

(a) Load-displacement curve

(b) Moment-rotation curve

Figure 5.13: Interaction diagram between moment and lateral load for monopile with $L/D = 4$ installed at sand with $D_r = 0.9$ presented in (a) absolute value and (b) normalized value.

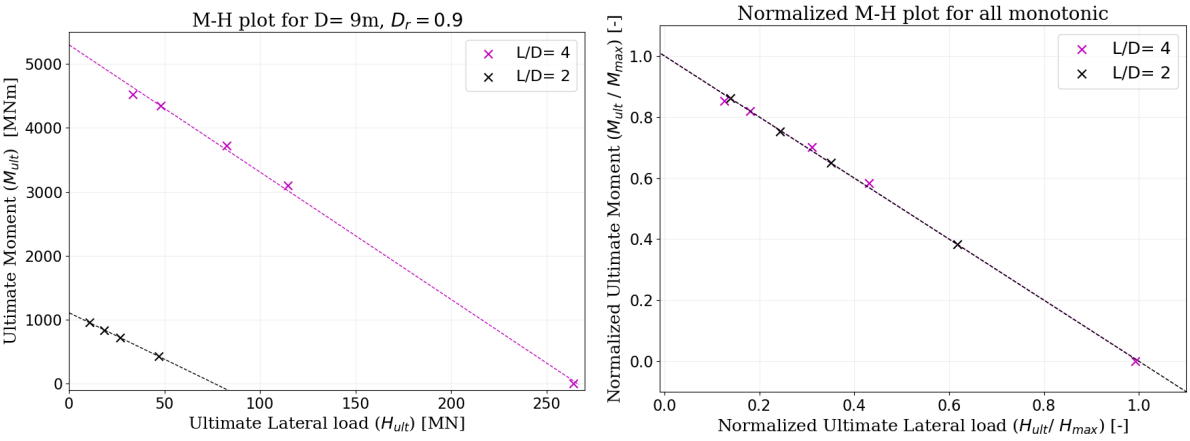

(a) Absolute value

(b) Normalized value

Figure 5.14: Interaction diagram between moment and lateral load for monopile with $D = 9m$ installed at sand with $D_r = 0.9$ presented in (a) absolute value and (b) normalized value.

Information regarding the effect of e/D on the distribution of four components in a simplified p distribution, when H_{ult} is applied, is presented in Figure 5.15 and 5.16. Increasing the pile e/D ratio is observed to increase the ratio between p_{max} and H_{ult} (Figure 5.15a). Regarding the depth of p_{max} (z_{max}), increasing the e/D ratio causes it to move into shallower depths (Figure 5.15b).

It is indicated that increasing the pile e/D ratio leads to a higher ratio of p_{base} to H_{ult} (Figure 5.16a). Analysis of the normalized rotational point (RP) (Figure 5.16b) reveals that reducing e/D causes the RP to shift to a deeper layer.

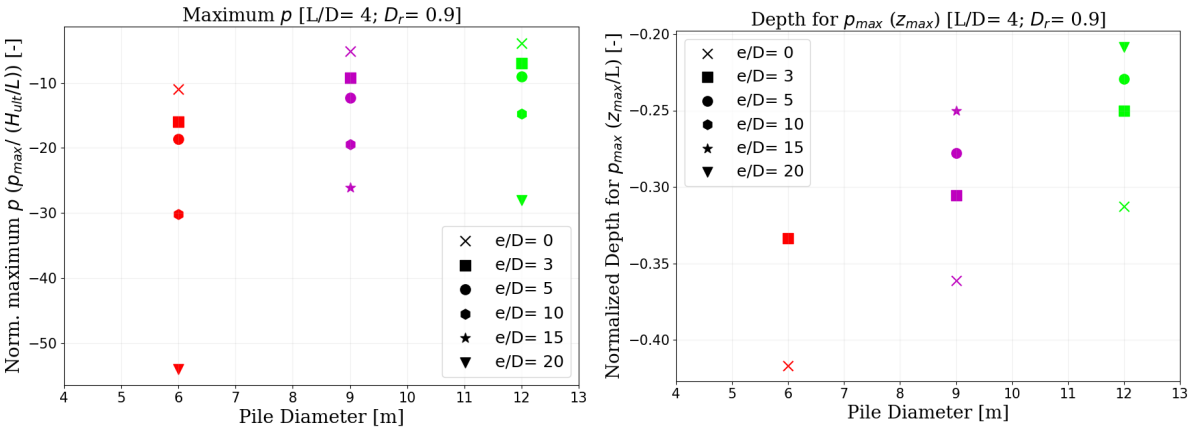

(a) Normalized p_{max} **(b)** Normalized z_{max}

Figure 5.15: The effect of load eccentricity (e/D) into the $p-y$ response in term of (a) Normalized maximum p response and (b) depth of maximum p response.

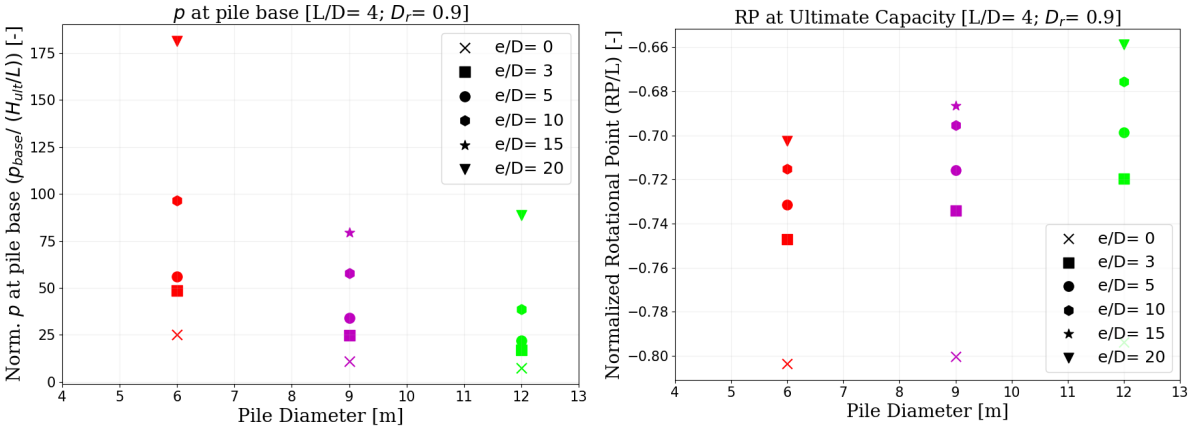

(a) Normalized p_{base} **(b)** Normalized RP

Figure 5.16: The effect of load eccentricity (e/D) into the $p-y$ response in terms of (a) Normalized p response at pile base and (b) depth of rotational point.

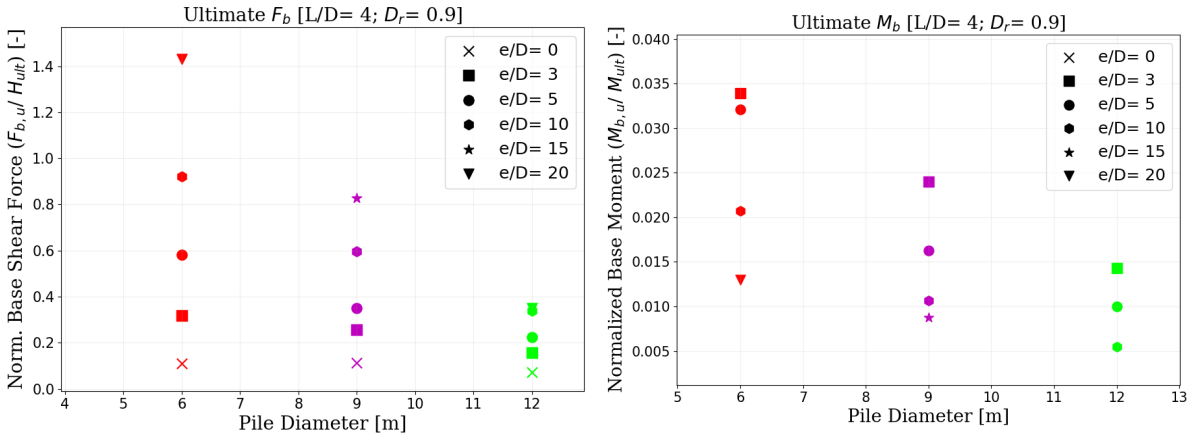

(a) Normalized $F_{b,u}$ **(b)** Normalized $M_{b,u}$

Figure 5.17: The effect of load eccentricity (e/D) into the base response when the ultimate load is applied, presented in terms of normalized (a) Base Shear Force and (b) Base Moment.

In addition, the analyses of the effect of load eccentricity (e/D) on the pile base reaction components

are presented in Figure 5.17. Examination of the ultimate base shear force ($F_{b,u}$) (Figure 5.17a) reveals that increasing the e/D ratio results in a higher $F_{b,u}/H_{ult}$ ratio. Increasing the e/D ratio is found to lower the value of $M_{b,u}/H_{ult}$ (Figure 5.17b). In conclusion, while the contribution of F_b to monopile stability significantly increases with an increase in the e/D ratio, the opposite trend is observed for M_b. Furthermore, the contribution of M_b is once again considered to be negligible (Figure 5.17b).

5.1.3. Sand Relative Density Effect

The influence of sand relative density (D_r) on pile bearing capacity is depicted through load-displacement and moment-rotation curves (Figure 5.18 and 5.19). Examination of the load-displacement curves for varying D_r (Figure 5.18a and 5.19a) reveals that an increase in D_r corresponds to higher values of H_{ult} but lower values of $y_{sb,u}$. In the moment-rotation curve (Figure 5.18b and 5.19b), it is evident that increasing D_r also results in a higher M_{ult}. A summary of the impact of D_r on lateral load and moment capacity is provided in Figure 5.20. It is observed that both the relationship between H_{ult} and D_r (Figure 5.20a) and the relationship between M_{ult} and D_r (Figure 5.20b) is almost linear. Observation at the D_r effect (Figure 5.19) indicate that $\theta_{sb} = 2^o$ consistently corresponds to $y_{sb} < 0.1D$.

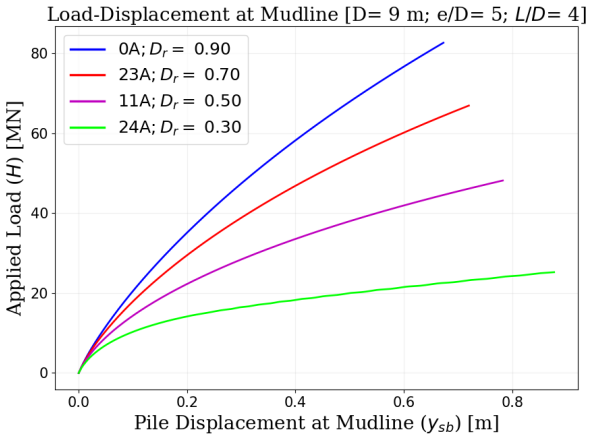

(a) Load-displacement curve

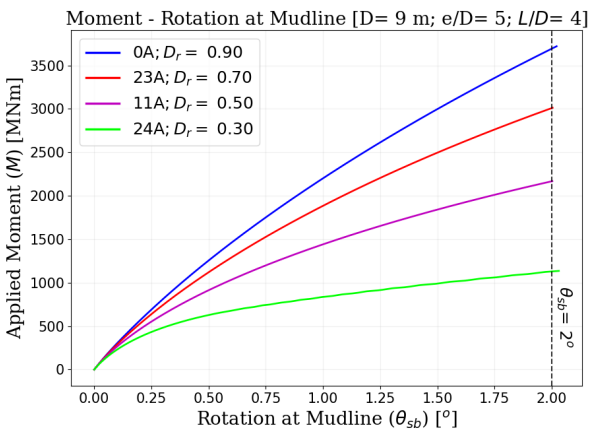

(b) Moment-rotation curve

Figure 5.18: The parametric analyses on the effect of sand relative density (D_r) into the monopile ultimate capacity presented in (a)Load-displacement and (b) Moment-rotation curves for the pile with $D = 9m, L/D = 4$.

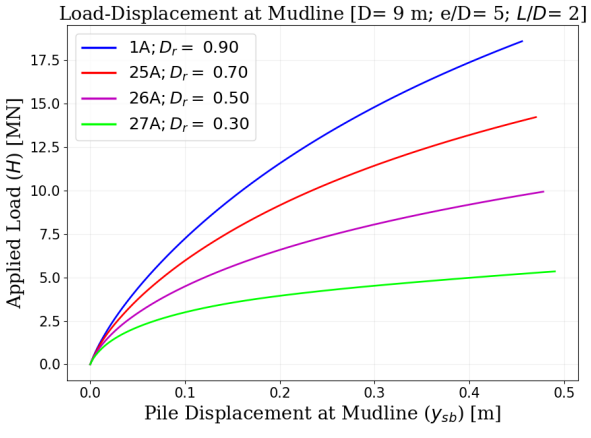

(a) Load-displacement curve

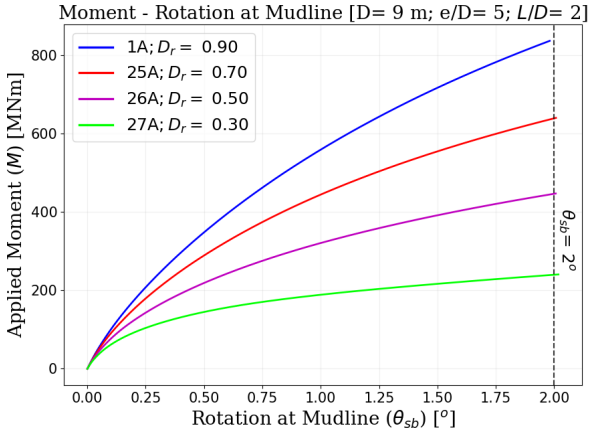

(b) Moment-rotation curve

Figure 5.19: The parametric analyses on the effect of sand relative density (D_r) into the monopile ultimate capacity presented in (a)Load-displacement and (b) Moment-rotation curves for the pile with $D = 12m, L/D = 2$.

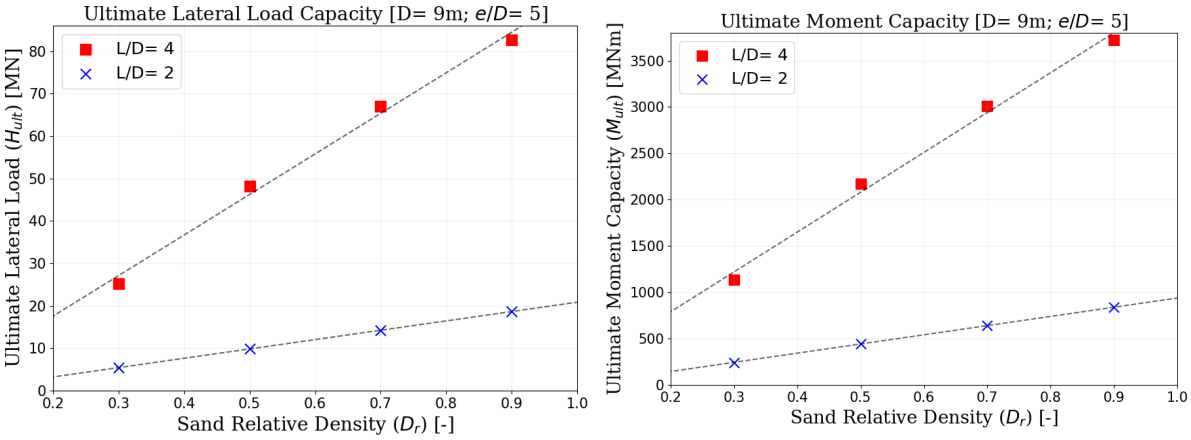

(a) Lateral load capacity

(b) Moment capacity

Figure 5.20: The effect of sand relative density D_r on (a)lateral load ultimate capacity and (b) ultimate moment capacity of the monopile.

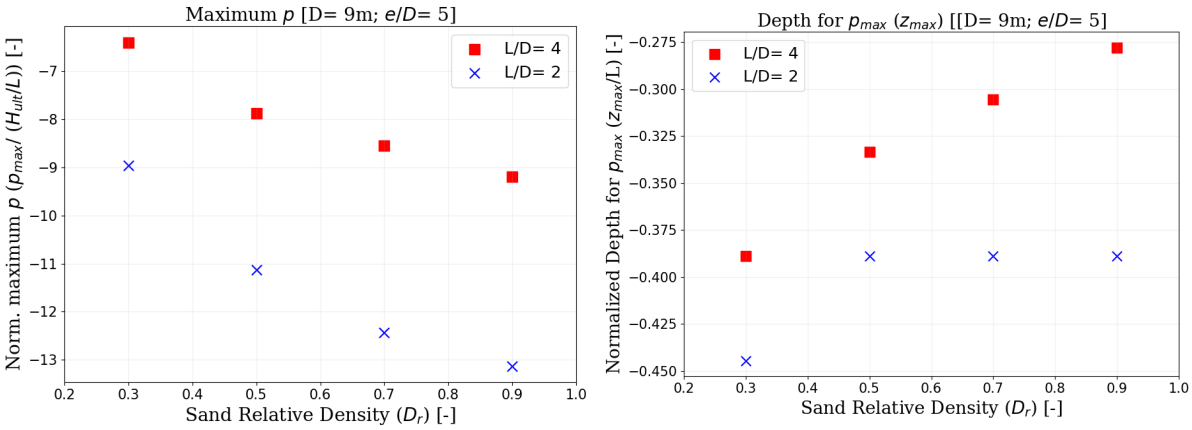

(a) Normalized p_{max}

(b) Normalized z_{max}

Figure 5.21: The effect of D_r into the $p-y$ response in term of (a) Normalized maximum p response and (b) depth of maximum p response.

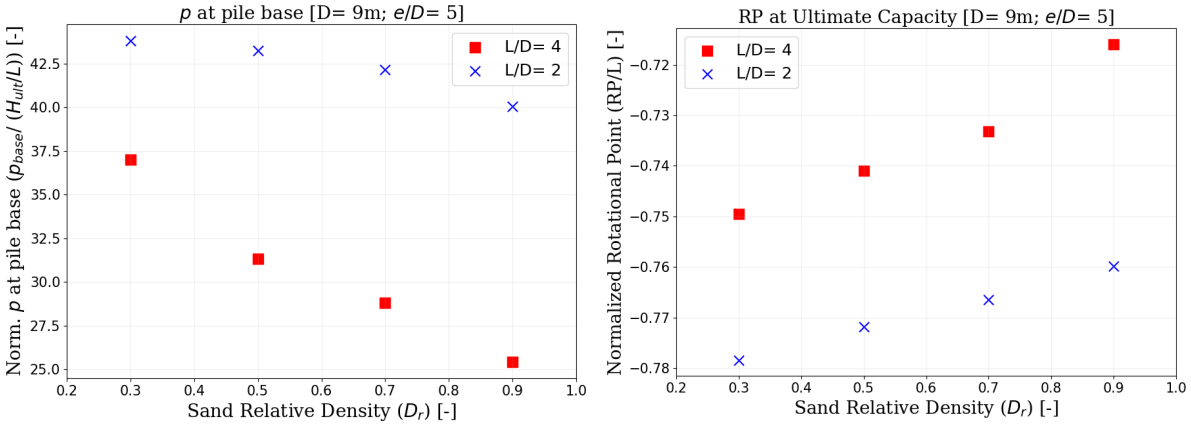

(a) Normalized p_{base}

(b) Normalized RP

Figure 5.22: The effect of D_r into the $p-y$ response in terms of (a) Normalized p response at pile base and (b) depth of rotational point.

Further discussion on the effect of D_r on the distribution of four components in a simplified p distribution, under the application of H_{ult}, is presented in Figure 5.21 and 5.22. It is shown that

increasing the D_r results in a higher $p_{max}/(H_{ult}/L)$ ratio (Figure 5.21a). Regarding the depth of p_{max} (z_{max}), increasing the D_r causes it to move into shallower depths (Figure 5.21b) for the pile with $L/D = 4$. For a shorter pile with $L/D = 2$, raising the D_r above 0.5 does not significantly alter the position of z_{max} (Figure 5.21b).

Furthermore, it is observed that increasing the D_r ratio results in a lower ratio of p_{base} to H_{ult} (Figure 5.22a). The analyses of the normalized rotational point (RP) (Figure 5.22b) reveal that decreasing the D_r ratio causes the RP to shift to a deeper layer.

Examination of base shear force when the ultimate load is applied ($F_{b,u}$) (Figure 5.23a) reveals that increasing the D_r ratio results in a lower $F_{b,u}/H_{ult}$ ratio. A similar trend is observed in the plot for the base moment when the ultimate moment is applied ($M_{b,u}$) (Figure 5.23b). In conclusion, base shear force and base moment components become more significant for monopiles with lower D_r.

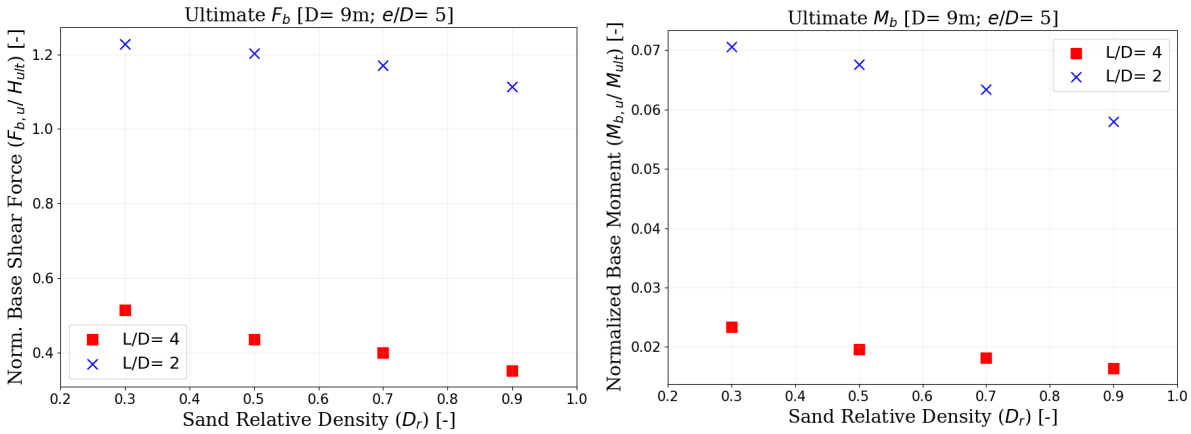

(a) Normalized $F_{b,u}$

(b) Normalized $M_{b,u}$

Figure 5.23: The effect of D_r into the base response when the ultimate load is applied, presented in terms of normalized (a) Base Shear Force and (b) Base Moment.

5.1.4. Discussion on Pile Relative Stiffness (K_r)

The pile relative stiffness ([33]) is a dimensionless parameter that can be calculated according to Equation 2.2. This parameter takes into consideration the pile geometry, properties, and soil properties in the calculation process (Eq. 2.2). Understanding this, efforts have been made to establish a correlation between the rotational behavior of the pile and K_r.

One aspect of interest is to determine the amount of rotation induced at the pile base when $\theta_{sb} = 2^o$. To comprehend this behavior, an analysis of the correlation between the ratio of θ_b over θ_{sb} and K_r is conducted (Figure 5.24). The results demonstrate that for L/D ratios of 2 or less, the θ_b/θ_{sb} ratio approaches 1. Two dashed black lines are provided in Figure 5.24 indicating the limit for rigid and flexible monopiles. These boundaries are created following the classification by [33] and calculated according to Equation 2.2. Further examination of the data plot suggests that the data points follow a distinct trendline forming an S-shaped curve when plotted on a logarithmic x-axis (Figure 5.24).

The S-shaped curve can be represented by various types of functions, including the sigmoid function, hyperbolic tangent function, and error function. After conducting a thorough study comparing these options, it is suggested that the hyperbolic tangent function provides a better fit to the data points compared to the other functions. Additionally, the hyperbolic tangent function offers simplicity in

expressing the relationship as follows:

$$\frac{\theta_{base}}{\theta_{sb}} = \tanh\left(\frac{K_r}{\alpha_{Kr}}\right) \tag{5.1}$$

Based on the curve-fitting process, the coefficient α_{Kr} for the Equation 5.1 is suggested to be $\alpha_{Kr} = 0.0108$. While this function (Eq. 5.1) may appear to well represent the data points, further investigation is necessary to validate its applicability to different sand types, beyond the specific Geba Sand used in this study.

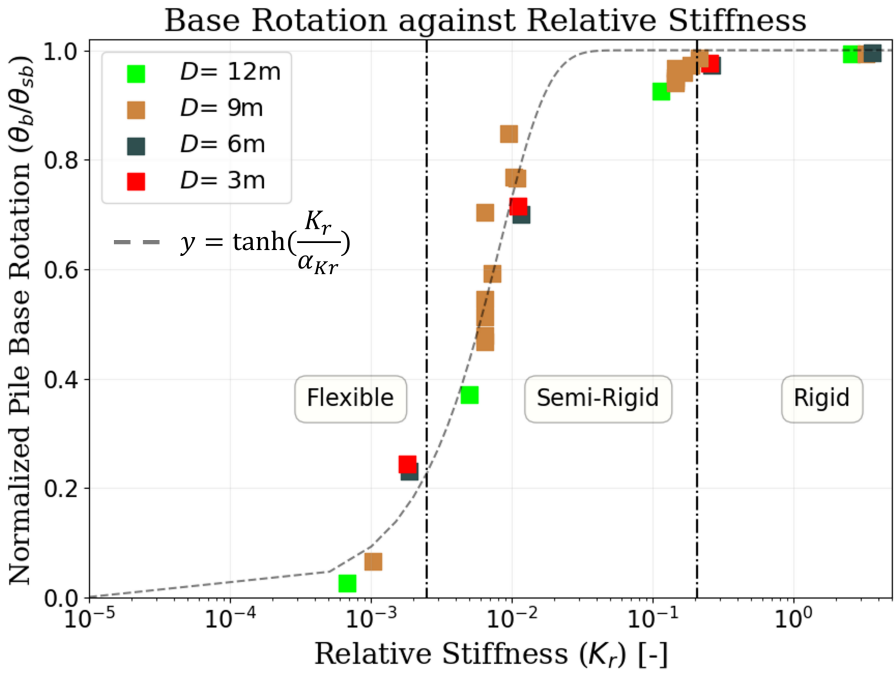

Figure 5.24: The plot of ratio between θ_b and θ_{sb} against the K_r.

5.2. Cyclic Load

The parametric analyses under cyclic loading are conducted on two key aspects: the accumulated rotation (θ_{acc}) and displacement (y_{acc}) at the mudline, which are calculated using Equation 4.6. In addition to this, the examination of the maximum and minimum base shear forces during peak loading (H_{max}) and unloading (H_{min}) are also provided. Notably, the presented analyses primarily emphasize the outcomes derived from cyclic loading analyses with $\zeta_b = 0.4$. The results of the cyclic load test with $\zeta_b = 0.1$ can be found in Appendix C.

5.2.1. Influence of Pile Geometry on Monopile Cyclic Response

The influence of pile geometry on θ_{acc} increment is examined for various L/D scenarios (Figure 5.25 and 5.26). When analyzing the monopile with $L/D = 4$, it becomes evident that increasing D results in a lower $\Delta\theta(N)$ over θ_s ratio during both the loading (Figure 5.25a) and unloading phases (Figure 5.25b). Upon closer examination of Figure 5.25 reveals that the values of $\Delta\theta(N)/\theta_s$ during the loading and unloading phases are nearly identical. Therefore, for other L/D ratios, the θ_{acc} analyses are provided solely for the loading phase (Figure 5.26).

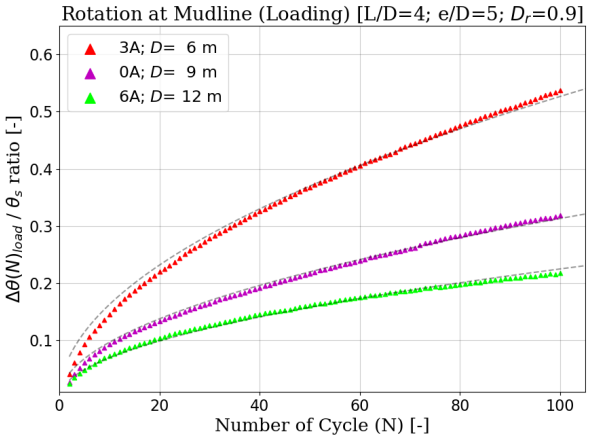

(a) θ_{acc} at loading

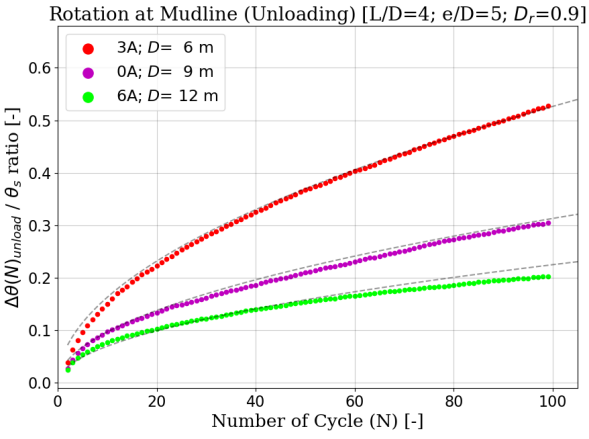

(b) θ_{acc} at unloading

Figure 5.25: The effect of pile geometry (D and L) on θ_{acc} at the mudline during cyclic load with $\zeta_b = 0.4$, presented during (a) loading phase and (b)unloading phase ($L/D = 4, e/D = 5, D_r = 0/9$).

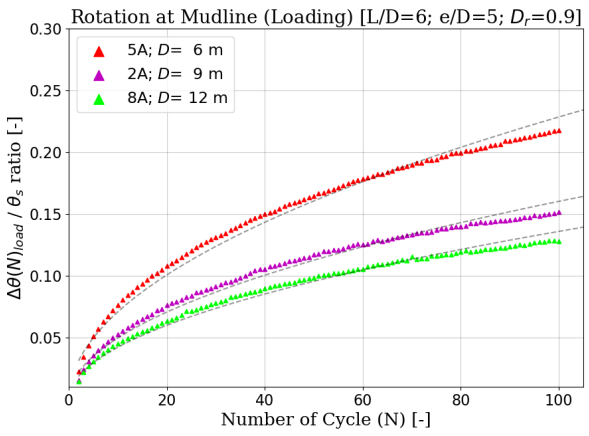

(a) θ_{acc} at loading $L/D = 6$

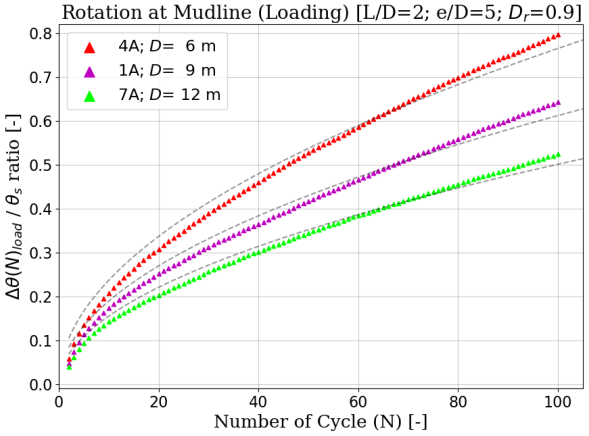

(b) θ_{acc} at loading $L/D = 2$

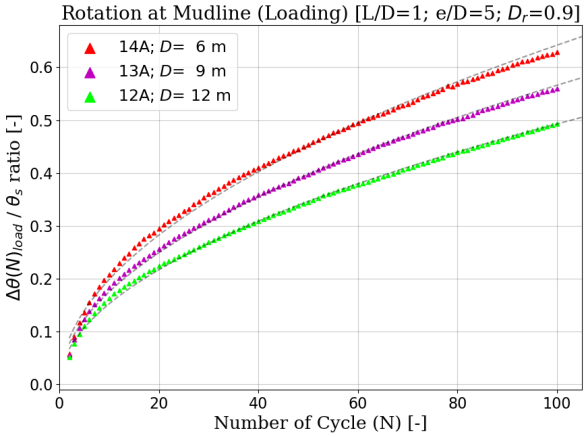

(c) θ_{acc} at loading $L/D = 1$

Figure 5.26: The effect of pile geometry (D and L) on θ_{acc} at the mudline during cyclic load with $\zeta_b = 0.4$, presented for monopile with (a) $L/D = 6$, (b) $L/D = 2$, and (c) $L/D = 1$ ($D_r = 0.9, e/D = 5$).

When considering the increments in the y_{acc}, it is apparent that the $\Delta y(N)/y_s$ value increases as D decreases (Figure 5.27 and 5.28). A more detailed observation of Figure 5.27 suggests that the values of $\Delta y(N)/y_s$ during the loading (Figure 5.27a) and unloading (Figure 5.27b) phases are nearly identical. Thus, for other L/D ratios, the y_{acc} analyses are also exclusively provided for the loading phase (Figure

5.28).

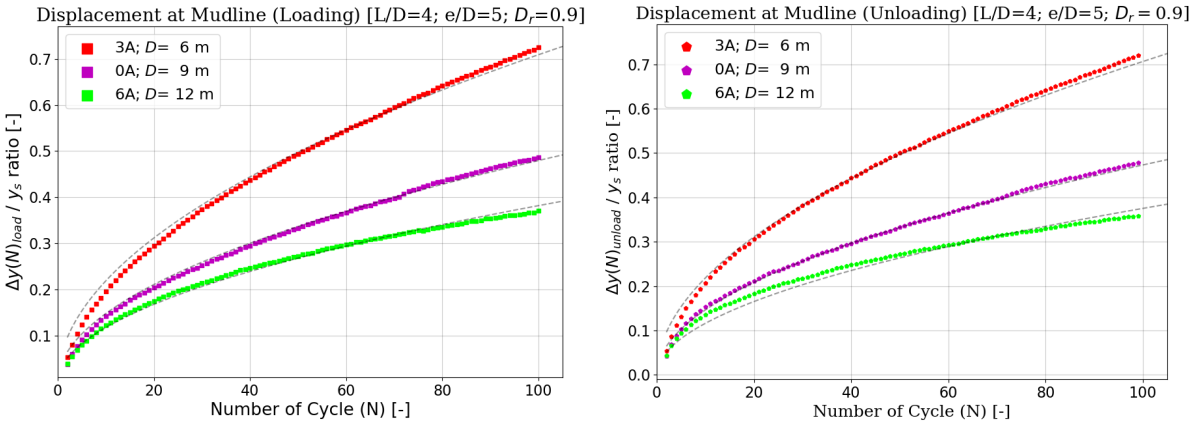

(a) y_{acc} at loading

(b) y_{acc} at unloading

Figure 5.27: The effect of pile geometry (D and L) on y_{acc} at the mudline during cyclic load with $\zeta_b = 0.4$, presented during (a) loading phase and (b)unloading phase ($L/D = 4, e/D = 5, D_r = 0.9$).

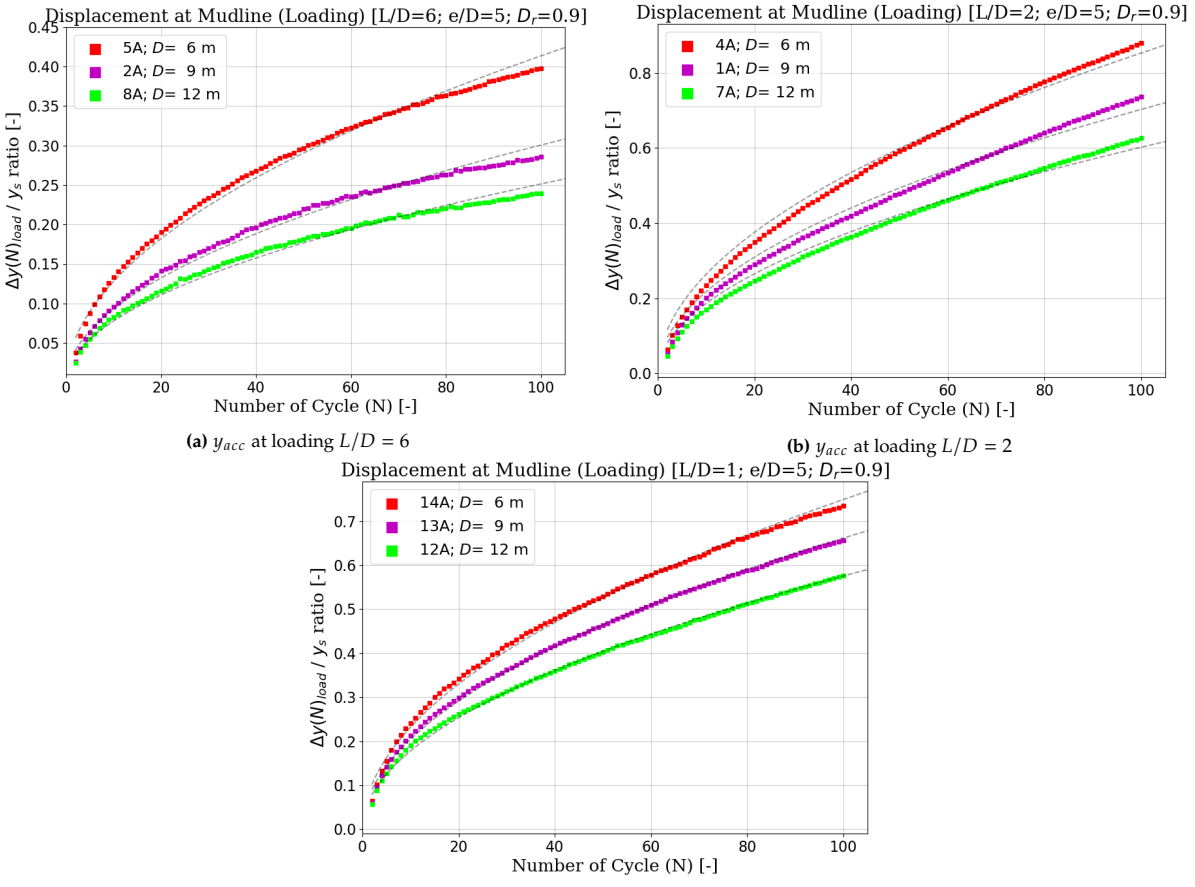

(a) y_{acc} at loading $L/D = 6$

(b) y_{acc} at loading $L/D = 2$

(c) y_{acc} at loading $L/D = 1$

Figure 5.28: The effect of pile geometry (D and L) on y_{acc} at the mudline during cyclic load with $\zeta_b = 0.4$, presented for monopile with (a) $L/D = 6$, (b) $L/D = 2$, and (c) $L/D = 1$ ($D_r = 0.9, e/D = 5$).

Increasing the L/D ratio results in a lower increment of accumulated rotation ($\Delta\theta(N)/\theta_s$) during both the loading and unloading phases (Figure 5.29a). However, it is important to note a deviation from this trend for a rigid monopile with $L/D = 1$ which tends to rotate under a more uniform

manner. Furthermore, the same trends are observed in the $\Delta y(N)/y_s$ values (Figure 5.29b). Upon closer examination of the increments in θ_{acc} and y_{acc}, it becomes evident that both $\Delta\theta(N)/\theta_s$ and $\Delta y(N)/y_s$ values as a function of the number of cycles (N) can be represented by an exponential function with the variable (α) set to 0.51.

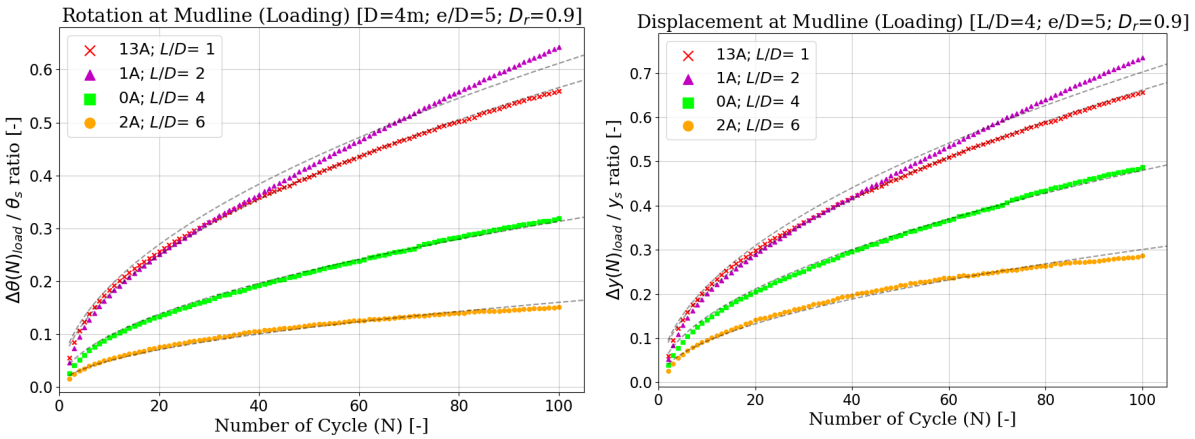

(a) θ_{acc} at loading **(b)** y_{acc} at loading

Figure 5.29: The effect of pile geometry (L/D) on (a)θ_{acc} (b) y_{acc} presented for the monopile with $D = 9m, L/D = 4, e/D = 5$ and installed in sand with $D_r = 0.9$.

The impact of the diameter geometry on the F_b when subjected to $H = 0.4H_{ult}$ and $H = 0$ is presented for various pile L/D ratios (Figure 5.30, 5.31, 5.32, and 5.33). Examining the F_b values under the application of H_{max} ($F_{b,max}$), it is evident that increasing the D results in higher $F_{b,max}$ values for rigid and semi-rigid monopile (Figure 5.30a, 5.32a, and 5.33a). Similarly, this trend is observed for the F_b values upon load release ($F_{b,min}$) (Figure 5.30b, 5.32b, and 5.33b).

A deviation from the general trend is evident for the monopile with an L/D of 6 (Figure 5.31). The analysis indicates that reducing the diameter (D) results in higher $F_{b,max}$ values (Figure 5.31a), while the magnitudes of $F_{b,min}$ remain relatively consistent (Figure 5.31b). This is due to the monopiles with $L/D = 6$ being classified as flexible monopile (Table 6.1). As established in the analysis, flexible piles exhibit relatively small displacements and rotations at the pile base when $\theta_{sb} = 2^o$ (Figure 5.24). Consequently, there is less mobilization at the pile base, leading to lower values of F_b.

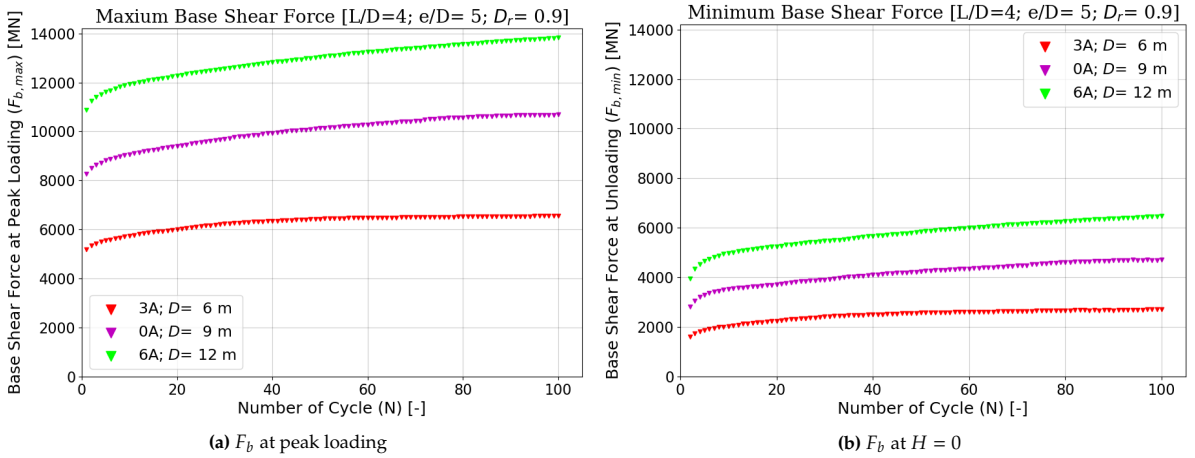

(a) F_b at peak loading **(b)** F_b at $H = 0$

Figure 5.30: The effect of pile geometry (D) on the F_b during (a)maximum loading applied and (b) load completely released ($L/D = 4, e/D = 5, D_r = 0.9$).

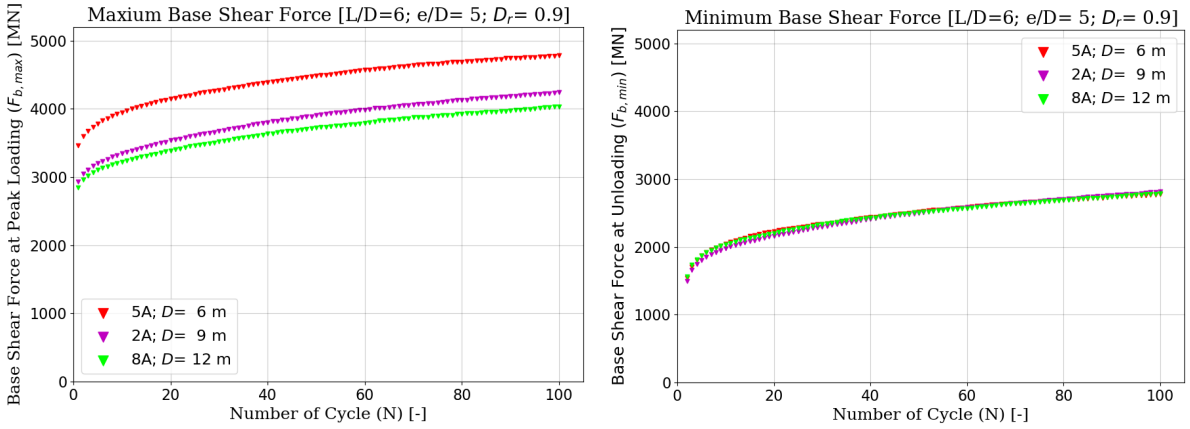

(a) F_b at H_{max} **(b)** F_b at $H = 0$

Figure 5.31: The effect of pile geometry (D) on the F_b during (a)maximum loading applied and (b) load completely released ($L/D = 6, e/D = 5, D_r = 0.9$).

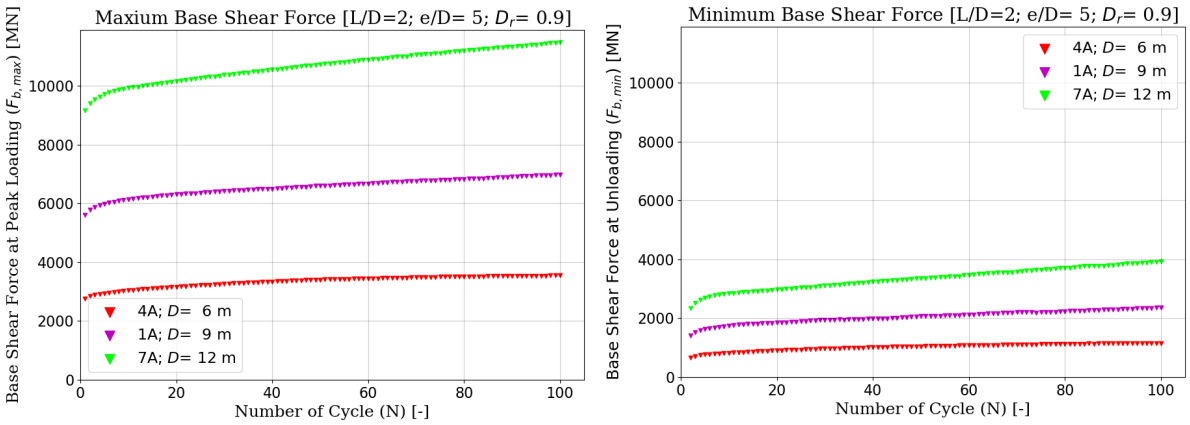

(a) F_b at peak loading **(b)** F_b at $H = 0$

Figure 5.32: The effect of pile geometry (D) on the F_b during (a)maximum loading applied and (b) load completely released ($L/D = 2, e/D = 5, D_r = 0.9$).

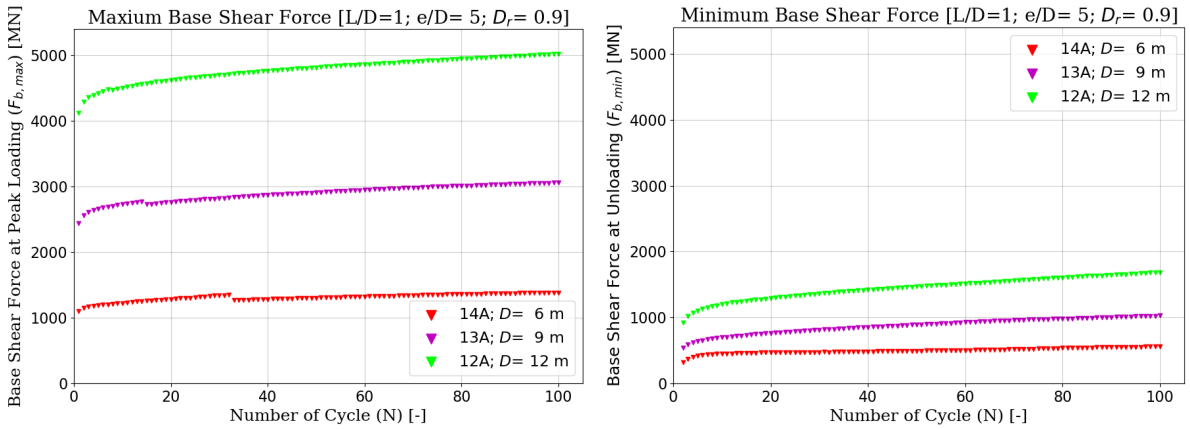

(a) F_b at peak loading **(b)** F_b at $H = 0$

Figure 5.33: The effect of pile geometry (D) on the F_b during (a)maximum loading applied and (b) load completely released ($L/D = 1, e/D = 5, D_r = 0.9$).

Additionally, the influence of the L/D ratio on $F_{b,max}$ and $F_{b,min}$ is presented in Figure 5.34. Upon examining the impact of the L/D ratio on $F_{b,max}$ (Figure 5.34a), it is apparent that a clear trend cannot

be deduced with changes in the L/D ratio and the same observation is made for $F_{b,min}$ (Figure 5.34b). However, when focusing on the analysis of semi-rigid monopiles (L/D = 2 and 4), it can be observed that increasing the L/D ratio leads to higher values of both $F_{b,max}$ (Figure 5.34a) and $F_{b,min}$ (Figure 5.34b). In contrast, for the flexible piles (L/D), the smallest values of $F_{b,max}$ and $F_{b,min}$ are observed due to the small contribution of F_b to monopile stability (Figure 5.9a). The analyses on the increment of $F_{b,max}$ over a cycle ($\Delta F_{b,max}(N)/F_{b,max;s}$) are also provided in Appendix C.

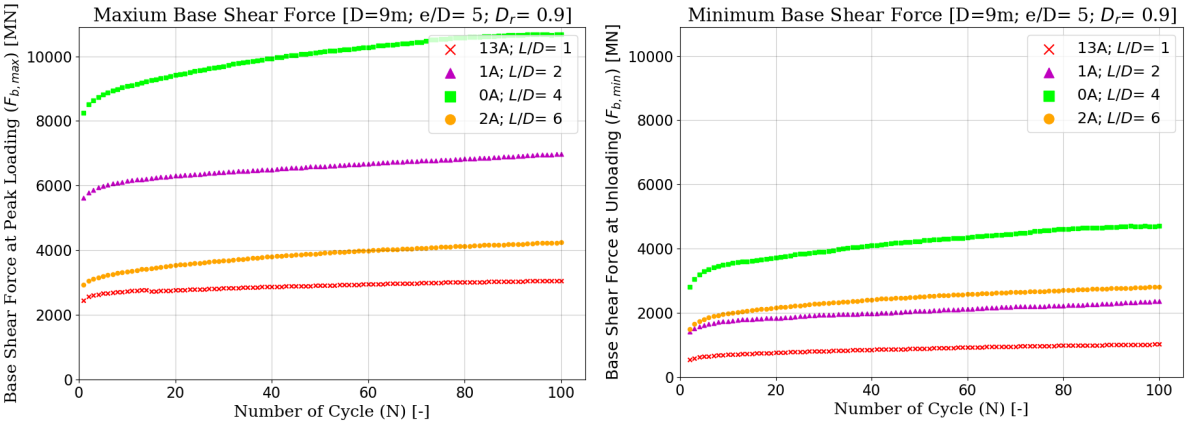

(a) F_b at peak loading

(b) F_b at $H = 0$

Figure 5.34: The effect of pile geometry (L/D) on the F_b during (a)maximum loading applied and (b) load completely released ($D = 9m, e/D = 5, D_r = 0.9$).

5.2.2. Influence of Load Eccentricity on Monopile Cyclic Response

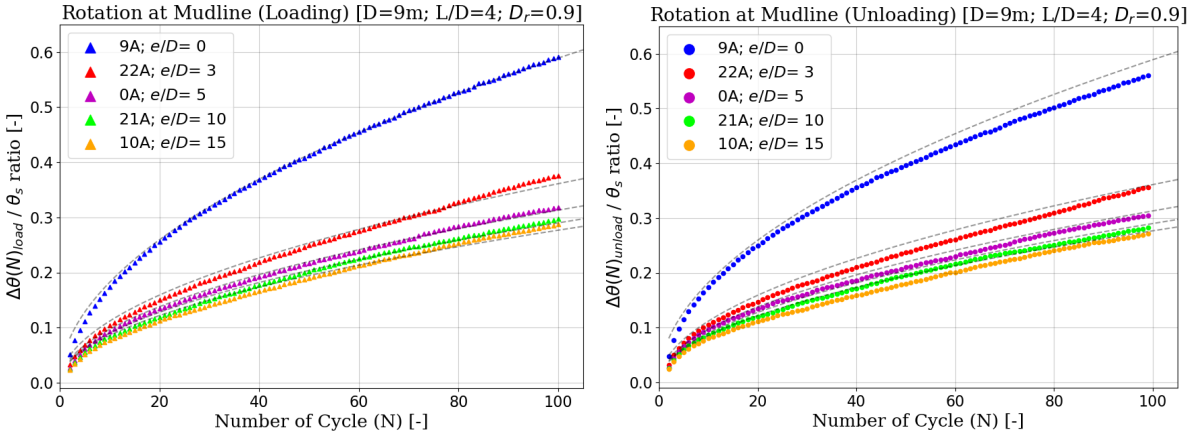

(a) θ_{acc} at loading

(b) θ_{acc} at unloading

Figure 5.35: The effect of load eccentricity (e/D) on on θ_{acc} at the mudline during cyclic load with $\zeta_b = 0.4$, presented during (a) loading phase and (b)unloading phase ($D = 9m; L/D = 4, D_r = 0.9$).

The influence of e/D on the increment of θ_{acc} is depicted in Figure 5.35. A more detailed analysis of Figure 5.35 reveals that an increase in e/D leads to a lower ratio of $\Delta\theta(N)$ over θ_s during both loading (Figure 5.35a) and unloading (Figure 5.35b). In contrast to the observed trend with D and L/D ratio (Figure 5.25), the values of $\Delta\theta(N)/\theta_s$ during loading and unloading phases exhibit differences when changing e/D. Furthermore, continuous increases in the e/D ratio do not significantly raise the $\Delta\theta(N)$ over θ_s ratio after a certain point, a phenomenon also found in Figure 5.11 and 5.12. A similar trend is observed for the $\Delta y(N)/y_s$ ratio during both loading (Figure 5.36a) and unloading phases (Figure 5.36b)

when varying the e/D ratio.

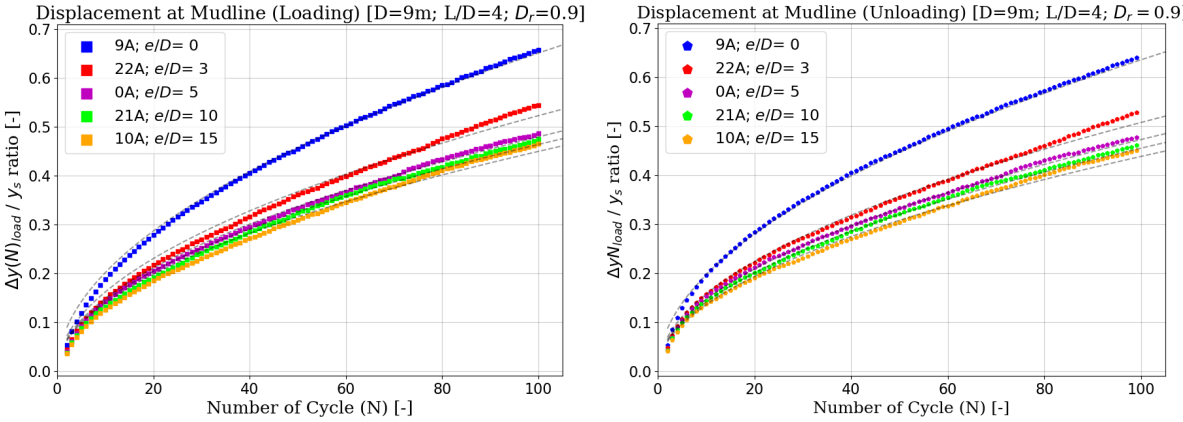

(a) y_{acc} at loading **(b)** y_{acc} at unloading

Figure 5.36: The effect of load eccentricity (e/D) on y_{acc} at the mudline during cyclic load with $\zeta_b = 0.4$, presented during (a) loading phase and (b) unloading phase ($D = 9m; L/D = 4, D_r = 0.9$).

Additionally, the impact of the e/D ratio on $F_{b,max}$ and $F_{b,min}$ is presented in Figure 5.37. Upon examining the influence of the e/D ratio on $F_{b,max}$ (Figure 5.37a), it is observed that modifications to the e/D do not significantly affect the $F_{b,max}$ values. The effect of e/D is more pronounced in the $F_{b,min}$ values (Figure 5.37b). Analysis of the $F_{b,min}$ values suggests that increasing the e/D results in lower $F_{b,min}$ values. However, continuous increases in the e/D ratio may lead to saturation in the $F_{b,min}$ value.

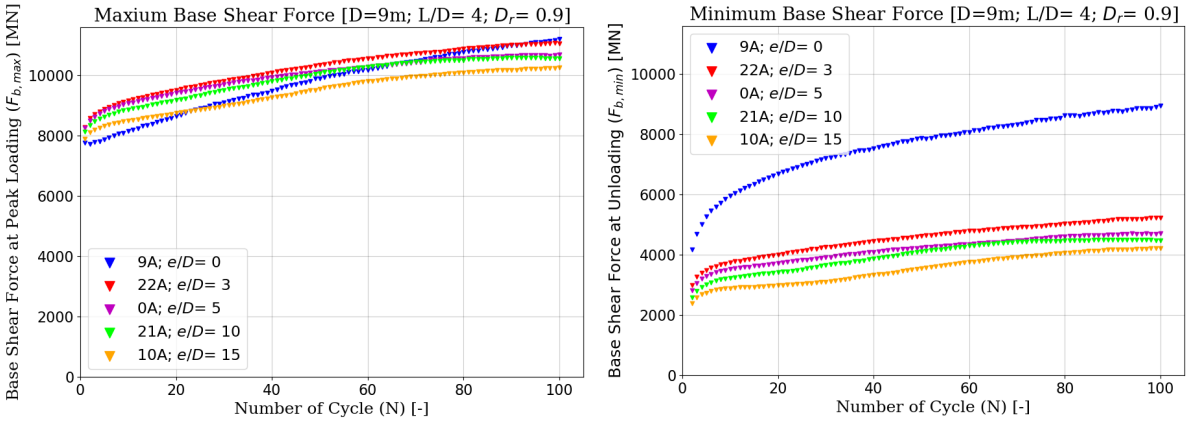

(a) F_b at peak loading **(b)** F_b at $H = 0$

Figure 5.37: The effect of load eccentricity (e/D) on the F_b during (a) maximum loading applied and (b) load completely released ($D = 9m, L/D = 4, D_r = 0.9$.

5.2.3. Influence of Sand Relative Density on Monopile Cyclic Response

The influence of D_r on the increment of θ_{acc} is illustrated in Figure 5.38. An analysis illustrated by Figure 5.38, reveals that reducing D_r leads to a lower ratio of $\Delta\theta(N)$ over θ_s during both loading (Figure 5.38a) and unloading (Figure 5.38b). Changes in D_r result in different $\Delta\theta(N)/\theta_s$ values during the loading and unloading phases. Deviations in the trend for the sand with $D_r = 0.3$ are possibly due to the relatively low D_r. A similar trend is observed for the $\Delta y(N)/y_s$ ratio during both loading (Figure 5.39a) and unloading phases (Figure 5.39b) when varying D_r.

Additionally, the impact of D_r on $F_{b,max}$ and $F_{b,min}$ is presented in Figure 5.40. Upon examining the

influence of D_r on $F_{b,max}$ (Figure 5.40a), it is observed that lowering D_r also reduces the $F_{b,max}$ value. The same trend is also found when evaluating the effect of D_r on $F_{b,min}$ (Figure 5.40b).

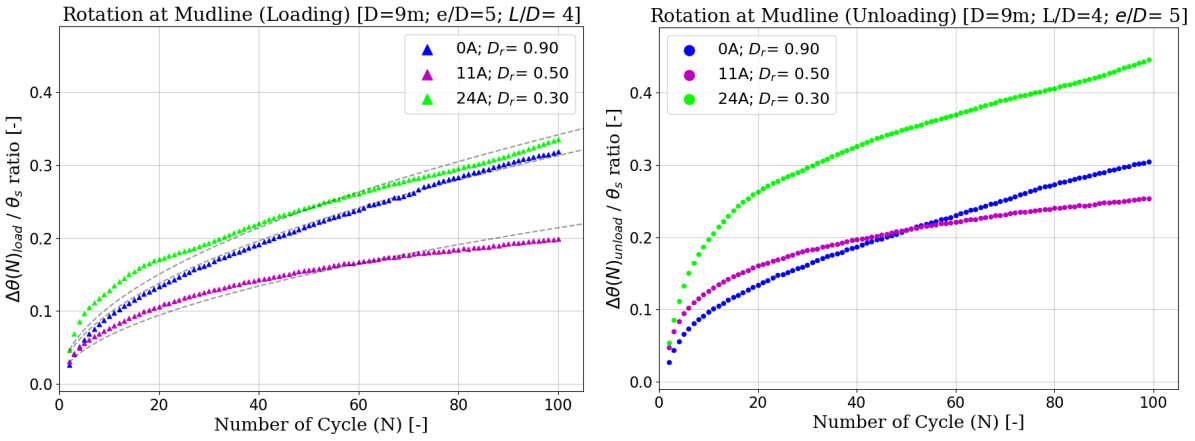

(a) θ_{acc} at loading **(b)** θ_{acc} at unloading

Figure 5.38: The effect of sand relative density (D_r) on θ_{acc} at the mudline during cyclic load with $\zeta_b = 0.4$, presented during (a) loading phase and (b) unloading phase ($D = 9m; L/D = 4, e/D = 5$).

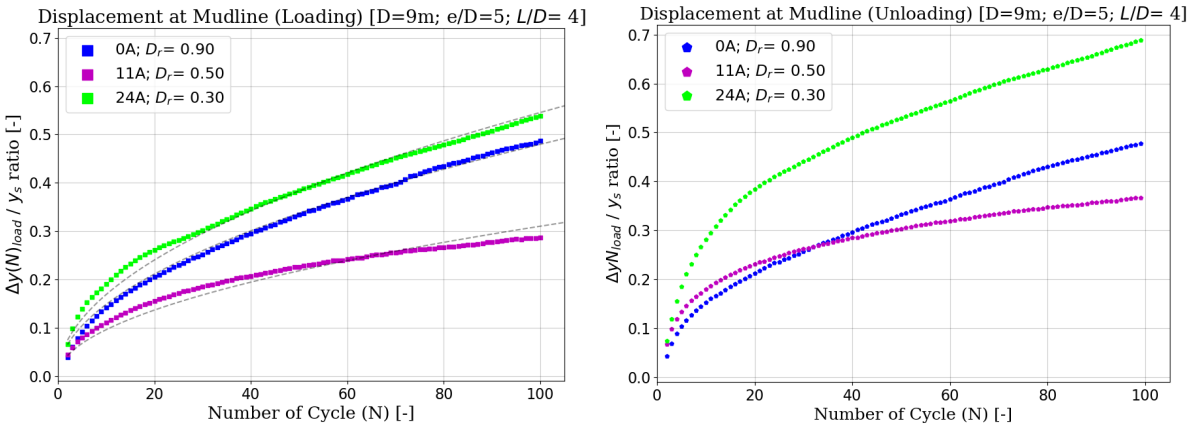

(a) y_{acc} at loading **(b)** y_{acc} at unloading

Figure 5.39: The effect of sand relative density (D_r) on y_{acc} at the mudline during cyclic load with $\zeta_b = 0.4$, presented during (a) loading phase and (b) unloading phase ($D = 9m; L/D = 4, e/D = 5$).

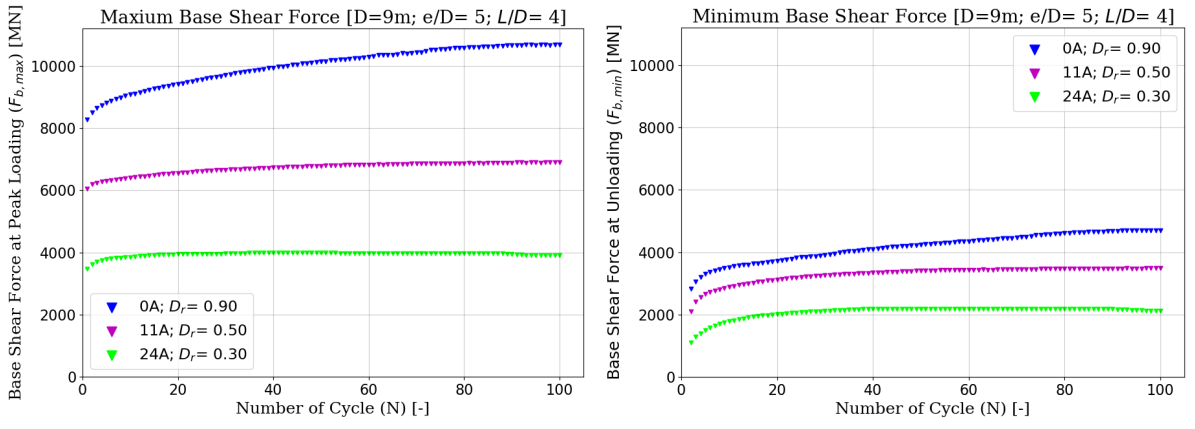

(a) F_b at peak loading **(b)** F_b at $H = 0$

Figure 5.40: The effect of pile relative density (D_r) on the F_b during (a) maximum loading applied and (b) load completely released ($D = 9m, L/D = 4, D_r = 0.9$).

6

Simplified Model for Pile Base Response

The development of a simplified model is considered important because employing 3D FE analyses requires a significant amount of computational time. Building upon the results presented in the previous chapter, the analysis of the 0D response is focused on the components of base shear force and base displacement ($F_b - y_b$). The results and analyses conducted to develop the 0D model are presented for both monotonic loading and cyclic loading in this chapter.

6.1. Monotonic Load

6.1.1. Hypothetical Maximum F_b ($F_{b,ref}$)

The objective behind establishing a hypothetical maximum base shear force ($F_{b,ref}$) is to determine a limiting value for the evolution of F_b during monotonic lateral loading. This calculation is based on the assumption that the stress and deformation conditions of the soil element beneath the pile base under lateral loading can be represented by a triaxial shearing test. Under this assumption, the $F_{b,ref}$ can be determined by adapting the approach by [37] and [40] (Eq. 2.4) following this expression:

$$F_b = \left(c_3.V + \frac{\pi}{4}D^2L\gamma'\right)\tan\phi_{peak} \tag{6.1}$$

The calculation of $F_{b,ref}$ assumes that all gravitational forces from the monopile are entirely transmitted to the pile base ($c_3 = 1$). The gravitational force is assumed to originate from the steel plate, with the steel properties detailed in Table 3.2, and the geometry is outlined in Table 4.1 and 5.1. The peak friction angle (ϕ_{peak}) (Table 6.1) is determined through Plaxis soil element testing and calibrated against soil laboratory tests with $D_r = 0.8$. The analysis reveals that the ϕ_{peak} for sand with $D_r = 0.9$ ranges between 38^o and 39^o (Table 6.1).

The calculated $F_{b,ref}$ values are provided in Table 6.1. After obtaining the $F_{b,ref}$ value, the ratio of $F_{b,u}$ to $F_{b,ref}$ is calculated. While in most cases the $F_{b,u}/F_{b,ref}$ ratio is less than 1, some cases yield a ratio greater than 1 (Table 6.1).

Table 6.1: Calculation result for $F_{b,ref}$ with the ratio between $F_{b,u}$ from model with $F_{b,ref}$.

Code	D[m]	L/D	e/D	D_r [-]	ϕ_{peak} [^{o}]	$F_{b,ref}$ [kN]^a	$F_{b,u}$ [kN]^b	Ratio a/b
0A	9	4	5	0.9	38.43	33779.9	29185.5	0.86
1A	9	2	5	0.9	38.57	18394.6	20719.9	1.13
2A	9	6	5	0.9	38.32	49072.9	10312.2	0.21
3A	6	4	5	0.9	38.51	10766.8	19333.2	1.80
4A	6	2	5	0.9	38.63	6034.7	9842.5	1.63
5A	6	6	5	0.9	38.43	15476.3	11993.2	0.77
6A	12	4	5	0.9	38.35	78699.1	34326.8	0.44
7A	12	2	5	0.9	38.51	42601.0	32933.7	0.77
8A	12	6	5	0.9	38.23	112423.5	10510.5	0.09
12A	12	1	5	0.9	38.63	24430.8	15143.4	0.62
13A	9	1	5	0.9	38.67	10656.1	9029.7	0.85
14A	6	1	5	0.9	38.72	3063.5	3673.2	1.20
20A	9	4	5	0.15	29.99	21205.1	17495.9	0.83
21A	9	4	10	0.9	38.43	36475.1	29008.6	0.80
22A	9	4	3	0.9	38.43	32701.9	29628.2	0.91
23A	9	4	5	0.7	35.67	29299.0	26805.3	0.91
24A	9	4	5	0.3	31.17	22837.2	12979.7	0.57
25A	9	2	5	0.7	35.78	15987.8	16665.7	1.04
26A	9	2	5	0.5	33.27	14031.2	11955.1	0.85
27A	9	2	5	0.3	31.03	12428.2	6573.0	0.53
28A	9	2	10	0.9	38.57	21103.3	21534.8	1.02
29A	9	2	3	0.9	38.32	17160.2	19869.6	1.16
30A	9	2	1	0.9	38.51	16196.7	17692.3	1.09
31A	9	4	5	0.1	29.57	20661.8	18097.3	0.88

These values, which are larger than 1, may be attributed to the fact that Equations 2.3 and 2.4 do not account for the evolution of vertical effective stress (σ'_{zz}) during the lateral loading phase. To investigate the evolution of $\sigma'zz$ during the lateral loading process, stress measurements were conducted at the pile base for both the reference case (0A) and Case 3A. The configuration and coordinates at the pile base for the stress measurement process are illustrated in Figure 6.1. The results of the stress measurement process are presented in Figure 6.2 for the reference case (Figure 6.2a) and Case 3A (Figure 6.2b). Examining these results, it is evident that σ'_{zz} evolves during the lateral loading process (Figure 6.2).

Upon evaluating the stress measurements in Figure 6.2, the evolution of σ'_{zz} at the pile base appears to depend on the location of the soil element with respect to the lateral load. Generally, the elements located in the positive $x-$axis experience a significant increase in their σ'_{zz}, while the elements at the negative $x-$axis experience stress release (Figure 6.2).

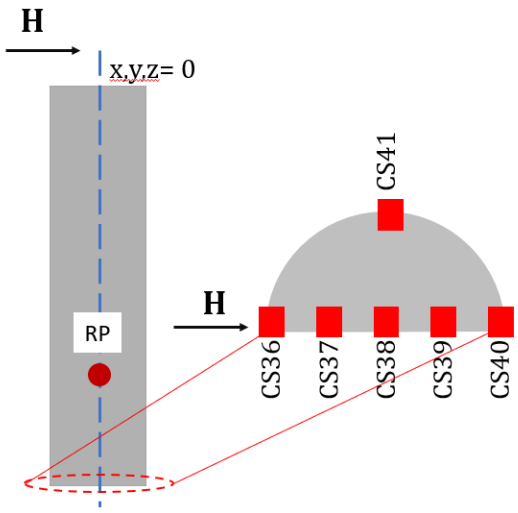

Code	X [m]	Y [m]	Z [m]
CS 36	-0. 5D - 0.1	0	-L
CS 37	- 0.25 D	0	-L
CS 38	0	0	-L
CS 39	0.25 D	0	-L
CS 40	0. 5D + 0.1	0	-L
CS 41	0	D/2	-L

Figure 6.1: The configuration and coordinate for the vertical stress (σ'_{zz}) recording process at the pile base.

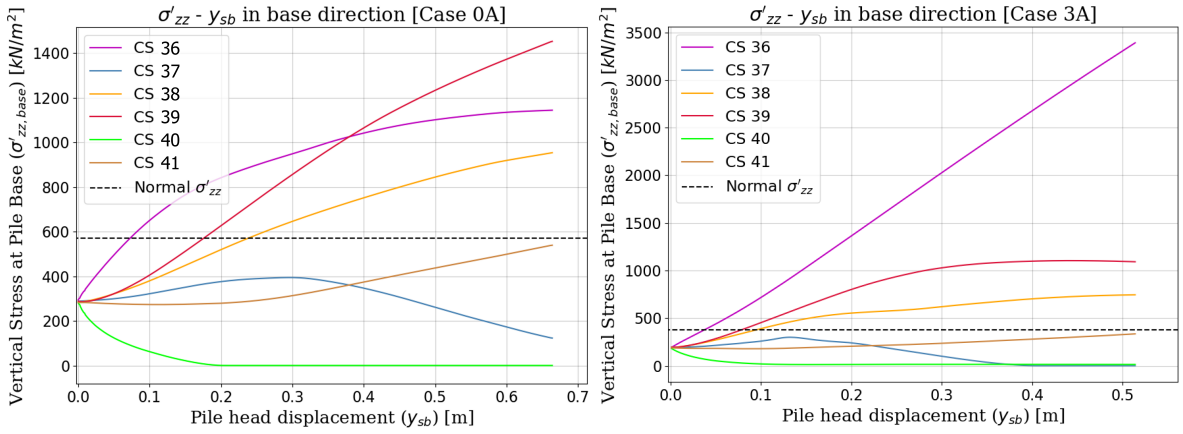

(a) Reference case ($D = 9m, L/D = 4, e/D = 5, D_r = 0.9$). **(b)** Case 3A ($D = 6m, L/D = 4, e/D = 5, D_r = 0.9$).

Figure 6.2: The stress recording result at the pile base for two different cases (a) Reference case/0A and (b) 3A (The black dashed line indicates σ'_{zz} under self-weight of the soil).

Despite the fact that Equations 2.4 and 2.3 do not account for the possibility of σ'_{zz} evolution during lateral loading, the obtained $F_{b,ref}$ using Equation 2.4 remains reasonably acceptable. The underlying concept behind this method assumes that the pile base is going to fail in a manner similar to shear failure in the triaxial element test. Another approach to calculating $F_{b,ref}$, such as the method proposed by [92], was also considered but found to be unsuitable in this case.

6.1.2. 0D $F_b - y_b$ Model for Montonic Response

To reconstruct the 0D $F_b - y_b$ response, a curve-fitting process is conducted using the $F_b - y_b$ data obtained from 3D FE analysis. As explained in chapter four, failure (ULS) is determined when θ_{sb} reaches 2^o. However, to thoroughly explore the response of the pile base, a push-to-fail (PTF) analysis is conducted with the objective of inducing continuous mobilization of the pile base. Two PTF analyses have been performed, one on the reference case ($D = 9m, L/D = 4, e/D = 5, D_r = 0.9$) and another on case 11A ($D = 9m, L/D = 4, e/D = 5, D_r = 0.5$). The results of these analyses and the $F_b - y_b$ response are presented in Figure 6.3a and 6.3b.

The 3D FE analyses for the reference case (0A) indicate that the $F_b - y_b$ response during monotonic lateral loading may be depicted following using a bi-linear curve (Figure 6.3a). The bi-linear function used to reconstruct the 0D $F_b - y_b$ relationship, for case 0A (Figure 6.3a) is derived from the modification of Equation 2.8 into the following expression:

$$F_b = A.F_{b,ref}.\min\left(1, \frac{y_b}{y_{b,cr}}\right) \tag{6.2}$$

where A represents a constant, and $y_{b,cr}$ denotes the critical y_b.

Examining the 3D FE results (Figure 6.3a), it is evident that the hardening effect during the loading process is not very pronounced and could possibly be considered negligible. The 3D FE analysis for Case 0A also suggests that when the applied lateral load exceeds $134.6MN$, the pile will be mobilized continuously. To represent this phenomenon, a limit on F_b is applied at $134.6MN$, and the bilinear function (Eq. 6.2) is used to construct the 0D $F_b - y_b$ curve for 0A (Figure 6.3a).

The analysis of Case 11A suggests that a different pile base response is expected when changing the sand relative density (D_r) (Figure 6.3b). In contrast to the reference case, the hardening effect during lateral loading is more pronounced, and the allowable y_b is also higher (Figure 6.3b). To capture this hardening effect and reconstruct the 0D $F_b - y_b$ response, both power law and hyperbolic tangent functions were considered. Upon completing the analyses, the hyperbolic tangent function was chosen to reconstruct the $F_b - y_b$ response for Case 11A.

The hyperbolic tangent function used to construct the 0D $F_b - y_b$ model for Case 11A is derived by modifying the API [30] function, originally proposed for creating the $p - y$ model (Eq. 2.1). To adapt this formula (Eq. 2.1) for constructing the 0D F_b - y_b curve, it is modified as follows (Eq. 6.3):

$$F_b = AF_{b,ref} \tanh\left|\frac{kL}{AF_{b,ref}}.y_b\right| \tag{6.3}$$

In Equation 6.3, k represents the modulus of sub-grade reaction (kN/m^3), and A represents a constant.

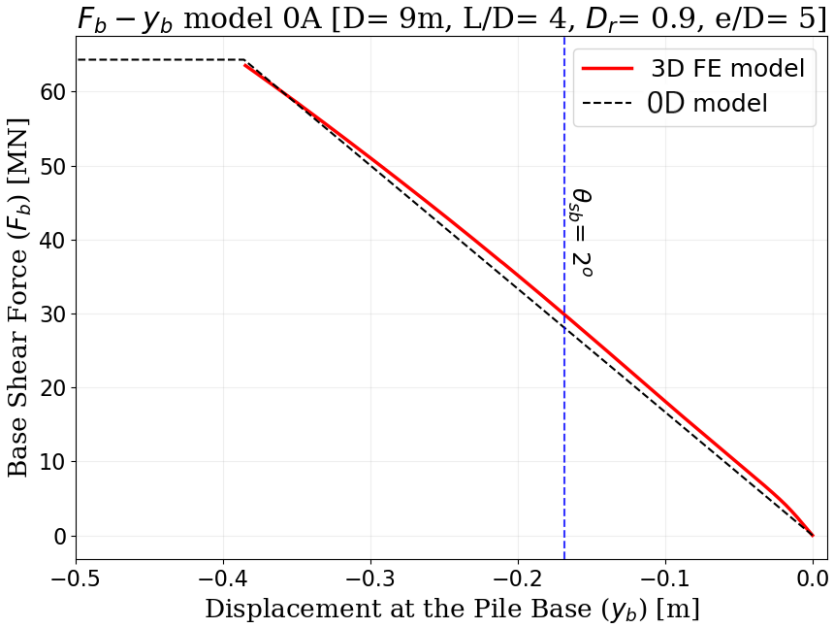

(a) $D = 9m, L/D = 4, e/D = 5, D_r = 0.9$

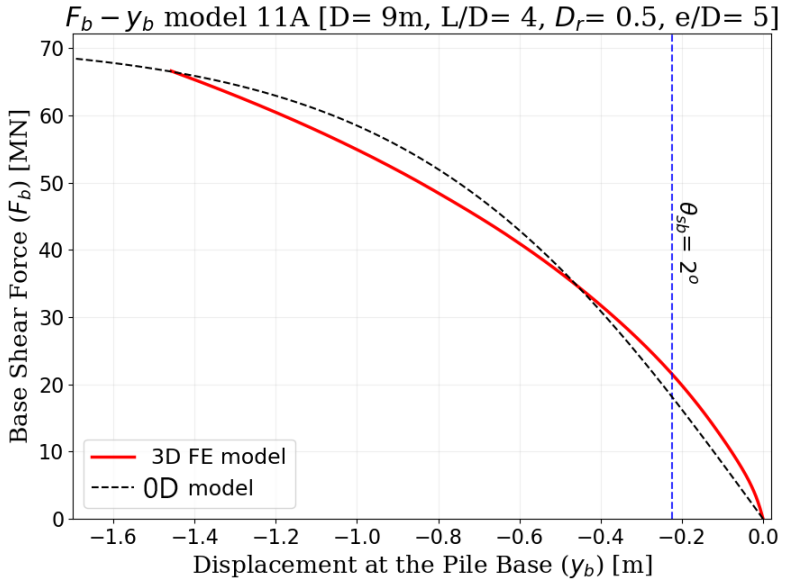

(b) $D = 9m, L/D = 4, e/D = 5, D_r = 0.5$

Figure 6.3: Comparison between F_b-y_b curve that obtained from 0D model with 3D FEM for (a) Reference Case (0A) and (b) Case 11A.

Ideally, the value of k for sand is a function of the friction angle (ϕ), and some recommended values can be found in [30]. However, in this analysis, the values of both A and k have been determined through a curve-fitting process involving the 0D model and 3D FE results. The curve-fitting process resulted in a value of k equal to $2.3MN/m^3$, with A being equal to 1.27. Subsequently, based on this function (Eq. 6.3) and the curve-fitting outcomes, the 0D F_b-y_b curve for Case 11A was established (Figure 6.3b).

Upon a thorough analysis (Figure 6.3), it becomes evident that at the ULS failure ($\theta_{sb} = 2^o$), the pile base is not necessarily at failure condition. Examining the $F_b - y_b$ response, it appears that the $F_b - y_b$ behavior up to the ULS failure can be approximated using a linear function (Figure 6.3), especially in the case of very dense sand. However, it is deemed insufficient to rely solely on a linear function to model the behavior until reaching the PTF capacity.

For dense sand, the $F_b - y_b$ response up to the defined PTF capacity can be effectively described using a bilinear function (Figure 6.3). The utilization of a bilinear function is considered to be more explicit when compared to a hyperbolic tangent function (Eq. 6.1). To reconstruct the 0D $F_b - y_b$ response, Equation 6.2 is employed.

The critical base displacement ($y_{b,cr}$) serves as a model parameter that may be influenced by pile geometry and relative density (D_r). Through an analysis of the ratio between y_b and D at ULS failure (Appendix B), it was determined that for very dense sand, the $y_{b,cr}$ value is suggested to be $0.04D$ or less. However, further investigation is required to comprehend the hardening behavior of medium sand.

Following Equation 6.2, additional curve-fitting procedures were conducted to reconstruct the 0D $F_b - y_b$ curve for the remaining cases (Appendix B). The process of reconstructing the 0D $F_b - y_b$ behavior is facilitated by setting the $y_{b,cr}$ value to $0.04D$. Therefore, the curve-fitting process was solely employed to determine suitable values for A. An overview of the values of A used in the fitting processes is presented in Table 6.2. Further investigation into the influences of D, L/D, e/D, and D_r on the values of A is deemed necessary in order to develop a more robust approach for constructing the 0D $F_b - y_b$ model.

Table 6.2: The values of A parameter that employed to reconstruct the 0D F_b-y_b model.

Case	A [-]	Case	A [-]
$D = 9m; L/D = 4; e/D = 5; D_r = 0.9$	0.87	$D = 9m; L/D = 4; e/D = 5; D_r = 0.5$	0.64
$D = 9m; L/D = 2; e/D = 5; D_r = 0.9$	1.00	$D = 12m; L/D = 1; e/D = 5; D_r = 0.9$	0.71
$D = 6m; L/D = 4; e/D = 5; D_r = 0.9$	1.43	$D = 9m; L/D = 1; e/D = 5; D_r = 0.9$	1.04
$D = 6m; L/D = 2; e/D = 5; D_r = 0.9$	1.50	$D = 6m; L/D = 1; e/D = 5; D_r = 0.9$	1.50
$D = 12m; L/D = 4; e/D = 5; D_r = 0.9$	0.61	$D = 9m; L/D = 4; e/D = 10; D_r = 0.9$	0.56
$D = 12m; L/D = 2; e/D = 5; D_r = 0.9$	0.70	$D = 9m; L/D = 4; e/D = 3; D_r = 0.9$	1.15
$D = 9m; L/D = 4; e/D = 15; D_r = 0.9$	0.41	$D = 9m; L/D = 4; e/D = 5; D_r = 0.7$	0.84

6.1.3. PISA curve

The Pile Soil Analysis (PISA) is one of few research projects that elaborate on the base moment, base shear force, and distribution moment contribution in addition to lateral soil reaction in the monopile equilibrium [93]. The initial PISA publication [93] proposed a 0D soil reaction model that included M_b, M_d, p, and F_b in the form of a load-displacement curve (Figure 6.4a). In subsequent PISA publications [19], [31], [94], [22], it was noted that the information required to recreate this curve was insufficient. Nevertheless, practical guidelines for offshore wind turbine (OWT) design concepts [95] have incorporated this curve (Figure 6.4a) into the design process.

The PISA curve (Figure 6.4a) is developed through a 0D (parameterized) approach to match the 3D FE response. In this curve (Figure 6.4a), these four components (distributed load, F_b, M_d, and M_b) are assumed to support the pile against displacement induced by the lateral load. Furthermore, the PISA curve assumes that the contributions of the base response components (F_b and M_b) to pile stability are relatively small when compared to the other two components (Figure 6.4a).

In Chapter 3, it was explained that, in this study, F_b is calculated based on the equilibrium principle (Eq. 3.11, Figure 3.8). The calculation process assumes that pile displacement due to lateral load is resisted by F_b and p only. Therefore, in terms of the load-displacement curve, only two components contribute namely F_b and Σp (Figure 6.4b).

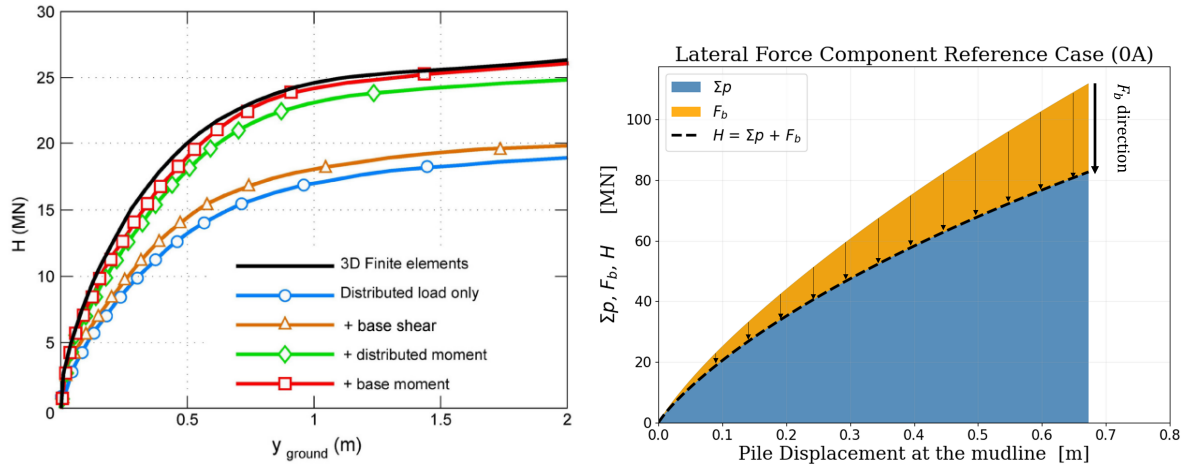

(a) PISA curve

(b) Reference case load curve

Figure 6.4: The load-displacement curve presented in terms of (a) PISA curve and (b) Lateral load components for reference case ($D = 9m, e/D = 5, L/D = 4, D_r = 0.9$).

The analysis of the direction and magnitude of F_b (Figure 4.15a and 4.31a) also differ from the

information that can be derived from the PISA curve (Figure 6.4). The findings suggest (Figure 4.15a and 4.31a) that F_b acts in the same direction as H. Additionally, the influence of F_b on lateral stability is larger compared to the conclusions drawn from the PISA method (Figure 6.4a).

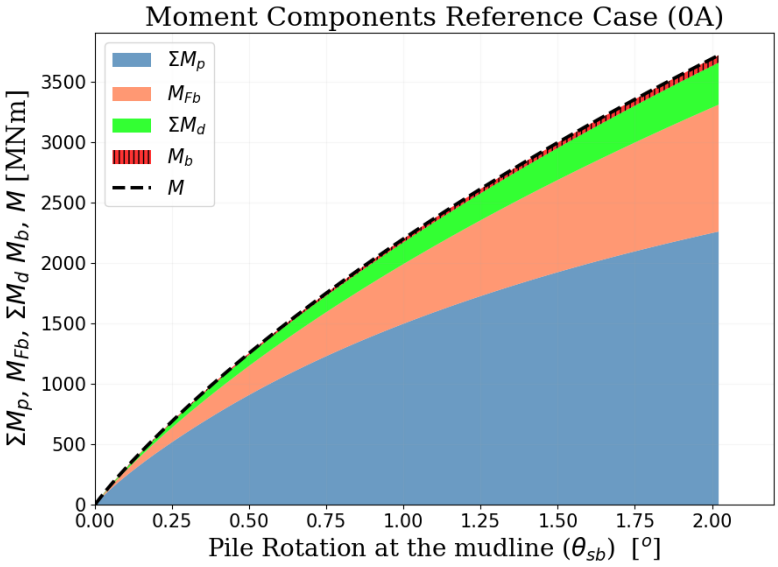

Figure 6.5: The moment-rotation curve presented with all moment components for the reference case ($D = 9m, e/D = 5, L/D = 4, D_r = 0.9$).

In this study, the calculation of M_b is also based on the equilibrium principle (Eq. 3.12). The calculation is conducted under the assumption that all soil reaction components (F_b, p, M_d, M_b) prevent the pile from rotating when a moment is applied. Consequently, a moment-rotation curve can be constructed with respect to the mudline (Figure 6.5).

Integrating all soil reaction components (F_b, M_d, p, M_b) into a load-displacement curve (Figure 6.4a), as performed by PISA, is considered to be less coherent. For example, attributing the role of preventing lateral pile movement to M_d (Figure 6.4a) is hard to describe. Therefore, it is recommended to combine all soil reaction components into a moment-rotation curve, following the example in Figure 6.5). To construct this curve (Figure 6.5), the F_b and p components can be transformed into moment components, as outlined in Equation 3.12 and 3.13.

6.2. Cyclic Load

Upon investigating the possibility of developing a 0D $F_b - y_b$ response under monotonic lateral loading, the research is extended to provide insights into constructing a 0D $F_b - y_b$ model under cyclic lateral loading. Examining the normalized $F_b - y_b$ curve for the reference case (Figure 6.6), it becomes evident that information regarding the evolution of the $F_b - y_b$ envelope during cyclic lateral loading is essential. This envelope should be able to capture the development of F_b and y_b as well as the ratcheting effect during cyclic loading. Furthermore, it is crucial to examine the increment in the accumulated displacement of the pile base ($\Delta y_b(N)$). Additionally, the investigation of the cyclic secant stiffness evolution under lateral loading is also conducted.

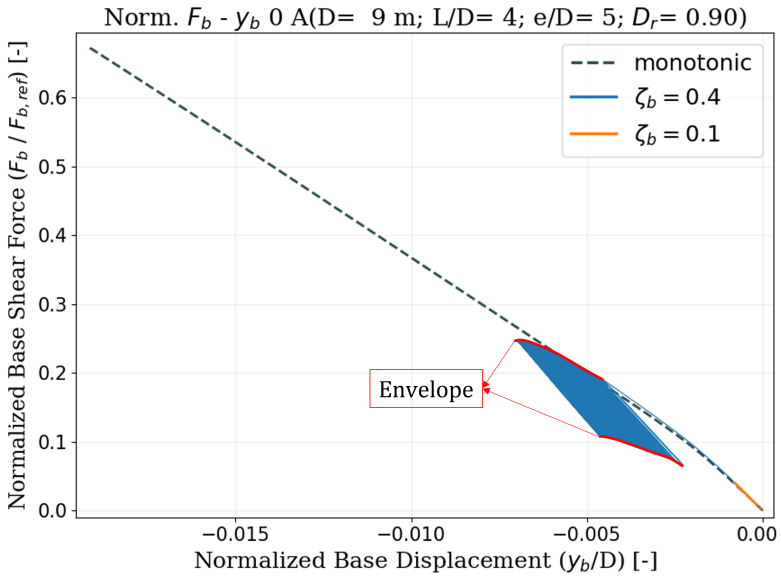

Figure 6.6: The normalized $F_b - y_b$ for the reference case ($D = 9m, e/D = 5, L/D = 4, D_r = 0.9$).

6.2.1. F_b Envelope

The F_b envelope is determined by normalizing the cyclic F_b response with their corresponding $F_{b,ref}$ values (Table 6.1). This normalization process takes the values of $F_{b,max}$ and $F_{b,min}$ to construct the F_b envelope. The F_b envelope for the reference case is presented in Figure 6.7. Examination of the normalized $F_{b,max}$ and $F_{b,min}$ values for two different load settings (Figure 6.7) reveals that the ζ_b parameters govern the evolution of the F_b envelope during the cyclic loading period.

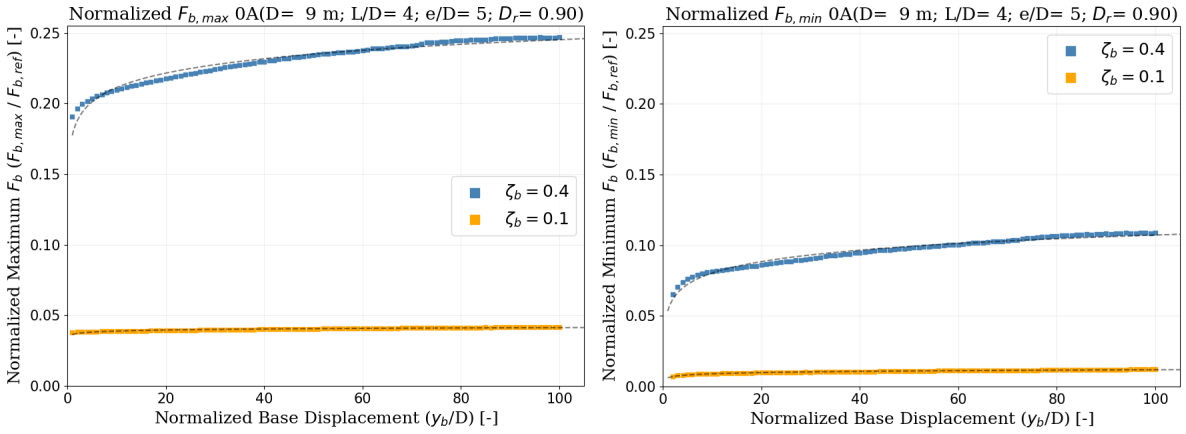

(a) Normalized $F_{b,max}$ **(b)** Normalized $F_{b,min}$

Figure 6.7: The F_b envelopes presented in term of normalized (a) $F_{b,max}$ and (b) $F_{b,min}$ against the $F_{b,ref}$ for the reference case ($D = 9m, e/D = 5, L/D = 4, D_r = 0.9$).

It is observed that, for the test with $\zeta_b = 0.4$, the ratio of $F_{b,max}$ relative to $F_{b,ref}$ continues to increase until cycle-80 before it reaches a terminal value (Figure 6.7a). A similar trend is observed for the $F_{b,min}$ ratio under the same ζ_b value (Figure 6.7b). Conversely, for the model with $\zeta_b = 0.1$, the increment in the $F_{b,max}$ and $F_{b,min}$ ratio is limited to cycle-20 (Figure 6.7). After this point, these ratio values generally remain constant. Since the parametric analysis of the absolute values of $F_{b,max}$ and $F_{b,min}$ was conducted in Chapter 5, the parametric analysis of the $F_{b,max}$ and $F_{b,min}$ ratios can be found in Appendix C. In addition, the analyses on the ratio between F_b, max over F_b, min are also provided in Appendix C.

6.2.2. Accumulated Displacement at Pile Base

The next component required to construct the envelope (Figure 6.6) is the information regarding the increment of base rotation accumulation ($\Delta y_b(N)$). The study on $\Delta y_b(N)$ is conducted using the same method employed to analyze displacement accumulation at the mudline (Figure 5.27, 5.28, 5.29, 5.36, and 5.39). The ratio of $\Delta y_b(N)/y_s$ is calculated by using the modified formula proposed by [37] (Eq. 4.6). The results of the $\Delta y_b(N)$ analyses for the reference case are provided in Figure 6.8.

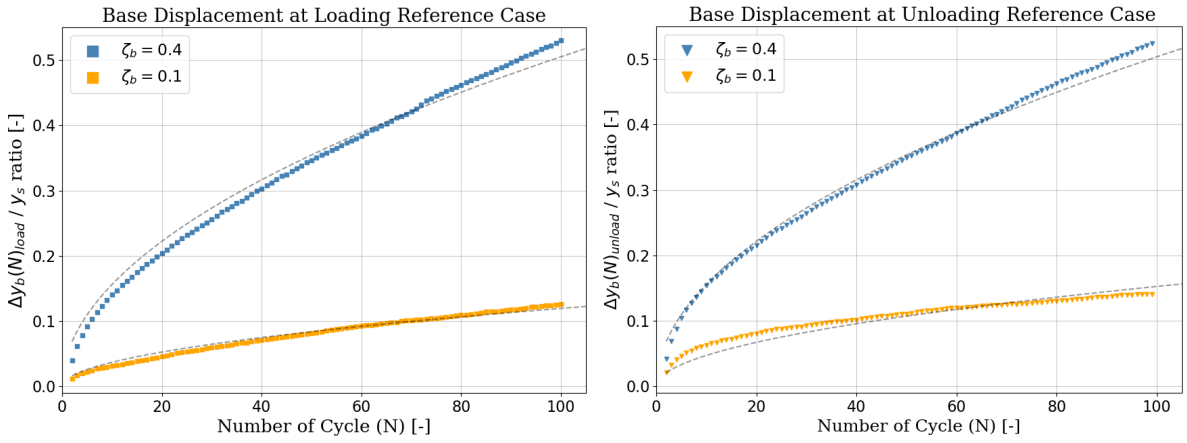

(a) Normalized $F_{b,max}$ **(b)** Normalized $F_{b,min}$

Figure 6.8: The increment of $\Delta y_b(N)$ by the number of cycle during the (a)H_{max} applied and (b)H_{min} applied for the reference case ($D = 9, L/D = 4, e/D = 5, D_r = 0.9$.

Observations on the reference case (Figure 6.8) indicate that the $\Delta y_b(N)/y_s$ ratio has not reached an asymptotic value even after 100 cyclic loading phases. This phenomenon is observed for both the loading (Figure 6.8a) and unloading (Figure 6.8a) phases. The value of ζ_b was found to only influence the magnitude of the ratio, as indicated by higher ζ_b values followed by higher $\Delta y_b(N)/y_s$ ratios. However, the $\Delta y_b(N)/y_s$ evolution trend is found to be the same for $\zeta_b = 0.4$ and $\zeta_b = 0.1$ (Figure 6.8).

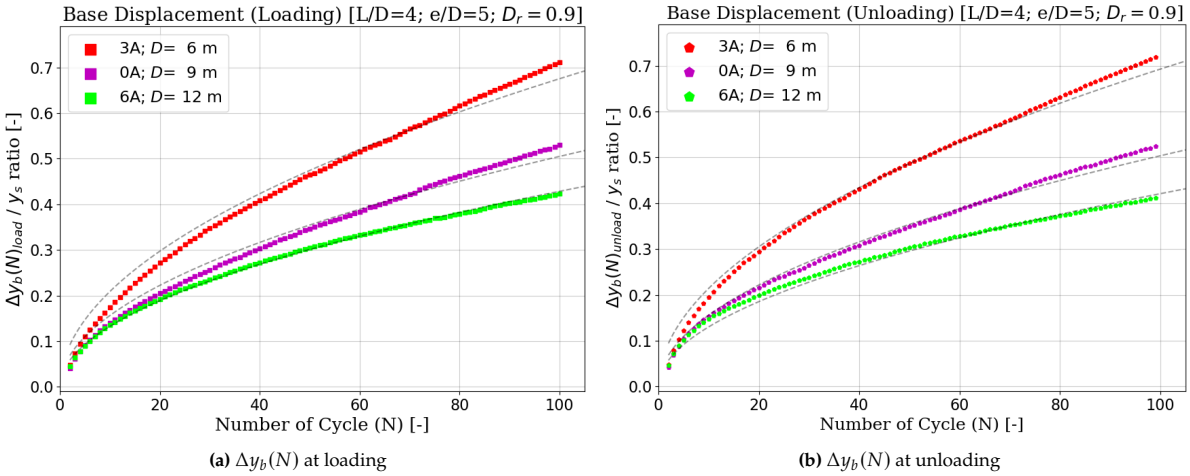

(a) $\Delta y_b(N)$ at loading **(b)** $\Delta y_b(N)$ at unloading

Figure 6.9: The effect of pile geometry (D and L) on $\Delta y_b(N)$ during cyclic load with $\zeta_b = 0.4$, presented during (a) loading phase and (b)unloading phase ($L/D = 4, e/D = 5, D_r = 0.9$).

In addition to the observations on the reference case, parametric analyses of the $\Delta y_b(N)/y_s$ ratio are also conducted. When analyzing the monopile with $L/D = 4$ (Figure 6.9), it becomes evident that increasing D results in a lower $\Delta y(N)$ over y_s ratio during both the loading (Figure 6.9a) and unloading phases (Figure 6.9b). Similar to previous analyses (Figure 5.27), the values of $\Delta y(N)/y_s$ during the

loading and unloading phases are found to be nearly identical. Therefore, for other L/D ratios, the $y_{acc,b}$ analyses are provided solely for the loading phase (Figure 6.10).

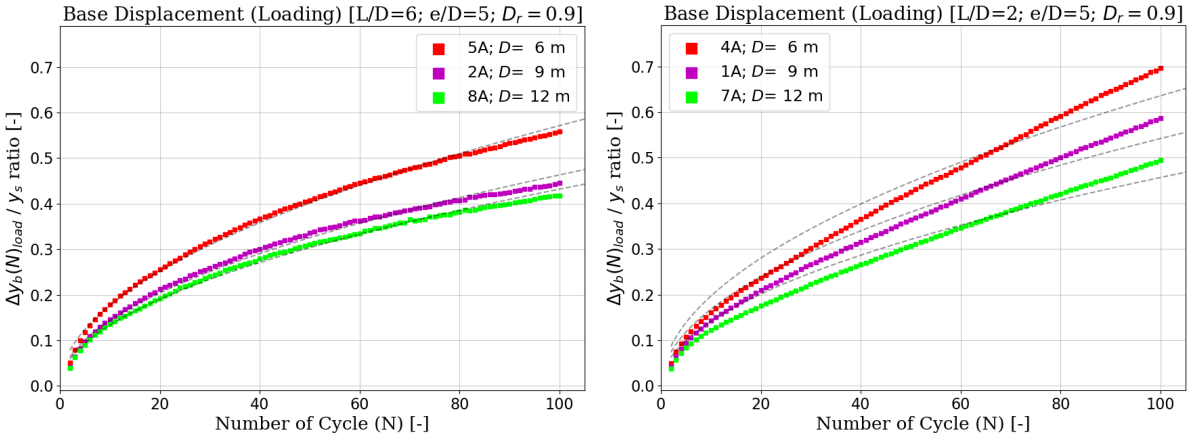

(a) $\Delta y_b(N)$ at loading $L/D = 6$

(b) y_{acc} at loading $L/D = 2$

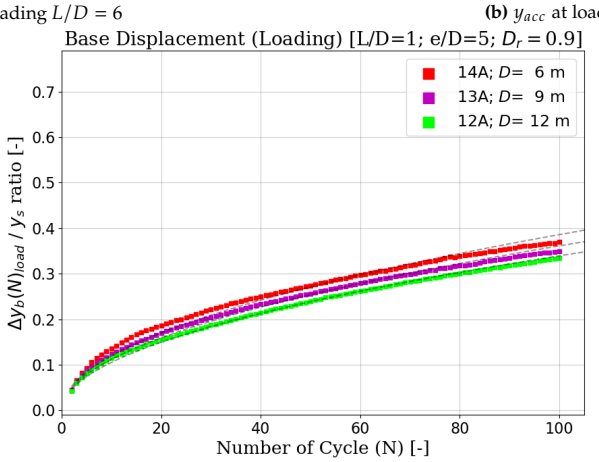

(c) y_{acc} at loading $L/D = 1$

Figure 6.10: The effect of pile geometry (D and L) on $\Delta y_b(N)$ during cyclic load with $\zeta_b = 0.4$, presented for monopile with (a) $L/D = 6$, (b) $L/D = 2$, and (c) $L/D = 1$ ($D_r = 0.9, e/D = 5$).

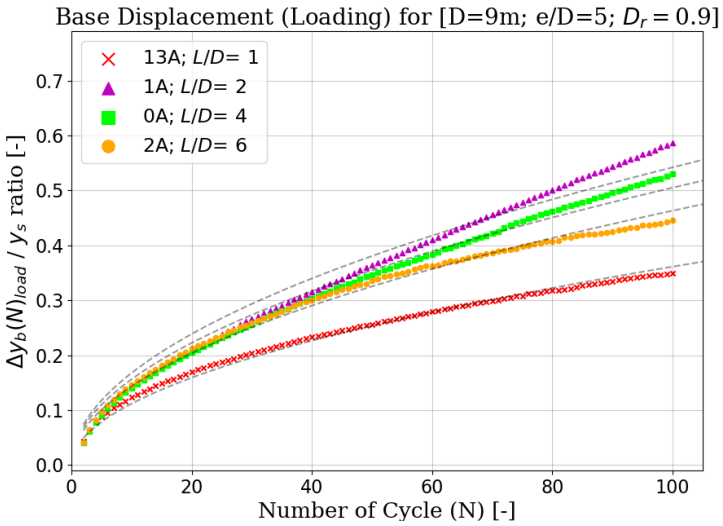

Figure 6.11: The effect of pile L/D on $\Delta y_b(N)$ during cyclic load with $\zeta_b = 0.4$, presented during (a)loading phase and (b)unloading phase ($D = 9m, e/D = 5, D_r = 0.9$).

Increasing the L/D ratio results in a lower increment of accumulated base rotation ($\Delta y(N)_b/y_s$) during both the loading and unloading phases (Figure 6.11). However, it is important to note a deviation from this trend for a rigid monopile with $L/D = 1$. Upon closer examination of the increments in $yacc, b$, it becomes evident that $\Delta y(N)_b/y_s$ values as a function of the number of cycles (N) can be represented by a power law function with the same variable, as mentioned in Chapter 5, (α) set to 0.51 for all cases.

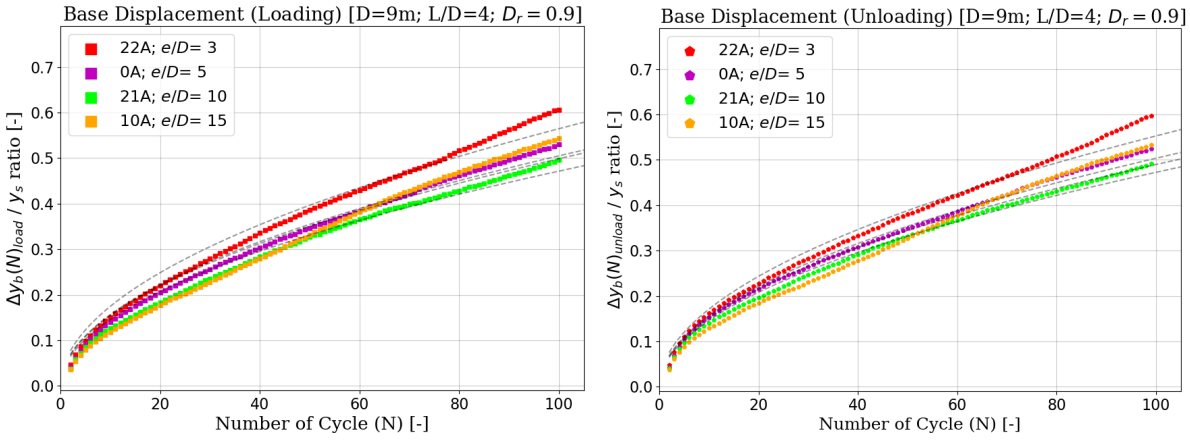

(a) $\Delta y_b(N)$ at loading **(b)** $\Delta y_b(N)$ at unloading

Figure 6.12: The effect of load eccentricity (e/D) on $\Delta y_b(N)$ during cyclic load with $\zeta_b = 0.4$, presented during (a) loading phase and (b)unloading phase ($D = 9m; L/D = 4, D_r = 0.9$).

The influence of e/D on the increment of $\Delta y_b(N)$ is depicted in Figure 6.12. A more detailed analysis of Figure 6.12 reveals that an increase in e/D leads to a lower ratio of $\Delta y(N)b$ over y_s during both loading (Figure 6.12a) and unloading (Figure 6.12b). The values of $\Delta y(N)b/y_s$ during the loading and unloading phases differ when changing ecc/D. Furthermore, continuous increases in the e/D ratio result in the saturation of the $\Delta y_b(N)$ over y_s ratio, a phenomenon also found in Figures 5.11 and 5.35.

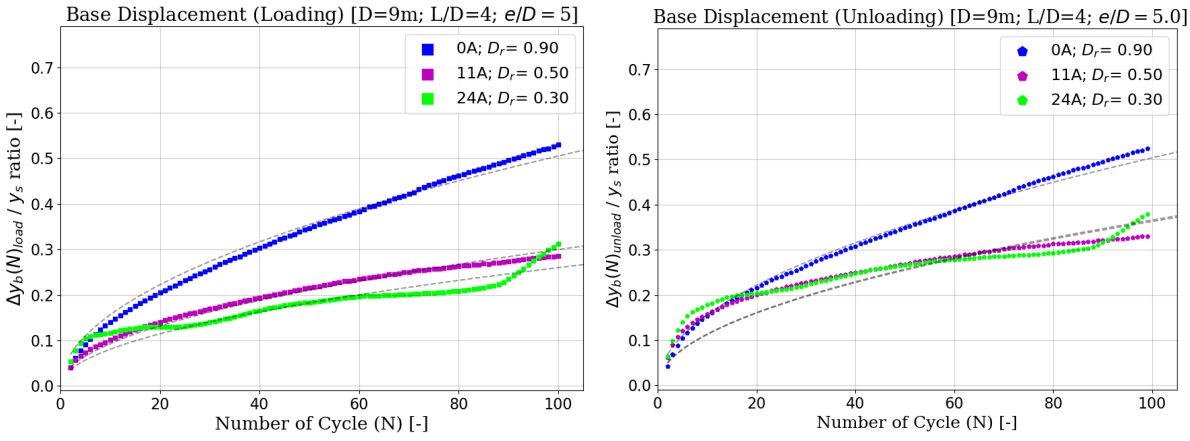

(a) $\Delta y_b(N)$ at loading **(b)** $\Delta y_b(N)$ at unloading

Figure 6.13: The effect of sand relative density (D_r) on $\Delta y_b(N)$ during cyclic load with $\zeta_b = 0.4$, presented during (a) loading phase and (b) unloading phase ($D = 9m; L/D = 4, e/D = 5$).

The influence of D_r on the increment of $\Delta y_b(N)$ is illustrated in Figure 6.13. An analysis depicted in Figure 6.13 reveals that reducing D_r leads to a lower ratio of $\Delta y(N)b$ over y_s during both loading (Figure 6.13a) and unloading (Figure 6.13b). Changes in D_r result in different $\Delta y_b(N)/y_s$ values during the loading and unloading phases. Deviations in the trend for the sand with $D_r = 0.3$ are possibly due to the relatively low D_r. Similar deviations are also observed in Figure 5.39). Additionally, the analyses

on the increment of $y_{acc,b}$ for the cyclic load with $\zeta_b = 0.1$ indicate that the same trend occurred over changing the investigated parameters (Appendix C).

6.2.3. Cyclic Secant Stiffness at Pile Base

In addition to investigating the $F_b - y_b$ envelope, it is also important to examine the stiffness response at the pile base during lateral cyclic loading. Understanding the evolution of stiffness can be crucial to verify the adequacy of the future 0D $F_b - y_b$ model in representing the pile base behavior. The stiffness evolution at the pile base is explored through the calculation of cyclic secant stiffness at the pile base ($K^{sec}_{cy,b}$). The process for calculating ($K^{sec}_{cy,b}$) is illustrated in Figure 6.14.

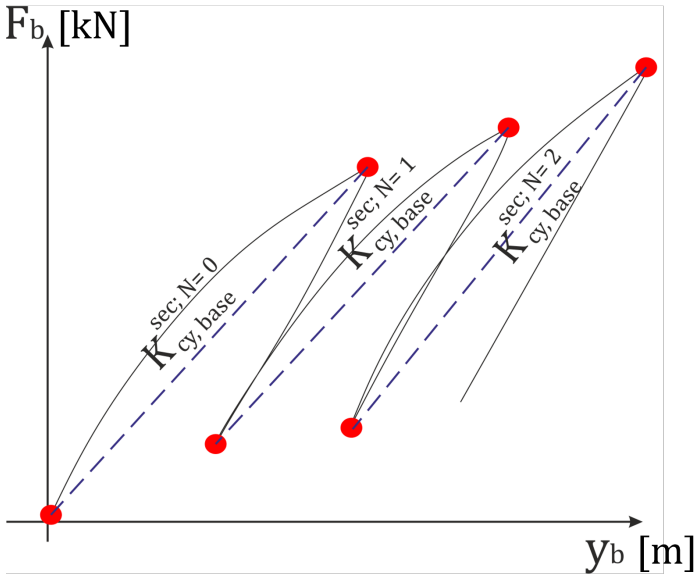

Figure 6.14: The figure to illustrate the $K^{sec}_{cy,b}$ calculation process.

The analysis of $K^{sec}_{cy,b}$ evolution for the reference case (Figure 6.15) indicates that the response of $K^{sec}_{cy,b}$ is governed by the number of cycles (N) and the ζ_b value. For higher H_{max} ($\zeta_b = 0.4$), the value of $K^{sec}_{cy,b}$ significantly increases until cycle-60. After this cycle, $K^{sec}_{cy,b}$ starts to approach a terminal value (Figure 6.15).

The analysis of the test with $\zeta_b = 0.1$ indicates that after 20 cycles, $K^{sec}_{cy,b}$ remains nearly stable until cycle-40 (Figure 6.15). After cycle 40, a softening behavior is observed, indicated by the degradation of $K^{sec}_{cy,b}$. Additionally, observations on y_b also indicate an acceleration of displacement accumulation, upon loading, after a certain number of cycles often occurred (Figure 6.6, Appendix C). Furthermore, the initial increase in $K^{sec}_{cy,b}$ at the second cycle is less than 10% of the $K^{sec}_{cy,b}$ at the first cycle (Figure 6.15).

The $K^{sec}_{cy,b}$ analysis is further extended to all semi-rigid monopiles with different ζ_b values (Figure 6.16). Only semi-rigid monopiles are considered, as for flexible piles, the contribution of F_b is less significant. Meanwhile, rigid monopiles, with K_r higher than 0.208 (Figure 5.24), are considered impractical. The analysis of the tests with $\zeta_b = 0.4$ (Figure 6.16a) indicates a significant increase in $K^{sec}_{cy,b}$ during the first 2 cycles. Afterward, $K^{sec}_{cy,b}$ continues to increase slightly until cycle 40, after which it remains constant and reaches a terminal value (Figure 6.16a).

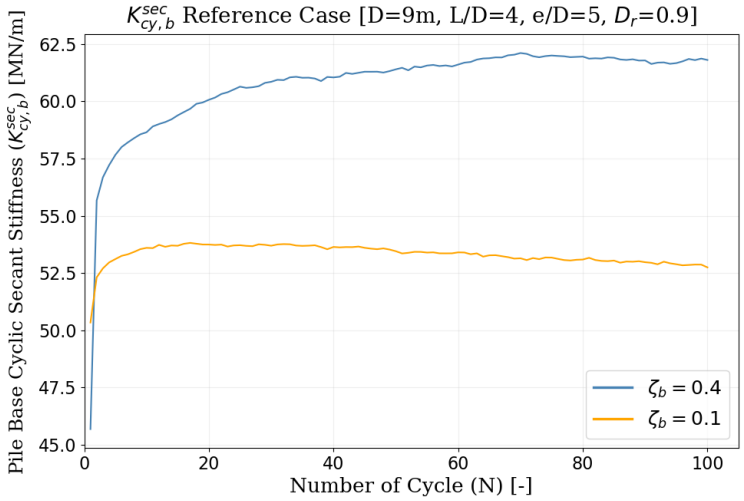

Figure 6.15: The result $K^{sec}_{cy,b}$ analysis for the reference case ($D = 9m, L/D = 4, e/D = 5, D_r = 0.9$).

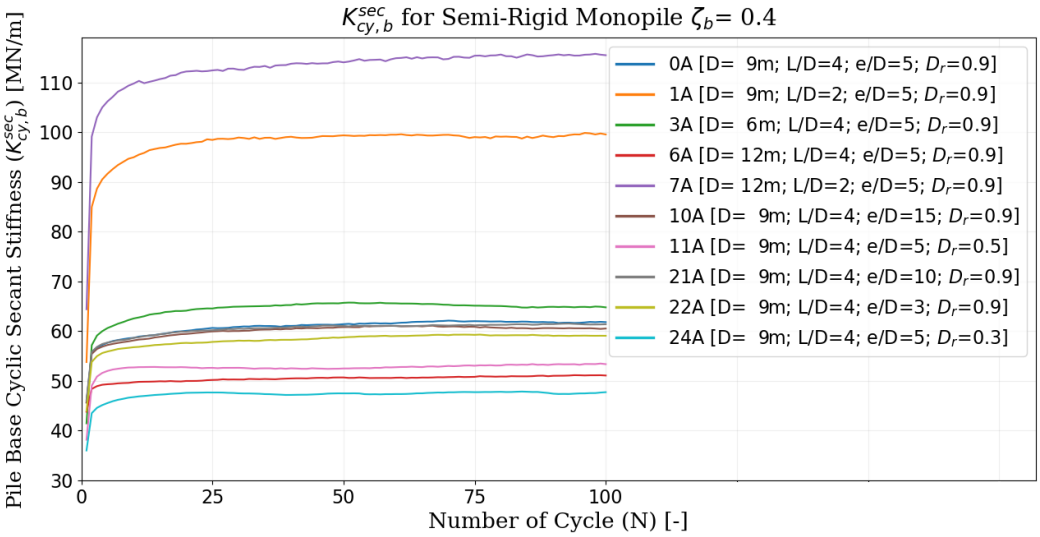

(a) $\zeta_b = 0.4$

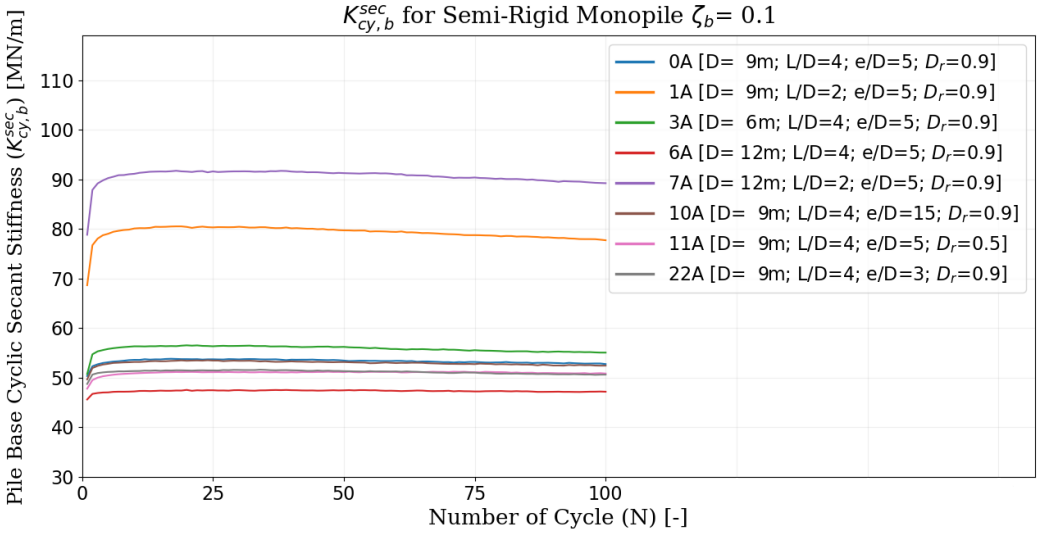

(b) $\zeta_b = 0.1$

Figure 6.16: he evolution of $K^{sec}_{cy,b}$ for semi-rigid monopile during the cyclic lateral loading with (a)$\zeta_b = 0.4$ and (b) $\zeta_b = 0.1$.

Subsequently, the analysis of semi-rigid monopile $K_{cy,b}^{sec}$ with $\zeta_b = 0.1$ is also provided in Figure 6.16b. This analysis indicates that the increase in $K_{cy,b}^{sec}$ during the first 2 cycles is lower compared to the test with $\zeta_b = 0.4$ (Figure 6.16a). The increase in $K_{cy,b}^{sec}$ during the first 2 cycles is known to be influenced by D and L. A higher D results in a larger increase in $K_{cy,b}^{sec}$, while a lower L leads to a higher increase in $K_{cy,b}^{sec}$. After the first 2 cycles, $K_{cy,b}^{sec}$ continues to slightly increase until it reaches a terminal value at cycle 20, remaining constant until cycle 40. Beyond 40 cycles, $K_{cy,b}^{sec}$ starts to diminish, indicating a softening behavior (Figure 6.16b).

7

Conclusions and Recommendations

7.1. Conclusion

The analyses have been done for monotonic and cyclic lateral loading and the conclusion of this study is summarized as follows:

1. The SANISAND-MS material model was effectively employed to simulate the accumulation of plastic strain resulting from lateral loading on large-diameter monopiles. This conclusion is based on a comparison of the results from the 3D FE analysis with the response obtained from the centrifuge test at 100 g.
2. The derivation of lateral soil reaction (p) from the model, relying on nodal stress (σ'_N, τ_2), resulted in p values that were sensitive to discretization size (Δ_z) (Appendix A). To reduce errors and mitigate this sensitivity effect, the total p (Σp) and total moment from p (ΣM_p) are computed using the trapezium integration method. Following this process, F_b and M_b values can be obtained using equilibrium principles.
3. The analysis of the distribution of p for the reference case suggests that the distribution of p along the monopile can be approximated using a simplified model (Figure 4.3). To build this simplified p model, four components are required: maximum p value (p_{max}), depth of maximum p value (z_{max}), rotational point (RP), and p at the pile base (p_{base}). This simplified model can also simplify the calculation of bending moments along the monopile.
4. The analysis of the $p - y$ response at the reference case indicates that a softening response is possible to occur at shallow depths. This response is also reflected by significant void ratio changes in the soil elements around the monopile at shallow depths.
5. The F_b component contributes significantly to the lateral balance equilibrium; therefore, the F_b spring must be included in the 0D soil reaction model. F_b is known to always act in the same direction as the applied load (H), and its magnitude increases progressively with increasing H.
6. Analysis of both monotonic and cyclic loading indicates that the contribution of M_b to the monopile moment balance is less significant. Thus, it is suggested to remove the base moment rotational spring from the 0D soil reaction model. The analysis of moment balance shows that ΣM_p decreases with increasing M, while other moment components (ΣM_d, M_b, M_{Fb}) progressively increase with

M. These four moment components act in the same direction to counteract M. Consequently, a more efficient 0D soil reaction model can be achieved by excluding the rotational spring at the pile base, which initially accounts for the M_b component (Figure 2.1c).

7. The cyclic lateral load analyses on the reference case indicate that:
   - After 100 cycles, the $\Delta\theta(N)/\theta_s$ and $\Delta y(N)/y_s$ ratios have not reached asymptotic values. This trend was observed for cyclic tests with $\zeta_b = 0.1$ and $\zeta_b = 0.4$.
   - The values of p, y, $\Delta\theta(N)/\theta_s$, $\Delta y(N)/y_s$, RP, $F_{b,max}$, and $F_{b,min}$ are higher with increased N and ζ_b.
   - The base response under cyclic loading shows higher values of F_b and Σp with increased N and ζ_b. For the moment component, ΣM_p is the only component that degrades with increased N.
8. The results of parametric studies are presented in Table 7.1 and 7.2.
9. The attempt to calculate $F_{b,ref}$ using the formula proposed by [37], with some modification, indicates that this formula does not consider the evolution of σ_{zz} during lateral loading. The stress recording process at the pile indicates that σ_{zz} at the pile base varies and evolves during lateral loading (Figure 6.2).
10. Constructing a 0D $F_b - y_b$ model must account for the soil D_r and L. Dense sand typically adheres to a bilinear function in their $F_b - y_b$ relationship, with limited evidence of hardening effects. Conversely, medium sand exhibits an apparent hardening response in the $F_b - y_b$ relationship. Additionally, a larger y_b is allowed for medium-dense sand compared to dense sand.
11. In contrast with the PISA curve ([93]), this study presents only F_b and p components in a load-displacement curve (Figure 6.4). It is considered more appropriate to present all components (M_b, ΣM_d, ΣM_p, M_{Fb} in a moment-rotation curve (Figure 6.5).
12. The analysis of the F_b envelope, which can be utilized for developing a 0D $F_b - y_b$ model, reveals that the ratio of $F_{b,max}$ and $F_{b,min}$ concerning $F_{b,ref}$ reaches a terminal value after 80 cycles for the test with $\zeta_b = 0.4$. In contrast, for the test with $\zeta_b = 0.1$, the terminal value is reached after 20 cycles. It is also observed that the ratio of $\Delta y_b(N)/y_s$ has not yet reached a terminal value even after 100 cycles for both the loading and unloading phases.
13. The development of a 0D $F_b - y_b$ model must also take into account the stiffness of the base response. The behavior of $K^{sec}_{cy,b}$ indicates that both the hardening and softening responses of the pile base are influenced by the number of cycles (N) and the ζ_b. Additionally, during the first 2 cycles, the behavior of $K^{sec}_{cy,b}$ is primarily governed by the pile diameter (D) and length (L).
14. In the case of very dense sand ($D_r = 0.9$), the behavior of the $F_b - y_b$ response under cyclic loading is primarily influenced by the ratcheting effect, with the hardening effect possibly being considered negligible. Conversely, for dense and medium sands, both the hardening and ratcheting effects need to be taken into consideration when developing the 0D $F_b - y_b$ model.

Table 7.1: The summary of the parametric analyses.

Parameter	Modification	H_{ult}	M_{ult}	$y_{sb,u}$	$F_{b,u}$	$M_{b,u}$	$p_{max}.L/H_{ult}$	z_{max}/L	$p_{base}.L/H_{ult}$
D	⇑	⇑	⇑	⇑	⇓	⇓	⇓	⇓	⇓
L/D	⇑	⇑	⇑	⇑[a]	⇓	⇓	⇓	⇓	⇓
e/D	⇑	⇓	⇑	⇓	⇑	⇓	⇑	⇓	⇑
D_r	⇓	⇓	⇓	⇑	⇑	⇑	⇓	⇑	⇑

⇑= increase, ⇓ = decrease, ^{a} = only for rigid and semi-rigid cases.

Table 7.2: The continous summary of the parametric analyses.

Parameter	Modification	RP/L	$\Delta\theta(N)/\Delta\theta_s$	$\Delta y(N)/\Delta y_s$	$F_{b,max}$	$F_{b,min}$	$\Delta y_b(N)/\Delta_{s,b}$
D	⇑	⇓	⇓	⇓	⇑^{a}	⇑^{a}	⇓
L/D	⇑	⇓	⇓^{b}	⇓^{b}	⇑^{c}	⇑^{c}	⇓^{b}
e/D	⇑	⇓	⇓	⇓	⇓	⇓	⇓
D_r	⇓	⇑	⇓	⇓	⇓	⇓	⇓

⇑= increase, ⇓ = decrease, ^{a} = only for rigid and semi-rigid cases, ^{b} = only for semi-rigid and flexible cases, ^{c} = only for semi-rigid cases .

7.2. Reccomendation

Some aspects of this project, require further investigation. To guide further investigations to be aligned with the objective and motivation of this research, recommendations are provided in this section.

1. In the current project, an attempt to create a 0D F_b-y_{base} model for monotonic lateral loading (Figure 6.3) has been made. However, it is necessary to conduct a more comprehensive study to find a function that can accurately depict the effect of the investigated parameters on the $F_b - y_b$ response. While a bi-linear function is proposed to capture the $F_b - y_b$ response for very dense sand in this project, a more holistic function is required to represent the hardening response observed in medium and dense sands.
2. A study to understand the ratcheting effect of the $F_b - y_b$ response is essential, especially if a 0D $F_b - y_b$ model for cyclic lateral loading is going to be constructed. Additionally, investigating the evolution of pile base stiffness during cyclic loading is necessary.
3. The base shear force and base moment values obtained in this study are based on 3D FEM simulations. To validate these results, further research involving physical modeling in a centrifuge or pile dynamic tests is recommended.
4. The calculations and models in this study were conducted on homogeneous sand and only focused on 1-way cyclic lateral loading. To further evaluate the results, additional analyses should be performed on non-homogeneous sand, where stiffness varies with depth. Moreover, investigating the response under symmetric cyclic loading is necessary. An example of the stiffness response under two-way cyclic loading is provided in Appendix C.
5. In this study, the value of the distributed moment is extracted from the 3D FE analysis, and the parametric studies do not include the M_d component. A study focusing on the distributed moment and the rotation response of pile elements is required to develop a complete 0D soil reaction model for large-diameter monopiles.

References

[1] D.-G. for Communication European Comission. "Delivering the european green deal." (2023), [Online]. Available: https://commission.europa.eu/strategy-and-policy/priorities-2019-2024/european-green-deal/delivering-european-green-deal_en (visited on 07/20/2023).

[2] C. Mario, "New directions of technologies pointing the way to a sustainable global society," *Sustainable Futures*, vol. 5, 2023. DOI: 10.1016/j.sftr.2023.100114.

[3] A. Peinado Gonzalo, T. Benmessaoud, M. Entezami, and F. P. García Márquez, "Optimal maintenance management of offshore wind turbines by minimizing the costs," *Sustainable Energy Technologies and Assessments*, vol. 52, 2022. DOI: https://doi.org/10.1016/j.seta.2022.102230.

[4] D. Saygin, R. Kempener, N. Wagner, M. Ayuso, and D. Gielen, "The implications for renewable energy innovation of doubling the share of renewables in the global energy mix between 2010 and 2030," *Energies*, vol. 9, pp. 5828–5865, 2015. DOI: https://doi.org/10.3390/en8065828.

[5] A. Arvesen and E. G. Hertwich, "Assessing the life cycle environmental impacts of wind power: A review of present knowledge and research needs," *Renewable and Sustainable Energy Reviews*, vol. 16, no. 8, pp. 5994–6006, 2012. DOI: 10.1016/j.rser.2012.06.023.

[6] M. I. Blanco, "The economics of wind energy," *Renewable and Sustainable Energy Reviews*, vol. 13, no. 6, pp. 1372–1382, 2009. DOI: https://doi.org/10.1016/j.rser.2008.09.004.

[7] GWEC, "Global offshore wind report 2022," Global Wind Energy Council, 2022.

[8] K. Gavin, D. Igoe, and P. Doherty, "Piles for offshore wind turbines: A state-of-the-art review," *Geotechnical Engineering*, vol. 164, pp. 245–256, GE4 2011. DOI: https://doi.org/10.1680/geng.2011.164.4.245.

[9] B. Byrne, "Foundation design for offshore wind turbines," *Géotechnique Lecture 2011*, 2011. [Online]. Available: https://eng.ox.ac.uk/media/9490/geotechnique_lecture_bwb_2011_web.pdf.

[10] T. Stehly and P. Duffy, "2020 cost of wind energy review," National Renewable Energy Laboratory, 2021. [Online]. Available: https://www.nrel.gov/docs/fy22osti/81209.pdf.

[11] W. Musial, P. Spitsen, P. Duffy, *et al.*, "Offshore wind market report: 2022 edition," U.S. Department of Energy, 2022.

[12] A. Myhr, C. Bjerkseter, A. Ågotnes, and T. A. Nygaard, "Levelised cost of energy for offshore floating wind turbines in a life cycle perspective," *Renewable Energy*, vol. 66, pp. 714–728, 2014. DOI: http://dx.doi.org/10.1016/j.renene.2014.01.017.

[13] E. Kementzetzidis, "Cyclic behaviour of laterally loaded (mono)piles in sand with emphasis on pile driving effecrts," PhD dissertation, Delft University of Technology, 2023.

[14] J. Song and M. Achmus, "Cyclic overlay model of p–y curves for laterally loaded monopiles in cohesionless soil," *Wind Energy Science*, vol. 8, pp. 327–339, 2023. DOI: https://doi.org/10.1680/geng.2011.164.4.245.

[15] DNVGL, "Dnvgl-st-0126 – support structure for wind turbines," Oslo: Det Norske Veritas, 2016.

[16] C. Golightly, "Tilting of monopiles long, heavy and stiff; pushed beyond their limit," *GROUND ENGINEERING*, pp. 20–23, Jan. 2014. [Online]. Available: https://cdn.ca.emap.com/wp-content/uploads/sites/9/2013/12/GE-January-2014-Tilting-of-monopiles-Golightly.pdf.

[17] E. Winkler, *Die Lehre von Elastizitat und Festigkeit (on Elasticity and Fixity)*. Dominicus, Prague, 1867.

[18] API, "*RP*2*A* − *WSD* - recommended practice for planning, designing, and constructing fixed offshore platforms," Washington: American Petroleum Institute, 2010.

[19] B. Byrne, R. McAdam, H. Burd, *et al.*, "Pisa: New design methods for offshore wind turbine monopiles," *Proceedings of the 8th International Conference Offshore Site Investigation AND Geotechnics*, pp. 142–161, 2017.

[20] E. Kementzetzidis, F. Pisanò, and A. V. Metrikine, "A memory-enhanced p-y model for piles in sand accounting for cyclic ratcheting and gapping effects," *Computers and Geotechnics*, vol. 148, 2022. DOI: 10.1016/j.compgeo.2022.104810.

[21] N. Gerolymos and G. Gazetas, "Development of winkler model for static and dynamic response of caisson foundations with soil and interface nonlinearities," *Soil Dynamics and Earthquake Engineering*, vol. 26, pp. 363–376, 2006. DOI: 10.1016/j.soildyn.2005.12.002.

[22] B. Byrne, A. Aghakouchak, R. Buckley, *et al.*, "Picaso: Cyclic lateral loading of offshore wind turbine monopiles," *Frontiers in Offshore Geotechnics IV: Proceedings of the 4th International Symposium on Frontiers in Offshore Geotechnics*, 2020.

[23] F. Pisanò, A. Askarinejad, H. Wang, S. Maghsoodi, K. Gavin, and M. Segeren, "Midas: Monopile improved design through advanced cyclic soil modelling," *Proceedings of the 20th International Conference on Soil Mechanics and Geotechnical Engineering*, pp. 2677–2682, 2022.

[24] H. Liu, J. A. Abell, A. Diambra, and F. Pisanò, "Modelling the cyclic ratcheting of sands through memory-enhanced bounding surface plasticity," *Géotechnique*, vol. 69, pp. 783–800, 2019. DOI: 10.1680/jgeot.17.P.307.

[25] Adnan Memija. "Deme installs xxl monopiles at arcadis ost 1." (2022), [Online]. Available: https://www.offshorewind.biz/2022/07/26/deme-installs-xxl-monopiles-at-arcadis-ost-1/ (visited on 07/26/2022).

[26] API, "Api recommended practice 2a-wsd planning, designing, and constructing fixed offshore platforms—load and resistance factor design," Washington: American Petroleum Institute, 2001.

[27] K. Abdel-Rahman and M. Achmus, "Finite element modelling of horizontally loaded monopile foundations for offshore wind energy converters in germany," *Frontiers in Offshore Geotechnics, ISFOG 2005 - Proceedings of the 1st International Symposium on Frontiers in Offshore Geotechnics*, pp. 391–396, 2005.

[28] D. Kallehave, C. L. Thilsted, and M. Liingaard, "Modification of the api p-y formulation of initial stiffness of sand," *Proceedings of the 7th International Conference Offshore Site Investigation and Geotechnics*, pp. 465–472, 2012. [Online]. Available: https://admin.onepetro.org/SUTOSIG/proceedings/OSIG12/All-OSIG12/SUT-OSIG-12-50/3358.

[29] DNVGL, "Dnv-os-j101 – offshore standard: Design of offshore wind turbine structures," Hellerup, Denmark: Det Norske Veritas, 2004.

[30] API, "*RP*2 – *GEO* - geotechnical and foundation design considerations," Washington: American Petroleum Institute, 2011.

[31] H. J. Burd, W. J. A. P. Beuckelaers, B. W. Byrne, *et al.*, "New data analysis methods for instrumented medium-scale monopile field tests," *Géotechnique*, vol. 70, no. 11, pp. 961–969, 2020. DOI: 10.1680/jgeot.18.PISA.002.

[32] C. N. Abadie, B. Byrne, and S. Levy-Paing, "Model pile response to multi-amplitude cyclic lateral loading in cohesionless soils," *Frontiers in Offshore Geotechnics III*, pp. 681–686, 2015. DOI: 10.1201/b18442-92.

[33] H. G. Poulos and T. Hull, *Role of analytical geomechanics in foundation engineering*. ASCE2, 1989.

[34] D. Kallehave, B. W. Byrne, C. LeBlanc Thilsted, and K. K. Mikkelsen, "Optimization of monopiles for offshore wind turbines," *Philosophical Transactions of the Royal Society of London Series A*, vol. 373, no. 2035, pp. 20 140 100–20 140 100, Jan. 2015. DOI: 10.1098/rsta.2014.0100.

[35] L. Arany, S. Bhattacharya, J. Macdonald, and S. Hogan, "Design of monopiles for offshore wind turbines in 10 steps," *Soil Dynamics and Earthquake Engineering*, vol. 92, pp. 126–152, 2017. DOI: https://doi.org/10.1016/j.soildyn.2016.09.024.

[36] H. P. Jostad, H. Liu, N. Sivasithamparam, and R. Ragni, "Cyclic capacity of monopiles in sand under partially drained conditions: A numerical approach," *Journal of Geotechnical and Geoenvironmental Engineering*, vol. 149, pp. 04022129-1 - 04022129–12, 2 2023. DOI: 10.1061/JGGEFK.GTENG-10435.

[37] C. Leblanc, G. Houlsby, and B. Byrne, "Response of stiff piles in sand to long-term cyclic lateral loading," *Géotechnique*, vol. 60, no. 2, pp. 79–90, 2010. DOI: 10.1680/geot.7.00196.

[38] P. Truong, B. M. Lehane, V. Zania, and R. T. Klinkvort, "Empirical approach based on centrifuge testing for cyclic deformations of laterally loaded piles in sand," *Géotechnique*, vol. 69, no. 2, pp. 133–145, 2019. DOI: 10.1680/jgeot.17.P.203.

[39] L. Reese and W. Van Impe, "Single piles and pile groups under lateral loading," *Applied Mechanics Reviews*, vol. 55, no. 1, B9–B10, Jan. 2002. DOI: 10.1115/1.1445326. [Online]. Available: https://doi.org/10.1115/1.1445326.

[40] W. Fuentes, M. Gil, and G. Rivillas, "A p–y model for large diameter monopiles in sands subjected to lateral loading under static and long-term cyclic conditions," *Journal of Geotechnical and Geoenvironmental Engineering*, vol. 147, no. 2, p. 04 020 164, 2021. DOI: 10.1061/(ASCE)GT.1943-5606.0002448.

[41] W. Li, B. Zhu, and M. Yang, "Static response of monopile to lateral load in overconsolidated dense sand," *Journal of Geotechnical and Geoenvironmental Engineering*, vol. 143, no. 7, p. 04 017 026, 2017. DOI: 10.1061/(ASCE)GT.1943-5606.0001698.

[42] P. Liu, C. Jiang, M. Lin, L. Chen, and J. He, "Nonlinear analysis of laterally loaded rigid piles at the crest of clay slopes," *Computers and Geotechnics*, vol. 126, 103715(1–11), 2020. DOI: https://doi.org/10.1016/j.compgeo.2020.103715. [Online]. Available: https://www.sciencedirect.com/science/article/pii/S0266352X20302780.

[43] C. Vallahban and F. Alikhanlou, "Short rigid piles in clay," *Journal of Geotechnical Engineering*, vol. 108, no. 10, pp. 1255–1271, 1982.

[44] L. Zhang and S. Ahmari, "Nonlinear analysis of laterally loaded rigid piles in cohesive soil," *International Journal for Numerical and Analytical Methods in Geomechanics*, vol. 37, no. 2, pp. 201–220, 2013. DOI: https://doi.org/10.1002/nag.1094.

[45] L. Wang, Y. Lai, Y. Hong, and D. Mašín, "A unified lateral soil reaction model for monopiles in soft clay considering various length-to-diameter (l/d) ratios," *Ocean Engineering*, vol. 212, p. 107 492, 2020. DOI: https://doi.org/10.1016/j.oceaneng.2020.107492.

[46] Y. Lai, L. Wang, Y. Hong, and B. He, "Centrifuge modeling of the cyclic lateral behavior of large-diameter monopiles in soft clay: Effects of episodic cycling and reconsolidation," *Ocean Engineering*, vol. 200, p. 107 048, 2020. DOI: https://doi.org/10.1016/j.oceaneng.2020.107048.

[47] X. Wan, J. P. Doherty, and M. F. Randolph, "Relationships between lateral and rotational load transfer stiffnesses and soil modulus for the elastic response of monopiles," *Computers and Geotechnics*, vol. 137, p. 104 256, 2021. DOI: https://doi.org/10.1016/j.compgeo.2021.104256.

[48] M. E. Kalinski, *Soil Mechanics Lab Manual*, 2nd ed. Washington DC, USA: Wiley, 2011.

[49] S. Lo, M. M. Rahman, and D. Bobei, "Limited flow characteristics of sand with fines under cyclic loading," *Geomechanics and Geoengineering: An International Journal*, vol. 5, no. 1, pp. 15–25, 2010.

[50] M. D. Bolton, "The strength and dilatancy of sands," *Géotechnique*, vol. 36, no. 1, pp. 65–78, 1986. DOI: 10.1680/geot.1986.36.1.65.

[51] A. Bishop, "Shear strength parameters for undisturbed and remoulded soils specimens," *In Stress-strain behaviour of soils*, vol. 9, pp. 3–58, 1972. DOI: (ed.R.H.G.Parry).London:Foulis.

[52] A. S. Vesić and G. W. Clough, "Behavior of granular materials under high stresses," *Journal of the Soil Mechanics and Foundations Division*, vol. 94, pp. 661–688, 1968. [Online]. Available: https://api.semanticscholar.org/CorpusID:126695930.

[53] Z. Yang, A. Elgamal, and E. Parra, "Computational model for cyclic mobility and associated shear deformation," *Journal of Geotechnical and Geoenvironmental Engineering*, vol. 129, no. 12, pp. 1119–1127, 2003. DOI: 10.1061/(ASCE)1090-0241(2003)129:12(1119).

[54] D. Wijewickreme, M. V. Sanin, and G. R. Greenaway, "Cyclic shear response of fine-grained mine tailings," *Canadian Geotechnical Journal*, vol. 42, no. 5, pp. 1408–1421, 2005. DOI: 10.1139/t05-058.

[55] X. Li, "A sand model with state-dependent dilatancy," *Geotechnique*, vol. 52, no. 3, pp. 173–186, 2002. DOI: 10.1680/geot.2002.52.3.173.

[56] Y. P. Vaid and S. Sivathayalan, "Fundamental factors affecting liquefaction susceptibility of sands," *Canadian Geotechnical Journal*, vol. 37, no. 3, pp. 592–606, 2000. DOI: 10.1139/t00-040.

[57] T. Wichtmann, A. Niemunis, and T. Triantafyllidis, "Strain accumulation in sand due to cyclic loading: Drained triaxial tests," *Soil Dynamics and Earthquake Engineering*, vol. 25, no. 12, pp. 967–979, 2005. DOI: https://doi.org/10.1016/j.soildyn.2005.02.022.

[58] M. Madhira and V. K. Kota, "A novel method to predict shaft and base responses of a pile from cyclic pile load test results," *Indian Geotechnical Journal*, 2023. DOI: 10.1007/s40098-023-00753-0. [Online]. Available: https://www.scopus.com/inward/record.uri?eid=2-s2.0-85164119717&doi=10.1007%2fs40098-023-00753-0&partnerID=40&md5=8334bf347e74e2c0396b9b7d72ab9122.

[59] H.-y. Liu and A. M. Kaynia, "Monopile responses to monotonic and cyclic loading in undrained sand using 3d fe with sanisand-msu," *Water Science and Engineering*, vol. 15, no. 1, pp. 69–77, 2022. DOI: https://doi.org/10.1016/j.wse.2021.12.001. [Online]. Available: https://www.sciencedirect.com/science/article/pii/S1674237021001186.

[60] H. Liu, F. Pisanò, H. P. Jostad, and N. Sivasithamparam, "Impact of cyclic strain accumulation on the tilting behaviour of monopiles in sand: An assessment of the miner's rule based on sanisand-ms 3d fe modelling," *Ocean Engineering*, vol. 250, p. 110 579, 2022. DOI: https://doi.org/10.1016/j.oceaneng.2022.110579.

[61] I. A. Richards, M. F. Bransby, B. W. Byrne, C. Gaudin, and G. T. Houlsby, "Effect of stress level on response of model monopile to cyclic lateral loading in sand," *Journal of Geotechnical and Geoenvironmental Engineering*, vol. 147, no. 3, p. 04 021 002, 2021. DOI: 10.1061/(ASCE)GT.1943-5606.0002447.

[62] I. A. Richards, "Monopile foundations under complex cyclic lateral loading," PhD dissertation, St. Peter's College, University of Oxford, 2019.

[63] A. Niemunis, T. Wichtmann, and T. Triantafyllidis, "A high-cycle accumulation model for sand," *Computers and Geotechnics*, vol. 32, no. 4, pp. 245–263, 2005. DOI: https://doi.org/10.1016/j.compgeo.2005.03.002. [Online]. Available: https://www.sciencedirect.com/science/article/pii/S0266352X05000534.

[64] K. H. Andersen and K. Høeg, "Deformations of soils and displacements of structures subjected to combined static and cyclic loads," *Publikasjon-Norges Geotekniske Institutt*, vol. 185, 1992.

[65] K. H. Andersen, R. Dyvik, K. Schrøder, O. E. Hansteen, and S. Bysveen, "Field tests of anchors in clay ii: Predictions and interpretation," *Journal of Geotechnical Engineering*, vol. 119, no. 10, pp. 1532–1549, 1993. DOI: 10.1061/(ASCE)0733-9410(1993)119:10(1532).

[66] I. CH001.tex, K. H. Andersen, and I. M. Lecturer, "The third issmge mcclelland lecture," 2015. [Online]. Available: https://api.semanticscholar.org/CorpusID:172131652.

[67] H. P. Jostad, G. Grimstad, K. H. Andersen, M. Saue, Y. Shin, and D. woo You, "A fe procedure for foundation design of offshore structures – applied to study a potential owt monopile foundation in the korean western sea," 2014. [Online]. Available: https://api.semanticscholar.org/CorpusID:22124046.

[68] H. P. Jostad, G. Grimstad, K. H. Andersen, and N. Sivasithamparam, "A fe procedure for calculation of cyclic behaviour of offshore foundations under partly drained conditions," 2015. [Online]. Available: https://api.semanticscholar.org/CorpusID:114947204.

[69] A. Puzrin and G. Houlsby, "A thermomechanical framework for rate-independent dissipative materials with internal functions," *International Journal of Plasticity*, vol. 17, no. 8, pp. 1147–1165, 2001. DOI: https://doi.org/10.1016/S0749-6419(00)00083-8. [Online]. Available: https://www.sciencedirect.com/science/article/pii/S0749641900000838.

[70] G. Houlsby, C. Abadie, W. Beuckelaers, and B. Byrne, "A model for nonlinear hysteretic and ratcheting behaviour," *International Journal of Solids and Structures*, vol. 120, pp. 67–80, 2017. DOI: https://doi.org/10.1016/j.ijsolstr.2017.04.031. [Online]. Available: https://www.sciencedirect.com/science/article/pii/S0020768317301889.

[71] C. N. Abadie, B. W. Byrne, and G. T. Houlsby, "Rigid pile response to cyclic lateral loading: Laboratory tests," *Géotechnique*, vol. 69, no. 10, pp. 863–876, 2019. DOI: 10.1680/jgeot.16.P.325.

[72] W. Fuentes, T. Wichtmann, M. Gil, and C. J. Lascarro, "Isa-hypoplasticity accounting for cyclic mobility effects for liquefaction analysis," *Acta Geotechnica*, vol. 15, pp. 1513–1531, 2020. DOI: https://doi.org/10.1007/s11440-019-00846-2. [Online]. Available: https://api.semanticscholar.org/CorpusID:198410708.

[73] W. Fuentes, T. Triantafyllidis, and A. Lizcano, "Hypoplastic model for sands with loading surface," *Acta Geotechnica*, vol. 7, pp. 177–192, 2012. DOI: https://doi.org/10.1007/s11440-012-0161-z.

[74] M.-J. Alipour and W. Wu, "Hypoplastic model with an inner memory surface for sand under cyclic loading," *Computers and Geotechnics*, vol. 162, 2023. DOI: 10.1016/j.compgeo.2023.105666.

[75] I. Herle and G. Gudehus, "Determination of parameters of a hypoplastic constitutive model from properties of grain assemblies," *Mechanics of Cohesive-frictional Materials*, vol. 4, no. 5, pp. 461–486, 1999. DOI: https://doi.org/10.1002/(SICI)1099-1484(199909)4:5<461::AID-CFM71>3.0.CO;2-P.

[76] R. Corti, A. Diambra, D. Muir Wood, D. Escribano Leiva, and D. Nash, "Memory surface hardening model for granular soils under repeated loading conditions," *Journal of Engineering Mechanics*, vol. 142, no. 12, 2016. DOI: 10.1061/(ASCE)EM.1943-7889.0001174.

[77] Y. F. Dafalias and M. T. Manzari, "Simple plasticity sand model accounting for fabric change effects," *Journal of Engineering Mechanics*, vol. 130, no. 6, pp. 622–634, 2004. DOI: 10.1061/(ASCE)0733-9399(2004)130:6(622).

[78] Y. F. Dafalias, A. G. Papadimitriou, and X. S. Li, "Sand plasticity model accounting for inherent fabric anisotropy," *Journal of Engineering Mechanics*, vol. 130, no. 11, pp. 1319–1333, 2004. DOI: 10.1061/(ASCE)0733-9399(2004)130:11(1319).

[79] P. Geotechnical, *Plaxis 3d-reference manual*, English, Bentley System Inc., Jun. 13, 2023, 588 pp., June 01, 2020.

[80] M. Taiebat and Y. F. Dafalias, "Sanisand: Simple anisotropic sand plasticity model," *International Journal for Numerical and Analytical Methods in Geomechanics*, vol. 32, no. 8, pp. 915–948, 2008. DOI: https://doi.org/10.1002/nag.651.

[81] H. Liu, A. Diambra, J. A. Abell, and F. Pisanò, "Memory-enhanced plasticity modeling of sand behavior under undrained cyclic loading," *Journal of Geotechnical and Geoenvironmental Engineering*, vol. 146, no. 11, p. 04 020 122, 2020. DOI: 10.1061/(ASCE)GT.1943-5606.0002362.

[82] H. Liu, E. Kementzetzidis, J. A. Abell, and F. Pisanó, "From cyclic sand ratcheting to tilt accumulation of offshore monopiles: 3d fe modelling using sanisand-ms," *Géotechnique*, vol. 72, no. 9, pp. 753–768, 2021. DOI: 10.1680/jgeot.20.P.029.

[83] H. Wang, B. Lehane, M. Bransby, L. Wang, and Y. Hong, "Field and numerical study of the lateral response of rigid piles in sand," *Acta Geotechnica*, vol. 17, no. 12, pp. 5573–5584, 2022. DOI: 10.1007/s11440-022-01532-6.

[84] C.-C. Fan and J. H. Long, "Assessment of existing methods for predicting soil response of laterally loaded piles in sand," *Computers and Geotechnics*, vol. 32, no. 4, pp. 274–289, 2005. DOI: https://doi.org/10.1016/j.compgeo.2005.02.004.

[85] N. el Kanfoudi, "On Modelling The Lateral Behaviour of Vibratory Driven Monopile Foundations for Offshore Wind Turbines," Master Thesis, Delft University of Technology, the Netherlands, 2016.

[86] H. Wang, B. Lehane, M. Bransby, A. Askarinejad, L. Wang, and Y. Hong, "A simple rotational spring model for laterally loaded rigid piles in sand," *Marine Structures*, vol. 84, p. 103 225, 2022b. DOI: https://doi.org/10.1016/j.marstruc.2022.103225. [Online]. Available: https://www.sciencedirect.com/science/article/pii/S0951833922000648.

[87] A. Tsetas, A. Tsouvalas, S. S. Gómez, *et al.*, "Gentle driving of piles (gdp) at a sandy site combining axial and torsional vibrations: Part i - installation tests," *Ocean Engineering*, vol. 270, p. 113 453, 2023. DOI: https://doi.org/10.1016/j.oceaneng.2022.113453. [Online]. Available: https://www.sciencedirect.com/science/article/pii/S0029801822027366.

[88] H. Liu, E. Kementzetzidis, J. A. Abell, and F. Pisanò, "From cyclic sand ratcheting to tilt accumulation of offshore monopiles: 3d fe modelling using sanisand-ms," *Géotechnique*, vol. 72, no. 9, pp. 753–768, 2022. DOI: 10.1680/jgeot.20.P.029.

[89] G. T. Houlsby and M. J. Cassidy, "A plasticity model for the behaviour of footings on sand under combined loading," *Geotechnique*, vol. 52, pp. 117–129, 2002. DOI: 10.1680/geot.2002.52.2.117. [Online]. Available: https://api.semanticscholar.org/CorpusID:109656744.

[90] "Generalized failure envelope for caisson foundations in cohesive soil: Static and dynamic loading," *Soil Dynamics and Earthquake Engineering*, vol. 78, pp. 154–174, 2015. DOI: https://doi.org/10.1016/j.soildyn.2015.07.012.

[91] J.-S. Chiou and H.-Y. Chien, "Theoretical interaction diagrams of a laterally loaded rigid caisson considering base shear and moment resistances," *Ocean Engineering*, vol. 261, p. 111 937, 2022. DOI: https://doi.org/10.1016/j.oceaneng.2022.111937.

[92] Z. Chen, Z. Zhang, W. Li, T. Wang, and J. Zhang, "Numerical study on the base shear force-displacement relationship for laterally loaded monopiles in dense sand," *Ocean Engineering*, vol. 286, p. 115 527, 2023. DOI: https://doi.org/10.1016/j.oceaneng.2023.115527.

[93] B. Byrne, R. Mcadam, H. Burd, *et al.*, "New design methods for large diameter piles under lateral loading for offshore wind applications," Jun. 2015, ISBN: 978-1-138-02848-7. DOI: 10.1201/b18442-96.

[94] H. J. Burd, C. N. Abadie, B. W. Byrne, *et al.*, "Application of the pisa design model to monopiles embedded in layered soils," *Géotechnique*, vol. 70, no. 11, pp. 1067–1082, 2020. DOI: 10.1680/jgeot.20.PISA.009.

[95] CFMS, "Recommendations for planning and designing foundations of offshore wind turbines (version 2.1)," Comite Francais de Mecanique des Sols et de Geotechnique, 2020.

A

Additional Figure for 3D FE Setup

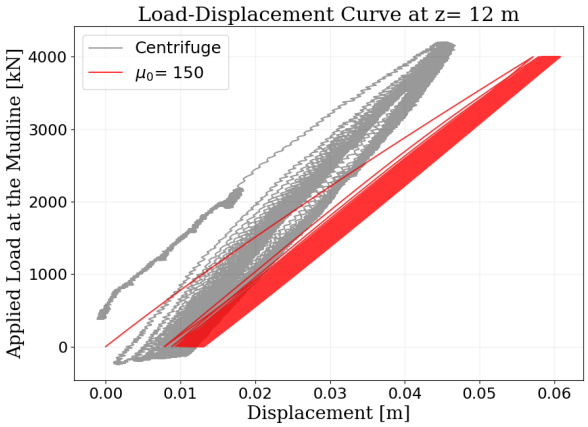

(a) μ_0 = 150, N= 41 cycles.

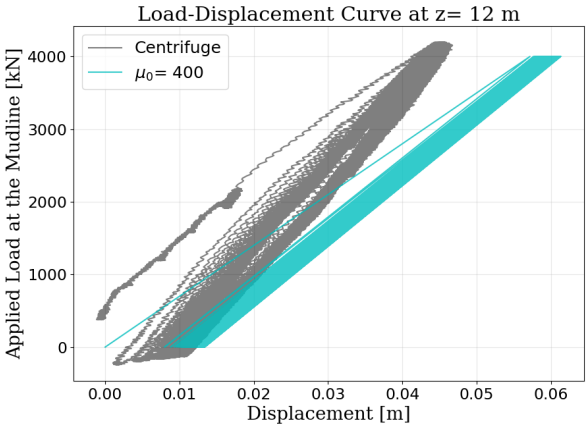

(b) μ_0 = 400, N= 100 cycles.

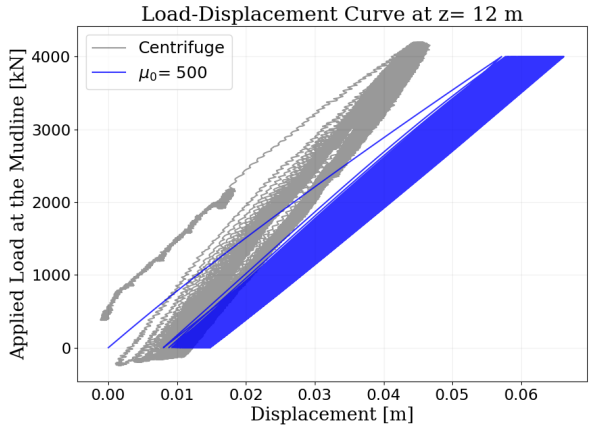

(c) μ_0 = 500, N= 100 cycles.

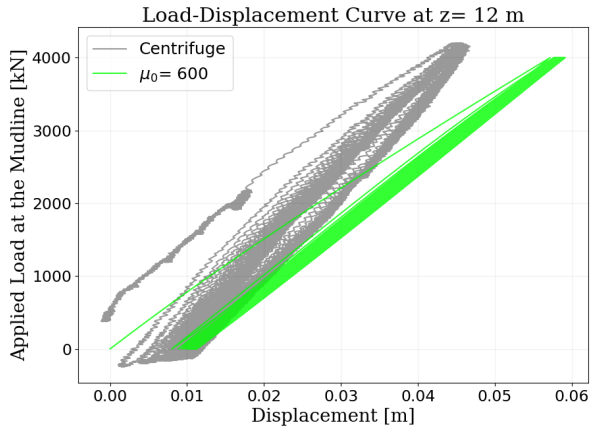

(d) μ_0 = 600, N= 25 cycles

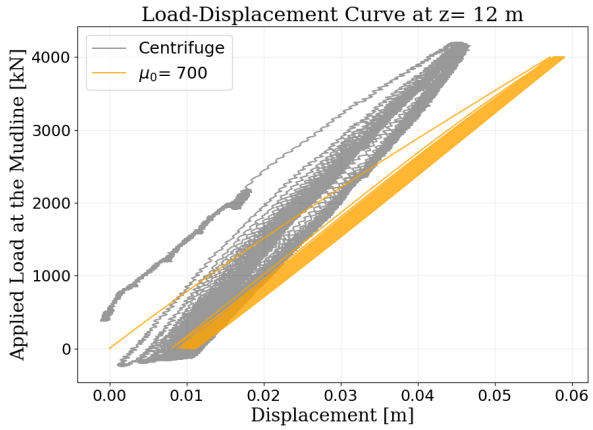

(e) μ_0 = 700, N= 25 cycles.

The calibration process between the model and centrifuge data with the load with ζ_b = 0.1 for (a) μ_0 = 150, (b) μ_0 = 400, (c) μ_0 = 500, (d) μ_0 = 600, and (e) mu_0 = 700 (test conducted by H. Wang (2022) and obtained from personal correspondence) .

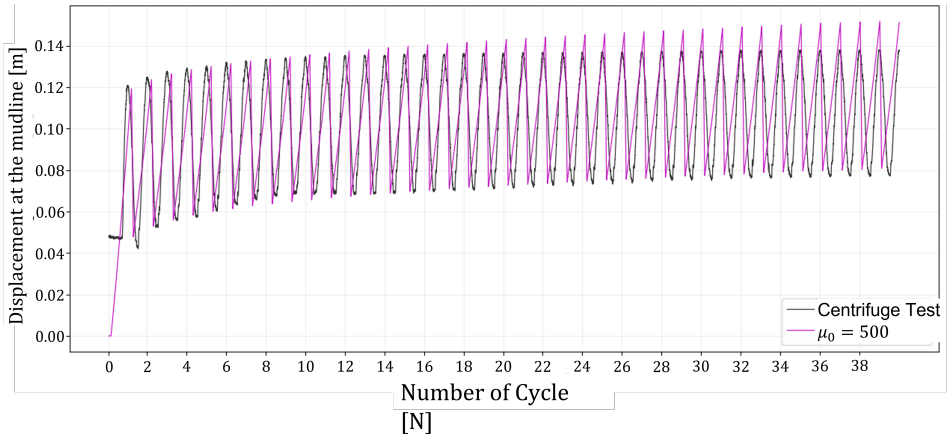

Calibration of μ_0 against the centrifuge data

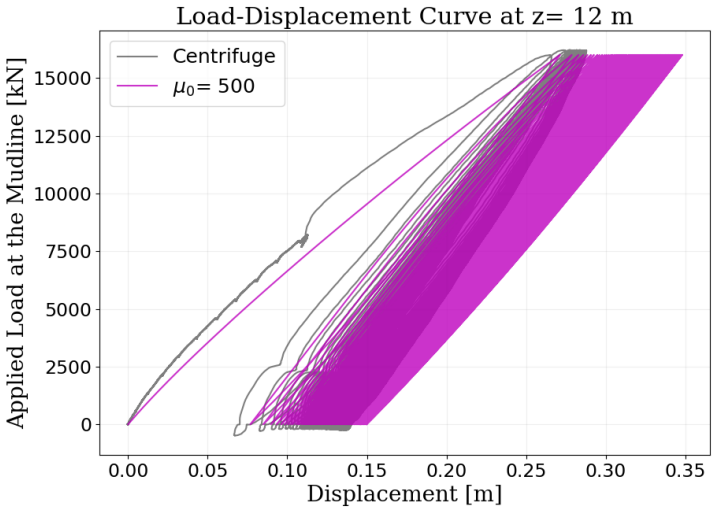

Load against displacement at the mudline for μ_0 = 500 calibrated against the centrifuge data (test conducted by H. Wang (2022) and obtained from personal correspondence).

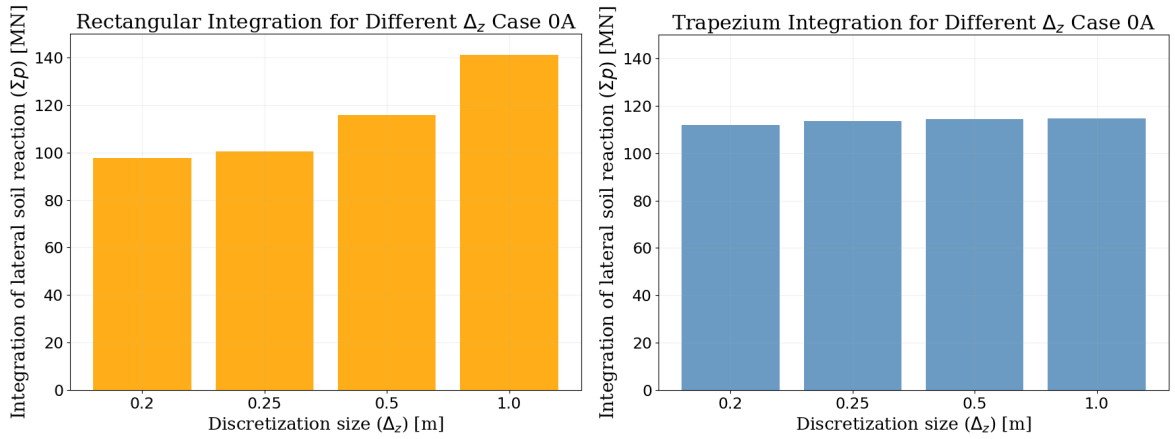

(a) Rectangular integration

(b) Trapezoidral Integration

The total lateral soil reaction (Σ_p) obtained from (a) rectangular integration method and (b) trapezium integration method for Case 0A ($D = 9m, L/D = 4, e/D = 5, D_r = 0.9$).

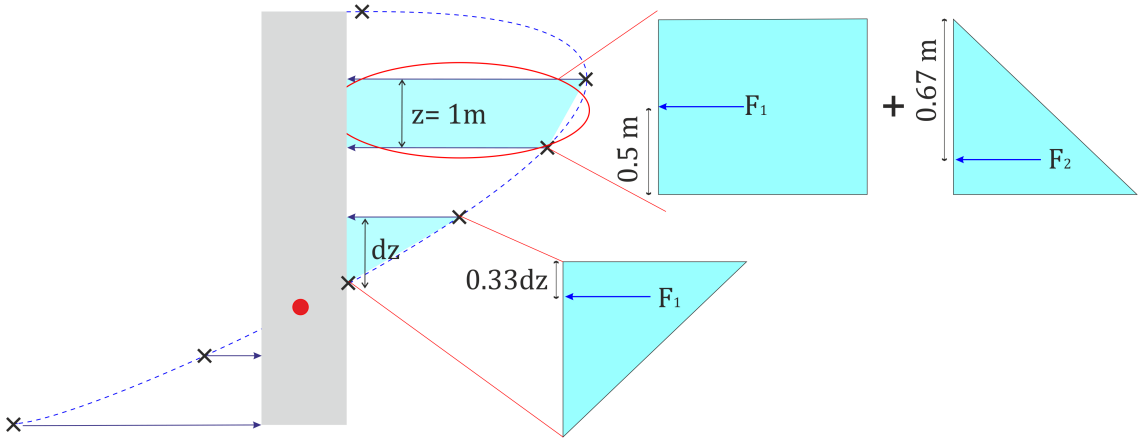

The method to calculate moment from lateral soil reaction.

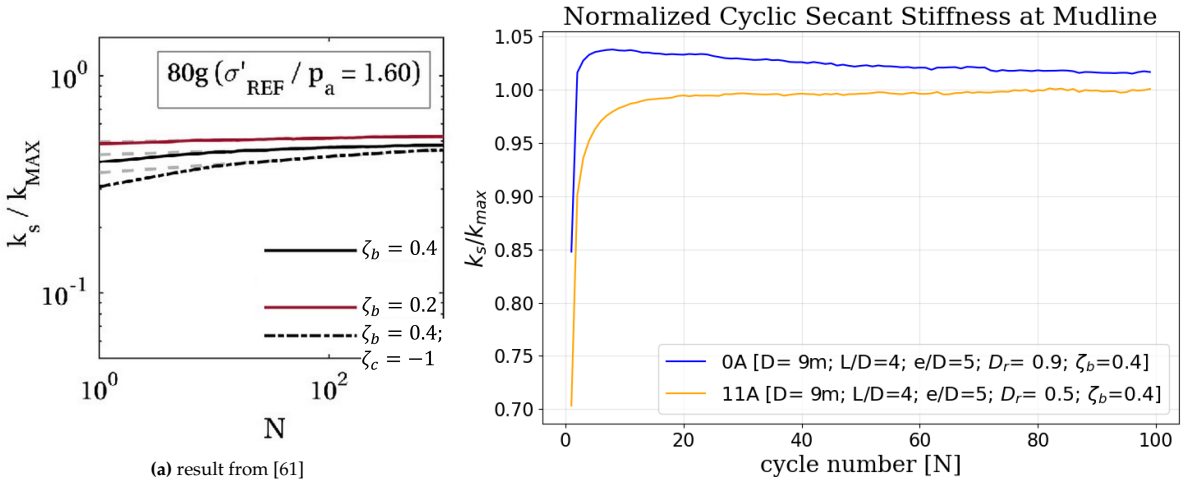

(a) result from [61]

(b) Model

Normalized cyclic secant stiffness evolution from (a) literature [61] and (b) 3D FE model.

B

Additional Figure and Table for Monotonic Analysis

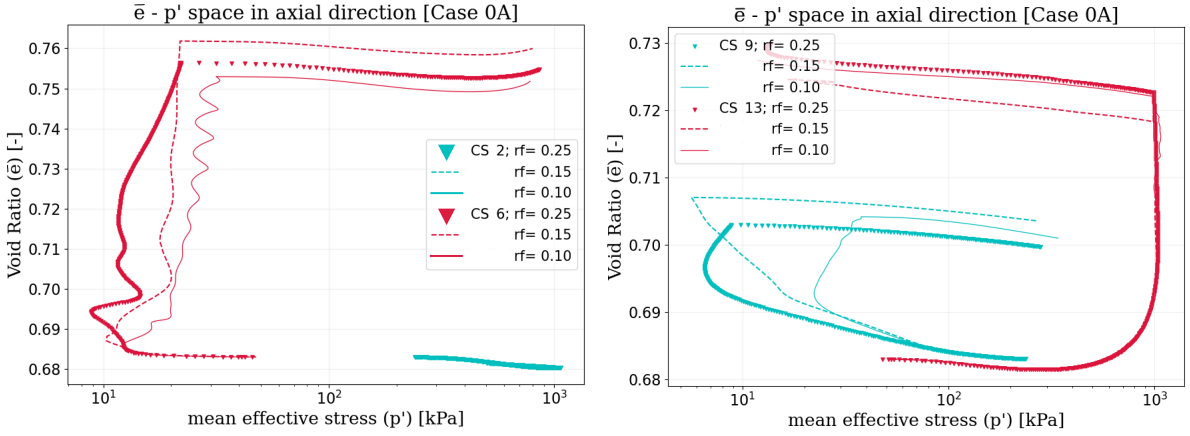

negative $x-$axis positive $x-$axis

The comparison between three different mesh sizes obtained using 3 rf (0.25, 0.15, 0.1) presented in $\bar{e} - p''$ space space in axial direction at (a) negative $x-$axis and (b) positive $x-$axis for Case 0A (D= 9m, L/D= 4, e/D= 5, D_r = 0.9).

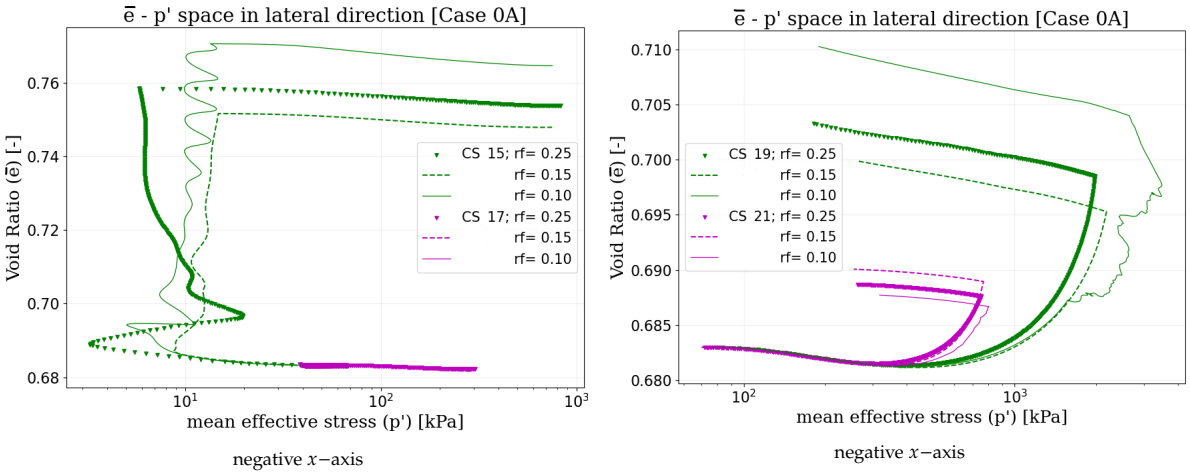

The comparison between three different mesh sizes obtained using 3 rf (0.25, 0.15, 0.1) presented in $\bar{e} - p''$ space in lateral direction at (a) negative $x-$axis and (b) positive $x-$axis for Case 0A (D= 9m, L/D= 4, e/D= 5, D_r = 0.9).

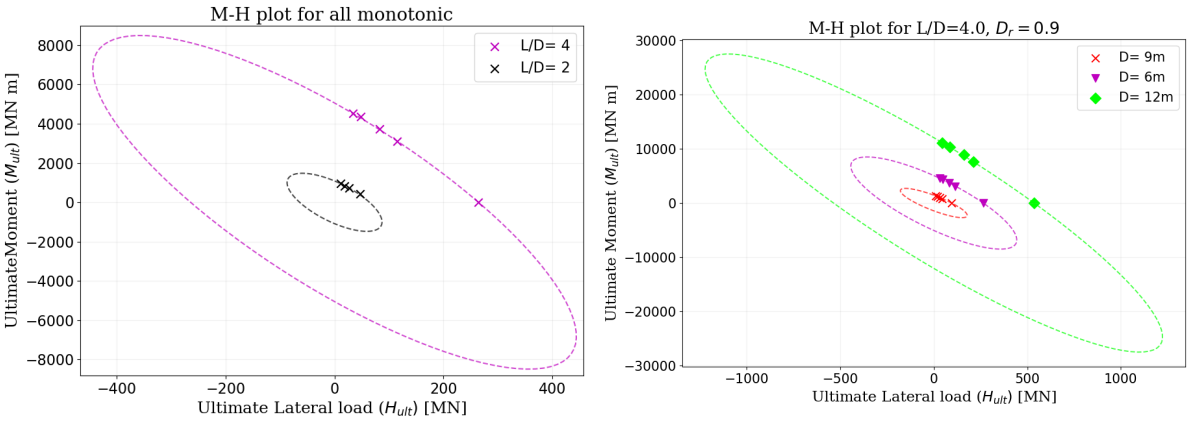

Full ellipse interaction diagram for the monopile for different (a) L/D and (b) D.

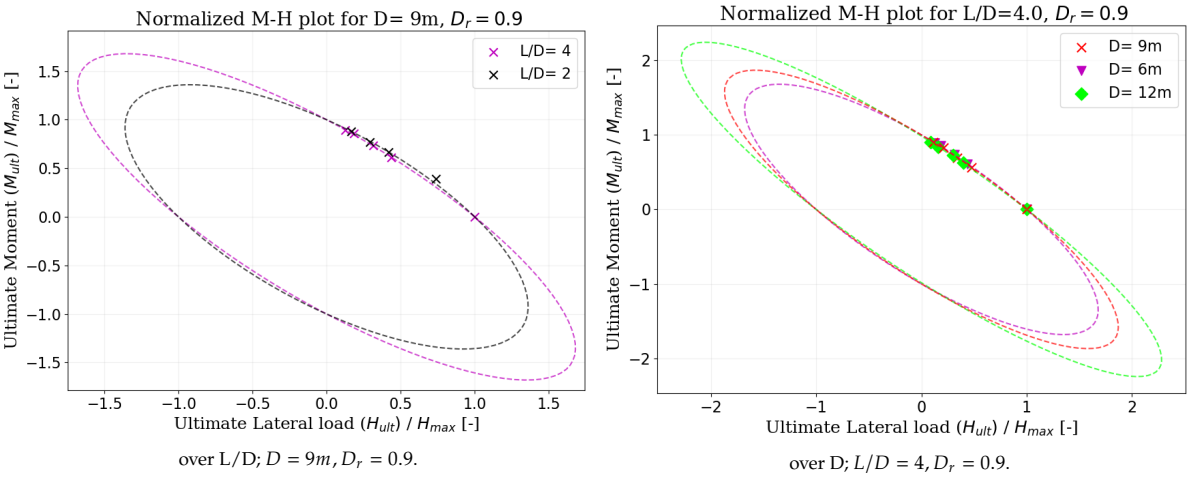

Normalized full ellipse interaction diagram for the monopile for different (a) L/D and (b) D.

The y_b/D ratio when ULS failure is obtained.

Case	y_b/D [%]	Case	y_b/D [%]
$D = 9m; L/D = 4; e/D = 5; D_r = 0.9$	1.92	$D = 9m; L/D = 4; e/D = 5; D_r = 0.5$	2.50
$D = 9m; L/D = 2; e/D = 5; D_r = 0.9$	1.52	$D = 12m; L/D = 1; e/D = 5; D_r = 0.9$	0.76
$D = 6m; L/D = 4; e/D = 5; D_r = 0.9$	2.53	$D = 9m; L/D = 1; e/D = 5; D_r = 0.9$	0.74
$D = 6m; L/D = 2; e/D = 5; D_r = 0.9$	1.54	$D = 6m; L/D = 1; e/D = 5; D_r = 0.9$	0.71
$D = 12m; L/D = 4; e/D = 5; D_r = 0.9$	1.37	$D = 9m; L/D = 2; e/D = 1; D_r = 0.9$	1.32
$D = 12m; L/D = 2; e/D = 5; D_r = 0.9$	1.47	$D = 3m; L/D = 2; e/D = 5; D_r = 0.9$	1.51
$D = 9m; L/D = 4; e/D = 15; D_r = 0.9$	1.87	$D = 3m; L/D = 4; e/D = 5; D_r = 0.9$	2.51
$D = 9m; L/D = 4; e/D = 10; D_r = 0.9$	1.90	$D = 9m; L/D = 4; e/D = 3; D_r = 0.9$	1.91
$D = 9m; L/D = 4; e/D = 5; D_r = 0.7$	2.11	$D = 9m; L/D = 4; e/D = 5; D_r = 0.3$	2.99
$D = 9m; L/D = 2; e/D = 5; D_r = 0.7$	1.54	$D = 9m; L/D = 2; e/D = 5; D_r = 0.7$	1.54
$D = 9m; L/D = 2; e/D = 10; D_r = 0.9$	1.63	$D = 9m; L/D = 2; e/D = 3; D_r = 0.9$	1.48

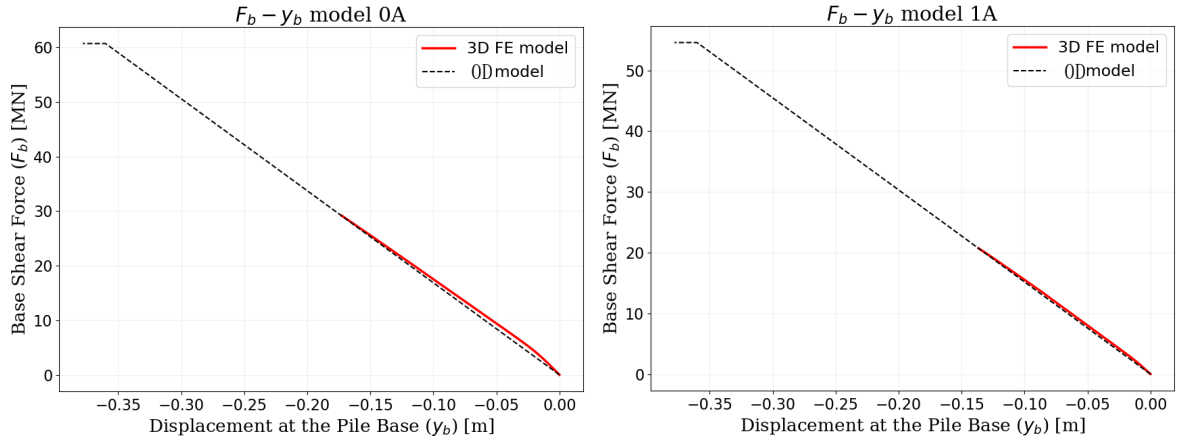

(a) $D = 9m, L/D = 4, e/D = 5, D_r = 0.9$ **(b)** $D = 9m, L/D = 2, e/D = 5, D_r = 0.9$

0D $F_b - y_b$ model for case (a) 0A and (b) 1A, the red line indicate the result from 3D FE model until $\theta_{sb} = 2^o$

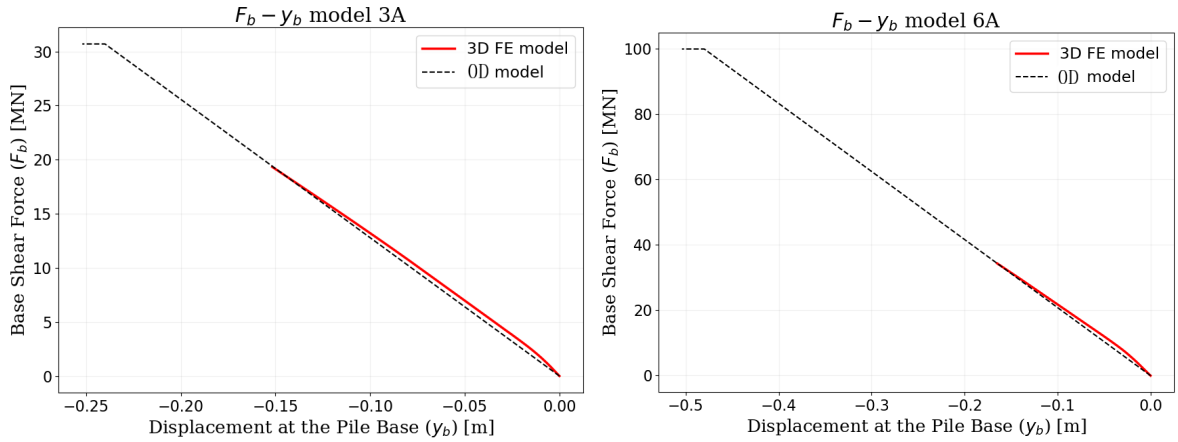

(a) $D = 6m, L/D = 4, e/D = 5, D_r = 0.9$ **(b)** $D = 12m, L/D = 4, e/D = 5, D_r = 0.9$

0D $F_b - y_b$ model for case (a) 3A and (b) 6A, the red line indicate the result from 3D FE model until $\theta_{sb} = 2^o$

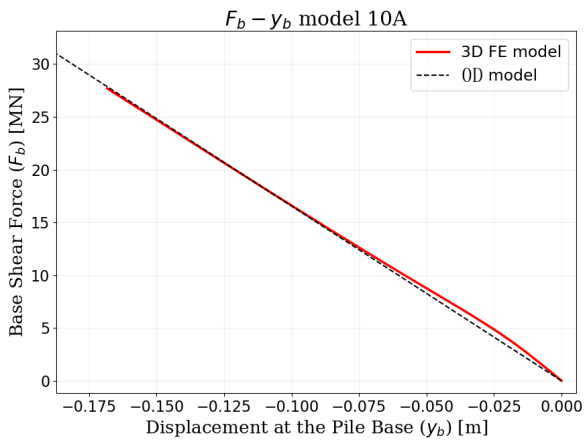

(a) $D = 9m, L/D = 4, e/D = 15, D_r = 0.9$

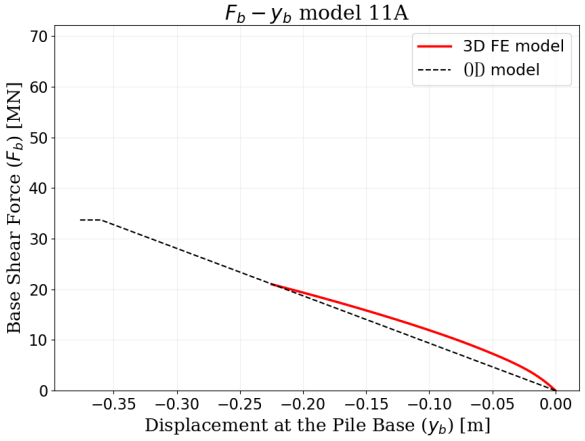

(b) $D = 9m, L/D = 4, e/D = 5, D_r = 0.5$

0D $F_b - y_b$ model for case (a) 10A and (b) 11A, the red line indicates the result from the 3D FE model until $\theta_{sb} = 2^o$

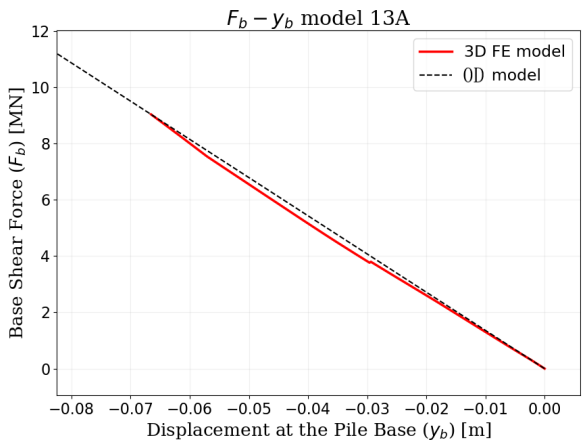

(a) $D = 9m, L/D = 1, e/D = 5, D_r = 0.9$

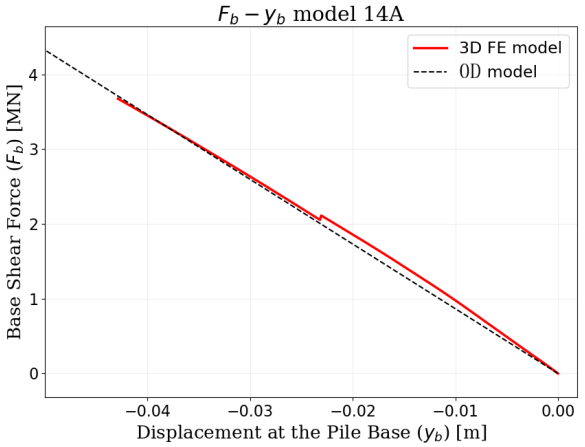

(b) $D = 6m, L/D = 1, e/D = 5, D_r = 0.9$

0D $F_b - y_b$ model for case (a) 13A and (b) 14A, the red line indicates the result from the 3D FE model until $\theta_{sb} = 2^o$

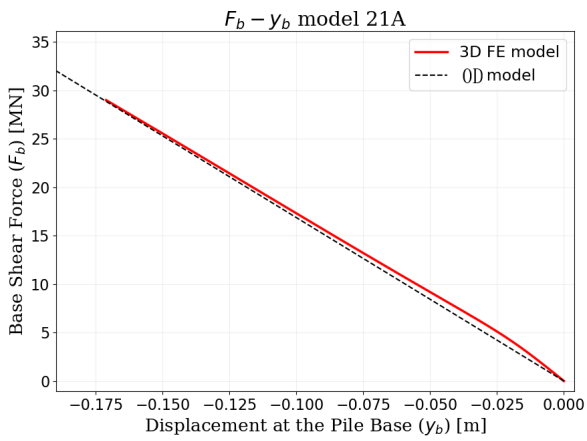

(a) $D = 9m, L/D = 4, e/D = 10, D_r = 0.9$

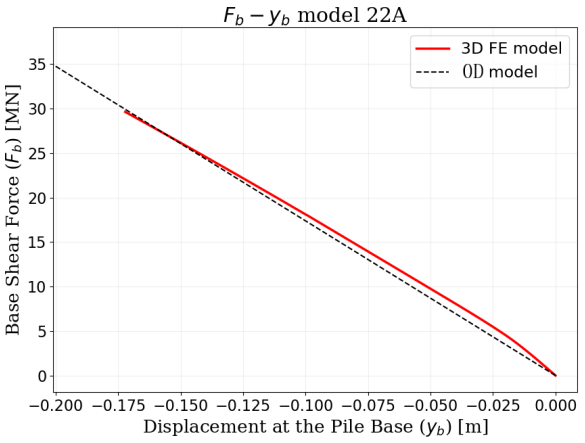

(b) $D = 9m, L/D = 4, e/D = 3, D_r = 0.9$

0D $F_b - y_b$ model for case (a) 21A and (b) 22A, the red line indicates the result from the 3D FE model until $\theta_{sb} = 2^o$

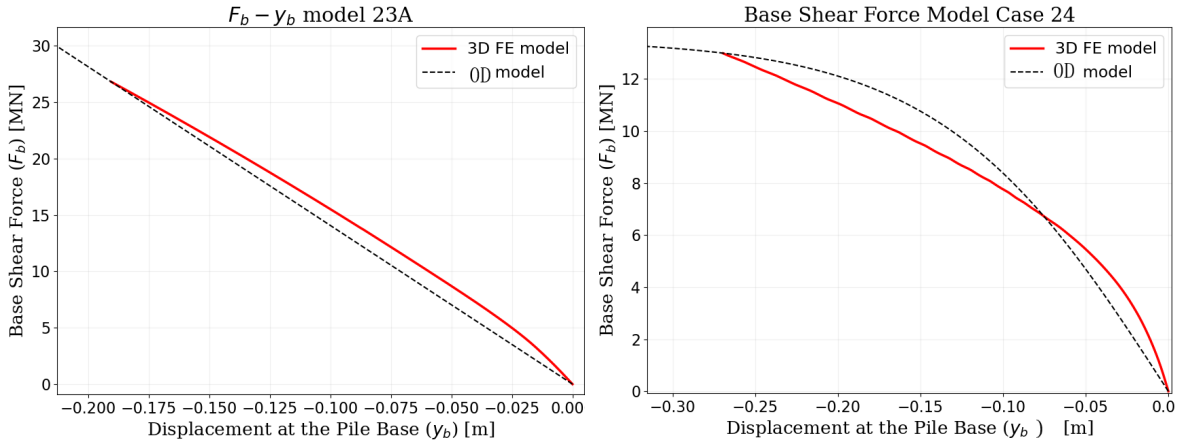

(a) $D = 9m, L/D = 4, e/D = 5, D_r = 0.7$

(b) $D = 9m, L/D = 4, e/D = 5, D_r = 0.3$

0D $F_b - y_b$ model for case (a) 23A and (b) 24A, the red line indicates the result from the 3D FE model until $\theta_{sb} = 2^o$

C

Additional Figures for Cyclic Analyses

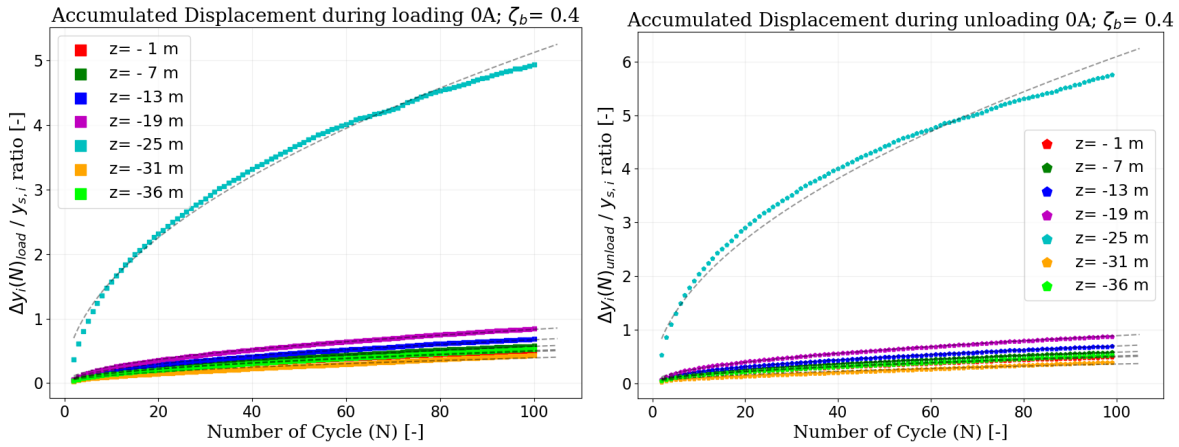

(a) Loading phase

(b) Unloading Phase

Full plot of normalized accumulated displacement (y_{acc}) at different depths for the reference case during (a) loading and (b) unloading, with load characteristic ζ_b = 0.4.

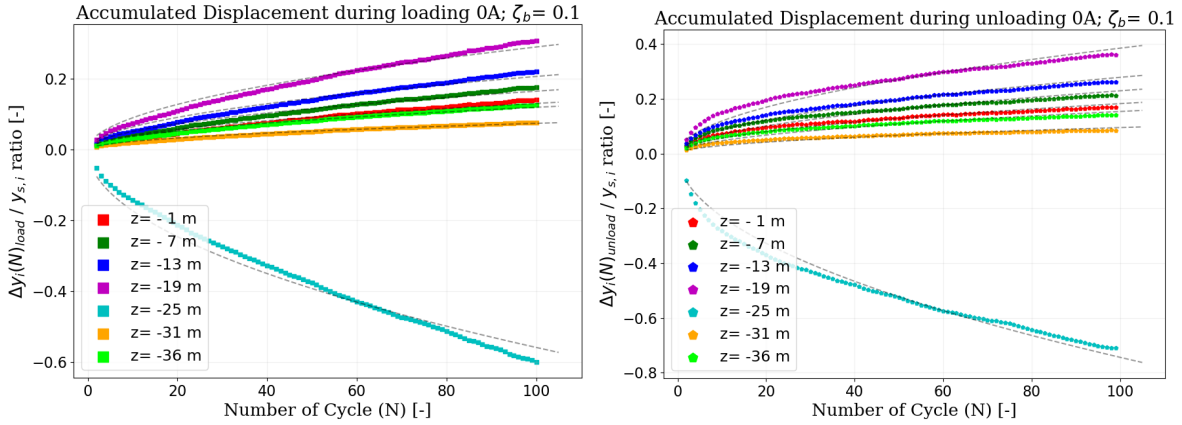

(a) Loading phase

(b) Unloading Phase

Full plot of normalized accumulated displacement (y_{acc}) at different depths for the reference case during (a) loading and (b) unloading, with load characteristic ζ_b = 0.1.

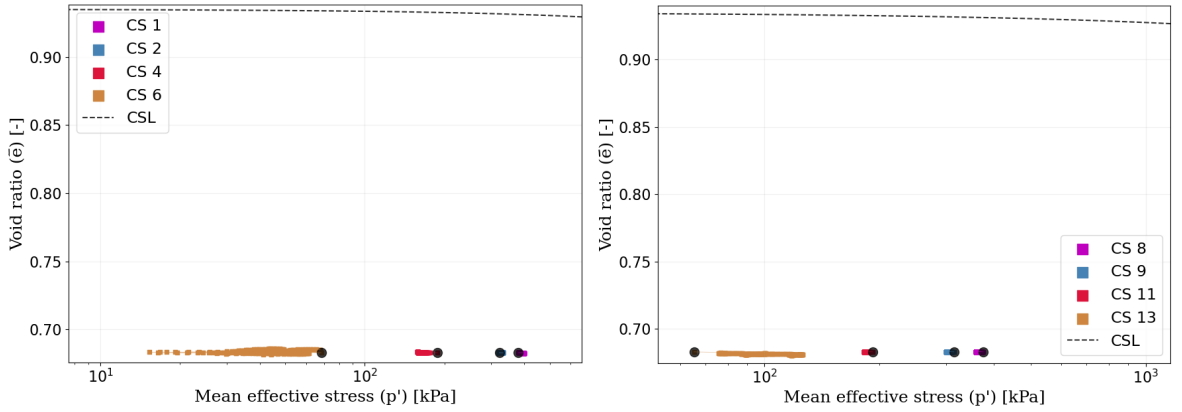

(a) negative $x-$ axis

(b) positive $x-$ axis

The Ψ evolution for the soil elements around the monopile recorded in the axial direction for the elements in (a) negative $x-$ axis and (b) positive $x-$axis (ζ_b = 0.1).

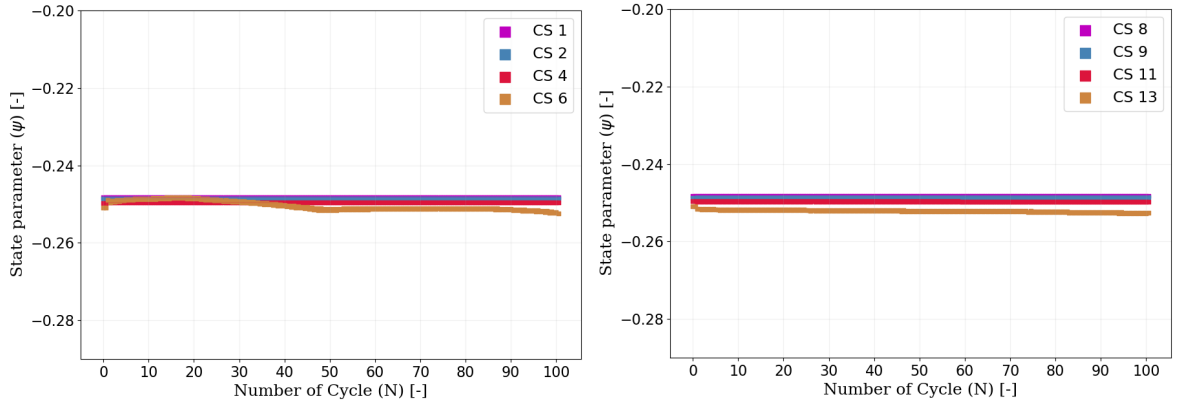

(a) negative $x-$ axis

(b) positive $x-$ axis

The Ψ evolution for the soil elements around the monopile recorded in the axial direction for the elements in (a) negative $x-$ axis and (b) positive $x-$axis (ζ_b = 0.1).

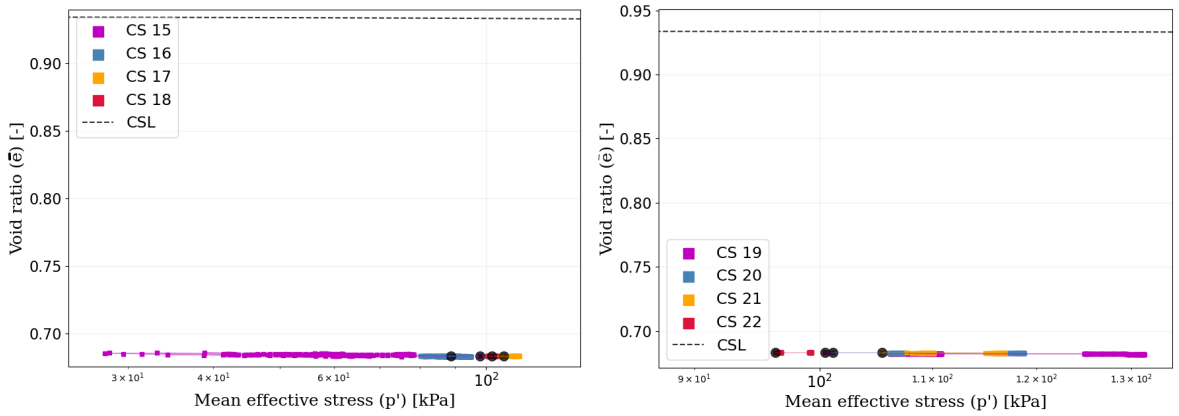

(a) negative $x-$ axis **(b)** positive $x-$ axis

The $\bar{e} - p'$ space for the soil elements around the monopile recorded in the lateral direction for the elements at $z = -D$ in (a) negative $x-$ axis and (b) positive $x-$axis ($\zeta_b = 0.1$).

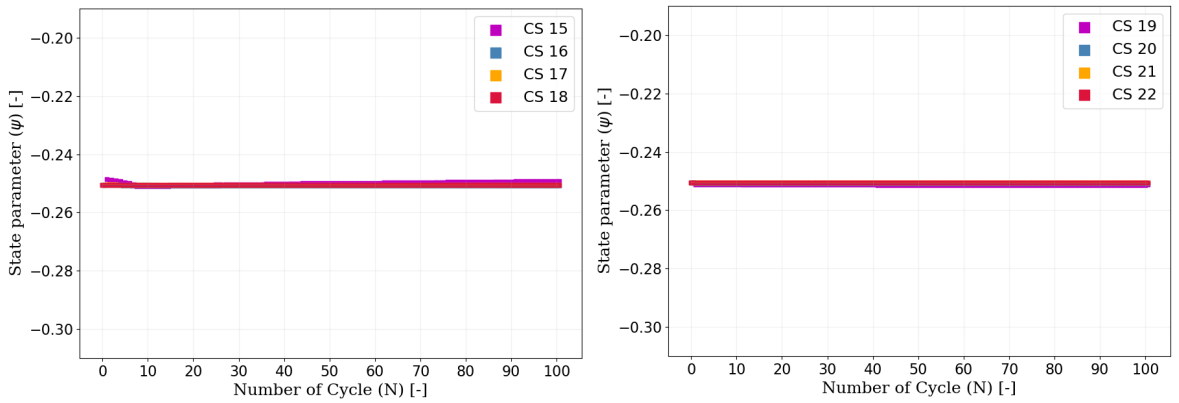

(a) negative $x-$ axis **(b)** positive $x-$ axis

The Ψ evolution for the soil elements around the monopile recorded in the lateral direction for the elements at $z = -D$ in (a) negative $x-$ axis and (b) positive $x-$axis ($\zeta_b = 0.1$).

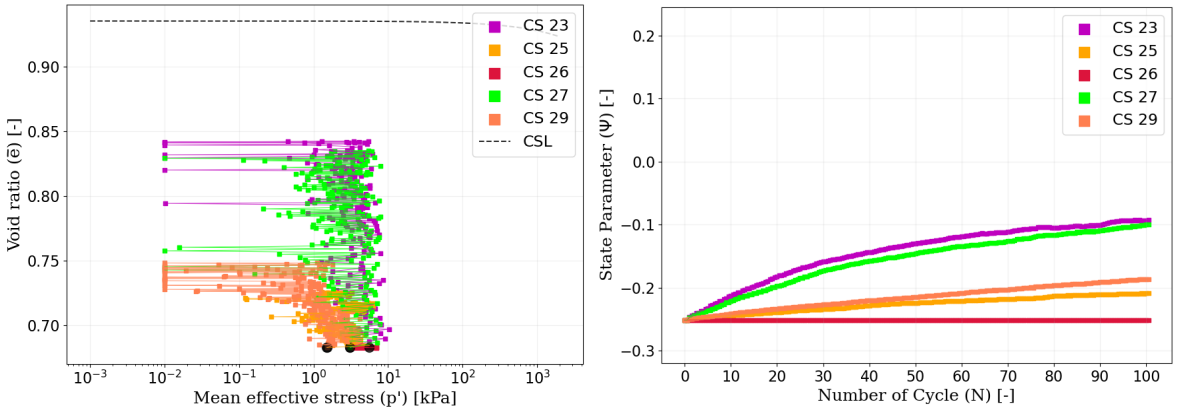

(a) $\bar{e} - p'$ space **(b)** Ψ evolution

The void ratio evolution for the soil elements near the mudline recorded in the radial direction and presented in (a) $\bar{e} - p'$ space and (b) Ψ evolution ($\zeta_b = 0.1$).

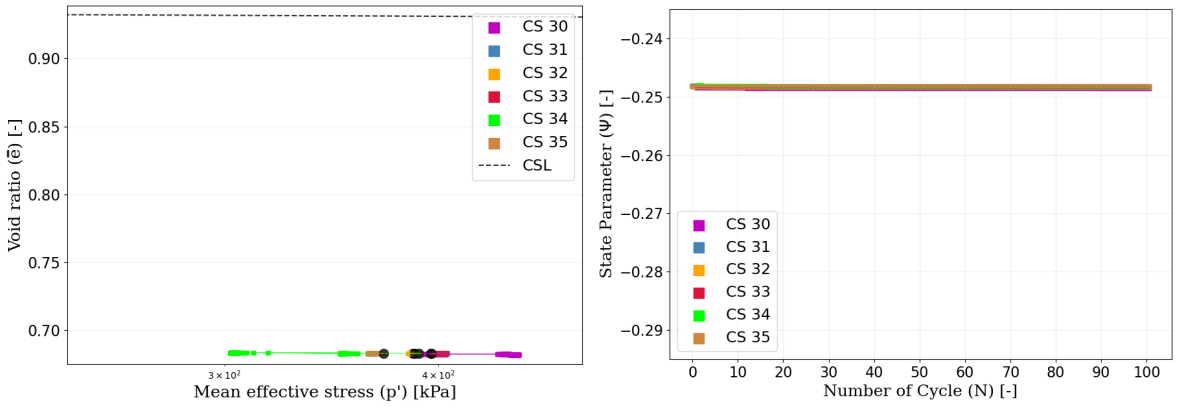

(a) $\bar{e} - p'$ space

(b) Ψ evolution

The void ratio evolution for the soil elements near the pile base presented in (a) $\bar{e} - p'$ space and (b) Ψ evolution.

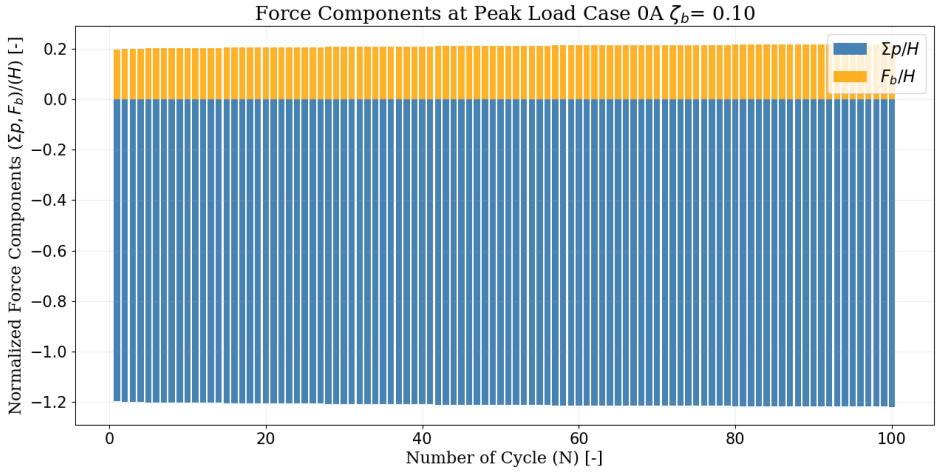

(a) Lateral force balance

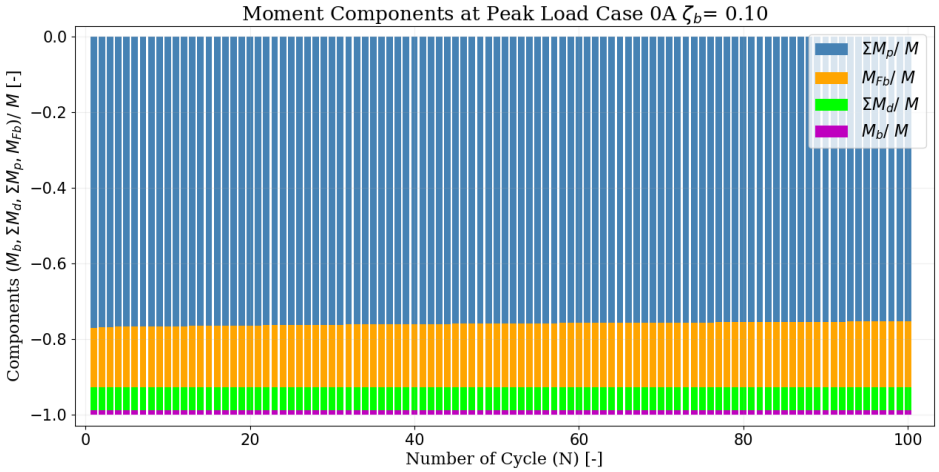

(b) Moment balance

The equilibrium analysis for the model under cyclic loading performed for (a) lateral balance and (b) moment balance ($\zeta_b = 0.1$).

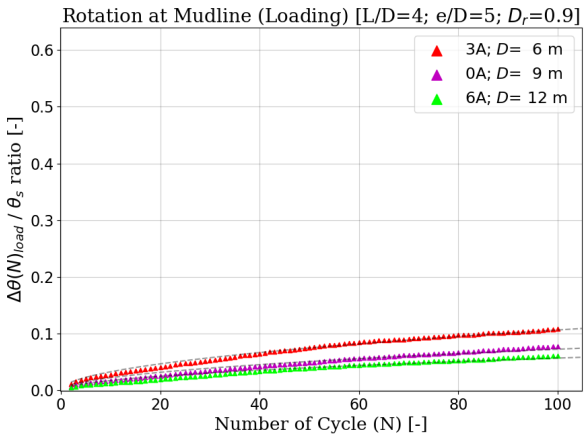

θ_{acc} at loading

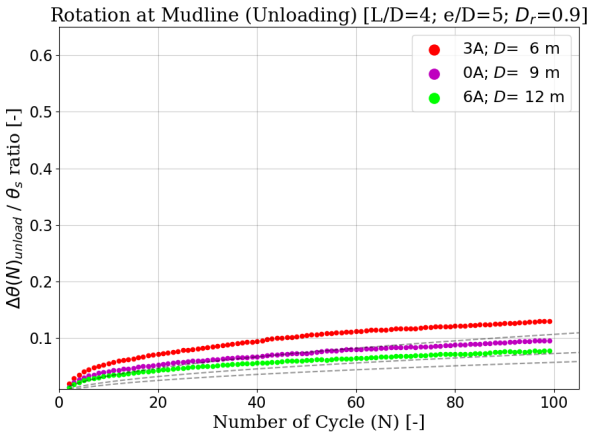

θ_{acc} at unloading

The effect of pile geometry (L and D) on θ_{acc} at the mudline during cyclic load with $\zeta_b = 0.1$, presented during (a) loading phase and (b)unloading phase ($L/D = 4, e/D = 5, D_r = 0/9$).

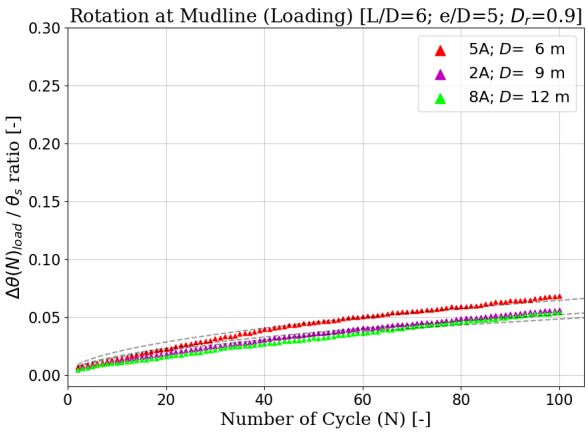

θ_{acc} at loading $L/D = 6$

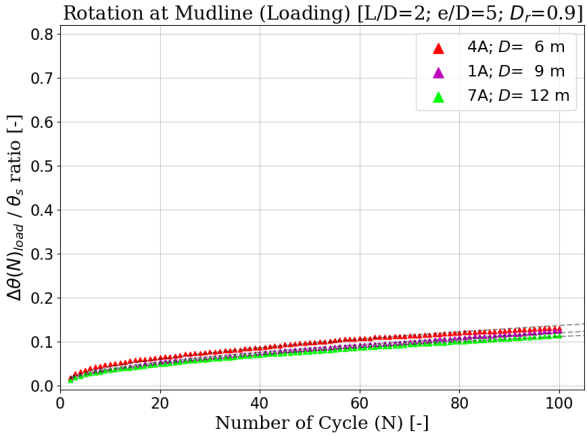

θ_{acc} at loading $L/D = 2$

The effect of pile geometry (L and D) on θ_{acc} at the mudline during cyclic load with $\zeta_b = 0.1$, presented for monopile with (a) $L/D = 6$ and (b) $L/D = 2$ ($D_r = 0.9, e/D = 5$).

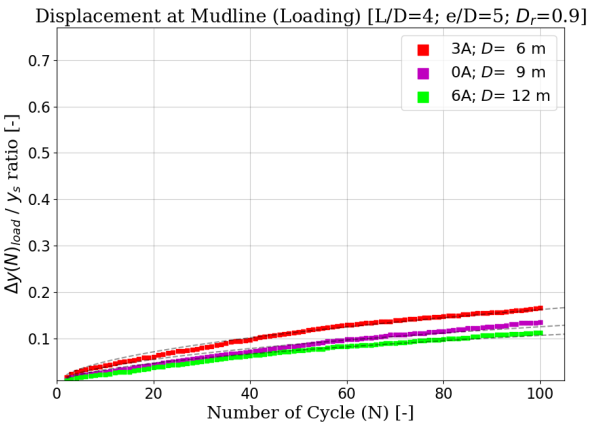

y_{acc} at loading

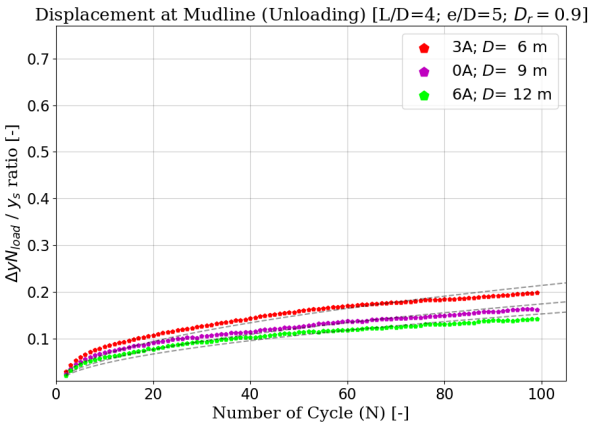

y_{acc} at unloading

The effect of pile geometry (L and D) on y_{acc} at the mudline during cyclic load with $\zeta_b = 0.1$, presented during (a) loading phase and (b)unloading phase ($L/D = 4, e/D = 5, D_r = 0.9$).

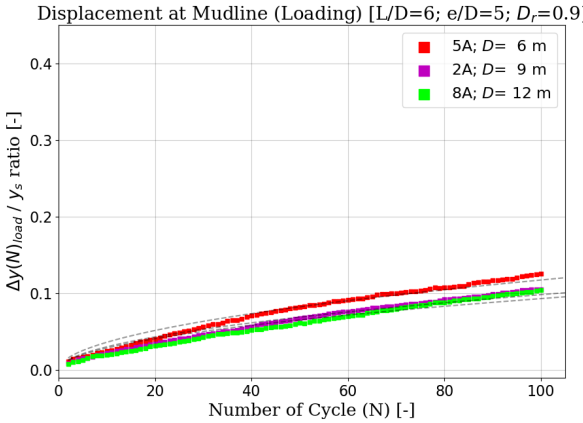

y_{acc} at loading $L/D = 6$

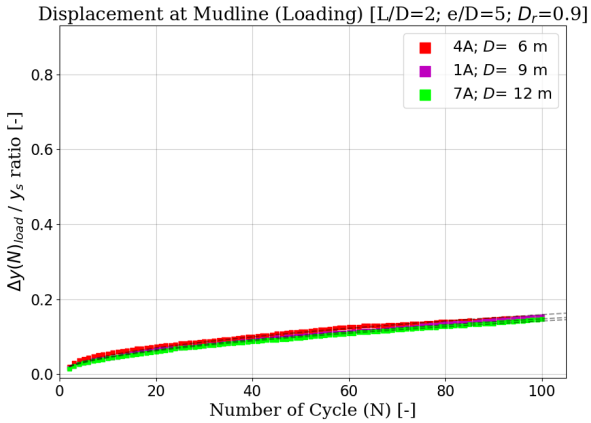

y_{acc} at loading $L/D = 2$

The effect of pile geometry (L and D) on y_{acc} at the mudline during cyclic load with $\zeta_b = 0.4$, presented for monopile with (a) $L/D = 6$ and (b) $L/D = 2$ ($D_r = 0.9, e/D = 5$).

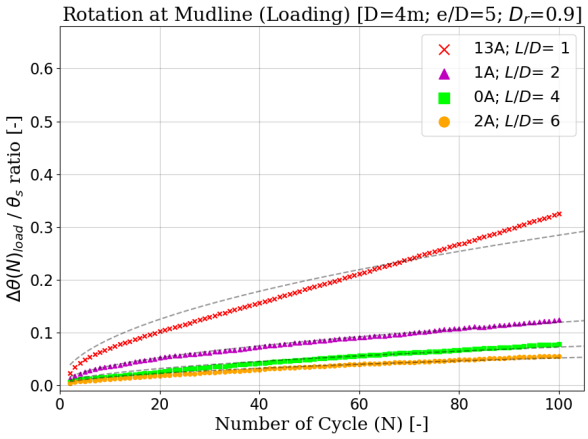

θ_{acc} at loading

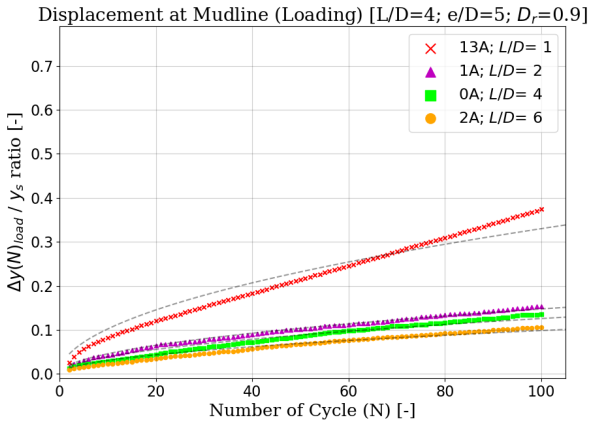

y_{acc} at loading

The effect of pile L/D on (a)θ_{acc} (b) y_{acc} presented for the monopile under cyclic load ($\zeta_b = 0.1$) with $D = 9m, L/D = 4, e/D = 5$ and installed in sand with $D_r = 0.9$.

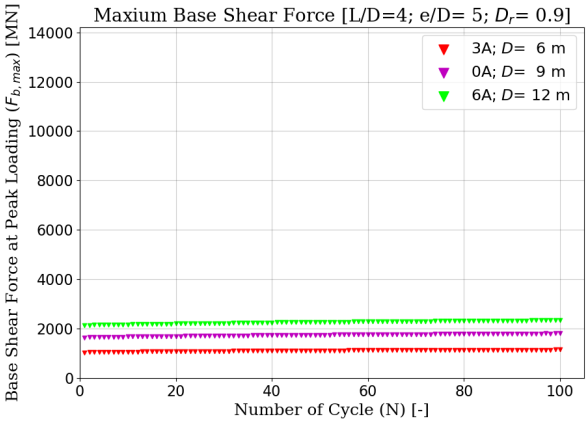

F_b at peak loading

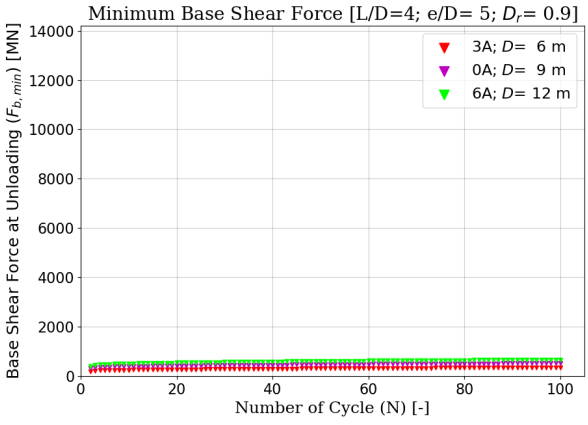

F_b at $H = 0$

The effect of pile geometry (L and D) on the F_b during (a)maximum loading applied and (b) load completely released ($L/D = 4, e/D = 5, D_r = 0.9, \zeta_b = 0.1$).

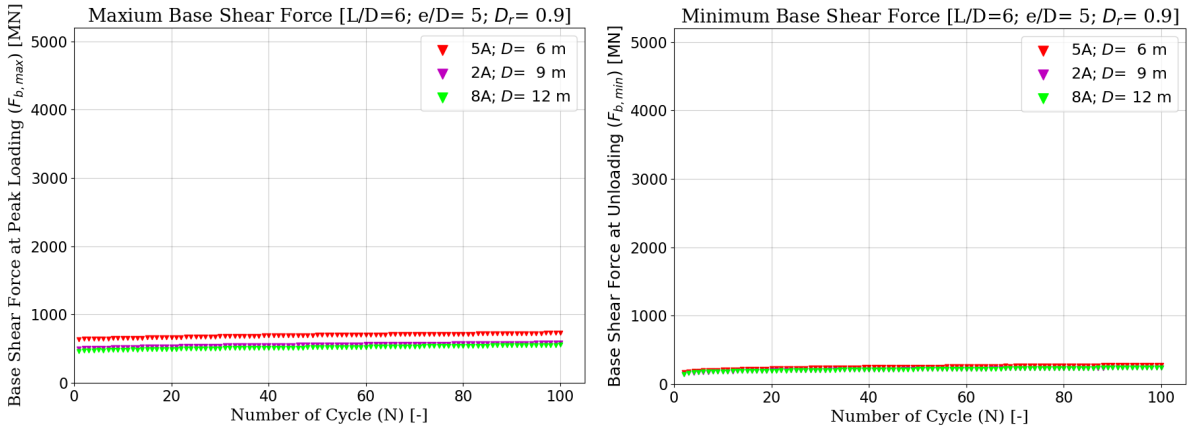

F_b at peak loading F_b at $H = 0$

The effect of pile geometry (L and D) on the F_b during (a)maximum loading applied and (b) load completely released ($L/D = 6, e/D = 5, D_r = 0.9, \zeta_b = 0.1$).

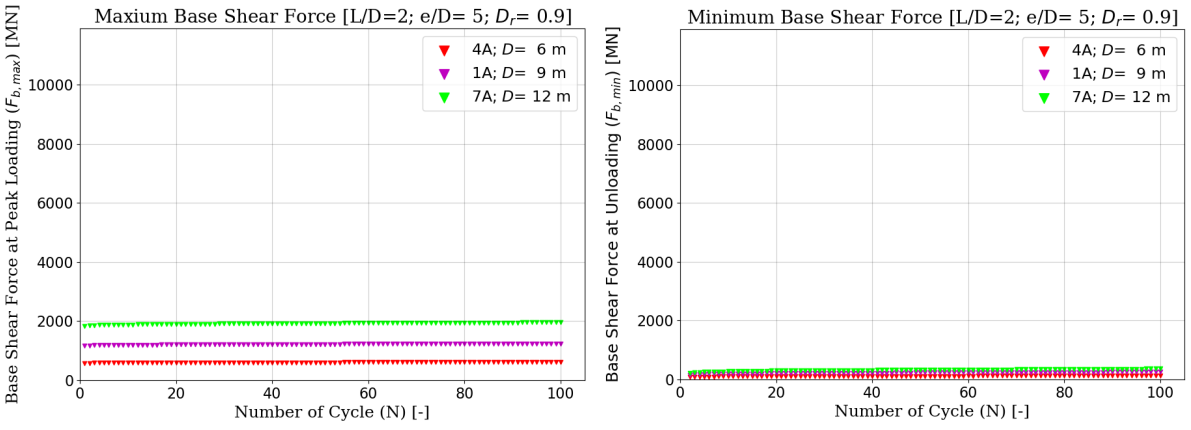

F_b at peak loading F_b at $H = 0$

The effect of pile geometry (L and D) on the F_b during (a)maximum loading applied and (b) load completely released ($L/D = 2, e/D = 5, D_r = 0.9, \zeta_b = 0.1$).

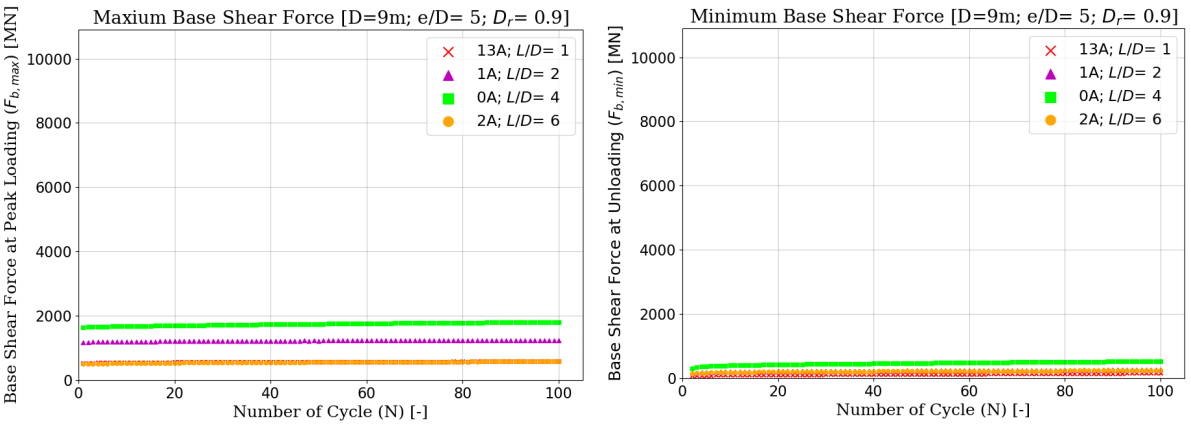

F_b at peak loading F_b at $H = 0$

The effect of pile L/D on the F_b during (a) maximum loading applied and (b) load completely released ($D = 9m, e/D = 5, D_r = 0.9, \zeta_b = 0.1$).

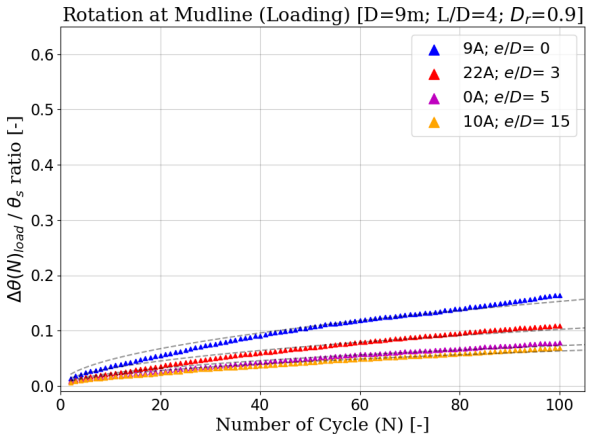

θ_{acc} at loading

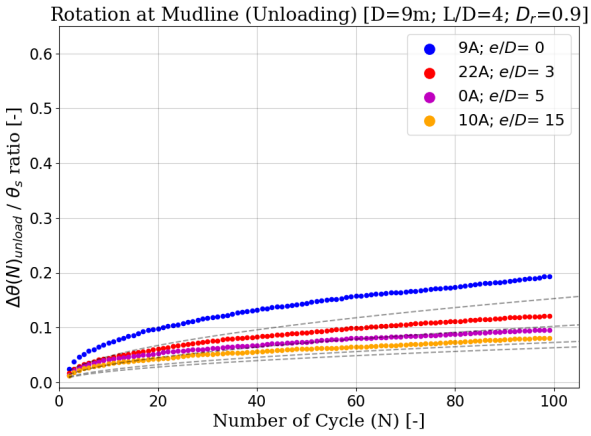

θ_{acc} at unloading

The effect of load eccentricity (e/D) on θ_{acc} at the mudline during cyclic load with $\zeta_b = 0.1$, presented during (a) loading phase and (b)unloading phase ($D = 9m; L/D = 4, D_r = 0.9$).

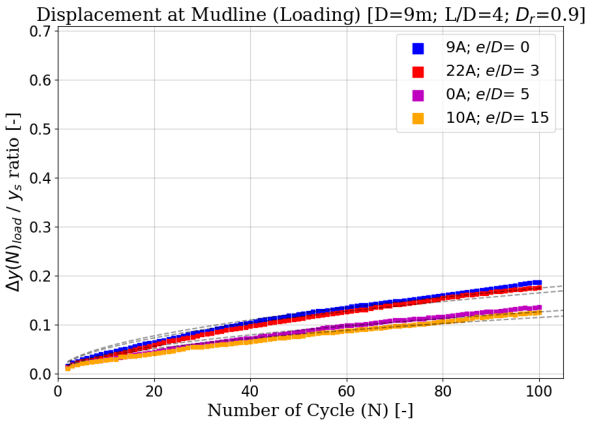

y_{acc} at loading

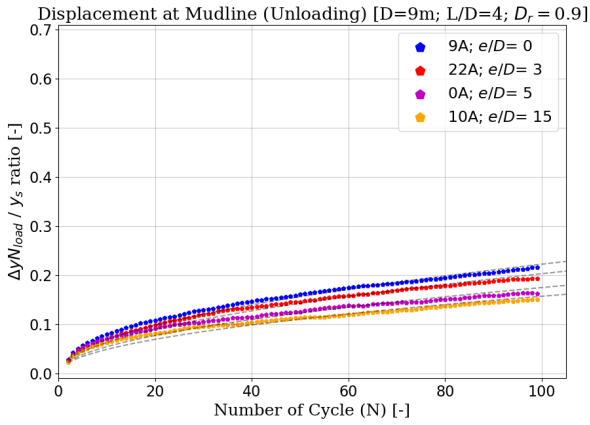

y_{acc} at unloading

The effect of load eccentricity (e/D) on y_{acc} at the mudline during cyclic load with $\zeta_b = 0.1$, presented during (a) loading phase and (b)unloading phase ($D = 9m; L/D = 4, D_r = 0.9$).

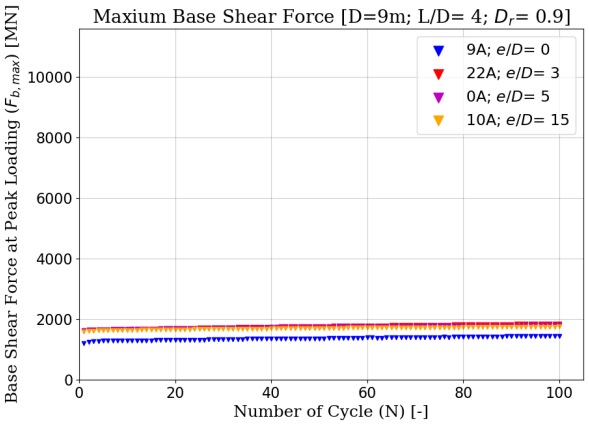

F_b at peak loading

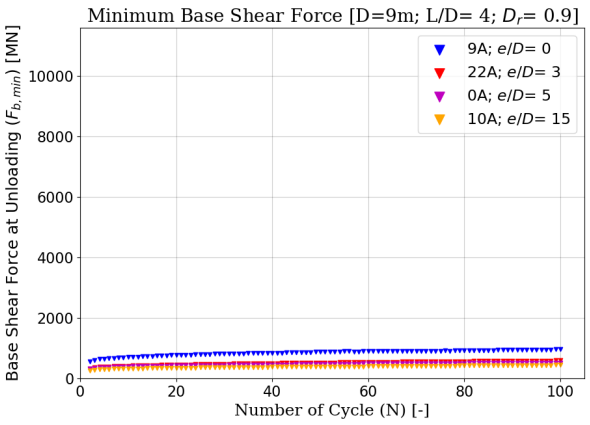

F_b at $H = 0$

The effect of load eccentricity (e/D) on the F_b during (a) maximum loading applied and (b) load completely released ($D = 9m, L/D = 4, D_r = 0.9, \zeta_b = 0.1$.

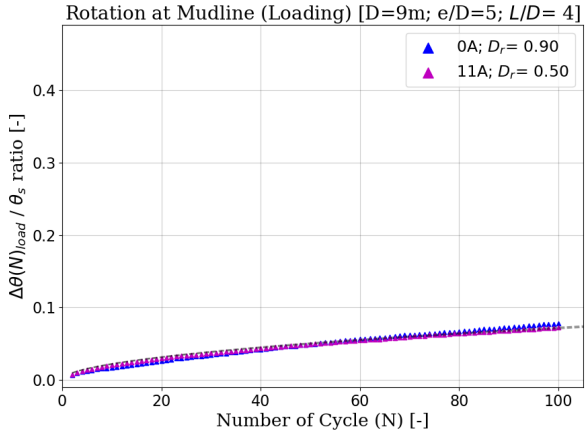

θ_{acc} at loading

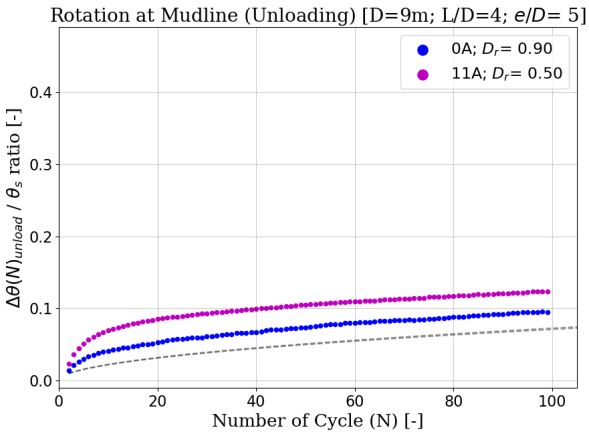

θ_{acc} at unloading

The effect of sand relative density (D_r) on θ_{acc} at the mudline during cyclic load with $\zeta_b = 0.1$, presented during (a) loading phase and (b) unloading phase ($D = 9m; L/D = 4, e/D = 5$).

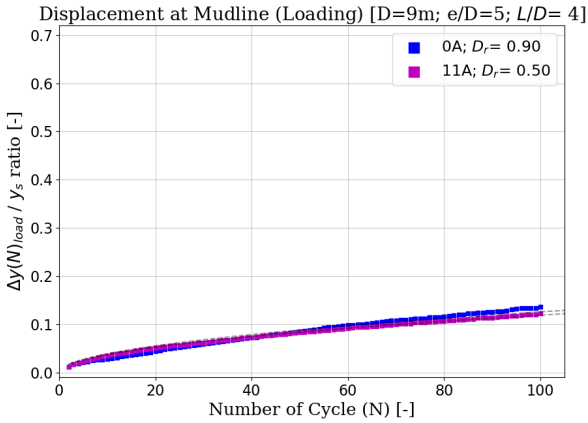

y_{acc} at loading

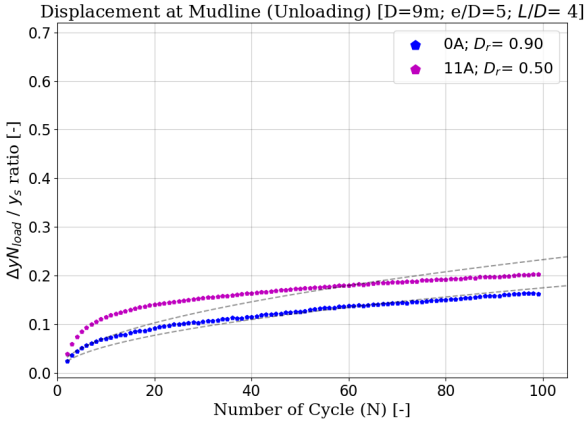

y_{acc} at unloading

The effect of sand relative density (D_r) on y_{acc} at the mudline during cyclic load with $\zeta_b = 0.1$, presented during (a) loading phase and (b) unloading phase ($D = 9m; L/D = 4, e/D = 5$).

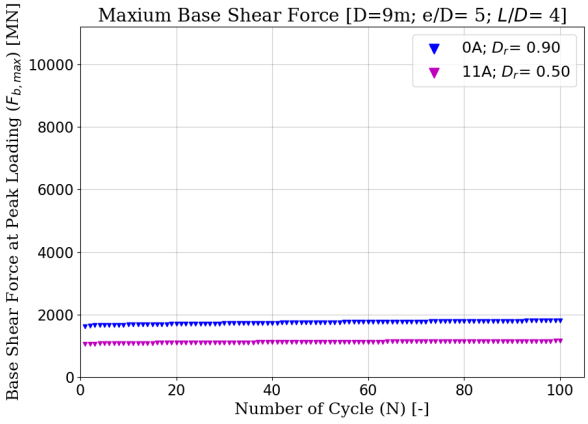

F_b at peak loading

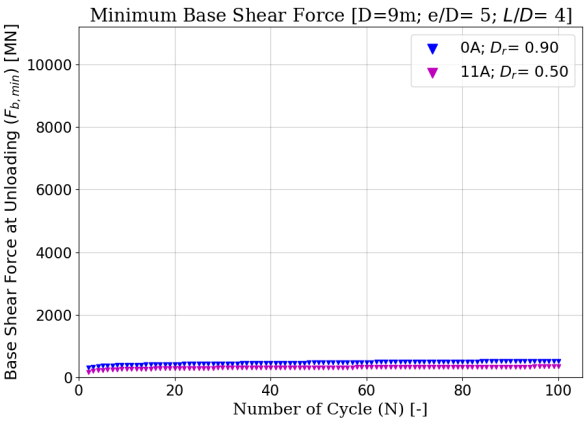

F_b at $H = 0$

The effect of pile relative density (D_r) on the F_b during (a) maximum loading applied and (b) load completely released ($D = 9m, L/D = 4, D_r = 0.9, \zeta_b = 0.1$).

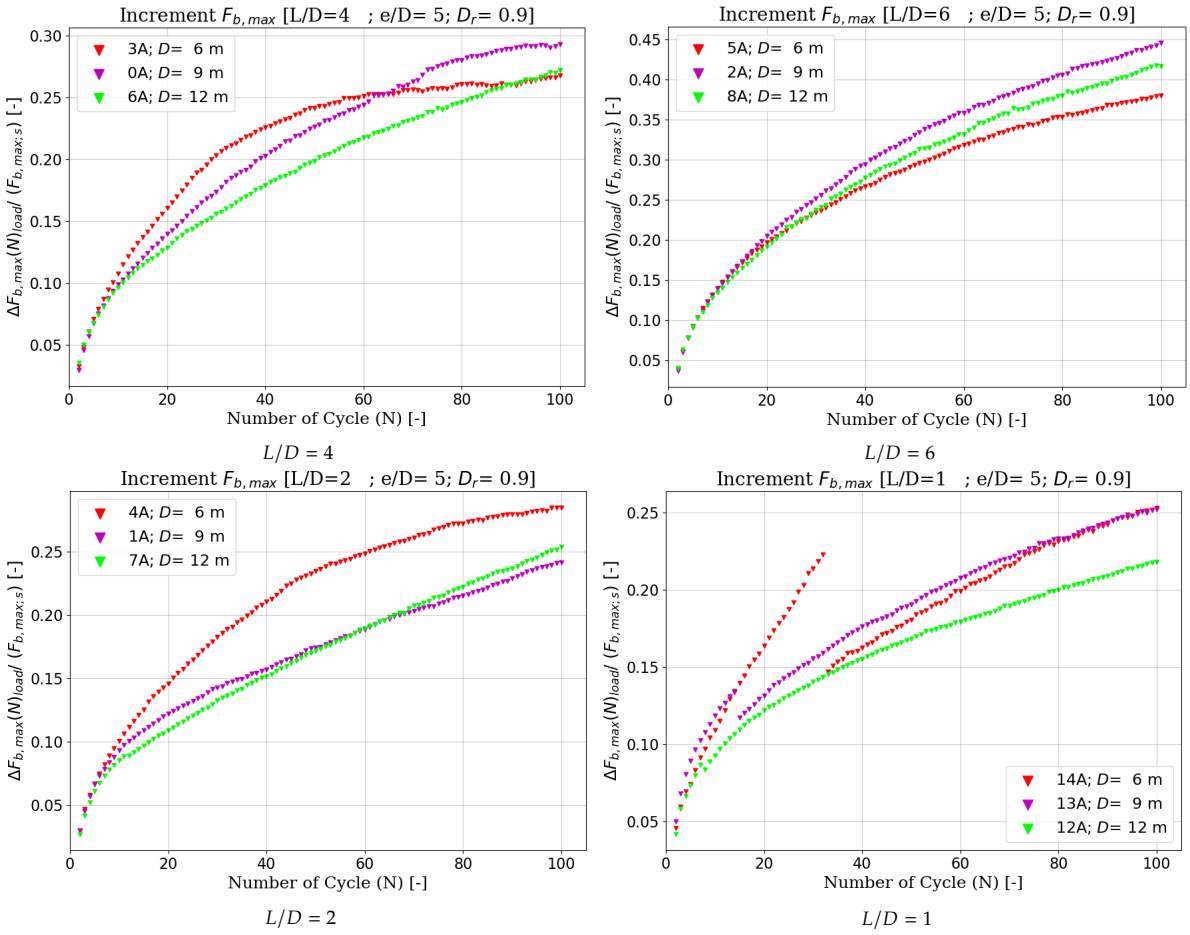

The effect of pile geometry (L and D) on the $\Delta F_{b,max}(N)/\ \Delta F_{b,max;s}$ for monopile with $e/D = 5$, installed in sand with $D_r = 0.9$ for (a) $L/D = 4$, (b) $L/D = 6$, (c) $L/D = 2$, and (d) (b) $L/D = 1$ with $\zeta_b = 0.4$

.

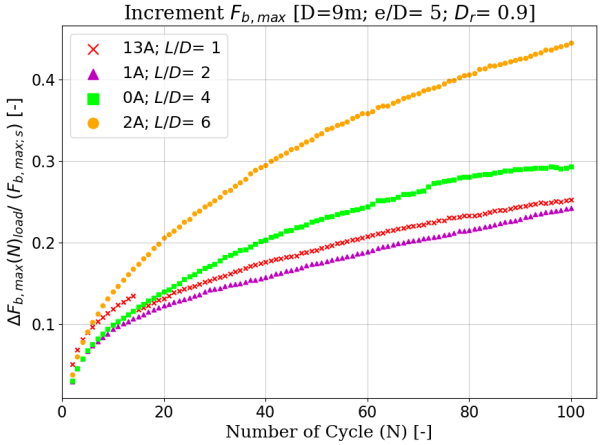

The effect of pile L/D on the $\Delta F_{b,max}(N)/\ \Delta F_{b,max;s}$ for monopile with $e/D = 5, D = 9m, D_r = 0.9, \zeta_b = 0.4$

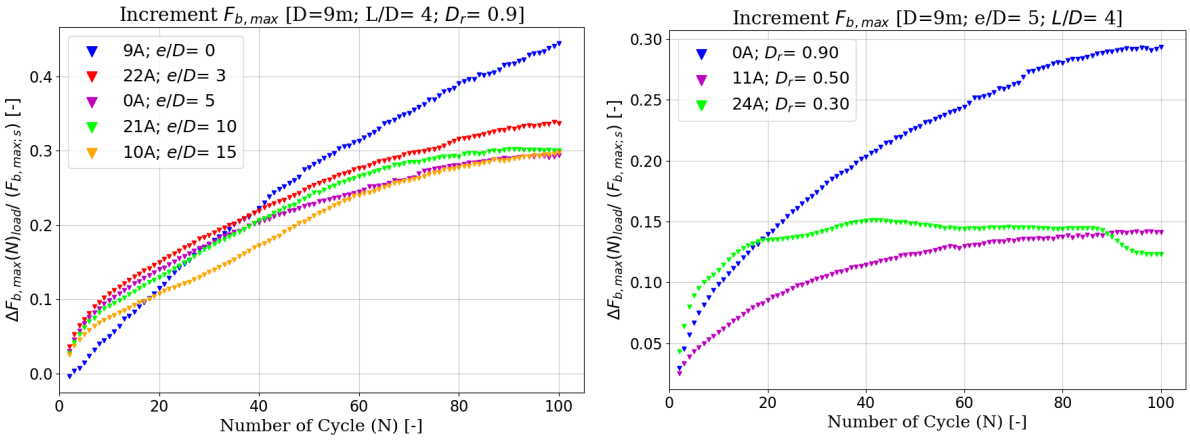

The effect of (a) e/D and (b) D_r on the $\Delta F_{b,max}(N)/\ \Delta F_{b,max;s}$ for monopile with $D = 9m, L/D = 4, \zeta_b = 0.4$

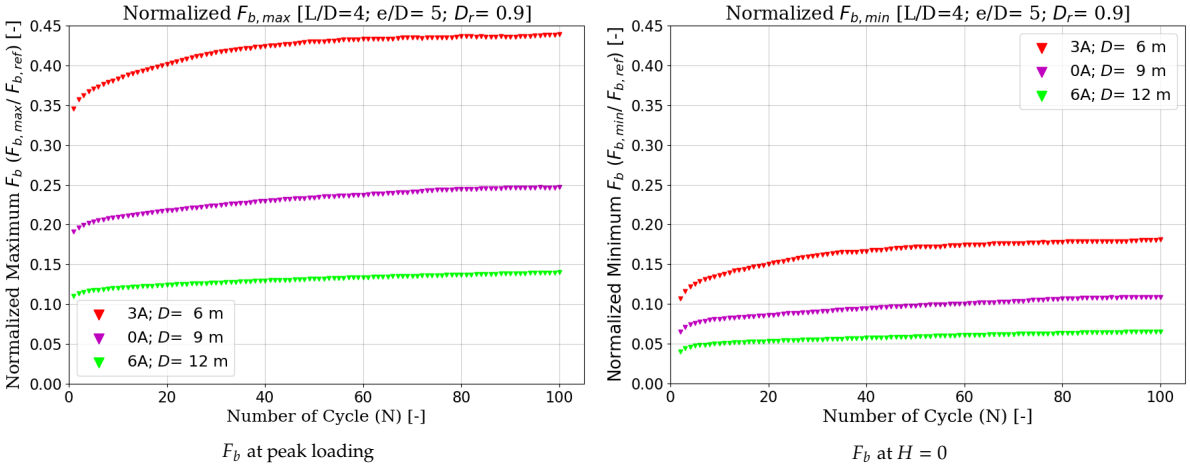

The effect of pile geometry (L and D) on the normalized F_b during (a)maximum loading applied and (b) load completely released ($L/D = 4, e/D = 5, D_r = 0.9, \zeta_b = 0.4$).

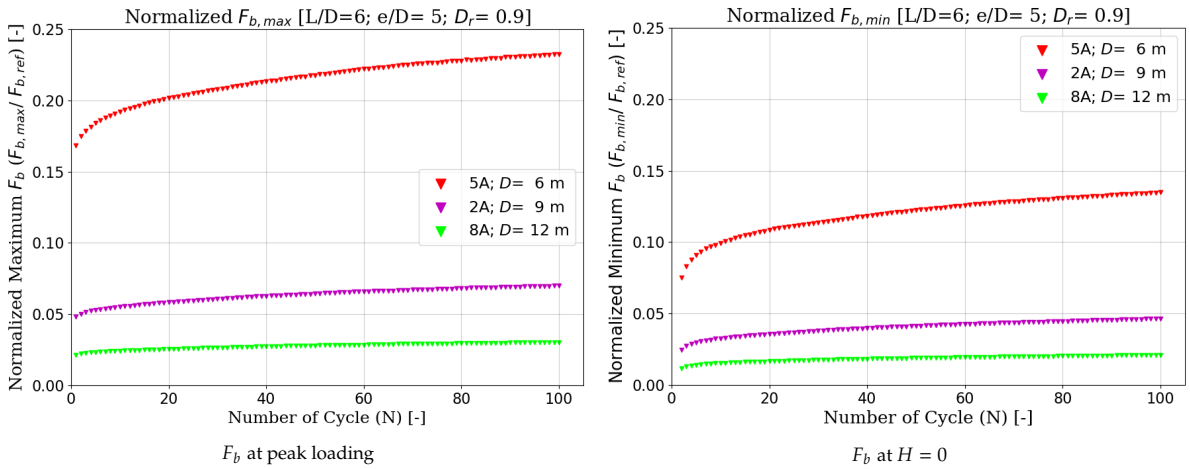

The effect of pile geometry (L and D) on the normalized F_b during (a)maximum loading applied and (b) load completely released ($L/D = 6, e/D = 5, D_r = 0.9, \zeta_b = 0.4$).

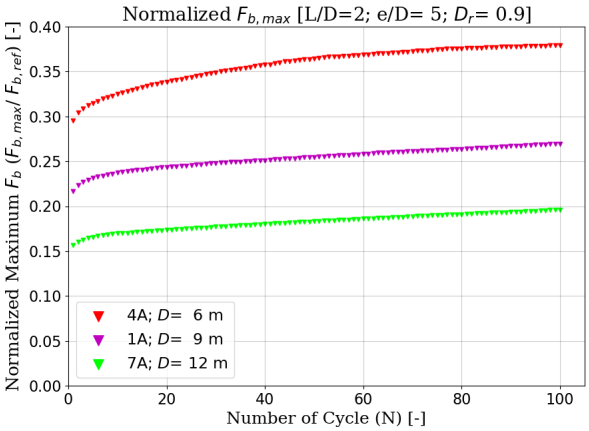

F_b at peak loading

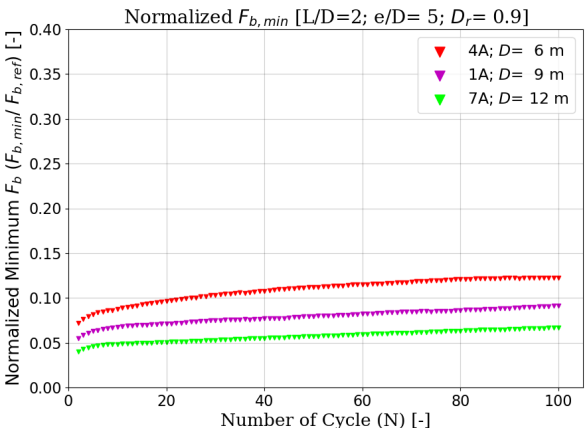

F_b at $H = 0$

The effect of pile geometry (L and D) on the normalized F_b during (a)maximum loading applied and (b) load completely released ($L/D = 2, e/D = 5, D_r = 0.9, \zeta_b = 0.4$).

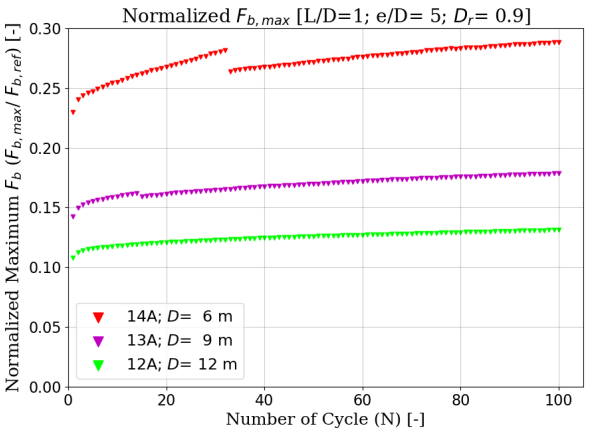

F_b at peak loading

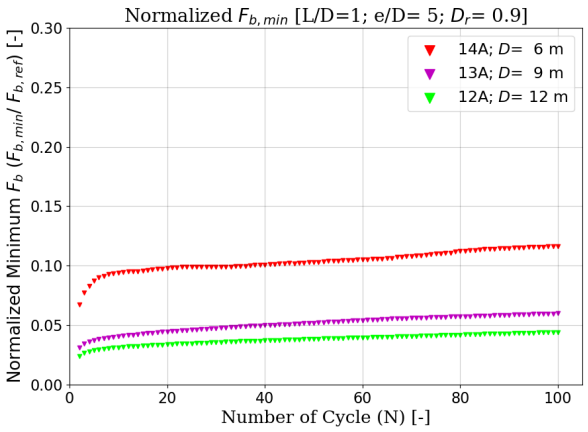

F_b at $H = 0$

The effect of pile geometry (L and D) on the normalized F_b during (a)maximum loading applied and (b) load completely released ($L/D = 1, e/D = 5, D_r = 0.9, \zeta_b = 0.4$).

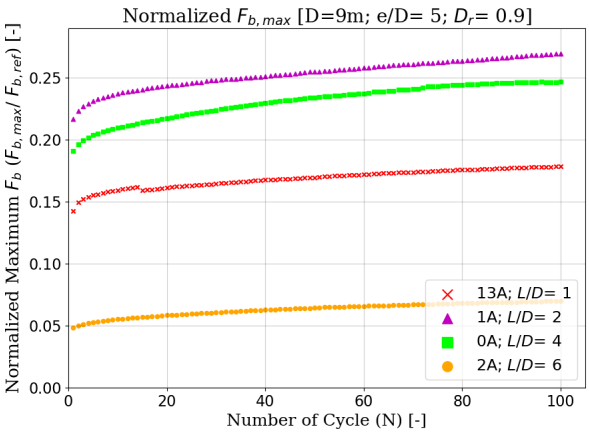

F_b at peak loading

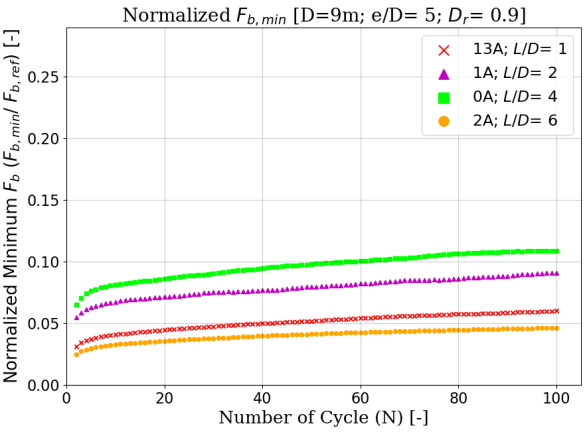

F_b at $H = 0$

The effect of pile L/D on the normalized F_b during (a)maximum loading applied and (b) load completely released ($D = 9m, e/D = 5, D_r = 0.9, \zeta_b = 0.4$).

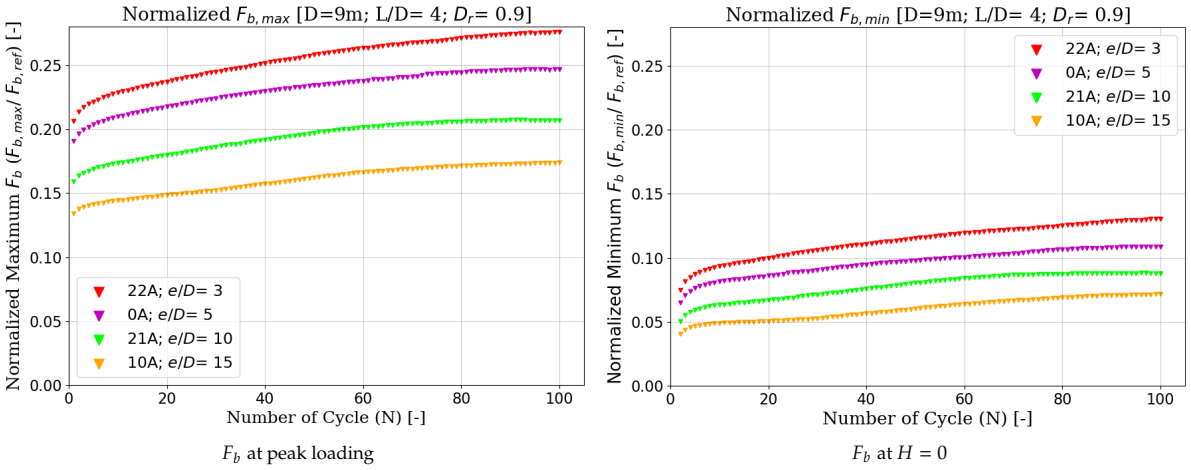

The effect of load eccentricity (e/D) on the normalized F_b during (a) maximum loading applied and (b) load completely released ($D = 9m, L/D = 4, D_r = 0.9, \zeta_b = 0.4$.

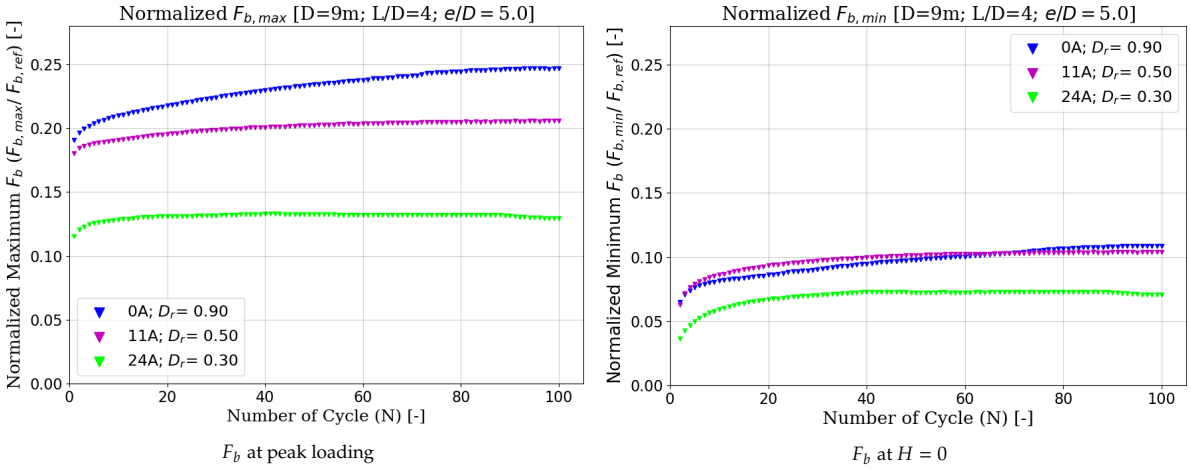

The effect of pile relative density (D_r) on the normalized F_b during (a) maximum loading applied and (b) load completely released ($D = 9m, L/D = 4, D_r = 0.9, \zeta_b = 0.4$).

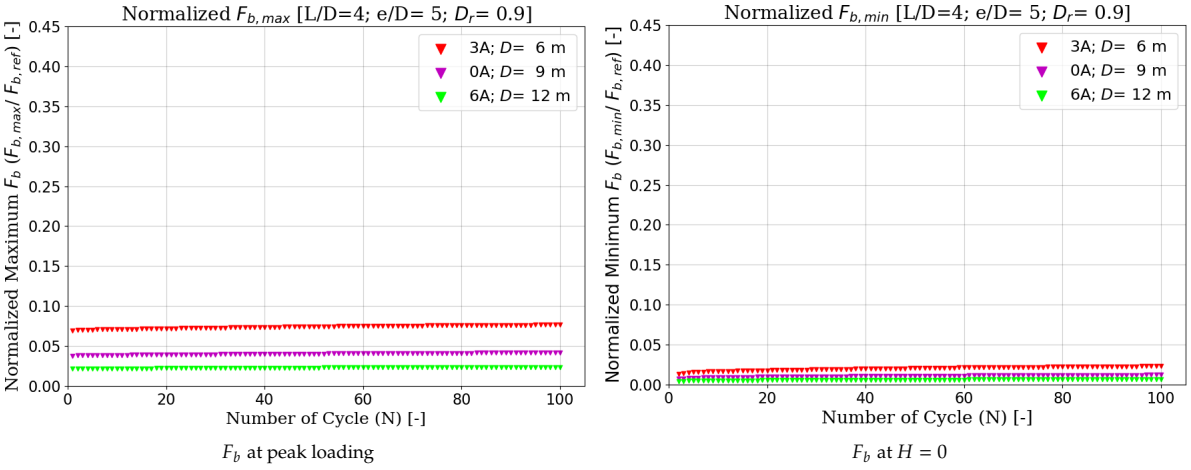

The effect of pile geometry (D and L) on the normalized F_b during (a) maximum loading applied and (b) load completely released ($L/D = 4, e/D = 5, D_r = 0.9, \zeta_b = 0.1$).

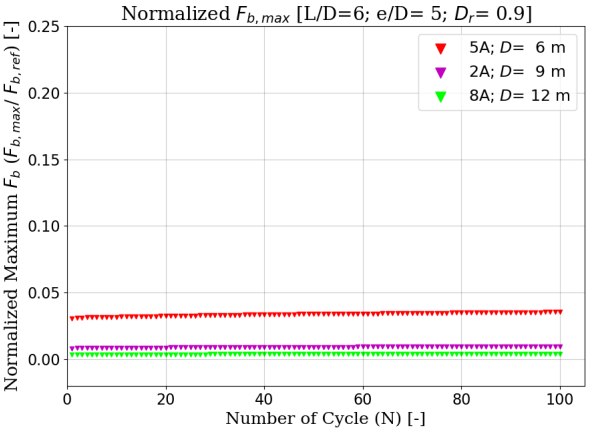

F_b at peak loading

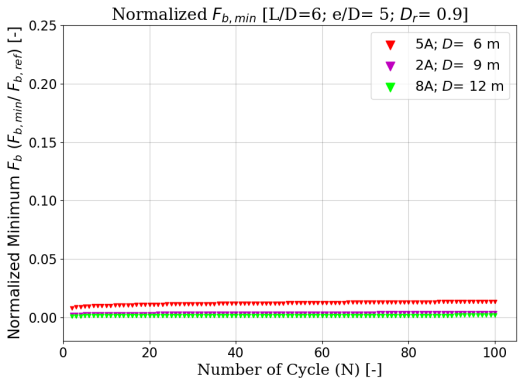

F_b at $H = 0$

The effect of pile geometry (D and L) on the normalized F_b during (a) maximum loading applied and (b) load completely released ($L/D = 6, e/D = 5, D_r = 0.9, \zeta_b = 0.1$).

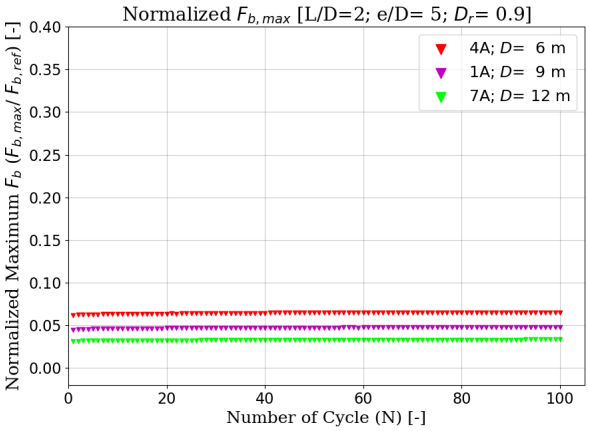

F_b at peak loading

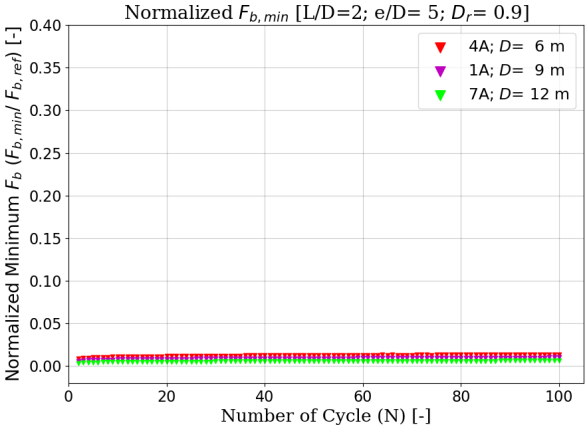

F_b at $H = 0$

The effect of pile geometry (D and L) on the normalized F_b during (a) maximum loading applied and (b) load completely released ($L/D = 2, e/D = 5, D_r = 0.9, \zeta_b = 0.1$).

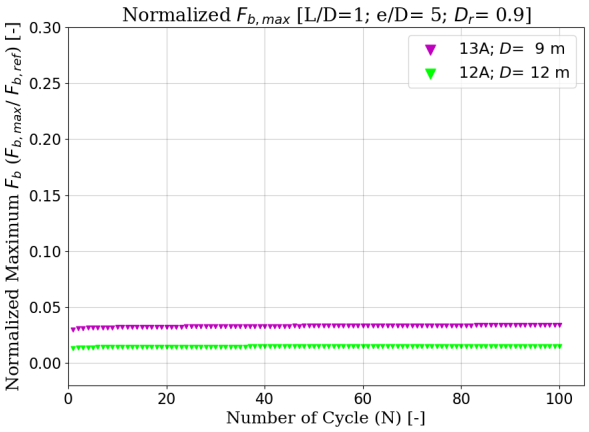

F_b at peak loading

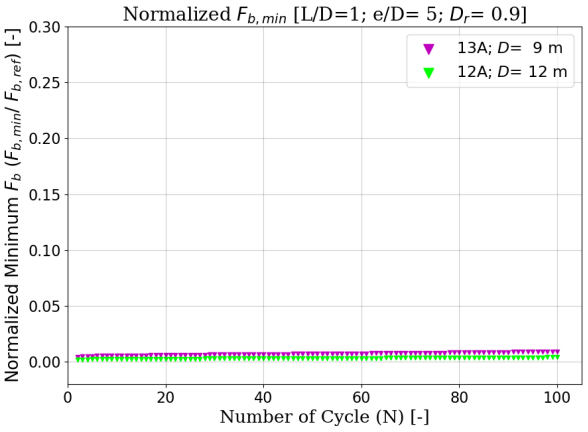

F_b at $H = 0$

The effect of pile geometry (D and L) on the normalized F_b during (a) maximum loading applied and (b) load completely released ($L/D = 1, e/D = 5, D_r = 0.9, \zeta_b = 0.1$).

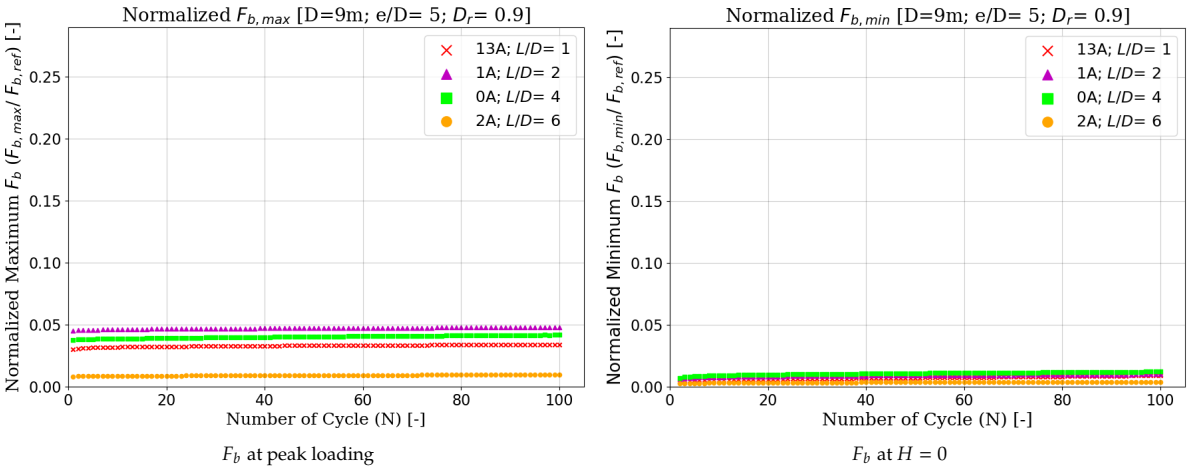

The effect of L/D on the normalized F_b during (a) maximum loading applied and (b) load completely released ($= 9m, e/D = 5, D_r = 0.9, \zeta_b = 0.1$).

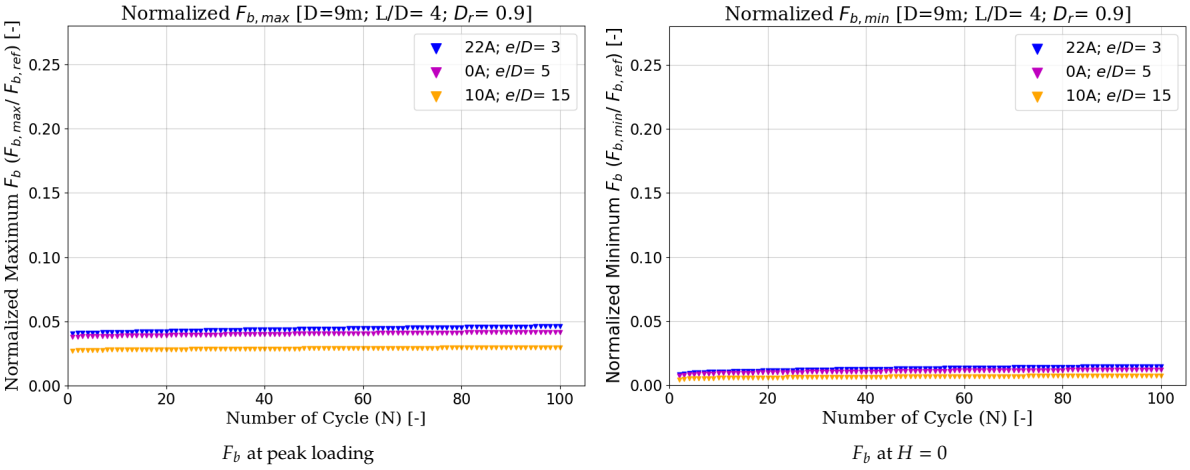

The effect of e/D on the normalized F_b during (a) maximum loading applied and (b) load completely released ($= 9m, L/D = 4, D_r = 0.9, \zeta_b = 0.1$).

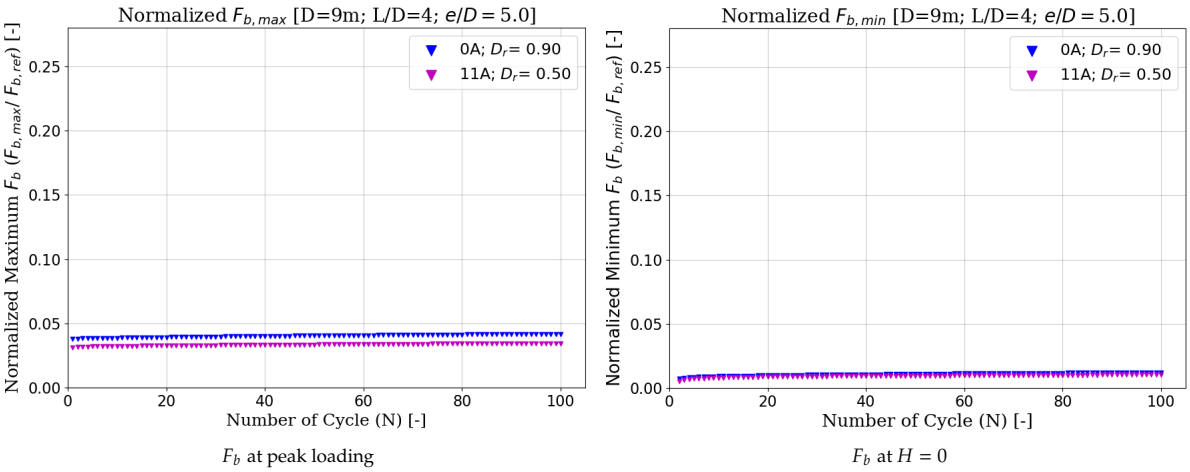

The effect of D_r on the normalized F_b during (a) maximum loading applied and (b) load completely released ($= 9m, L/D = 4, e/D = 5, \zeta_b = 0.1$).

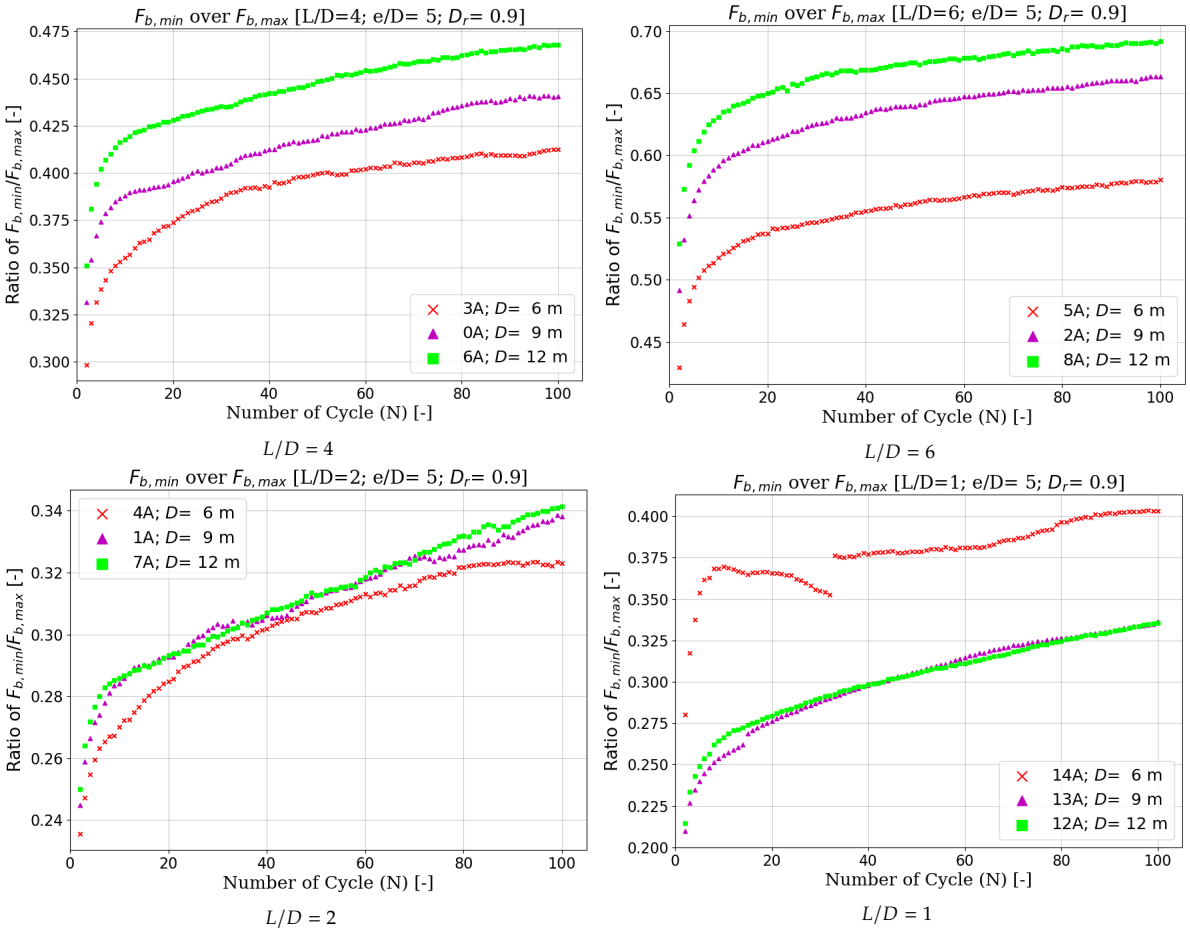

The effect of pile geometry (L and D) on the ratio $F_{b,max}/F_{b,min}$ for monopile with $e/D = 5$, installed in sand with $D_r = 0.9$ for (a) $L/D = 4$, (b) $L/D = 6$, (c) $L/D = 2$, and (d) (b) $L/D = 1$; with $\zeta_b = 0.4$

.

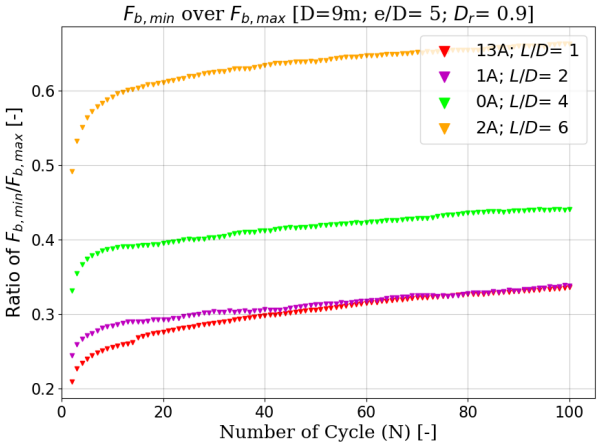

The effect of pile L/D on the ratio $F_{b,max}/F_{b,min}$ for monopile with $e/D = 5, D = 9m, D_r = 0.9, \zeta_b = 0.4$

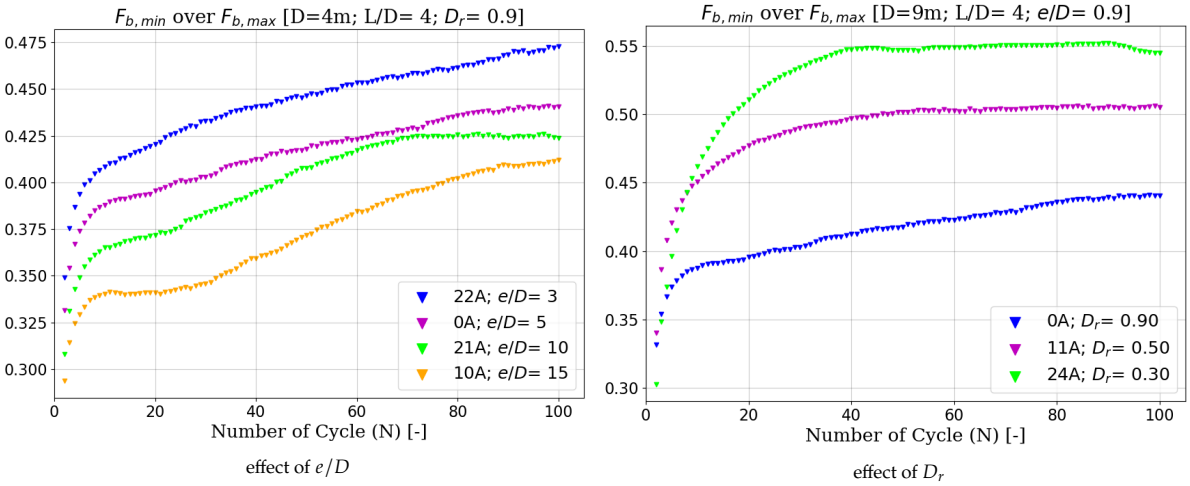

The effect of (a) e/D and (b) D_r on the ratio $F_{b,max}/F_{b,min}$ for monopile with $D = 9m, L/D = 4, \zeta_b = 0.4$

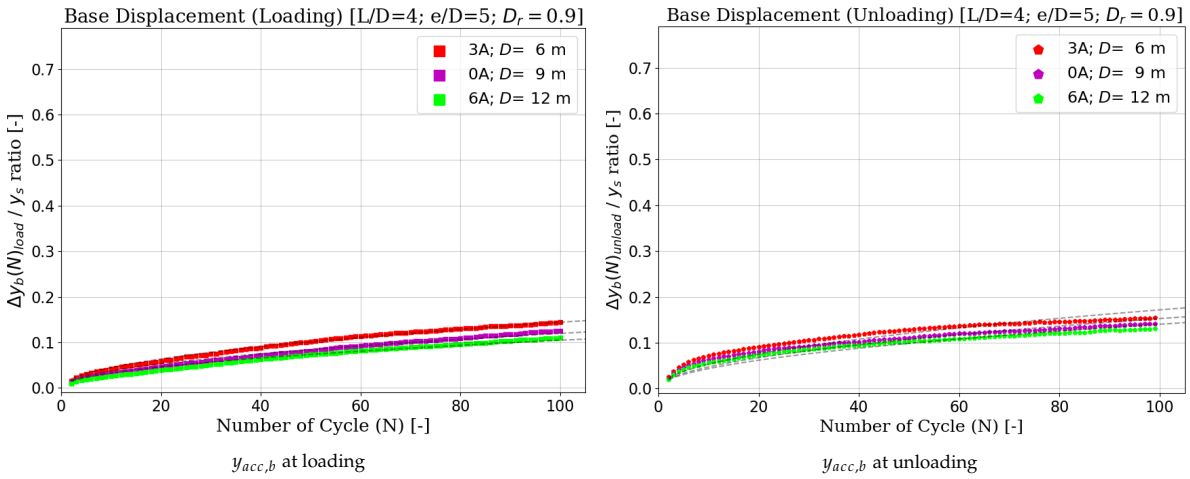

The effect of pile geometry (L and D) on y_{acc} at pile base during cyclic load with $\zeta_b = 0.1$, presented during (a) loading phase and (b)unloading phase ($L/D = 4, e/D = 5, D_r = 0/9$).

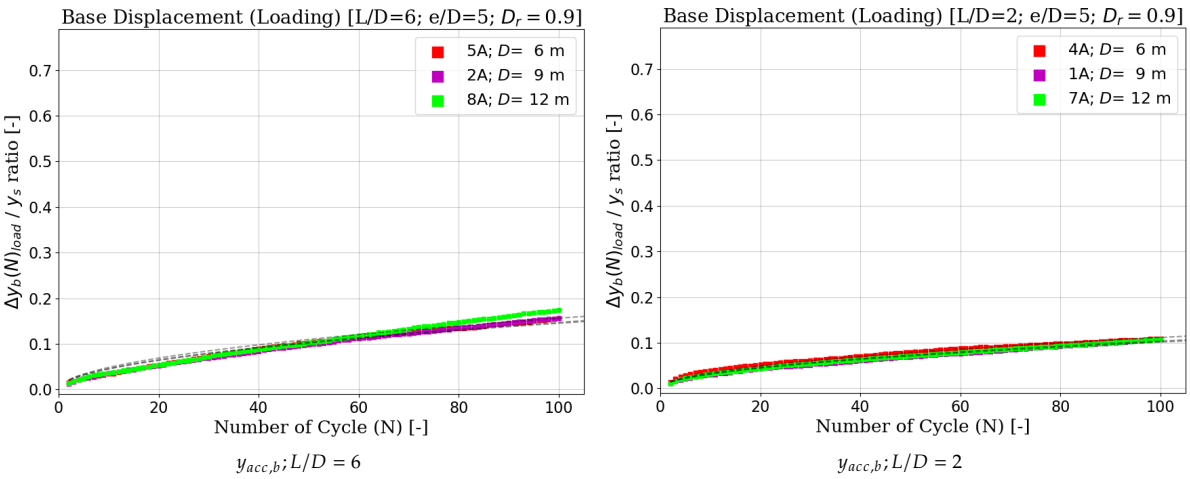

The effect of pile geometry (L and D) on y_{acc} at pile base during cyclic load with $\zeta_b = 0.1$, presented during loading phase for pile with (a)$L/D = 6$ adn (b) $L/D = 2$ for cases with ($e/D = 5, D_r = 0.9$)

.

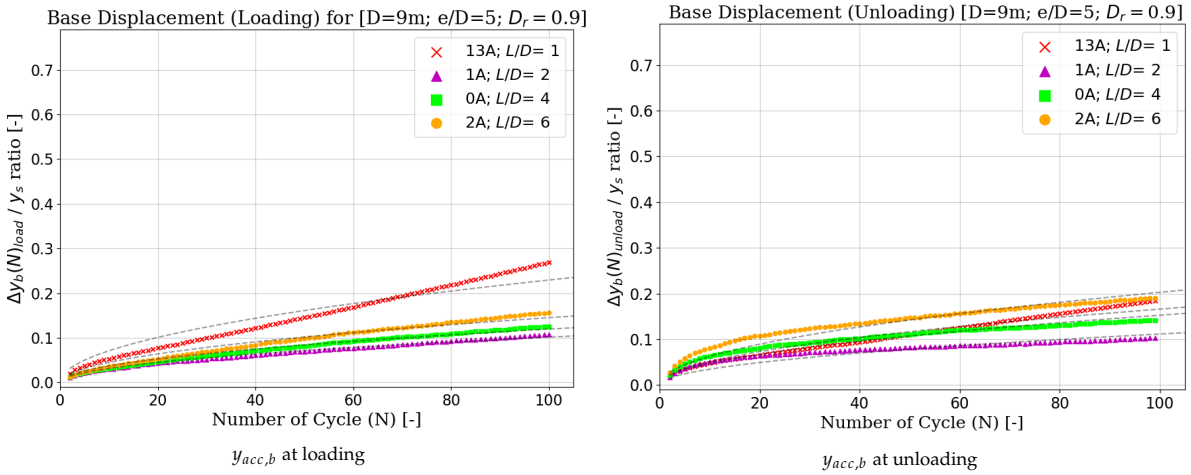

The effect of pile L/D on y_{acc} at pile base during cyclic load with $\zeta_b = 0.1$, presented during (a) loading phase and (b)unloading phase ($D = 9m, e/D = 5, D_r = 0/9$).

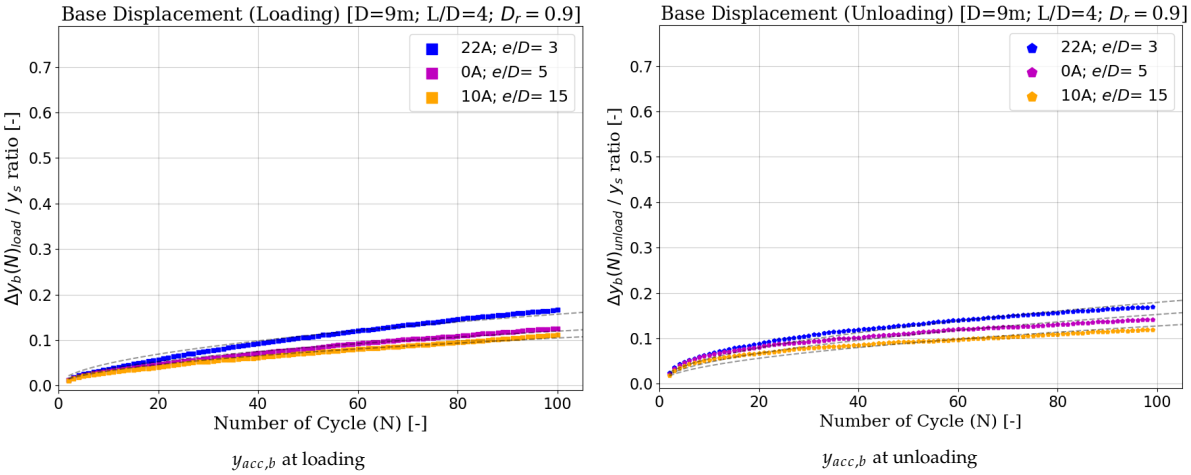

The effect of e/D on y_{acc} at pile base during cyclic load with $\zeta_b = 0.1$, presented during (a) loading phase and (b)unloading phase ($D = 9m, L/D = 4, D_r = 0/9$).

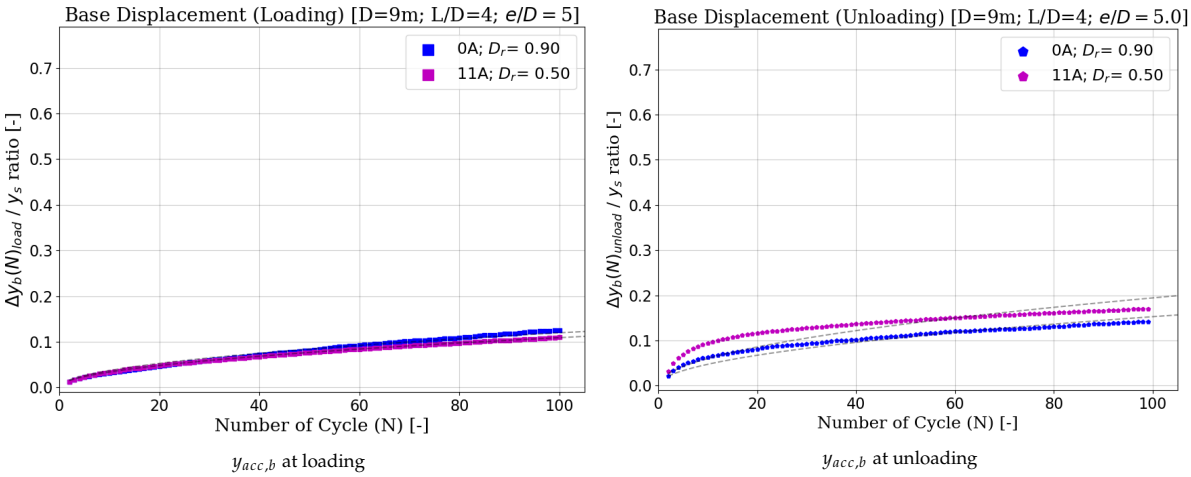

The effect of D_r on y_{acc} at pile base during cyclic load with $\zeta_b = 0.1$, presented during (a) loading phase and (b)unloading phase ($D = 9m, L/D = 4, e/D = 5$).

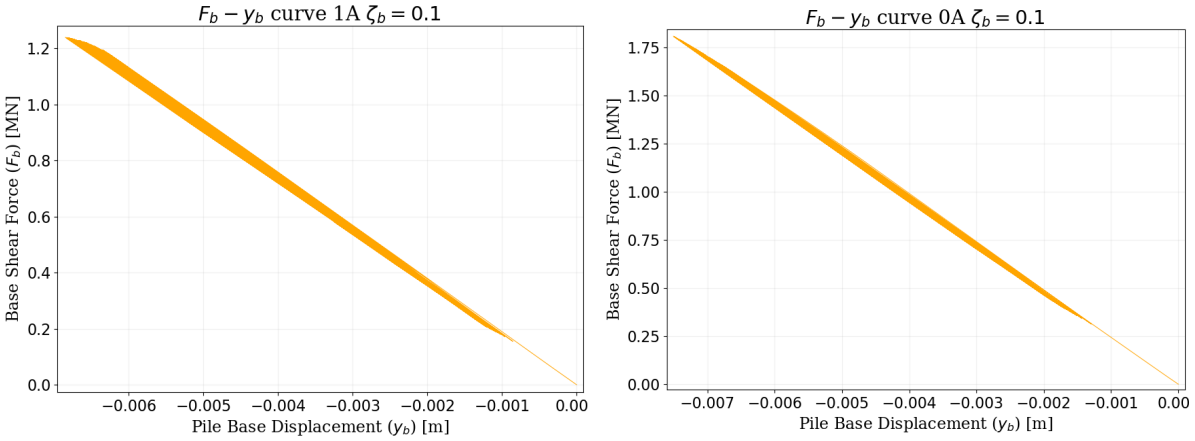

0A ($D = 9m; L/D = 4; e/D = 5; D_r = 0.9$) 1A ($D = 9m; L/D = 2; e/D = 5; D_r = 0.9$)

The $F_b - y_b$ curve for (a) Case 0A and (b) Case 1A with $\zeta_b = 0.1$ indicate an acceleration in accumulated displacement at the end of cycles.

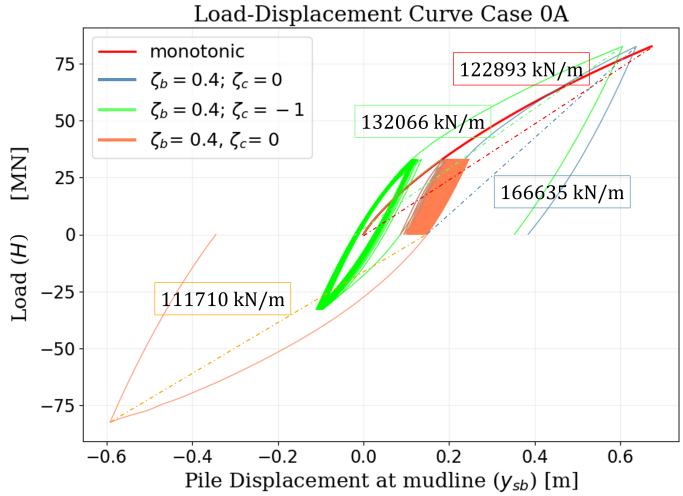

Load-Displacement Curve for monotonic test only and monotonic loading that imposed after 40 cyclic loading.

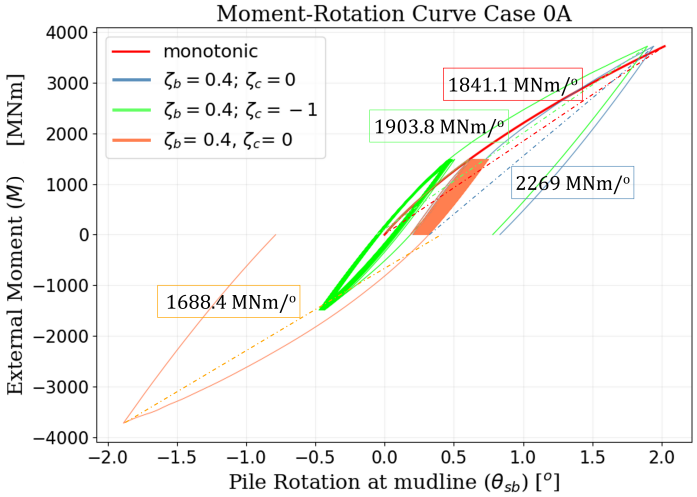

Moment-Rotation Curve for monotonic test only and monotonic loading that imposed after 40 cyclic loading.